



HAL
open science

Electrochemical modification of the liquid – liquid interface with mesoporous silica

Lukasz Poltorak

► **To cite this version:**

Lukasz Poltorak. Electrochemical modification of the liquid – liquid interface with mesoporous silica. Other. Université de Lorraine, 2015. English. NNT : 2015LORR0105 . tel-01751800

HAL Id: tel-01751800

<https://hal.univ-lorraine.fr/tel-01751800v1>

Submitted on 29 Mar 2018

HAL is a multi-disciplinary open access archive for the deposit and dissemination of scientific research documents, whether they are published or not. The documents may come from teaching and research institutions in France or abroad, or from public or private research centers.

L'archive ouverte pluridisciplinaire **HAL**, est destinée au dépôt et à la diffusion de documents scientifiques de niveau recherche, publiés ou non, émanant des établissements d'enseignement et de recherche français ou étrangers, des laboratoires publics ou privés.



AVERTISSEMENT

Ce document est le fruit d'un long travail approuvé par le jury de soutenance et mis à disposition de l'ensemble de la communauté universitaire élargie.

Il est soumis à la propriété intellectuelle de l'auteur. Ceci implique une obligation de citation et de référencement lors de l'utilisation de ce document.

D'autre part, toute contrefaçon, plagiat, reproduction illicite encourt une poursuite pénale.

Contact : ddoc-theses-contact@univ-lorraine.fr

LIENS

Code de la Propriété Intellectuelle. articles L 122. 4

Code de la Propriété Intellectuelle. articles L 335.2- L 335.10

http://www.cfcopies.com/V2/leg/leg_droi.php

<http://www.culture.gouv.fr/culture/infos-pratiques/droits/protection.htm>



Sujet de thèse:

Modification électrochimique de l'interface liquide – liquide avec de la silice mésoporeuse

Par

Lukasz Poltorak

Pour l'obtention de titre de

Docteur

Rapporteurs:

Prof. Edmond Magner – Professeur à University of Limerick, Irlande;

Prof. Sabine Szunerits – Professeur à l'Université de Lille, Lille, France ;

Examineurs:

Dr. Ritu Katakya – Reader à Durham University, Durham, United Kingdom;

Dr. Alain Walcarius – Directeur de Recherche à LCPME, Viller-lès-Nancy, France;

Dr. Grégoire Herzog – Chargé de Recherche à LCPME, Viller-lès-Nancy, France.

Prof. Jean-Luc Blin - Professeur à l'Université de Lorraine, Vandœuvre-lès-Nancy, France.

Ecole Doctorale:

Synthèse, Simulations, Applications: de la Molécule aux Edifices Supramoléculaires (SESAMES) ED 412.

Date de soutenance prévue: 25.09.2015

Laboratoire de Chimie Physique et Microbiologie pour l'Environnement (LCPME)

Unité mixte de recherche – UMR 756

405 Rue de Vandoeuvre, 54600, Villers-lès-Nancy, France



A thesis:

Electrochemical modification of the liquid – liquid interface with mesoporous silica

by

Lukasz Poltorak

for the

Doctor degree

Reviewers:

Prof. Edmond Magner – Professor at University of Limerick, Ireland;

Prof. Sabine Szunerits – Professor at Lille 2 University, Lille, France;

Examiners:

Dr. Ritu Katakya – Reader at Durham University, Durham, United Kingdom;

Dr. Alain Walcarius – Directeur de Recherche at LCPME, Villers-lès-Nancy, France;

Dr. Grégoire Herzog – Chargé de Recherche at LCPME, Villers-lès-Nancy, France;

Prof. Jean-Luc Blin - Professor at University of Lorraine, Vandœuvre-lès-Nancy, France.

PhD school:

Synthèse, Simulations, Applications: de la Molécule aux Edifices Supramoléculaires (SESAMES) ED 412.

Planned defense date: 25.09.2015

Laboratoire de Chimie Physique et Microbiologie pour l'Environnement (LCPME)

Unité mixte de recherche – UMR 756

405 Rue de Vandoeuvre, 54600, Villers-lès-Nancy, France

Dedication

I dedicate this thesis to my loved,
wonderful and ever supporting wife
who is with me through thick and thin.

Acknowledgements

ACKNOWLEDGEMENTS

At the very beginning I am glad to express my deepest gratitude to two big personalities, my supervisors, **Alain Walcarius** and **Grégoire Herzog**. Being a member of ELAN team was a great pleasure and it was possible as they trusted in me. For the last three years I could unceasingly count on their priceless scientific advices and help. I will miss our very fruitful discussions, which has resulted in series of interesting discoveries. The time, which they have invested in me, resulted in my tremendous personal development – I am in their debt.

I would also like to acknowledge other people who have contributed to this work. I will especially highlight **Manuel Dossot** and **Jérôme Grausem** who have helped me a lot with the Raman spectroscopy, **Cédric Carteret** for his help with infra-red spectroscopy, **Mathieu Etienne** for his help with SECM, **Neus Vila** for advices concerning organic synthesis, **Christelle Despas** for help with ion chromatography and **Marc Hebrant** for his engagement during HPLC analysis.

I am also indebted to the people who were involved in other aspects of my work. Particularly, I would like to acknowledge **Marie-José Stébé**, **Andreea Pasc** and **Melanie Emo** for SAXS analysis and precious discussions, **Aurélien Renard** for XPS analysis, **Jaafar Ghanbaja** and **Sylvie Migot** for TEM imaging and **Lise Salsi** for the SEM imaging.

A special acknowledgement goes to my office mates and good friends: **Doktorka Veronika Urbanova**, **Ievgien Mazurenko** and **Daniel Alonso Gamero Quijano**.

Next in row are lab mates. With **Ivan Vakulko** and **Khaoula Hamdi** we started our theses at the same time. **Wissam Ghach** introduced me to the laboratory organization. **Lin Zhang** started her thesis at the end of 2013. **Mohana Afsharian** first did her master training in 2013 and then, in 2104 joined ELAN team as a PhD student. During my third year **Maciek Mierzwa**, **Tauqir Nasir**, **Cheryl Maria Karman** and **Stephane Pinck** became a part of our team. **Martha Collins** and **Maizatul Najwa Binti Jajuli**, both working with liquid – liquid interface, did master internship in our team in 2015. Together we were a dozen or so nationalities working under one roof. It was a great pleasure to be a part of such multicultural team.

Acknowledgements

One period of my PhD was a DocSciLor 2015 organization. For great fun and new experience I am glad to gratitude **Fernanda Bianca Haffner, Hugo Gattuso, Ileana-Alexandra Pavel, Ivan and Maciek.**

I also want to acknowledge **Claire Genois** for taking care about the laboratory organization, which has made our lives easier. I cannot omit the work shop team: **Jean-Paul Moulin** also known as **Monsieur Moustache**, **Gérard Paquot** and **Patrick Bombardier**. I am very grateful for their technical support.

My acknowledgements also go to **Marie Tercier, Christelle Charbaut**, and **Jacqueline Druon** for their help with all administration issues and of course to all LCPME members.

Last but not least I appreciate a financial support from **Région Lorraine** and to **Ecole Doctorale SESAMES** (ED 412, Université de Lorraine) for my PhD grant.

Table of content

Abstract – English version	1
Résumé – Version Français	3
Frequently used abbreviations	5
1. Chapter I. Bibliographical introduction	6
1.1. Electrified interface between two immiscible electrolyte solutions.....	6
1.1.1. Liquid – liquid interface structure.....	7
1.1.2. Charge transfer reactions at the ITIES	8
1.1.2.1. Simple ion transfer reaction.....	9
1.1.2.2. Assisted/facilitated ion transfer	11
1.1.2.3. Electron transfer across ITIES.....	14
1.1.2.4. Electrochemically induced interfacial adsorption	15
1.1.3. Potential window and limiting current.....	16
1.1.4. Electrochemical instability at the electrified liquid – liquid interface in the presence of ionic surfactants.....	21
1.1.5. Miniaturization of the ITIES.....	22
1.2. Sol – Gel Process of Silica employing Template Technology.....	25
1.2.1. Nomenclature and physicochemical properties of silicon and silicon containing compounds.....	25
1.2.2. The Sol – Gel process of silica	27
1.2.2.1. Hydrolysis.....	28
1.2.2.2. Condensation	29
1.2.2.3. Dissolution	30
1.2.2.4. Curing.....	30
1.2.3. Templates – towards surface engineering.....	30
1.2.4. A soft template for a Sol-Gel process of mesoporous silica thin films.....	32
1.2.5. Functionalized mesoporous silica films prepared by Sol-Gel processing	33
1.3. Liquid – liquid interface modification	34
1.3.1. Metals at the electrified liquid – liquid interface.	34
1.3.1.1. Au deposition at the ITIES	35
1.3.1.2. Ag deposition at the electrified ITIES	38

Table of content

1.3.1.3.	Pd and Pt deposition at the electrified ITIES	40
1.3.2.	Phospholipids at the electrified liquid – liquid interface	41
1.3.3.	Organic polymers at the polarized liquid – liquid interface	44
1.3.4.	Carbon based materials at/near polarized liquid – liquid interface.....	47
1.3.5.	Silica modified liquid – liquid interface	51
1.3.5.1.	Three phase junction systems	52
1.3.5.2.	Neat, non-polarized liquid – liquid interface <i>in situ</i> modification with silica material.....	53
1.3.5.3.	Electrified Interface between Two Immiscible Electrolyte Solutions modification with silica materials	58
1.3.5.3.1.	<i>Ex situ</i> modification.....	58
1.3.5.3.2.	<i>In situ</i> modification.....	61
2.	Chapter II. Experimental part.....	63
2.1.	Chemicals	63
2.2.	Electrochemical set-ups.....	66
2.3.	Composition of electrochemical cells. The aqueous and the organic phase preparation	71
2.4.	Instrumentation.....	74
2.5.	Protocols.....	76
2.5.1.	Preparation procedure of BTPPA ⁺ TPBCl ⁻	76
2.5.2.	Preparation procedure of CTA ⁺ TPBCl ⁻	77
2.5.3.	Preparation procedure of TBA ⁺ TPBCl ⁻	79
2.5.4.	Preparation procedure of PH ⁺ TPBCl ⁻	80
2.5.5.	Protocol of organic counter electrode preparation	82
2.5.6.	Single pore microITIES protocol of preparation	85
2.5.7.	Protocol of preparation of trimethylbenzhydrylammonium iodide	89
3.	Chapter III. Templated Sol – Gel process of silica at the electrified liquid – liquid interface.....	92
3.1.	Results and discussion.....	94
3.1.1.	Electrochemical study.....	94
3.1.2.	Characterization of silica deposits electrogenerated at the ITIES	100
3.1.3.	Spectroscopic analysis	100
3.1.4.	BET analysis	103
3.1.5.	Morphological characterization	104

Table of content

3.2. Conclusion.....	106
4. Chapter IV. Silica electrodeposition using cationic surfactant as a template at miniaturized ITIES	108
4.1. Electrochemical and morphological study of silica deposits at the array of microITIES	108
4.1.1. Surfactant-template assisted Sol-Gel process of silica at the microITIES	109
4.1.1.1. Factors affecting silica deposition at the array of microITIES.....	111
4.1.1.1.1. Influence of $[CTA^+]_{org}$ and $[TEOS]_{aq}$	111
4.1.1.1.2. Influence of the pore center-to-center distance	113
4.1.1.1.3. Influence of the scan rate.....	115
4.1.2. Morphological study	119
4.1.3. Spectroscopic and electrochemical characterization of deposits	123
4.1.4. Conclusion	127
4.2. <i>In situ</i> confocal Raman spectroscopy study of interfacial silica deposition at microITIES.....	128
4.2.1. Raman spectroscopy analysis of the liquid – liquid interface at open circuit potential.....	130
4.2.2. Ion transfer followed by Raman spectroscopy.....	132
4.2.3. Interfacial silica deposition followed by Raman spectroscopy.....	134
4.2.4. Conclusions.....	138
4.3. Electrochemical evaluation of microITIES modified with silica deposits.....	140
4.3.1. Blank experiment before and after modification	140
4.3.2. Single charge ion transfer before and after modification.....	141
4.3.3. Multicharged ion transfer before and after modification.....	144
4.3.4. Electroanalytical properties of microITIES modified with silica deposits.....	146
4.3.5. Conclusion	150
5. Chapter V. Local pH change at the ITIES induced by ion transfer and UV photolysis	152
5.1. Synthesis and characterization of trimethylbenzhydrylammonium iodide	153
5.2. Electrochemical characterization of PH^+ transfer at macroITIES.....	161
5.3. Study of photodecomposition of PH^+ species	163
5.4. Local pH change induced by electrochemical transfer and photodecomposition of PH^+ species	168
5.5. Silica deposition induced by local pH decrease	174
5.6. Conclusion.....	177

Table of content

6. General conclusions	178
7. Further directions	191
7.1. Silica deposits – SECM characterization	191
7.2. Silica deposits functionalization.....	193
7.3. Interfacially active base.....	195
8. References.....	198
Appendix I. Nanopipette preparation and silanization.....	221
Appendix II. Protocol of preparation of 3-azidopropyltrimethoxysilane	223

Abstract – English version

This work combines the electrochemistry at the interface between two immiscible electrolyte solutions (ITIES) with the Sol – Gel process of silica leading to an interfacial modification with mesoporous silica using soft template. In the first part of this work the macroscopic liquid – liquid interface was employed to separate the aqueous solution of the hydrolyzed silica precursor species (tetraethoxysilane (TEOS)) from the cationic surfactant (cetyltrimethylammonium (CTA⁺)) dissolved in the dichloroethane. The silica material deposition was controlled by the electrochemical CTA⁺ transfer from the organic to the aqueous phase. Template transferred to the aqueous phase catalyzed the condensation reaction and self-assembly resulting in silica deposition at the interface. A variety of initial synthetic conditions were studied with cyclic voltammetry: influence of [CTA⁺]_{org} and [TEOS]_{aq}, polarity of the organic phase, pH of the aqueous phase or deposition time scale etc. [CTA⁺]_{org} was found to be limiting factor of the deposition reaction. Characterization of silica material was also performed in order to study its chemical functionalities (XPS and infra-red spectroscopy were used) and morphology confirming mesostructure (SAXS and TEM were employed in this regard).

Silica deposition at the miniaturized ITIES (membranes supporting array of micrometer in diameter pores were used in this regard) was the second part of this work. Silica interfacial synthesis performed *in situ* resulted in stable deposits growing on the aqueous side of the interface. Mechanical stability of the supported silica deposits allowed further processing – silica material was cured. Based on imaging techniques (e.g. SEM) it was found that deposits form hemispheres for longer experimental time scales. Interfacial reaction was also followed with *in situ* confocal Raman spectroscopy. Molecular characteristics of the interface were changed dramatically once CTA⁺ species were transferred to the aqueous phase. An array of microITIES modified with silica was also assessed by ion transfer voltammetry of five interracially active species different in size, charge and nature. Ion transfer of each ion was affected in the presence of mesoporous silica at the ITIES.

Finally the local pH change at the liquid – liquid interface was induced by ion transfer and UV photolysis of trimethylbenzhydrylammonium initially dissolved in the organic phase. The local pH change was confirmed with the local pH measurement (iridium oxide Pt microdisc modified electrode was used in this regard). Interfacial deposition triggered by pH

decrease was shown to be feasible once TEOS precursor was dissolved in the organic phase whereas the CTA^+Br^- was dissolved in the aqueous phase.

Interfacial modification with mesoporous silica materials was shown to possess promising properties for improving selectivity at the ITIES. This particular analytical parameter can be further improved by silica functionalization, which could be continuation of this work.

Résumé – Version Français

Ce travail combine l'électrochimie à l'interface liquide - liquide avec le procédé sol - gel pour la modification interfaciale avec de la silice mésoporeuse. Dans la première partie de ce travail, l'interface liquide – liquide macroscopique a été utilisée pour séparer la solution aqueuse de l'espèce de précurseur de silice hydrolysées (tétraéthoxysilane (TEOS)) de l'agent tensioactif cationique (cetyltriméthylammonium (CTA^+)) qui a agi comme un template et a été dissous dans le dichloroéthane. Le dépôt de matériau de silice a été déclenché par le transfert du CTA^+ à partir de la phase organique vers la phase aqueuse. CTA^+ qui a transféré à la phase aqueuse a catalysé la réaction de condensation de la silice sur l'interface liquide – liquide. Différents conditions initiales de synthèse ont été étudiées par voltampérométrie cyclique: $[\text{CTA}^+]_{\text{org}}$ et $[\text{TEOS}]_{\text{aq}}$, polarité de la phase organique, le pH de la phase aqueuse ou temps de déposition, etc. $[\text{CTA}^+]_{\text{org}}$ est le facteur limitant la réaction de déposition. La caractérisation de la silice a également été réalisée. Les fonctionnalités chimiques ont été évaluées par spectroscopie XPS et infra-rouge. La mésostructure de la silice a été confirmée par SAXS et TEM.

Le dépôt de silice à des interfaces liquide – liquide miniaturisées était la deuxième partie de ce travail. Les dépôts stables sur le côté de l'interface ont été synthétisés *in situ* par voie électrochimique. La stabilité mécanique des dépôts de silice permis un traitement thermique de la silice.

Basé sur les techniques d'imagerie (par exemple SEM) il a été constaté que les dépôts forment des hémisphères pour des temps plus long. La réaction interfaciale a également été suivie *in situ* par spectroscopie Raman confocale. Caractéristiques moléculaires de l'interface ont été modifiées de manière spectaculaire une fois les espèces CTA^+ ont été transférés à la phase aqueuse. Les interfaces liquide – liquide miniaturisés et modifiés ont également été évaluée avec le transfert voltampérométrique de cinq ions différentes (en taille, charge et nature des espèces). Le transfert de chaque d'ion a été affectée par la présence de silice mésoporeuse à l'interface liquide – liquide.

Enfin, le changement de pH local à l'interface liquide - liquide a été induit avec le transfert d'ions et de photolyse UV de triméthylbenzhydrylammonium initialement dissous dans la phase organique. La diminution de pH local a été confirmée par la mesure du pH local

(microdisque en Pt modifié avec de l'oxyde d'iridium a été utilisé à cet égard). Le dépôt interfacial de silice déclenchée par la diminution du pH local a été démontré une fois que le précurseur TEOS a été dissous dans la phase organique tandis que le CTA^+Br^- a été dissous dans la phase aqueuse.

La modification interfaciale avec des matériaux de silice mésoporeuse a été démontrée pour posséder des propriétés prometteuses pour améliorer la sélectivité de capteur électroanalytiques basés sur l'interface liquide – liquide. Ce paramètre analytique particulier peut être encore amélioré par la fonctionnalisation de silice, ce qui pourrait être la poursuite de ce travail.

Frequently used abbreviations: In alphabetic order

BET – Brunauer–Emmett–Teller isotherm

BTPPA⁺ – Bis(triphenylphosphoranyldiene)
cation

CE – Counter electrode

CTA⁺ – Cetyltrimethylammonium cation

CV – Cyclic Voltammetry

D_i – Diffusion coefficient

D'_i – Apparent diffusion coefficient

DCE – Dichloroethane

DecFc – Decamethylferrocene

DMFc – 1,1'-Dimethylferrocene

EtOH – Ethanol

ΔG – Gibbs energy of transfer

ITIES – Interface between Two
Immiscible Electrolyte Solutions

LOD – Limit of detection

NMR – Nuclear Magnetic Resonance

4OBSA⁻ – 4-Octylbenzenesulfonic anion

PAMAM – Poly(amidoamine)

PH⁺ – Trimethylbenzhydrylammonium
cation

RE – Reference electrode

S – Spacing factor or in the other words
pore center-to-center distance

SAXS – Small Angle X-ray Scattering

SECM – Scanning Electrochemical
Microscopy

SEM – Scanning Electron Microscopy

TBA⁺ – Tetrabutylammonium cation

TEA⁺ – Tetraethylammonium cation

TEM – Transmission Electron Microscopy

TEOS – Tetraethoxysilane

TMA⁺ – Tetramethylammonium cation

TPBCl⁻ – Tetrakis(4-chlorophenylborate)anion

XPS – X-ray Photoelectron Spectroscopy

δ – Diffusion layer thickness

$\Delta\Phi$ – Interfacial Galvani potential
difference

Chapter I. Bibliographical introduction

First chapter gives an overview of the issues being an introduction to the consequential work. It is divided in three main parts: (i) the general information concerning electrified liquid – liquid interface including its structure, the charge transfer reactions, electrochemical behavior and miniaturization; (ii) the Sol-Gel process of silica and the examples of its application in electrochemistry and (iii) the approaches that were used for the liquid – liquid interface modification with metals, phospholipids, polymers, carbon materials and finally silica materials.

1.1. Electrified interface between two immiscible electrolyte solutions

At the very beginning, it is important to clarify a terminology developed in electrochemistry for the liquid – liquid interface based systems. The terms as electrified, polarized or non-polarized liquid – liquid interface were used alternatively with the interface between two immiscible electrolyte solutions (ITIES) among the literature of the subject and hence they are also use in the present work. From electroanalytical point of view, the ITIES bears plenty of high quality properties: (i) first of all under proper conditions it can be polarized; (ii) it is self-healing in the same manner as the mercury electrodes; (iii) it is free from defects down to a molecular level; (iv) lack of preferential nucleation sites offers a unique way to study a deposition process; (v) the electrochemical theories developed for the solid electrodes are applicable at the ITIES. (vi) What is setting the ITIES apart is the detection not restricted to the reduction or the oxidation reactions, which can arise from ion transfer reactions and (vii) the ITIES as an electrochemical sensor has good sensitivity and reasonable limits of detection. In the following subchapters, the most significant aspects – from this work point of view – are discussed and divided into: (i) interfacial structure, (ii) different types of interfacial charge transfer reactions, (iii) the polarized and the non-polarized

interfaces, (iv) electrochemical instability phenomena occurring in the presence of surface active molecules adsorption and (v) miniaturization at the ITIES. More comprehensive set of information dealing with the electrochemical aspects of the ITIES are available in number of reviews.^{1,2,3,4,5,6,7,8,9}

1.1.1. Liquid – liquid interface structure

The structure of the liquid – liquid interface was proposed for the first time in 1939 when Verwey and Niessen based on Gouy-Chapman theory described an electric double layer as two back-to-back electric double layers with opposite charge separated by a continuous geometric boundary (**Figure 1.1 a**).¹⁰ First experimental report dealing with the interfacial structure was given by Gavach *et al.* almost 40 years later. By measuring the interfacial tension versus the concentration of different tetraalkylammonium ions they proved presence of specific adsorption, which was explained in terms of ion pair formation at the liquid – liquid interface.¹¹

One year later the same group proposed what we know today as the ‘modified Verwey-Niessen’ model (**Figure 1.1 b**). The experimental approach consisted in control of interfacial Galvani potential difference between a sodium bromide aqueous solution and a tetraalkylammonium tetraphenylborate organic solution by addition of tetraalkylammonium bromide to the aqueous phase and subsequent interfacial tension measurement – giving the electrocapillary curve. This work has brought two main characteristics to the interfacial model: the first, has treated the interface as a ‘compact layer’ of oriented dipole molecules; the second has assumed very small potential drop across the interface.¹²

Furthermore, the presence of mixed solvent layer at the interface, was confirmed *via* surface excess study of water at the interface between organic solvents of different polarity.^{13,14} Results indicated that surface excess of water at the liquid – liquid interface was not enough to form a monolayer, which in turn has suggested that these ions penetrates an interfacial region (**Figure 1.1 c**).

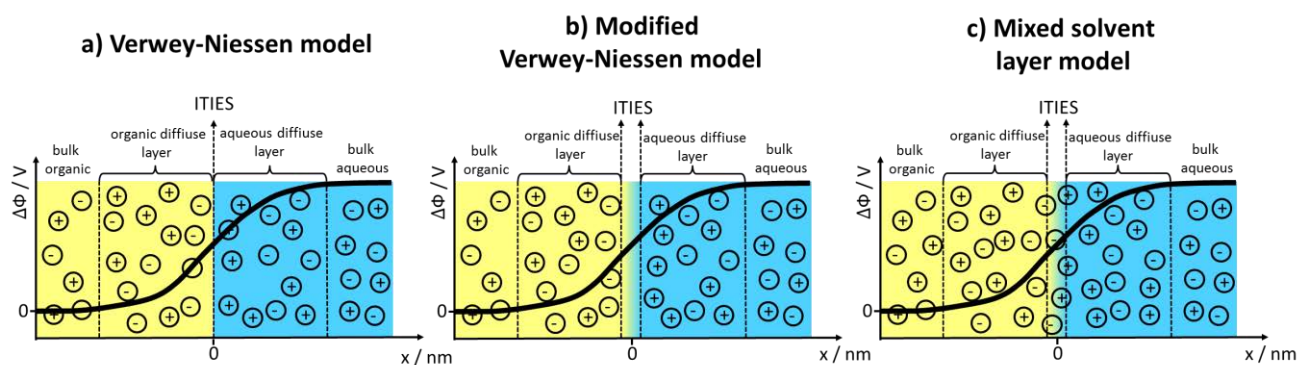


Figure 1.1. Different models for the ITIES structure. Black solid lines correspond to potential distribution across the polarized liquid – liquid interface.

An important aspect of the ITIES structure is its thickness. Existence of capillary waves at the liquid – liquid interface designates its boundaries. Qualitative parameter – mean-square interfacial displacement – allowed the estimation of upper and lower limits of the interface.¹⁵ The results based on molecular dynamic calculations for a typical interfacial tension values between H₂O and DCE indicated that the size of the interface is in the order of around 10 Å.^{16,17} The complex nature and the unique character of the liquid – liquid interface narrows the study of its structure down to few spectroscopic techniques: scattering of X-ray and neutrons¹⁸ and non-linear optical methods (sum-frequency vibrational spectroscopy¹⁹ and second harmonic generation²⁰).

1.1.2. Charge transfer reactions at the ITIES

At the ITIES, each of immiscible phases can be characterized with its own inner Galvani potential. Under open circuit potential when no charge transfer is observed, the species in one phase, say an aqueous are too hydrophilic to be transferred to the organic phase and species from the organic phase are too hydrophobic to transfer to the aqueous phase. The system equilibrium can be disrupted by introduction of external solute to one of phases (partition of species driven by interfacial Galvani potential difference leads to the interfacial ion transfer reaction until the equilibrium is established) or by external interfacial polarization. The quantity of energy that has to be delivered to the system in order to transfer one of the components to the neighboring phase can be given by standard transfer Gibbs energy whereas the partition of the species between two immiscible phases are conditioned by

interfacial Galvani potential difference. In principle charge transfer reaction across the ITIES can be divided into three main groups: (i) simple ion transfer, (ii) assisted/facilitated ion transfer and (iii) electron transfer between the redox couple O_1/R_1 in one phase and redox couple O_2/R_2 in the latter. The proceeding description is given for the three above mentioned charge transfer thermodynamics enriched with practical examples. The examples and characteristics of electrochemically induced liquid – liquid interface adsorption reaction are also briefly discussed.

1.1.2.1. Simple ion transfer reaction

If one will consider that ion (i) is transferred from the aqueous to the organic phase *via* simple ion transfer reaction, than the standard transfer Gibbs energy ($\Delta G_{(i)}^{0,aq \rightarrow org}$) will be defined as the difference between standard Gibbs energy of solvation ($\mu^{0,org}$) and hydration ($\mu^{0,aq}$):

$$\Delta G_{(i)}^{0,aq \rightarrow org} = \mu^{0,org} - \mu^{0,aq} \quad (1.1)$$

Standard transfer Gibbs energy ($\Delta G_{(i)}^{0,aq \rightarrow org}$) can be converted to standard transfer potential ($\Delta_{org}^{aq} \Phi_{(i)}^0$) by introduction of $z_{(i)}F$ factor according to equation 1.2:

$$\Delta_{org}^{aq} \Phi_{(i)}^0 = \frac{\Delta G_{(i)}^{0,aq \rightarrow org}}{z_{(i)}F} \quad (1.2)$$

For the charged species (i), the ion transfer equilibrium condition, at constant temperature and pressure is given by following equality:

$$\tilde{\mu}_{(i)}^{aq} = \tilde{\mu}_{(i)}^{org} \quad (1.3)$$

Where $\tilde{\mu}_{(i)}^{0,x}$ is the electrochemical potential of charged species (i) expressed in form of equation 1.4:

$$\tilde{\mu}_{(i)}^x = \mu_{(i)}^{0,x} + RT \ln a_{(i)}^x + z_{(i)}F\Phi^x \quad (1.4)$$

Where $\mu_{(i)}^0$ is the standard chemical potential, Φ^x is the inner Galvani potential, $a_{(i)}^x$ is the activity of the specie and x correspond to the aqueous (aq) or the organic (org) phase. The equality from equation 1.3 can be developed by substitution with equation 1.4:

$$\mu_{(i)}^{0,aq} + RT \ln a_{(i)}^{aq} + z_{(i)} F \Phi^{aq} = \mu_{(i)}^{0,org} + RT \ln a_{(i)}^{org} + z_{(i)} F \Phi^{org} \quad (1.5)$$

Separation of the Galvani potential difference – $\Delta_{org}^{aq} \Phi = \Phi^{aq} - \Phi^{org}$ – on one side and rest of the components on the second side of the equality yields in the Nernst equation for ion transfer at the ITIES:

$$\Delta_{org}^{aq} \Phi = \Phi^{aq} - \Phi^{org} = \Delta_{org}^{aq} \Phi_{(i)}^0 + \frac{RT}{z_{(i)} F} \ln \frac{a_{(i)}^{org}}{a_{(i)}^{aq}} \quad (1.6)$$

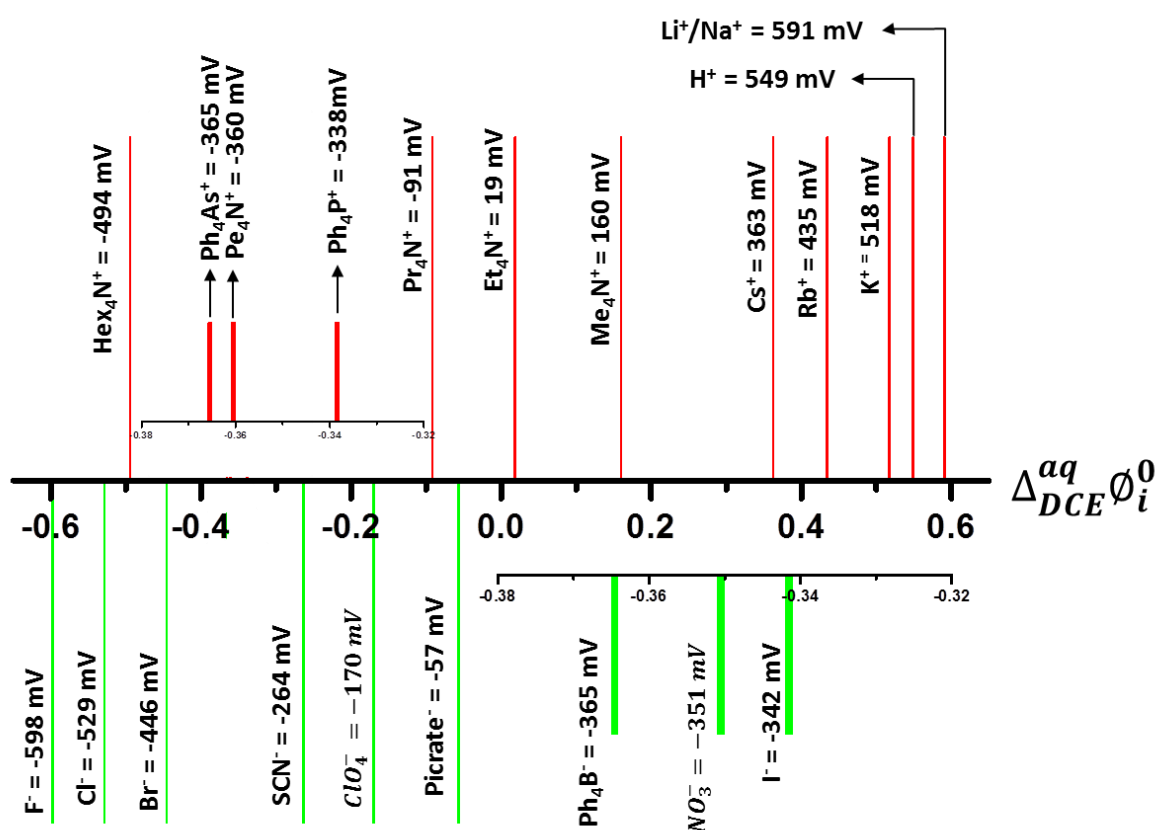


Figure 1.2. Standard ion-transfer potentials for different anionic and cationic species across the dichloroethane – water interface. The abbreviations stand for: Ph₄P⁺ – tetraphenyl phosphonium; Ph₄As⁺ – tetraphenylarsonium; Ph₄B⁻ – tetraphenylborate and Alkyl₄N⁺ – correspond to tetraalkylammonium compounds. Figure prepared based on ref.^{1,21}

Where $\Delta_{org}^{aq} \Phi_{(i)}^0$ is the standard transfer potential or in the other words standard Gibbs energy expressed in the voltage scale as it was shown with equation 1.2, $a_{(i)}^x$ is the activity for the ion (i), in the aqueous or organic phase, R is the gas constant ($8.31 \text{ J/mol} \cdot \text{K}$) and T is the temperature. Equation 1.6 can be expressed with concentration instead of activity as:

$$\Delta_{org}^{aq} \Phi = \Delta_{org}^{aq} \Phi'_{(i)} + \frac{RT}{z_{(i)}F} \ln \frac{C_{(i)}^{org}}{C_{(i)}^{aq}} \quad (1.7)$$

Where $\Delta_{org}^{aq} \Phi'_{(i)}$ correspond to formal transfer potential.^{1,4}

Simple ion transfer reaction is considered as the easiest to study and above mentioned deliberations provide qualitative parameters (standard transfer potential or standard Gibbs energy difference) that can be measured with electrochemical techniques. **Figure 1.2** includes the $\Delta_{org}^{aq} \Phi_{(i)}^0$ values for different cationic and anionic species measured at the water – dichloroethane interface.

1.1.2.2. Assisted/facilitated ion transfer

This type of interfacial transfer induces host-guest interaction between ion (i) in one phase and ligand (L) dissolved in a second, immiscible phase. Nernst like equation for simple ion transfer reaction can be easily adapted to describe the facilitated ion transfer. To do so, some assumptions have to be made:

- Ion is initially present in the aqueous phase, whereas ligand able to complex transferring ion is present in the organic phase;
- Complexation is taking place in the organic phase;
- Concentration of ions in the aqueous phase is in excess over their concentration in the organic phase;
- Under open circuit potential complex formation in the organic phase prevails, hence ion concentration in the organic phase can be neglected and;
- The aqueous phase concentration of ligand is neglected.

To facilitate consideration we can assume that the complexation is of 1:1 stoichiometry type, which can be written as:



For given reaction the association constant is given by:

$$K_a = \frac{a_{L-(i)}^{org}}{a_L^{org} a_{(i)}^{aq}} \quad (1.9)$$

The $\Delta_{org}^{aq} \Phi$ for the facilitated ion transfer can be written in the form of equation 1.10:

$$\Delta_{org}^{aq} \Phi = \Delta_{org}^{aq} \Phi_{L-(i)}^0 + \frac{RT}{z_{(i)}F} \ln \frac{a_{L-(i)}^{org}}{a_{(i)}^{aq}} \quad (1.10)$$

With the apparent standard transfer potential, $\Delta_{org}^{aq} \Phi_{L-(i)}^0$

$$\Delta_{org}^{aq} \Phi_{L-(i)}^0 = \Delta_{org}^{aq} \Phi_{(i)}^0 + \frac{RT}{z_{(i)}F} \ln(K_a a_L^{org}) \quad (1.11)$$

First report concerning assisted ion transfer reaction at the electrified liquid – liquid interface derives from Czechoslovakia at that time,²² where Koryta has studied potassium transfer from the aqueous phase to a nitrobenzene solution containing dibenzo-18-crown-6 ionophore. Beyond doubts complexation agent being dissolved in the organic phase lowered the Gibbs energy of transfer and allowed the ions to transfer at lower interfacial potential difference values. This novelty opened the way to study species, whose detection was limited by rather narrow potential window. Complex nature of the facilitated ion transfer reaction involves several mechanisms divided – in respect to a complexation/dissociation location – into: **ACT** (aqueous complexation followed by transfer), **TOC** (transfer followed by complexation), **TIC** (transfer by interfacial complexation) and **TID** (transfer by interfacial dissociation).²³ All four mechanisms are illustrated on **Figure 1.3**.

The model of the facilitated ion transfer reaction at the ITIES can be referred to as historical potassium transfer facilitated by dibenzo-18-crown-6.²² To date, facilitated transfer of ionic compounds allowed the improvement of the still poor selectivity of the ITIES – guided by specific interaction between the host (ionophore, ligand) and the guest (target ion). The assisted transfer of heavy metals, which detection is of highest importance, had also attracted a lot of experimental attention. Series of five cyclic thioether ligands were found to be proper ionophores for the assisted transfer of cadmium, lead, copper and zinc.²⁴ Synthetic molecule – ETH 1062 – incorporated into gelled polyvinylchloride-2-nitrophenylethyl ether polymer membrane was used in cadmium detection from the aqueous solution.²⁵ The ion transfer voltammetry of silver ions being dissolved in the aqueous phase indicated that upon addition of 1,5-cyclooctadiene to the organic phase (1,6-dichlorohexane) its transfer becomes

shifted from the potential range where it was partially masked by background ion transfer to a less positive potential where clear peak-like response was formed.²⁶ Work devoted for divalent copper cations assisted transfer by 6.7-dimethyl-2,3-di(2-pyridyl)quinoxaline ligands, showed that the half-wave potential of free ion transfer was shifted by around 400 mV to a less

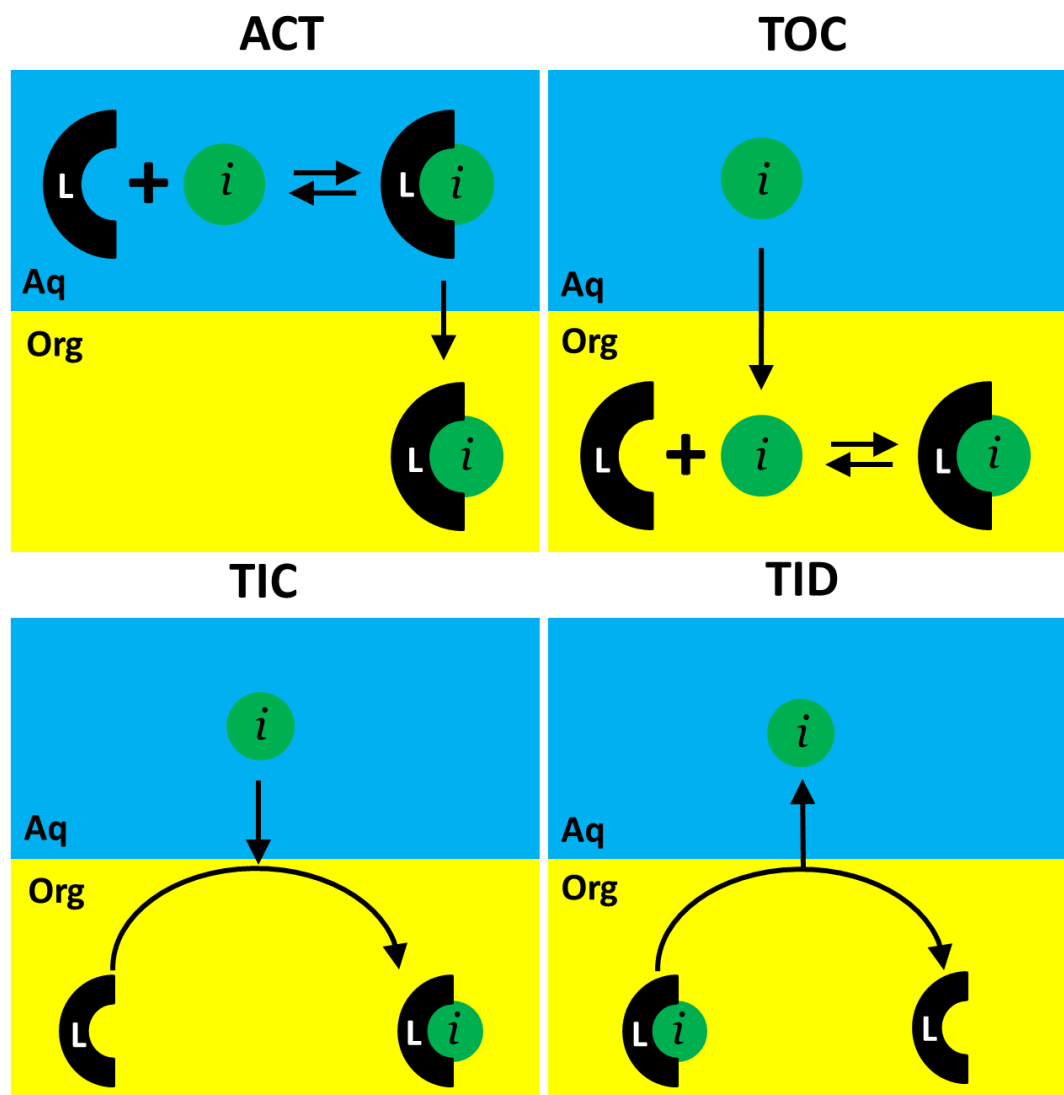


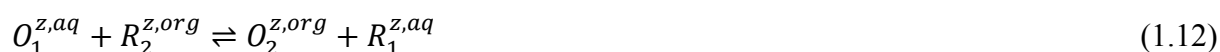
Figure 1.3. Four mechanisms of possible assisted ion transfer reaction. Designations: L – ligand, i – ionic species, ACT – aqueous complexation followed by transfer, TOC – transfer followed by complexation, TIC – transfer by interfacial complexation and TID – transfer by interfacial dissociation.

positive potential values in the presence of ligands in the organic phase. Among other examples, much attention was given to calix[4]arenes synthetic ionophores, first time applied by Zhan *et al.*²⁷ towards alkali metal detection. Subsequent works from other groups – dealing

with analogical ionophore derivatives – have shown that in the presence of alkali and alkaline-earth metals, selective detection at the ITIES can be slightly improved²⁸ or directed towards potassium (once 5.11.17.23-tetra-tertbutyl-25-27-bis(2'-amino-methylpyridine)-26-28-dihydroxy calix[4]arene was used)²⁹ or calcium cations (for 5.11.17.23-tetra-tert-butyl-25-27-diethoxycarbonylmethoxy-26-28-dimethoxy calix[4]arene).³⁰ O'Dwyer and Cunnane have studied the facilitated transfer of silver cations with O,O''-Bis[2-(methylthio)ethyl]-tert-butyl calix[4]arene.³¹ Since host-guest interaction for calix[4]arene ionophores are not limited to metal cations it has been shown that its modification with urea group allowed the detection of anions (phosphate, chloride and sulphate with selectivity towards phosphate anions).³² An example of facilitated transfer of proton was also given. Reymond *et al.* have shown that in the presence of piroxicam derivatives in the organic phase, H⁺ undergoes transfer by interfacial complexation/dissociation (TIC/TID) reaction.³³

1.1.2.3. Electron transfer across ITIES

Properly selected two redox pairs O₁/R₁ and O₂/R₂ dissolved in the aqueous and the organic phase respectively under potentiostatic conditions may lead to the electron transfer reaction across the ITIES.¹



For the reaction 1.12 at constant temperature and pressure the electrochemical potentials equilibrium will be given as:

$$\tilde{\mu}_{O_1}^{0,aq} + \tilde{\mu}_{R_2}^{0,org} = \tilde{\mu}_{O_2}^{0,org} + \tilde{\mu}_{R_1}^{0,aq} \quad (1.13)$$

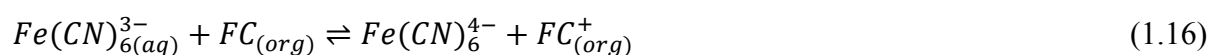
Substitution of eq. 1.4 to eq. 1.13 and proper transformation will yield the Nernst like equation for the electron transfer reaction across the ITIES:

$$\Delta_{org}^{aq} \Phi = \Delta_{org}^{aq} \Phi_{el}^0 + \frac{RT}{F} \ln \frac{a_{O_2}^{org} a_{R_1}^{aq}}{a_{O_1}^{aq} a_{R_2}^{org}} \quad (1.14)$$

where $\Delta_{org}^{aq} \Phi_{el}^0$ is the standard Galvani potential difference for the electron transfer from the aqueous to the organic phase, related with the free Gibbs energy of the electron transfer reaction *via* equation 1.15:

$$\Delta_{org}^{aq} \Phi_{el}^0 = \frac{\Delta_{org}^{aq} G_{el}^0}{F} \quad (1.15)$$

The electron transfer reaction at the ITIES depends from the relative reduction potential of two redox couples separated between two immiscible phases and hence can occur spontaneously (if the interfacial potential difference is high enough to trigger redox reaction) or can be controlled potentiometrically. The studies of the electron transfer reaction were performed with variety of electrochemical techniques as for instance: SECM,^{34,35} cyclic voltammetry,^{36,37} ac impedance³⁸ etc. The process of an interfacial electron transfer reaction was first time observed by Samec *et al.* for the system composed from hexacyanoferrate redox couple in the aqueous phase and ferrocene in the nitrobenzene phase.³⁹



Since that time this particular type of interfacial charge transfer reaction accompanied the work focused on electrocatalysis,⁴⁰ photoinduced interfacial reaction^{41,42} or interfacial modification with the metals, polymers and metal/polymers deposits. The latter is discussed in more details in the **subsections 3.1 and 3.3.**

1.1.2.4. Electrochemically induced interfacial adsorption

At the ITIES the interfacial adsorption was reported for two following class of species: (i) amphiphilic ions and (ii) large and multicharged species e.g. dendrimers. The study of amphiphilic molecules adsorption, e.g. phospholipids, under applied potential conditions is most of all performed by electrocapillary curves measurements.^{43,44,45} The adsorption of phosphatidylcholine phospholipid from the organic phase and its complexation with the different ionic species (K^+ , H^+ , Fe^{2+} , Fe^{3+} , $IrCl_6^{2-}$, $IrCl_6^{3-}$) from the aqueous solution was followed by cyclic voltammetry (which gave characteristic triangular signal in the presence of adsorption) and contact angle measurements at different interfacial potentials values (contact angle for the studied droplet tend to increase with the polarization towards more positive potentials in the presence of phospholipid adsorption).⁴⁶

Recently, dendrimers – repetitively branched molecules with the generation growing with number of molecular branches – attracted a lot of scientific attention as drug carriers,⁴⁷ molecular gates,⁴⁸ soft templates⁴⁹ etc. whereas the electrochemistry at the ITIES was shown

as a good electroanalytical tool for their determination.^{50,51} It has been shown that dendrimers with growing size and charge exhibit complex behavior at the electrified liquid – liquid interface. Molecular dynamics simulations employed to study adsorption of model dendrimer of a third generation at the liquid – liquid interface has shown that molecules possessing amphiphilic structure have higher stability at the interface.⁵² The interfacial adsorption rather than interfacial transfer was reported for Poly-L-Lysine dendritic family (from generation 2 to generation 5)⁵³ and higher generation of poly(amidoamine) and poly(propyleimine) dendrimers.⁵⁴ Interfacial adsorption was also voltammetrically observed for biomolecules as insulin,⁵⁵ hen egg-white lysozyme⁵⁵ and hemoglobin.⁵⁶ The last biomolecule, additionally to adsorption process was shown to facilitate the transfer of anionic part of the organic phase supporting electrolyte, and subsequently decrease its Gibbs energy of transfer.

Such species do not exhibit the characteristics of reversible transfer: (i) the peak-to-peak separation exceeds $0.059V/n$; (ii) forward and reverse peak current ratio $\neq 1$; (iii) deviation from linearity for current – concentration (calibration) curves and (iv) the reverse peak current terminated with abrupt current drop rather than diffusion limited tail. For surface active molecules adsorption – (v) so-called ‘electrochemical instability’ manifested by unrepeatable current spikes was reported and is discussed in the **subsection 1.1.4**.⁵⁷ Additionally for hemoglobin (vi) a thin layer film was visible at the ITIES after repetitive cycling.⁵⁶

1.1.3. Potential window and limiting current

A polarizable electrode is ideal when, in the absence of Faradaic processes, no current flows through it over the whole potential range. A current – potential characteristic of a polarizable electrode in real conditions is presented on **Figure 1.4 (a)**. Decrease and increase in current at a negative and a positive potential ends arise from an electrolyte or an electrode material decomposition. An ideally non-polarizable electrode, on the contrary, under current flow conditions does not change its potential for infinite current range. In real conditions the electrode potential becomes highly stable only for limited current range as it is presented on **Figure 1.4 (b)**. Deviations from stability are induced by reactions occurring at the electrode surface.

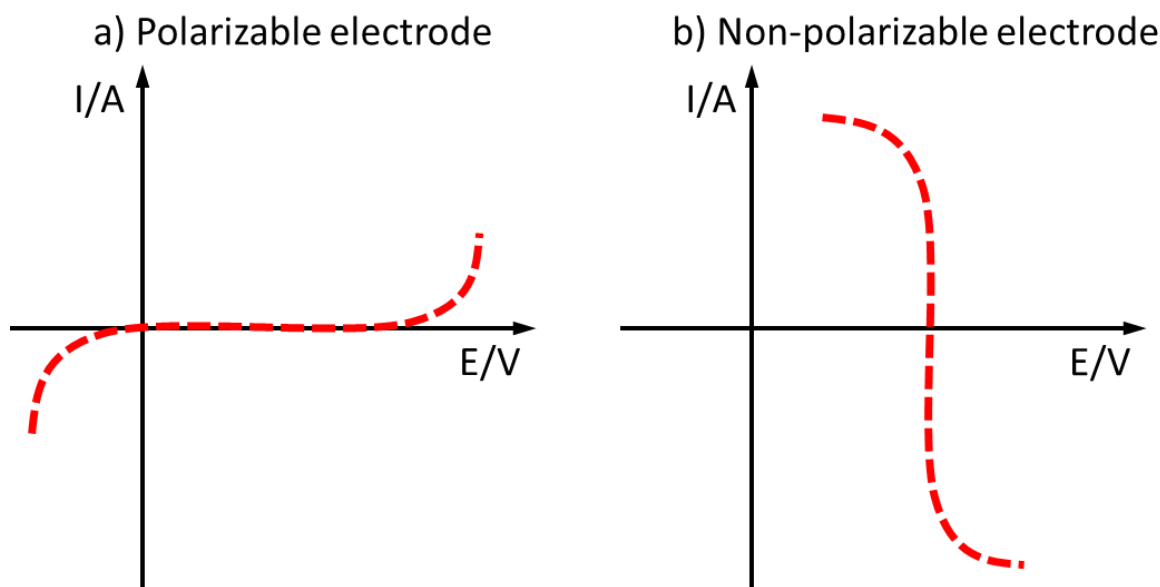


Figure 1.4. Current – potential characteristics for a) polarizable and b) non-polarizable electrodes.

Similar behavior can be distinguished at the ITIES. In that case, the solid conductor is replaced with an immiscible electrolyte phase and the polarization becomes purely an ionic process. If we assume that the aqueous phase contains highly hydrophilic salt (A^+B^-) of ideally zero solubility in the organic phase, and the organic phase contains highly lipophilic salt (C^+D^-) of ideally zero solubility in the aqueous phase then the ideally polarized interface can be described as the interface impermeable to the charged particles transfer in whole potential range. In other words, it means that the ions should possess infinite Gibbs energy of transfer, which of course is far from the truth. In experimental conditions, a polarizable interface can be constructed between highly hydrophilic salt dissolved in the aqueous phase (NaCl, LiCl ect...) and highly lipophilic salt (tetrabutylammonium tetrakis(4-chlorophenylborate) (TBA^+TPBCl^-)) dissolved in the organic phase. One or both phases can also be replaced with respectively a hydrophilic (1-butyl-3-H-imidazolium nitrate)⁵⁸ or the hydrophobic (1-octyl-3-methylimidazolium bis(perfluoroalkylsulfonyl)imid)⁵⁹ ionic liquids.

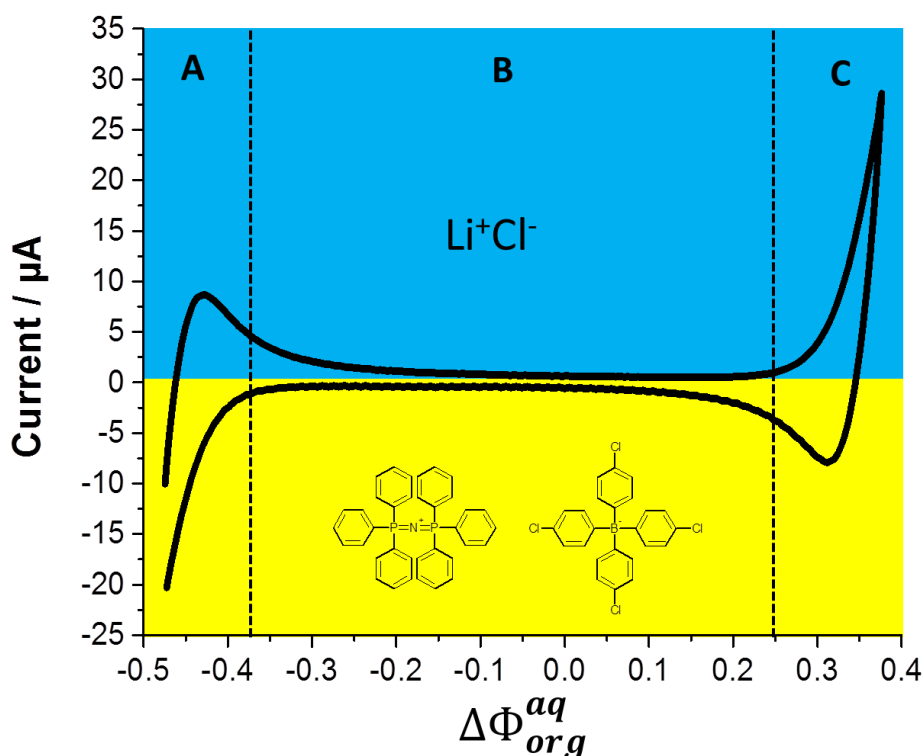


Figure 1.5. Voltammogram recorded only in the presence of the aqueous (LiCl) and the organic ($\text{BTPPA}^+\text{TPBCl}^-$) supporting electrolytes. Regions A and C correspond to electrolyte ion transfer currents whereas region B is the potential window, among which the interface is impermeable for all ionic species present in both phases.

Figure 1.5 illustrates cyclic voltammogram recorded at the polarized interface between aqueous solution of LiCl and organic solution of bis(triphenylphosphoranyldiene) ammonium tetrakis(4-chlorophenylborate) ($\text{BTPPA}^+\text{TPBCl}^-$). Region between two vertical dashed lines (**marked as B**) correspond to polarizable part of the interface – **potential window**. In this particular part of a cyclic voltammogram, the change in inner potentials between two immiscible phases does not induce noticeable change in chemical composition of the aqueous and the organic medium. In other words interface is impermeable for the charge transfer and resulting current is only due to charging of double layer capacitance at both sides of the liquid – liquid interface. The potential window is limited by supporting electrolyte ions transfer (**part A and C**). Once the standard transfer potential of the less hydrophobic (in case of ions transferring from the aqueous to the organic phase) or the less hydrophilic (for ions crossing the interface from the organic side of the interface) ion is reached, they start to cross the interface. The available potential window in voltammetric

study is dependent on the solvent used and the nature of supporting electrolytes as is shown in **Table 1.1**.

Table 1.1. Comparison of the different organic solvents, organic phase electrolytes and aqueous phase electrolytes in terms of available potential window widths.

Organic phase solvent	[Organic phase electrolyte]	[Aqueous phase electrolyte]	Potential window width	Ref.
Valeronitrile	10 mM BTPPA ⁺ TPBCl ⁻	100 mM LiCl	100 mV	60
Caprylonitrile	10 mM BTPPA ⁺ TPBCl ⁻	100 mM LiCl	200 mV	60
2-octanone	10 mM BTPPA ⁺ TPBCl ⁻	100 mM LiCl	250 mV	60
2-decanone	10 mM BTPPA ⁺ TPBCl ⁻	100 mM LiCl	350 mV	60
3-nonanone	10 mM BTPPA ⁺ TPBCl ⁻	100 mM LiCl	350 mV	60
o-NPOE	1 mM TPAs ⁺ TPB ⁻	10 mM LiCl	350 mV	61
o-NPOE	20 mM TPA ⁺ TPB ⁻	10 mM LiCl	350 mV	62
5-nonanone	10 mM BTPPA ⁺ TPBCl ⁻	100 mM LiCl	400 mV	60
5-nonanone	10 mM BTPPA ⁺ TPBCl ⁻	100 mM LiCl	400 mV	60
1,2-DCE	100 mM TOctA ⁺ TPBCl ⁻	50 mM Li ₂ SO ₄	600 mV	63
o-NPOE	5 mM TBA ⁺ TPBCl ⁻	10 mM LiCl	620 mV	64
1,2-DCE	10 mM BTPPA ⁺ TPBCl ⁻	100 mM LiCl	650 mV	60
1,2-DCE	1 mM BTPPA ⁺ TFPB ⁻	5 mM NaCl	700 mV	65
1,4-DCB	100 mM TOctA ⁺ TPBCl ⁻	50 mM Li ₂ SO ₄	700 mV	63
1,2-DCE	1 mM BTPPA ⁺ TFPB ⁻	5 mM NaCl	700 mV	65
1,2-DCE	1 mM BTPPA ⁺ TFPB ⁻	5 mM LiF	800 mV	65
1,2-DCE	1 mM BTPPA ⁺ TFPB ⁻	5 mM MgSO ₄	825 mV	65
1,6-DCH	100 mM TOctA ⁺ TPBCl ⁻	50 mM Li ₂ SO ₄	850 mV	63
(1:1 v:v) 1,2-DCE:CH	1 mM BTPPA ⁺ TFPB ⁻	5 mM NaCl	920 mV	65
1,2-DCE	10 mM BTPPA ⁺ TFPB ⁻	10 mM MgSO ₄	970 mV	65
(1:1 v:v) 1,2-DCE:CH	1 mM BTPPA ⁺ TFPB ⁻	5 mM LiF	970 mV	65
(1:1 v:v) 1,2-DCE:CH	1 mM BTPPA ⁺ TFPB ⁻	5 mM MgSO ₄	1000 mV	65
(1:1 v:v) 1,2-DCE:CH	1 mM BTPPA ⁺ TFPB ⁻	2000 mM MgSO ₄	1000 mV	65
1,2-DCE	TBA ⁺ TPFPB ⁻	0.5 mM HCl	1050 mV	66
(1:1 v:v) 1,2-DCE:CH	10 mM BTPPA ⁺ TFPB ⁻	10 mM MgSO ₄	1120 mV	65

The abbreviation stand for: 1,2-DCE – 1,2-dichloroethane; 1,4-DCB – 1,4-dichlorobutane; 1,6-DCH – 1,6-dichlorohexane; CH – cyclohexane; o-NPOE – 2-nitrophenyl octyl ether; BTPPA⁺ - Bis(triphenylphosphoranyldiene)ammonium cation; TPBCl⁻ - tetrakis(4-chlorophenyl) anion; TFPB⁻ - tetrakis[3,5-bis(trifluoromethyl)phenyl]borate anion; TBA⁺ - tetrabutylammonium cation; TPA⁺ - tetrapentylammonium cation; TPB⁻ - tetraphenylborate; TPAs⁺ - tetraphenylarsonium cation; TFPB⁻ - tetrakis(pentafluorophenyl)borate anion and TOctA⁺ is the tetraoctylammonium cation.

At the ITIES, resulting current is associated with the direction of ion transfer as it is shown on **Figure 1.6**. Positive current is recorded once cations are moving from the aqueous to the organic phase or anions from the organic to the aqueous phase, whereas negative current is when cation are transferring from the organic to the aqueous phase and anions from the aqueous to the organic phase. With this in mind, the association of ion transfer to the

positive and the negative end of the voltammogram from **Figure 1.5** becomes simplified. Limiting current on the lower potential scale side (**part A on Figure 1.5**) originates from chloride transfer (positive peak corresponds to $Cl_{org \rightarrow aq}^-$ whereas the negative current is due to $Cl_{aq \rightarrow org}^-$). Positive end of potential window is limited by TPBCl⁻ transfer ($TPBCl_{aq \rightarrow org}^-$ results in the negative current peak and $TPBCl_{org \rightarrow aq}^-$ can be observed as a positive current increase).

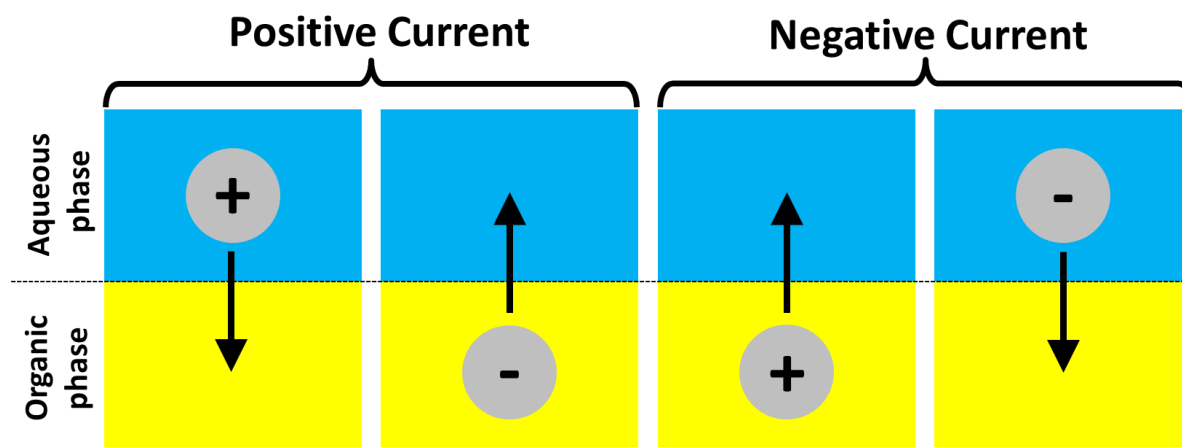


Figure 1.6. Direction of ion transfer associated with the current response.

Non-polarizable interface occurs when both immiscible phases contain at least one common ion, which can freely cross the interface. In an ideal case, the current originating from common ion transfer in any direction should not induce any changes in interfacial potential difference. According to Nernst like equation for ion transfer reaction (eq. 1.6), the potential distribution is depended on the ionic species separated between two immiscible phases. At non-polarized interface, binary electrolyte (1:1; 2:2 etc.) A^+B^- or electrolytes containing common ion – A^+B^-/A^+C^- – are distributed between two phases and hence interfacial potential difference does not depend on their concentration.^{67,68} Systems employing non-polarized interface are used to study the kinetics of electron transfer reactions.⁶⁹

1.1.4. Electrochemical instability at the electrified liquid – liquid interface in the presence of ionic surfactants

Electrochemical instability, term proposed and explained by Kakiuchi,^{70,71} explains the instability of the electrified liquid – liquid junction in the presence of ionic molecules undergoing both: partitioning and adsorption processes. Potential depended adsorption of surface active ions was shown to reach a maximum value for the interfacial potential difference, $\Delta_{org}^{aq} \Phi$, at around standard ion transfer potential difference of surface active ion i , $\Delta_{org}^{aq} \Phi_i^0$. A consequence of maximal adsorption is the drop in an interfacial tension that leads to the thermodynamic instability. Further deliberation concerning electrocapillary curves in the presence of surface active ions adsorption has led to a conclusion, that for some $\Delta_{org}^{aq} \Phi$ values, double layer capacitance becomes negative. Since a negative value of capacitance has no physicochemical meaning, real systems compensates the energy lost by emulsification or escapes from instability by Marangoni type movements (transfer of charged species among the liquid – liquid interface induced by surface tension gradients). Thermodynamically forbidden region can be referred to as an instability window. Its width depends on the interfacial tension change upon surfactant adsorption (dependent from surfactant concentration and Gibbs free energy of adsorption, $(\Delta G_{ads,i}^0)$), curvature of electrocapillary curve and location of potential of zero charge against $\Delta_{org}^{aq} \Phi^0$.^{70,71}

The concepts of an electrochemical instability model do not assumed presence of specific adsorption of the ionic species, which is the case in real systems. Kakiuchi and Kitazumi improved previous model based on Gouy's double layer theory by introduction of the inner layer localized between two diffuse double layers. The new model describes potential dependency of interfacial capacitance, excess charge of ionic species in the aqueous phase and shape of electrocapillary curves in the presence of specific adsorption.^{72,57}

On cyclic voltammetry curves, in the presence of surface active ions, the electrochemical instability manifests itself as irregular current spikes in the vicinity of half-wave potential of transferring species. These characteristics were confirmed for anionic surfactants (alkansulfonate and alkyl sulfate salts),^{73,74,44} cationic surfactant (decylamine)^{44,75} and alkaline-earth metals facilitated transfer by complexation agent -

polyoxyethylene(40)isooctylphenyl ether (Triton X-405).⁷⁶ The abundance of current irregularities is highly depended from the experimental time scale and intensifies for lower scan rates. Low concentration of dodecansulfonate (0.2 mM)⁷⁴ do not induce anomalies at cyclic voltammograms due to weak adsorption (fluctuation appears once the concentration reaches 0.5 mM). This confirms that the electrochemical instability can be triggered once surface coverage reaches crucial value.

1.1.5. Miniaturization of the ITIES

In electroanalytical chemistry, miniaturization possesses two advantages over the macroscopic system. First of all, it improves the sensitivity as a reason of increased mass transfer to a solid – liquid or the liquid – liquid interface arising from radial diffusion zone geometry.⁷⁷ Second characteristic lies in the interfacial surface area, which decreases as the system becomes smaller, which in turn lowers the capacitance current and improves limits of detection.⁷⁸ In case of liquid – liquid interface, miniaturization additionally improves its mechanical stability whereas the developments in the field of lithographical techniques allow the design and performance of well-defined supports.

At the ITIES, the miniaturization was first time performed by Taylor and Girault who have supported the liquid – liquid interface in a pulled glass tube resulting in 25 μm in inner tip diameter.⁷⁹ Repeatable single pore microITIES could be also prepared by using a metal wire with a fixed diameter as a template, and a glass tube melted around. The wire removal of a wire by etching releases the pore that can be subsequently used to support the ITIES.⁸⁰ With development of new technologies the dimensions of the single ITIES could be further decreased up to the nanometer level – especially when LASER pulling approach was employed.⁸¹ The geometrical and voltammetric properties of three kinds of ITIES were compiled in **Table 1.2**. It is worth noting that the miniaturized liquid – liquid interface can possess an asymmetrical diffusion zone profile on both sides of the interface as it is shown i.e. for microITIES scheme from **Table 1.2**. In that case, the mass transfer inside the pore is dominated by linear diffusion and hence the charge transfer reaction is a diffusion limited process. On the pore ingress, mass transfer is enhanced by hemispherical diffusion zone, which makes the charge transfer diffusion non-limited process.

Table 1.2. Comparison between three different dimensions of ITIES.

Dimensions	Macro ITIES	Micro ITIES	Nano ITIES
Schemes			
Conditions r – is the interfacial radius δ – is the diffusion layer thickness	$r \gg \delta$ r [mm, cm]	$r < \delta$ r [μm]	$r < \delta$ r [nm]
Signal current	$I_{org \to aq} = 268600n^{3/2}AD^{1/2}Cv^{1/2}$ $I_{aq \to org} = 268600n^{3/2}AD^{1/2}Cv^{1/2}$	$I_{org \to aq} = 268600n^{3/2}AD^{1/2}Cv^{1/2}$ $I_{aq \to org} = 4NnFDcr$	$I_{org \to aq} = 4f(\Theta)nFDcr$ ⁸¹ Non silanized pipette: ⁸¹ $I_{aq \to org} = 3.35\pi nFDcr$
Signal shape	$org \to aq$ – tail finished peak $aq \to org$ – tail finished peak	$org \to aq$ – wave like signal $aq \to org$ – tail finished peak	$org \to aq$ – tail finished peak $aq \to org$ – wave like signal

n – is the charge, F – the Faraday constant, A – the surface area, D – the diffusion coefficient, C – the concentration, v – the scan rate, N – the number of pores (in case of array), r – the ITIES radius and $f(\Theta)$ is a function of the tip inner angle.

The application of arrays of geometrically regular nano-⁸² and microITIES,⁸³ as in the case of solid state electrochemistry, have gave better electroanalytical response since under proper geometrical conditions the ensemble can be treated as a sum of individual pores. Different characteristics of the regular arrays of microITIES are shown in **Table 1.3**.

Table 1.3. Voltammetric characteristics for the array of different arrays of microITIES.⁸⁴

Type of array	Individual small diffusion layers	Individual diffusion layers	Overlapped diffusion layers	Heavily overlapped diffusion layers
<p>Scheme</p> <p>D – is the diameter r – is the radius δ – is the diffusion layer thickness S – is the pore center to center distance</p>				
Characteristics	$\delta < r$ $\delta < S$	$\delta > r$ $\delta < S$	$\delta > r$ $\delta > S$	$\delta > r$ $\delta \gg S$
Voltammetric response	<i>org</i> → <i>aq</i> – tail finished peak <i>aq</i> → <i>org</i> – tail finished peak	<i>org</i> → <i>aq</i> – tail finished peak <i>aq</i> → <i>org</i> – wave like signal	<i>org</i> → <i>aq</i> – tail finished peak <i>aq</i> → <i>org</i> – wave like signal	<i>org</i> → <i>aq</i> – tail finished peak <i>aq</i> → <i>org</i> – tail finished peak
Scan rate (<i>v</i>) dependency	$I \propto v^{1/2}$	No	No	$I \propto v^{1/2}$

1.2. Sol – Gel Process of Silica employing Template Technology

The aspects described in the following subsections are: (i) chemistry and properties of silicon containing compounds, (ii) the Sol – Gel process of silica and (iii) template methods used for electrodes structuring – and each is described in regard to the content of the present work rather than giving comprehensive overview covering a set of very broad subjects. The first part covers the most relevant information including a nomenclature, chemical and physical properties of silicon and silicon containing compounds. Next, the Sol – Gel processing of silica materials is discussed chronologically – from the raw material to the final product – silica – formation. Third part describes the available template methods developed for the electrode surface engineering. Next, examples of the templated Sol – Gel processing of mesoporous silica are given, which emerge from solid state supports modification. Finally, the functionalization possibilities of mesoporous silica materials are briefly described.

1.2.1. Nomenclature and physicochemical properties of silicon and silicon containing compounds

Silicon (Si) is the second (after the oxygen) most abundant atom in the earth crust (around 28% by mass). Its physico-chemical properties are shown in **Table 1.4**. **Si** comprises of variety of silicate minerals (quartz, tridymite or cristobalite) or synthetic chemicals. In order to avoid any confusion, it is important to give one, commonly accepted terminology used to name silicon containing compounds. The term ‘**silica**’ will be used alternatively with its IUPAC name **silicon dioxide** (SiO_2). SiH_4 is called **silane**. The anionic species containing silicon atom, as for instance SiO_4^{4-} or $[\text{SiF}_6]^{2-}$ are called **silicates**. The term ‘**silanol**’ can be used when at least one OH group is attached to one silicon atom. **Silicic acid** is the silanol with the general formula $[\text{SiO}_x(\text{OH})_{4-2x}]_n$.

Table 1.4. Physicochemical properties of silicon atom.

Atomic number	14	Electron configuration	[Ne] 3s ² 3p ²	Atomic radius (non-bonded)	2.10Å ⁸⁵
Group	14	Melting Point	1410°C ⁸⁶ 1414°C ⁸⁵		
Period	3	Boiling Point	2355°C ⁸⁶ 3265°C ⁸⁵	Most common Oxidation states	-4, +4,
Block	p	Density	2.33 g/cm ³ (at 25°C) ^{86,85}	Electronegativity	1.90
Atomic weight and isotopes	28.085 ²⁸ Si –92.223% ²⁹ Si – 4.685% ³⁰ Si – 3.092%	Covalent radius	1.14 Å ⁸⁶	Bond enthalpies⁸⁵	
				H-Si	318 kJ mol ⁻¹
				Si-Si	222 kJ mol ⁻¹
				O-Si	452 kJ mol ⁻¹
				C-Si	301 kJ mol ⁻¹

Organosilicon compounds are when there is a covalent bond between silicon and carbon atom. Once two silicon atoms from two different organosilicon compounds are connected by oxygen atom, **siloxane** compound is being formed. The polymers with the skeletal structure formed from **siloxane** units are called **silicone**. **Siloxides** are the compounds with the general formula R₃SiOM, where R is the organic group and M is the metal cation. **Silicon alkoxides or alkoxy silanes** are the compounds of silicon and alcohol with the general formula Si(OR)₄ where R is the organic substituent (for example tetramethoxysilane, tetraethoxysilane, tetrapropoxysilane etc.).⁸⁷ The chosen silicon containing compounds can be found on **Figure 1.7**.

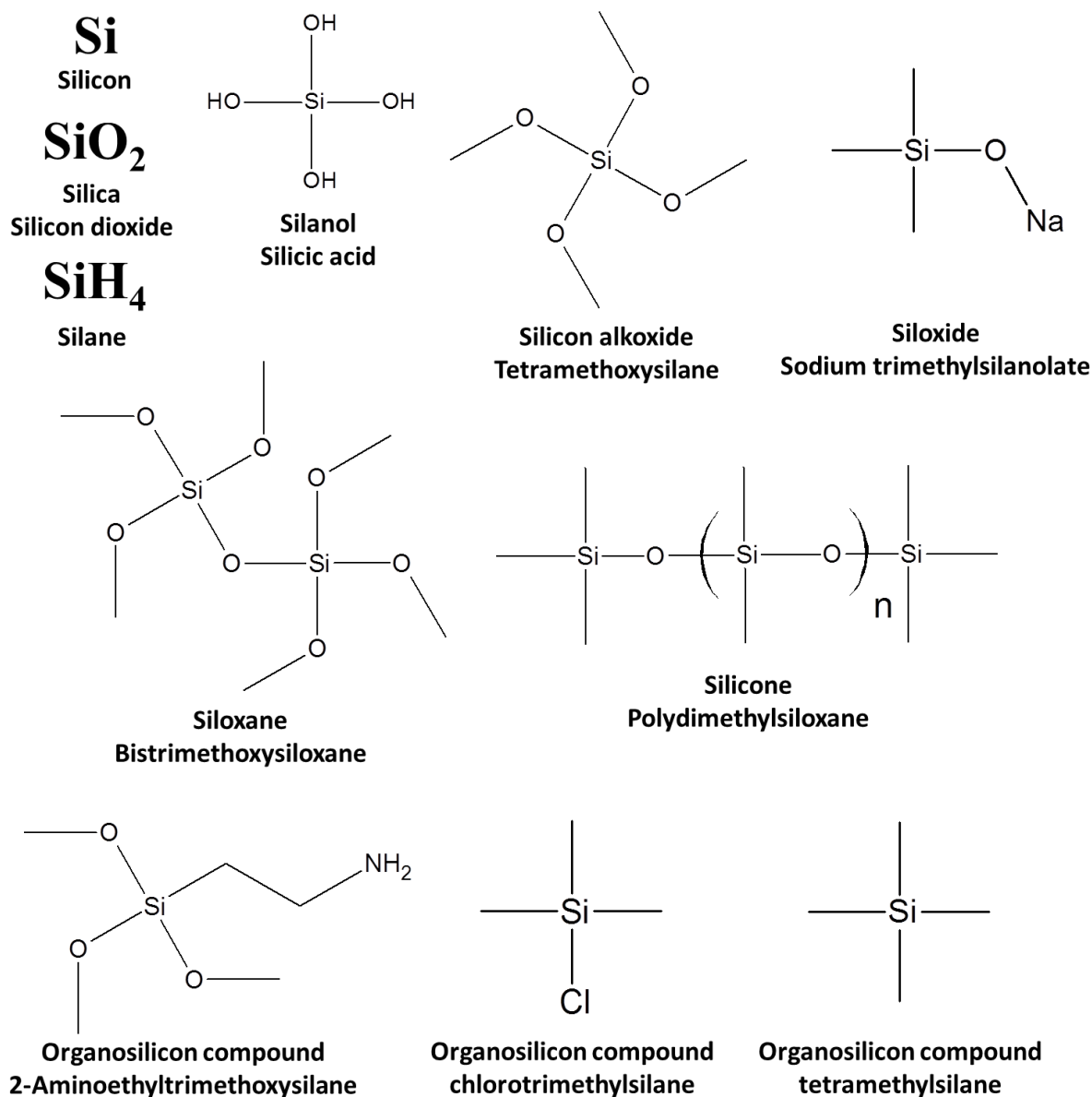


Figure 1.7. Examples of silicon containing compounds.

1.2.2. The Sol – Gel process of silica

The Sol – Gel processing of silica and silicates is a two-stage process which involves (i) hydrolysis with the final aim to reach sol (small particle dispersion in the liquid medium) and (ii) condensation, which results is the gel phase (relatively rigid polymerized and non-crystalline network possessing different in size pores). Apart from hydrolysis and condensation steps, one has to take into account other reactions that might occur, as for instance silica dissolution at higher pH values. Moreover, the gel phase usually needs further

post-treatment to cure not fully cross-linked silica matrix in order to obtain the solid material. All these steps have been well studied and described,⁸⁸ hence only a brief description will be given in here.

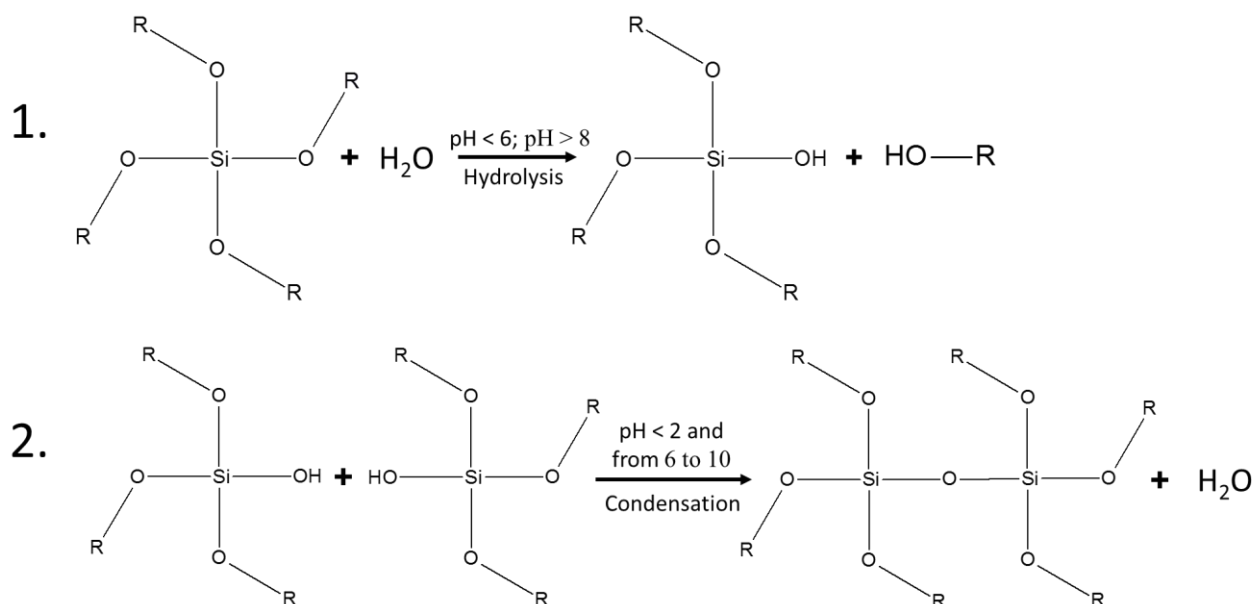


Figure 1.8. Hydrolysis (1) and condensation (2) reactions of tetraalkoxysilane.

1.2.2.1. Hydrolysis

The rate of hydrolysis of alkoxy silane species as a function of the pH is shown on **Figure 1.9** (blue curve). The reaction rate is slowest at a near neutral pH. Increasing concentration of protons or hydroxides species in the aqueous media leads to increase in hydrolysis rate. The reaction mechanism can be referred to as the nucleophilic substitution of S_N2 type, namely nucleophilic attack on the positively charged silicon atom, which takes place synchronously with the cleavage of the Si–OR bond. The hydrolysis reaction is shown on **Figure 1.8 (1)**. The rate of the hydrolysis reaction can be affected by the reaction medium – polar and protic solvents through formation of hydrogen bond may increase the efficiency of Si–OR bond cleavage – whereas the increasing hydrophobic character of R substituent shows the opposite effect.⁸⁸

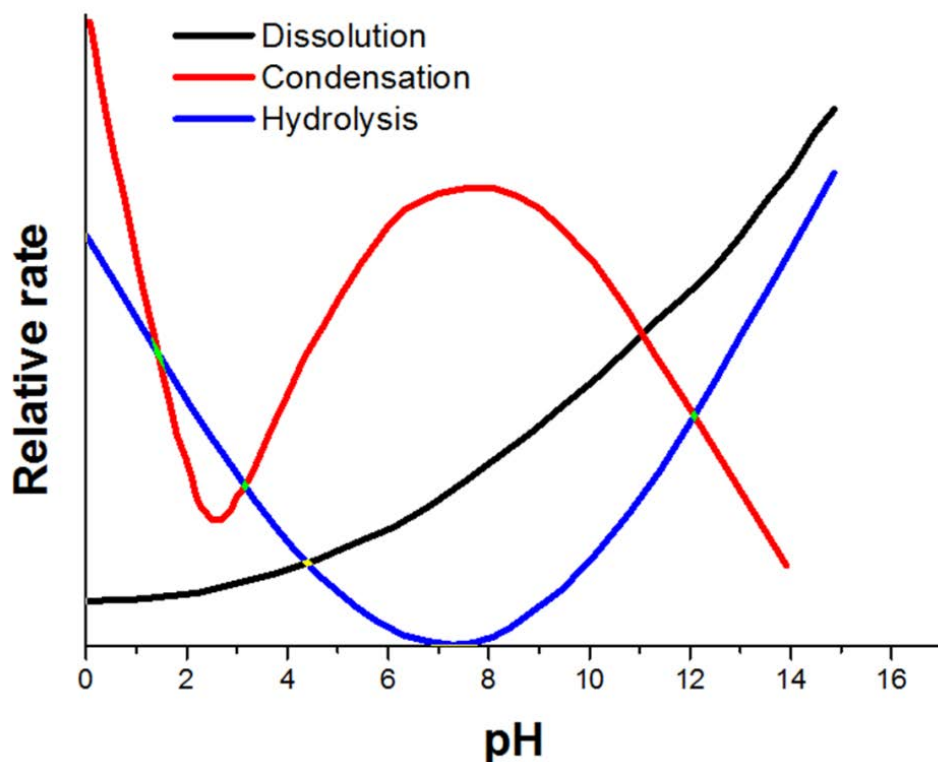


Figure 1.9. Schematic change in the relative rate for hydrolysis, condensation and dissolution of alkoxy silane and its products. Figure was adopted from ref⁸⁸

1.2.2.2. Condensation

Second step of the Sol – Gel process is the condensation reaction – see red curve on **Figure 1.9** for the kinetics versus pH dependence. The reaction takes place most efficiently in two pH ranges. The first, around the neutral pH conditions where the nucleophilic attack on the positively charged silicon atom is performed by deprotonated silanol moieties and the second range, at the acidic pH values ($\text{pH} < 2$), where deprotonated silanol moieties are even more attracted by positively charged silicon atom due to formation of protonated species - SiOH_2^+ . Condensation reaction leads to silicates polymerization and finally the formation of a gel (according to reaction (2) from **Figure 1.8**). The gelation process is dependent from a variety of factors: (i) temperature – polymerization can be thermally activated and can be significantly reduced at high temperatures; (ii) pH – gelation was found to be slowest at intermediate values and fastest at low and high values; (iii) solvent – decreasing content of water in reaction media leads to increase in the gelation time, as well as use of volatile additives.⁸⁸

1.2.2.3. Dissolution

The sol – gel process is said to be inhibited once the dissolution rate exceeds over the condensation rate. Dissolution rate versus pH is represented by the black line on **Figure 1.9**. Silicates or silica dissolution takes place under high pH condition – using strong bases – or in the presence of hydrofluoric acid. The mechanism of dissolution is similar in both cases and involves nucleophilic attack of OH^- or F^- on the positively charged silicon atom and subsequent cleavage of Si–O bond.^{88,87}

1.2.2.4. Curing

The silica structure in the gel state is not yet rigid. The matrix is flexible, not fully cross-linked and the reactions of hydrolysis, condensation and dissolution can still affect final structure of the silica network. The fulfillment of the condensation is performed with the drying process, which involves the following stapes: (i) reduction of the gel volume; (ii) successive emptying the liquid content from pores driven by capillary pressure and (iii) diffusion of the residual solvent to the surface and evaporation. The drying process is accompanied by formation of cracks due to the high surface tension at the interface between empty pores and liquid filled pores, which creates large pressure difference. Crack formation can be somehow overcome by generation of thin materials, the use of surface active species decreasing surface tension, drying under freeze-drying conditions or doping the silica with other more ‘elastic’ materials.⁸⁸

1.2.3. Templates – towards surface engineering

The idea behind template technology is very straightforward and assumes the use of the geometrically well-defined ‘mold’, which is then used to grow the material of interest, usually on the basis of the bottom-up approach. In electrochemistry, an electrode surface modification has many advantages: increase in the electroactive surface area (once conductive material is grown), enhancement in the mass transport via diffusion or improvement in the catalytic efficiency for the increasing number of nucleation sites (especially for near-atomic range of

roughness). Deposition of electrically insulating materials, as for instance porous silica, is of highest interest from the analytical point of view, especially when the deposit exhibits some degree of selectivity towards the analyte in the presence of a contaminant. Depending on pores dimension three main class of porosity can be distinguish: (i) microporous materials – are when the pore widths is less than 2 nm; (ii) mesoporous materials – with the pore widths between 2 and 50 nm and (iii) macroporous materials – with the pore widths greater than 50 nm.⁸⁹

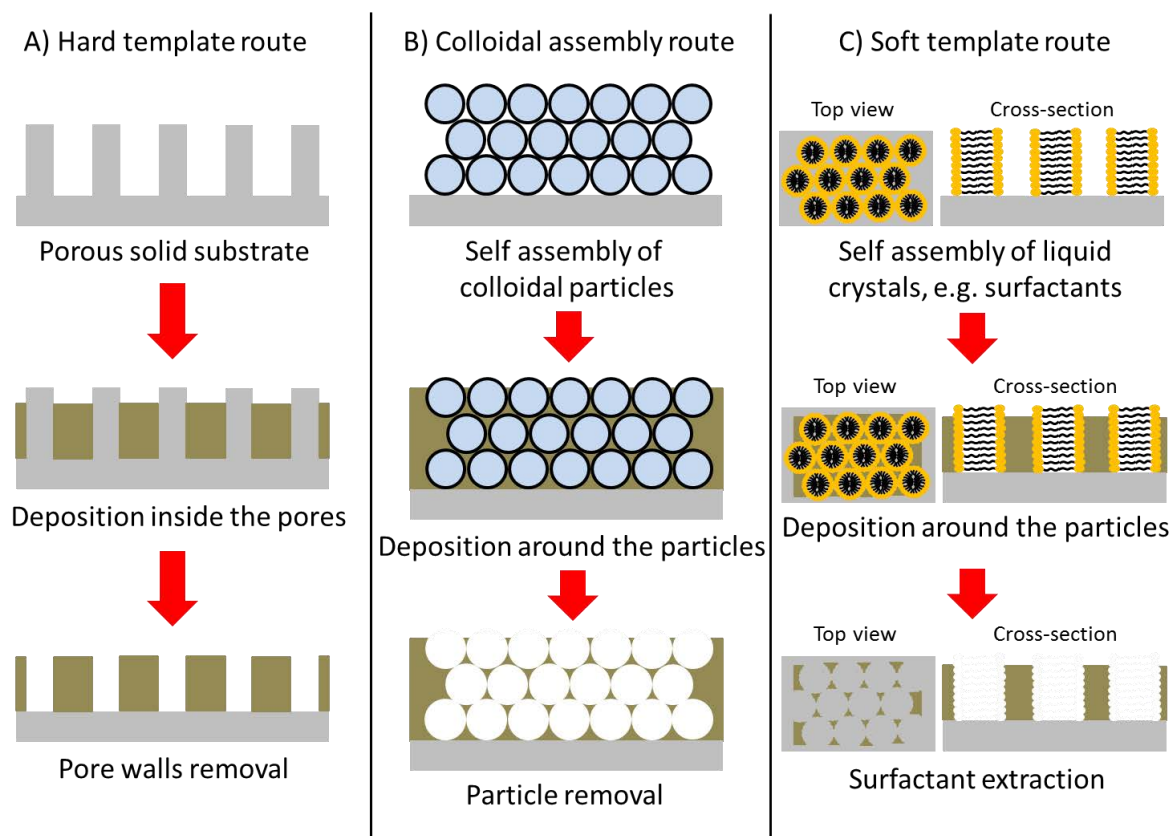


Figure 1.10. Illustrative schemes for hard, colloidal assembly and soft template route.

Walcarius has divided the templates into three main groups: hard templates, colloidal crystal assemblies and soft templates.⁹⁰ Hard template is the term reserved for a solid porous substrate that is modified within the pores and the deposit is then released by removal of surrounding pore walls (see **Figure 1.10 A**). Template route employing colloidal particles was classified as an intermediate option bearing the rigidity of the hard templates and self-assembly properties of soft templates (see **Figure 1.10 B**). The last group – shown on **Figure 1.10 C** – belongs to ‘soft’ mater, in this case liquid crystals formed by amphiphilic species (able to form variety of spatial arrangements: micelles, vesicles, cubic, hexagonal or lamellar

liquid crystal structures), which is the most versatile method as the template extraction can be performed under mild condition without affecting deposit properties.

Silica or silicate materials can exhibit dual role since they were used as templates (in form of colloidal assemblies for instance)⁹¹ and were easily templated as shown in the following subsection.

1.2.4. A soft template for a Sol-Gel process of mesoporous silica thin films

Evaporation Induced Self-Assembly (EISA) is the method, which allows the formation of a silica film with controlled mesostructure and pore size by varying: chemical parameters and processing conditions. In general, in such a method, the sol solution (containing template and silica precursor species) is contacted with the solid support interface and the volatile components (e.g. H₂O, EtOH and HCl) of the reaction media are left to evaporate. Reducing the volume of the sol solution results in condensation of the silica precursor around the template matrix (which tend to form liquid crystal phases once its critical micelle concentration is reached). Once solvent is evaporated the silica film is formed.⁹² Variety of processing methods were developed for EISA process, examples include: dip-coating – with the substrate being immersed to the sol solution and subsequently pulled out at a known rate;⁹³ spin-coating – centrifugal force is used to spread the sol solution over the support;⁹⁴ casting – when the sol is simply poured on the support and left for evaporation⁹⁵ or spraying – transferring the sol solution on the material in the form of aerosol.⁹⁶ Under proper conditions, all the above methods allow the formation of ordered films with pores oriented horizontally to the support plane.

Deposition of mesoporous silica at solid electrodes in the manner which does not exclude the electrical contact between the medium phase and a conductive substrate is challenging. Deposition of mesoporous silica films with high symmetry and controlled pore orientation – preferentially perpendicular to the substrate plane – is achievable by Electrochemically Assisted Self-Assembly (EASA).^{97,98} In such an approach, the condensation of silica precursor is catalyzed by OH⁻ electrogeneration at sufficiently low cathodic potential. Under these conditions, the cationic surfactants (cetyltrimethylammonium cations) present in the

reaction media form hexagonally packed liquid crystal phase growing perpendicular to the electrode surface. The condensation of silica and self-assembly of soft templates occur simultaneously. The resultant thin film, after thermal curing, shows highly ordered silica network with the pores oriented normal to the underlying support.

1.2.5. Functionalized mesoporous silica films prepared by Sol-Gel processing

The introduction of chemical functionalities possessing different physico-chemical properties allows of material chemical and physical properties to be altered. It is especially important in analytical chemistry since it improves the selectivity once the system is designed to favors the detection of analyte and in parallel, inhibits the detection of contaminant (e.g. based on charge, hydrophilic/hydrophobic or host – ligand interactions). The sensor becomes even more versatile when surface nanoarchitecture is additionally adjusted. Such attributes are easily feasible for highly ordered mesoporous silica films with pores oriented normal to the surface plane prepared by EASA method.⁹⁹ The functionalized mesoporous silica prepared by the Sol – Gel process has two possible synthetic routs: (i) direct co-condensation with organosilanes and (ii) co-condensation and deposition followed by chemical reaction. The first method involves hydrolysis of alkoxy silanes with organosilanes bearing the functional group of interest. An electrochemical deposition leads to functionalized silica film formation. Such an approach allowed the introduction of simple functionalities as for instance methyl – up to 40% mmol,¹⁰⁰ amine – up to 10% mmol⁹⁹ or thiol – up to 10% mmol¹⁰¹ groups without lost in mesostructure order. The second method is composed from two steps. Initially the organosilanes with the reactive organic group are co-condensate with the alkoxy silanes and electrodeposited at the solid electrode surface. The second step involves the reaction between the organic functionalities from the silica framework and properly selected reagent. A pioneering example was developed by Vilá *et al.* who electrogenerated azide functionalized oriented and ordered mesoporous silica films (for up to 40% mmol of azide group bearing silanes in the initial sol solution) that were further modified by alkyne-azide ‘click’ reaction with ethynylferrocene or ethynylpyridine.¹⁰²

1.3. Liquid – liquid interface modification

Liquid – liquid interfaces can be modified *ex situ* (with material performed prior to its interfacial deposition) or *in situ* (when the interfacial reaction results in deposit formation). Electrochemistry at the ITIES can be the driving force for the interfacial modification as it can be a tool for deposits evaluation. The following description of the examples emerging from electrified liquid – liquid interface modification is divided into: (i) metal interfacial deposition, (ii) phospholipids at the ITIES, (iii) interface modification with organic polymers, (iv) carbon based materials (with some examples emerging from semi-modified ITIES e.g thin layer ITIES supported with carbon based electrodes or three phase junction set-ups) and finally (v) silica materials. The last group gives an overview on the recent development in the field of liquid – liquid interface modification with silica materials. It covers the reports dealing with the electrified ITIES as well as the neat liquid – liquid interface modification.

1.3.1. Metals at the electrified liquid – liquid interface.

Metal deposition at the liquid – liquid interface involves metal precursor dissolved in one phase and the electron donor dissolved in the latter. The mechanism of deposition follows the homogeneous or the heterogeneous electron transfer reaction and results in the interfacial formation of metallic films or metal NPs. Historically, the first report dealing with the metal interfacial electrogeneration was communicated by Guinazzi *et al.* who reported the formation of metallic Cu film at the ITIES between aqueous solution of CuSO_4 and dichloroethane solution of $\text{TBA}^+\text{V}(\text{CO})_6^-$ once the current was passed through the system.¹⁰³ From that time the electrified liquid – liquid interface has attracted significant scientific interest towards metal deposition. In the following section, a few examples emerging from Au, Ag and Pd and Pt interfacial electrodeposition are given.

1.3.1.1. Au deposition at the ITIES

Au NPs and Au films deposition at the electrified liquid – liquid interface is very recent topic which is gaining ground every year. The first report dealing with potential controlled deposition of preformed Au NPs at the liquid – liquid interface was by Su *et al.*, who have shown that mercaptosuccinic acid stabilized Au NPs, suspended in the aqueous phase can undergo a reversible interfacial adsorption under controlled Galvani potential difference.¹⁰⁴ Reversible assembly of Au NPs taking place at the negative end of the voltammetric potential window could not be followed by current characteristics and hence, was studied by electrocapillary curves constructed under different Au NPs concentrations. Adsorption of negatively charged citrate-coated Au NPs was also observed at negative potentials by capacitance measurements.¹⁰⁵

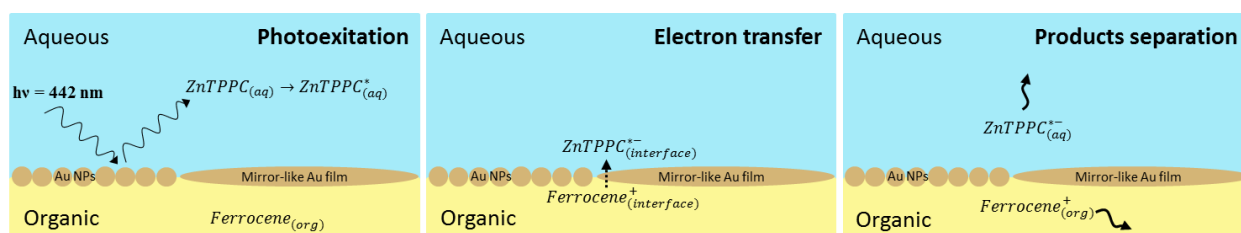
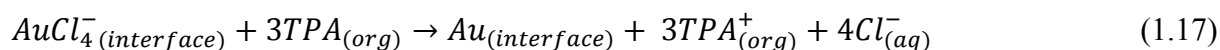


Figure 1.11. Schemes representing following steps of photocurrent evolution at the Au (NPs or mirror-like film) modified ITIES. ZnTPPC is the meso-tetra(4-carboxyphenyl)porphyrin. Figure was prepared based on ref¹⁰⁶.

Cheng and Schiffrin reported as a first *in situ* Au particle formation at the electrified ITIES. The deposition reaction was triggered by the electron transfer between $Fe(CN)_6^{4-}$ in the aqueous phase and $AuCl_4^-$ in the DCE.¹⁰⁷ Interestingly Gründer *et al.* have not observed any Au^0 formation under similar conditions unless some preferential nucleation sites were introduced to the system (Pd NPs adsorbed at the ITIES).¹⁰⁸ Schaming *et al.* extended Au^0 modified liquid – liquid interface to photovoltaics applications.¹⁰⁶ The liquid – liquid interface was modified with Au NPs or mirror-like Au films. Photo-excited meso-tetra(4-carboxyphenyl)porphyrin was located in the aqueous phase, whereas the ferrocene species were dissolved in the dichloroethane. Modified interface irradiation at the 442 nm – under total internal reflection conditions – has led to the increase in photocurrent (resulting as electron transfer from ferrocene in the organic phase to excited porphyrin from the aqueous

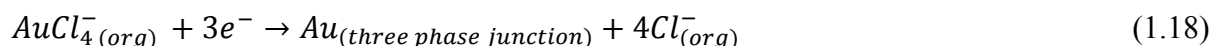
phase – see **Figure 1.11** for details) with significantly greater efficiency for the mirror-like deposit as compared with the Au NPs.¹⁰⁶

Other reductants for Au precursor were also used. The interfacial reduction of the $AuCl_4^-$, on its transfer from organic phase containing tri-(p-tolyl)amine reductant to the aqueous phase, could be observed by metallic Au formation confirmed with microfocus X-ray absorption near-edge structure spectroscopy.⁷ Uehara *et al.* studied gold NPs formation in the system containing gold precursor ($AuCl_4^-$ or $AuCl_2^-$) initially dissolved in the aqueous or the organic (dichloroethane) phase and triphenylamine (TPA) reductant in the organic phase.¹¹⁰ Voltammetric Au NPs deposition with $AuCl_4^-$ in the aqueous phase and TPA in organic phase starts with the $AuCl_4^-_{aq \rightarrow org}$ transfer (with $E_{1/2 AuCl_4^-_{aq \rightarrow org}} = 115 \text{ mV}$), which is followed by interfacial $AuCl_4^-$ reduction on the back transfer to the aqueous phase:



No spontaneous reaction was found to take place when $AuCl_4^-$ was initially dissolved in the DCE together with TPA. Higher reactivity was found for $AuCl_2^-$ electron transfer induced reduction and hence it was used for Au NPs deposition for further analysis. The effect of time and potential were examined. The particle size distribution depended on the conditions applied. NPs as small as 3 nm were obtained at lower potentials and shorter deposition times. The NPs size increased up to 50 nm at higher potential and longer deposition times.¹¹⁰

One example from group of Opallo emerges from Au modified three phase junction system.¹¹¹ The cell composition was the ITO electrode crossing the liquid – liquid interface constituted between the organic phase containing a gold precursor salt – tetraoctylammonium tetrachloroaurate – and aqueous solution of a hydrophilic salt – KPF_6 – see **Figure 1.12**. The electrochemical reduction, which was taking place only at the three phase junction, led to gold deposition:



which was coupled with the ion transfer reaction – relatively hydrophobic PF_6^- ions transfer to the organic phase and repeal of Cl^- to the aqueous phase:



The NPs deposition was performed by chronoamperometry. Size distribution (from 110 to 190 nm) and the shapes (most of all rounded particles were formed) were found to be unaffected after initial growth.

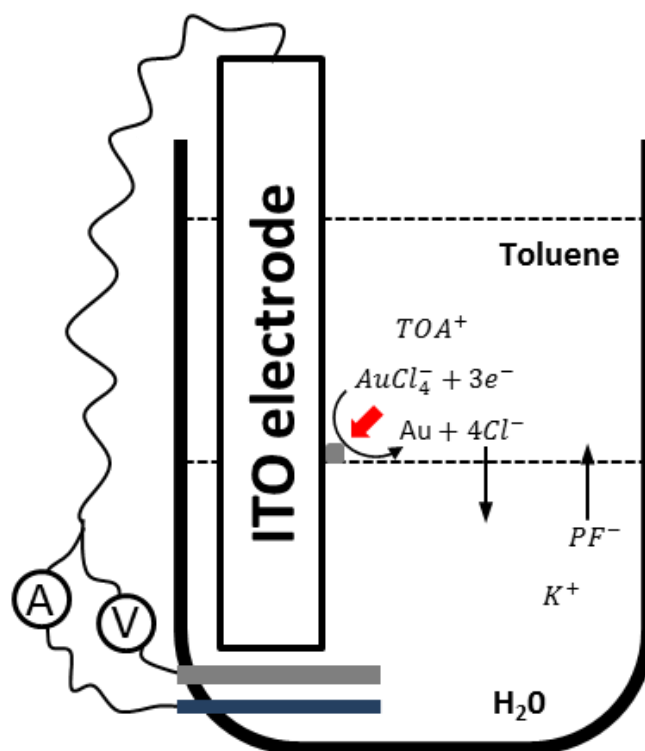


Figure 1.12. Three phase junction set-up used for Au NPs deposition. TOA⁺ is the tetraoctylammonium cation.

Another issue employing liquid – liquid interface modification with Au NPs found application as liquid-mirrors.¹¹² The optical and electrochemical properties of the gold mirror like films prepared from Au NPs were found to be depended from the surface coverage, NPs size and the polarization of the incident irradiation as well as its wavelength.¹¹³ It was found for instance that the films prepared from 60 nm Au NPs for the surface coverage parameter equal to 1.1 (indicating the formation of one monolayer) exhibited the maximum reflectivity (for S-polarized light under green laser irradiation). Moreover, the films were found to be conductive starting from surface coverage equal to 0.8 (as confirmed with the SECM).

1.3.1.2. Ag deposition at the electrified ITIES

Interfacial electrodeposition of Ag films at the liquid – liquid interface from so-called the three phase junction system was studied in a series of by Efrima.^{114,115,116} Deposition was performed by reduction of aqueous Ag^+ with the conventional three electrode set-up with silver working electrode ‘touching’ the liquid – liquid interface. In the set of referred works the authors included detailed study of the effect of the organic phase solvent, concentration of the silver precursor, potential of the silver reduction, presence of surfactants etc. on the film formation morphology. For instance, once the aqueous phase was contacted with the low surface tension solvents, deposits were thinner, shinier and possessed higher degree of ramification. In contrary, the silver films electrogenerated at the interface between water and organic solvents of higher surface tension were black and required much longer deposition times.¹¹⁶

Guo *et al.* studied the formation of Ag nanoparticles at the miniaturized (nano- and micro-ITIES).¹¹⁷ Interfacial polarization allowed the electron transfer from the organic phase containing BuFc to reduce Ag^+ from the aqueous phase and subsequent formation of Ag NPs. Single particle deposition was shown to take place at the microITIES lesser than 0.5 μm . In another study, Li *et al.* used SECM in anodic generation mode for the generation of Ag NPs (see Figure 1.13).¹¹⁸

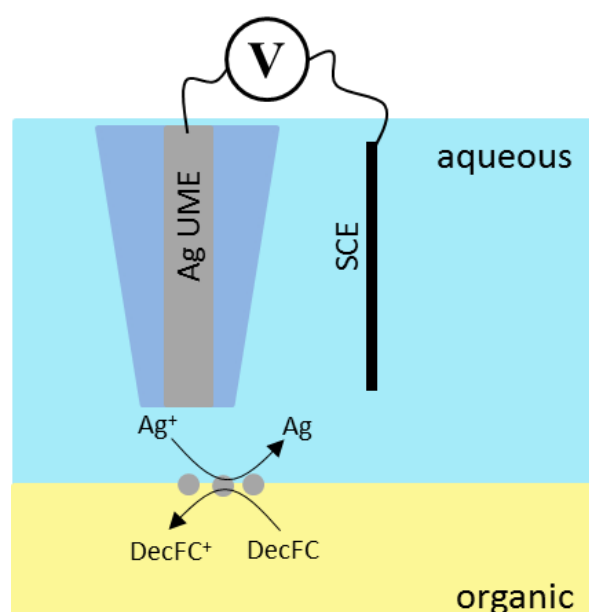
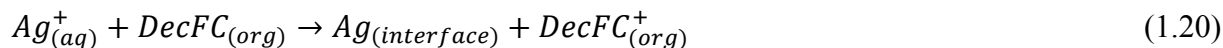


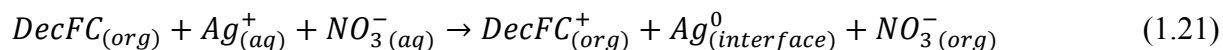
Figure 1.13. The scheme representing Ag NPs deposition by SECM anodic dissolution of silver UME. Adapted from ref.¹¹⁸

The Ag disc ultramicroelectrode was first oxidized above the liquid – liquid interface to give Ag^+ ions, which thereafter were reduced to metallic Ag by decamethylferrocene dissolved in the DCE. The heterogeneous electron transfer reaction can be written as:



It was found that the interfacial potential difference established with the common ion method had a weak effect on the nucleation and the growth process.

Ag deposition at the ITIES driven by the free energy and ion transfer was reported by Schutz and Hasse.¹¹⁹ The aqueous phase was a solution of $AgNO_3$ whereas the organic phase (nitrobenzene or n-octanol) contained DecFC or ferrocene as reductant. The spontaneous transfer of $NO_3^-_{(aq \rightarrow org)}$ triggered the reduction of Ag^+ (present in the aqueous phase) by the reductant from the organic phase. The reaction was driven by the rule of charge neutrality of the system. For DecFC the reaction can be schematically written as:



In the subsequent work, it was shown that the presence of the dust pollutants in the air – adsorbing at the interface before contacting two phases – give some preferential site for the nucleation process and has led to deviation from initially obtained – whisker like fibers – morphologies.¹²⁰

An interesting approach was introduced for Ag NPs electrodeposition at the liquid – liquid interface separating bulk aqueous phase from the thin layer organic phase (nitrobenzene) supported by graphite electrode.¹²¹ Two approaches for Ag NPs electrogeneration were studied. The first at OCP, where the Ag^+ from the aqueous phase was spontaneously reduced by the DecFC from the organic phase (see **Figure 1.14 A**) and the second, with the potentially controlled DecFC⁺ regeneration at the graphite electrode (see **Figure 1.14 B**). The authors noticed that regardless of the deposition technique employed, the $ClO_4^-_{(aq \rightarrow org)}$ or $NO_3^-_{(aq \rightarrow org)}$ interfacial transfer, promoting the reaction at OCP or being induced by the DecFC⁺ electrochemical regeneration, was suppressed by the increasing Ag NPs coverage.

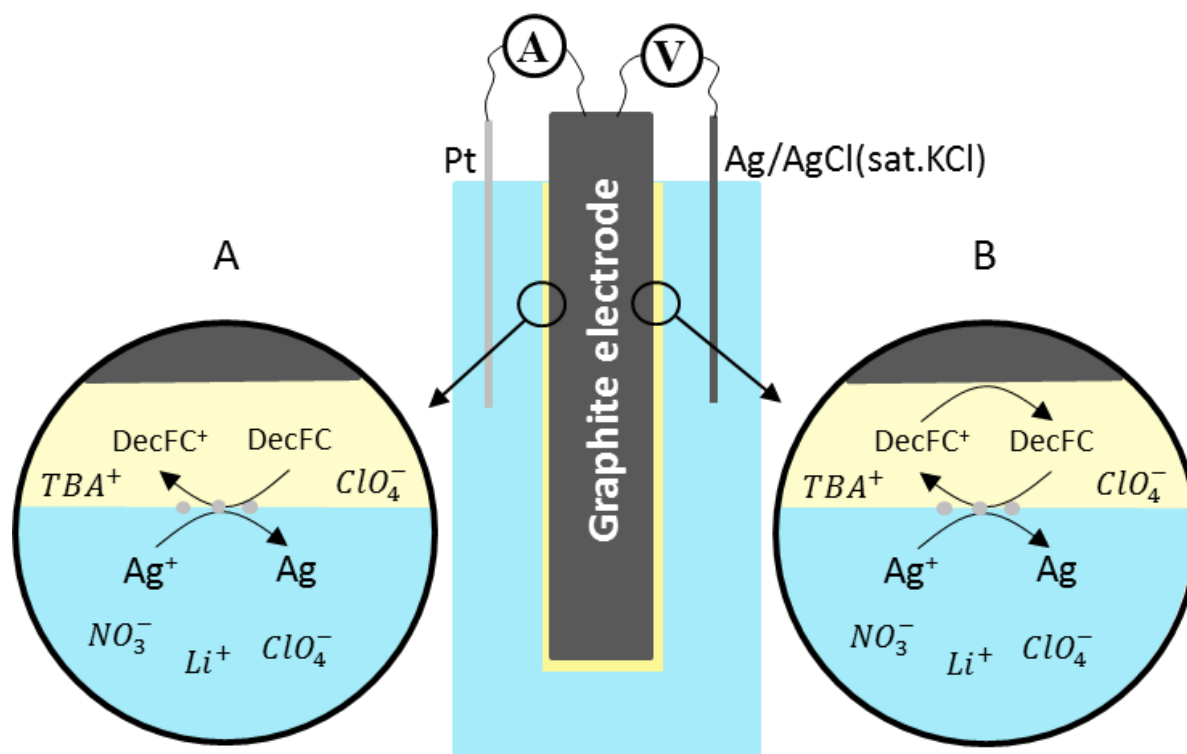


Figure 1.14. Thin layer organic phase liquid – liquid interface approach for the Ag NPs electrodeposition approach. A – Corresponds to the open circuit potential electrodeposition and B – corresponds to the potential controlled electrodeposition. Adapted from ref.¹²¹

1.3.1.3. Pd and Pt deposition at the electrified ITIES

Deposition of metallic Pd and Pt NPs at the ITIES was usually performed under potentiostatic interfacial reduction of metal-chloro-complex present in the aqueous phase by heterogenous electron transfer reaction from organic phase containing reductant – for instance 1,1'-dimethylferrocene¹²² or butylferrocene.¹²³ An electrochemically induced liquid – liquid interface modification with both metals attracted a lot of attention concerning mechanistic studies of nucleation process. Johans *et al.* have proven on the basis of theoretical model that Pd NPs nucleation is free from preferential nucleation sites.¹²⁴ The size of the Pd particles was also found to have an effect on their surface activity and based on quantitative thermodynamic considerations it was shown that only particles exceeding a critical radius can stay at the interface and further grow. When the interfacial tension was lowered by the adsorption of phospholipid molecules following changes were noticed: (i) the nucleation kinetics was significantly decreased (kinetics of growth was found to be unaffected); (ii) the critical radius

and consequently, the particles size of the same surface activity had to increase and (iii) more energy was required to trigger the electron transfer reaction.¹²⁵

In order to eliminate NPs agglomeration found in all previous works, the ITIES was miniaturized using an alumina membrane with the mean pore diameter of 50 nm¹²⁶ and 100 nm.¹²⁷ Interestingly the growth of NPs was observed only in some of the pores, which was explained by autocatalytic effected followed by an interfacial nucleation. Other explanation of such a behavior was given by Trojáněk *et al.* who studied initial nucleation rates of the Pt NPs and with the wide range of values obtained (from nucleation rate approaching zero up to $207 \cdot 10^{-5} \text{cm}^{-2} \text{s}^{-1}$), they concluded that the presence or lack of nucleus formation is dictated by probability.¹²²

Pd and Pt are known for a long time as extremely versatile catalysts. This feature was also feasible at the liquid – liquid interface. For instance, pre-formed Pd NPs activated electrochemically by heterogeneous electron transfer reaction from the organic phase containing decamethylferrocene were used to catalyze the dehalogenation reaction of organic substrate being dissolved in the aqueous phase.¹²⁸ Hydrogen evolution reaction was also catalyzed by Pd and Pt NPs (with the first having slightly better efficiency) electrogenerated *in situ* at the ITIES by metal precursor reduction with decamethylferrocene – electron donor which also served as a reductant for the aqueous phase protons.¹²⁹ Trojáněk *et al.* show the catalytic effect of Pt NPs modified ITIES on the oxygen reduction reaction obtaining the rate constant one order of magnitude greater as compared with the unmodified liquid – liquid interface.¹³⁰

1.3.2. Phospholipids at the electrified liquid – liquid interface

Phospholipids are a class of lipids being a part of all biological cell membranes. Phospholipids with the phosphate polar head group and the fatty acid tails are amphiphilic and biological membranes owe a unique double layer structure to this particular property. The nature of the functional groups attached to the phosphate groups results in five main types of compounds: phosphatidylcholines (PC), phosphatidylserines (PS), phosphatidylethanolamines (PE), phosphatidic acids (PA) and phosphatidylinositides (PI). Among each family, the

number and saturation of carbon in alkyl chain may differ, with the exception of phosphatidylinositides where additionally inositol group can be substituted with one, two or three phosphate groups.¹³¹ Modification with phospholipids were successfully applied to the solid/liquid,^{132,133} air/liquid¹³⁴ and at the liquid – liquid interfaces.¹³⁵ Model phospholipid monolayers are well-defined and controllable systems, which represents half part of the biological membrane. The phospholipid modified liquid – liquid interface can also provide the information about pH equilibrium, adsorption – desorption reaction of the lipids at and from the liquid – liquid interface, association – dissociation interaction of phospholipids with charged species from both sides of the interface as discussed in series of papers from Mareček *et al.*^{136,137,138}

The interface modified with a phospholipid monolayer can be studied by the simple ion transfer process across the artificial half part of biological membrane. For instance, adsorption of phosphatidylcholines on the water-1,2-dichloroethane interface had almost no effect on the transfer of tetraethylammonium cations.¹³⁹ As discussed in mentioned work, the phospholipids at the ITIES form ‘*island-like clusters*’ which partially cover the interface and the electrochemical signal is due to the transfer of electroactive species through cluster free domains. In order to control a compactness of the adsorbed monolayer, the surface pressure control – with the Langmuir trough technique – as an additional degree of freedom was introduced.^{140,141} Even though the monolayer quality could be controlled by lateral compression, the large planar area gave rise to a potential distribution and become unstable due to the dissolution of the adsorbed phospholipids in the organic phase. To overcome such difficulties, the Langmuir trough used to control surface pressure of the adsorbed phospholipid monolayer was used as the aqueous half-part of electrochemical cell. The second, organic phase was specially designed PTFE cell containing gelled *o*-nitrophenyloctylether (*o*-NPOE) – poly(vinyl chloride) (PVC), which was immersed into the monolayer, resulting in gel-liquid interface (see. **Figure 1.15**).¹⁴²

The effect of 1,2-dioctadecanoyl-*sn*-glycero-3-phosphocholine (DSPC) monolayer onto the adsorption and the kinetics of charge transfer for TEA⁺, propranolol, metoprolol and tacrine has been studied by cyclic voltammetry and AC voltammetry.¹⁴² Comparison of the calculated values of admittance and apparent capacitance in the presence and absence of ion transfer through DSPC monolayer allowed concluding what follows: (i) all studied ions tend to interact with the phospholipid membrane; (ii) rate constant of TEA⁺, propranolol and metoprolol decrease with increasing phospholipid deposition surface pressure. No change was

observed for tacrine and (iii) calculated apparent capacitance values in the presence and the absence of ion transfer indicated that charge transfer reaction of tacrine and partially the metoprolol are coupled with the adsorption process. In subsequent work, electrochemical impedance spectroscopy was used to evaluate interaction between four similar in structure therapeutics (aminacrine, tacrine, velnacrine and proflavine) and – different in composition – phospholipid monolayers adsorbed at the ITIES. The results indicated that the preferable adsorption site in the organic phase for velnacrine and proflavine is the polar head group region whereas tacrine and aminacrine prefer hydrocarbon tail domains.¹⁴³

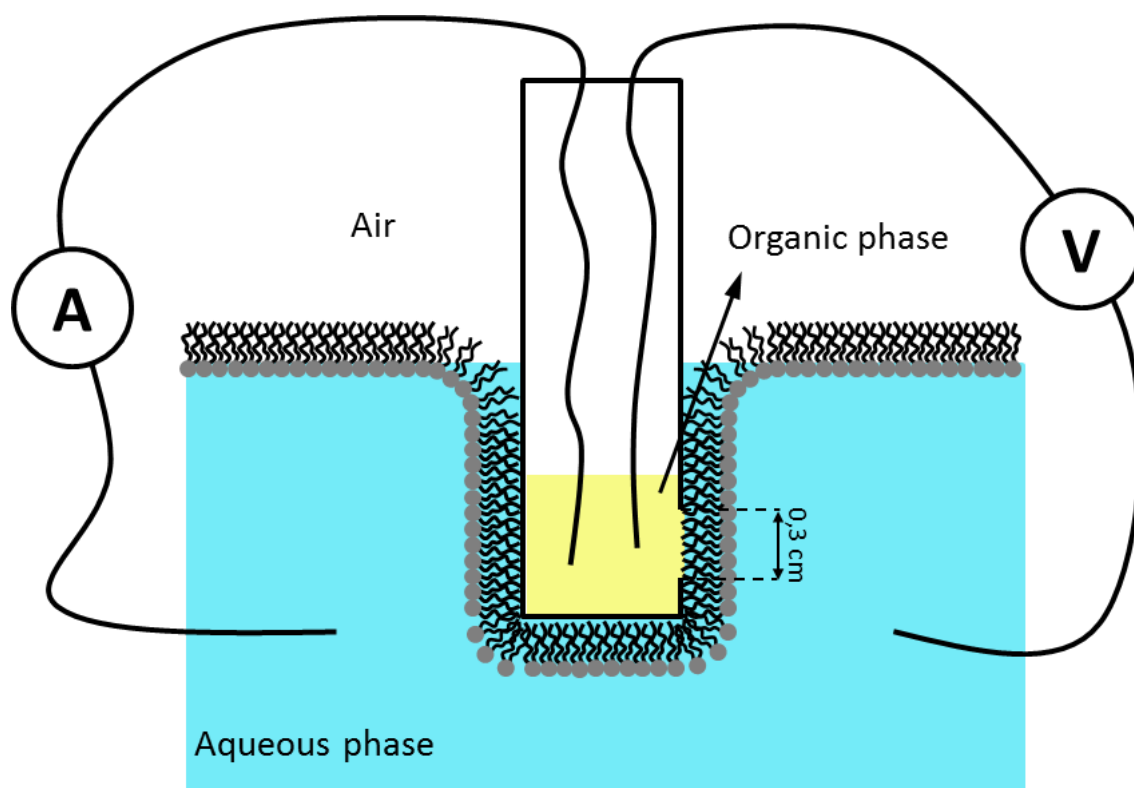


Figure 1.15. Simplified electrochemical cell allowing the compact phospholipid monolayer formation at the electrified organic gel – aqueous phase interface. Adapted from ref.¹⁴²

Phospholipid monolayer modified ITIES was employed for other bioimportant molecules study. The interaction of dextran sulfate/Ru nanoparticles¹⁴⁴, dextran sulfate (DS)^{145,146} or/and gramicidine (gA)¹⁴⁶ with monolayers composed from different phospholipids affected the rate constant of different ions transfer across the monolayer. The presence of DS among the phospholipid monolayer decreased the rate constant for the TEA⁺ and metoprolol in opposite to the gA modified monolayer, which slightly enhanced its rate constant. For the monolayers

coupled with the DS/Ru nanoparticles it was demonstrated that the rate constant was reduced by the factor of 2/3 for aminacrine and 1/2 for tacrine with respect to bare phospholipid monolayer. For broader image of the ITIES modified with the phospholipid monolayer it is convenient to reach review publications devoted to this particular topic.^{135,147,148}

1.3.3. Organic polymers at the polarized liquid – liquid interface

It was mainly the group of Cunnane which introduced and developed the concept of electropolymerization of the organic polymers at the liquid – liquid interface. First report, describes the electron transfer reaction between Fe^{3+}/Fe^{2+} redox couple in the aqueous phase and the 1-methylpyrrole (**Figure 1.16 A**) or 1-phenylpyrrole (**Figure 1.16 B**) monomer (Mon) in the organic phase:¹⁴⁹



Radical cation electrogeneration was followed by oligomers formation in the organic phase without any interface modification. It was also shown that N-phenylpyrrole present in the organic phase can facilitate semi-reversible Ag^+ transfer from the aqueous phase, which results in the formation of polymer coated silver nanoparticles in the organic phase (no direct evidence was given besides from electron absorption measurement).¹⁵⁰

Mareček *et al.* were the first who modified the ITIES with a free standing polymer layer.¹⁵¹ The interface modification with pyrrole containing polymers was triggered by the potentiostatic electron transfer between interfacially adsorbed monomer (**Figure 1.16 C** – 4-(pyrrol-1-yl)phenyloxyacetic acid) and Ce^{4+} dissolved in the aqueous phase. Interfacial measurement allowed the study of polymerization reaction. Interestingly, ion transfer voltammetry of TMA^+ and PF_6^- with simultaneous polymer deposition showed that an increasing number of voltammetric cycles has led to the formation of compact layer, which acted as physical barrier and hence charge transfer was first reduced and consequently significantly subtracted. Potential shift in current peaks was observed for facilitated transfer of K^+ by DB18C6 in presence of polymer film at the liquid – liquid interface and no additional resistance to mass transfer was encountered when facilitated transfer of H^+ by DB18C6 was probed.

The liquid – liquid interface electro-modification with polythiophene was the subject of works by Cunnane *et al.* Interfacial polymerization was controlled by the heterogeneous electron transfer between Ce^{4+}/Ce^{3+} in the aqueous phase and 2,2':5',2'' terthiophene monomer (**Figure 1.16 D**) from the organic phase controlled with the use of external power source¹⁵² or by employing potential determining ions.¹⁵³ It was found that interfacial modification with polythiophene film requires concentrations > 1 mM (lower concentration has led to oligomers formation in the organic phase only). The mechanism of interfacial deposition¹⁵³ starts with the heterogeneous electron transfer with the $\Delta_{org}^{aq} \Phi_{1/2} = 24$ mV and formation of the radical cation of the monomer – $Mon^{\bullet+}$:



Formation of the $Mon^{\bullet+}$ at sufficiently high potential results in formation of sexithiophene (6M) according to reaction:



Elongation of oligomers lowers their oxidation potential which results in the formation of oligomeric cation radical:



which precipitates at the liquid – liquid interface



The roughness of the polymer film was found to be in the order of tens of nanometer as measured with the AFM.¹⁵⁴ Direct electro-polymerization at the liquid – liquid interface was also reported for polythiophene. The oxidation potential for the monomer was found to be $> +1.85$ V and in case of the studied system (aqueous phase was the 0.1 M $Ce^{4+}/0.01$ M Ce^{3+} redox couple, 0.2 M H_2SO_4 and 0.1 M Li_2SO_4 whereas the organic phase was solution of 1 mM TPAsTPBF and 1 mM 2,2':5',2'' terthiophene) it was overlaid with a background current limiting the potential window. The presence of growing polymer layer additionally inhibited the transfer of the organic phase electrolyte ions (TPAs⁺ on the negative site and TPBF⁻ on the positive site of the potential window), which was attributed to the formation of physical obstacle.¹⁵⁵

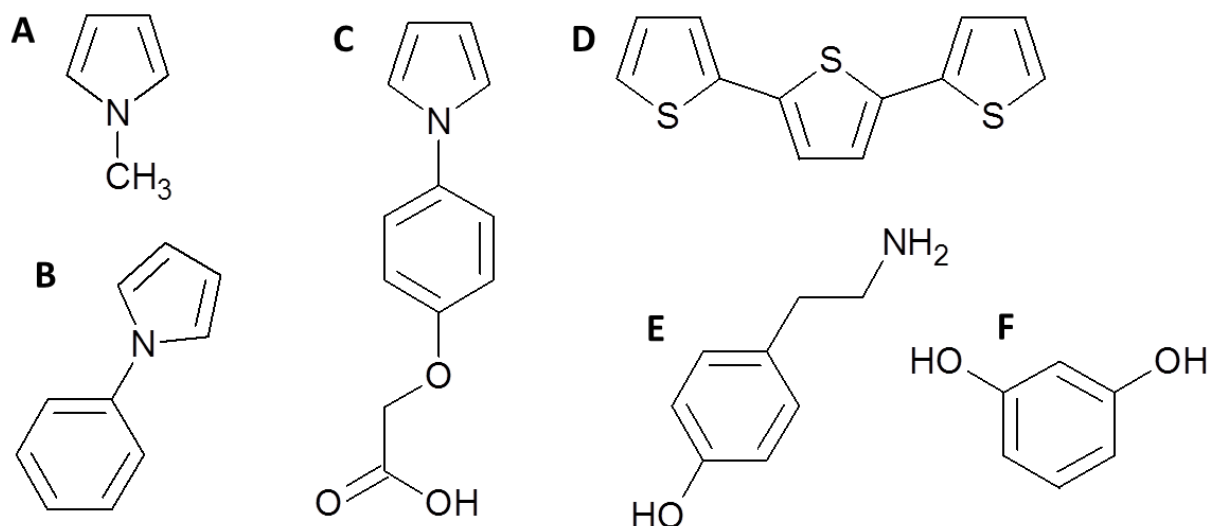
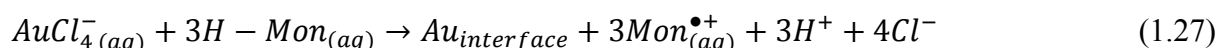
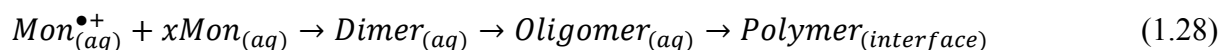


Figure 1.16. Structures of the monomers used for the electropolymerization at the electrified liquid – liquid interface: A – 1-methylpyrrole, B – 1-phenylpyrrole, C – 4-(pyrrol-1-yl)phenoxyacetic acid, D – 2,2':5',2'' terthiophene, E – tyramine and F – resorcinol.

Electrodeposition of polymer – Au NPs hybrid material was also investigated by Cunnane *et al.* Gold precursor – tetraoctylammonium tetrachloroaurate ($TOAAuCl_4$) and organic electrolyte were initially dissolved in dichloroethane whereas the organic polymer monomer – tyramine (**Figure 1.16 E**) or resorcinol (**Figure 1.16 F**) – was dissolved in the aqueous electrolyte solution. The most probable mechanism of polymer – Au NPs hybrid material formation¹⁵⁶ starts with the ion transfer of $AuCl_4^-$ ($org \rightarrow aq$) where it undergoes homogeneous electron transfer with the monomer species:



Evolution of radical cation in the aqueous phase triggers the polymerization reaction:



The formation of the compact layer at the ITIES was confirmed by the blocking effect for the ions crossing the interface with a subsequent voltammetric cycling (attributed to the grown of the polymer thickness). Growth of the film and size distribution of embedded Au NPs were studied under different experimental conditions *i.e.* type of monomer, gold precursor to the monomer concentration ratio,¹⁵⁷ pH of the aqueous phase¹⁵⁷ and interfacial Galvani potential difference.¹⁵⁸ The results are depicted in **Table 1.5**.

Table 1.5. Characteristics of the polymer – Au NPs composites generated at the electrified liquid – liquid interface

Synthesis method	$[AuCl_4^-]_{org}$	$[Monomer]_{aq}$	pH_{aq}	Au NPs size distribution	Ref.
CV	$[AuCl_4^-] = 0.2 \text{ mM}$	$[Tyramine] = 1 \text{ mM}$	2	Very little film generated	Ref. [157]
CV	$[AuCl_4^-] = 0.2 \text{ mM}$	$[Tyramine] = 1 \text{ mM}$	10	~15 nm	Ref. [157]
CV	$[AuCl_4^-] = 1 \text{ mM}$	$[Tyramine] = 0.5 \text{ mM}$	10	~15 nm	Ref. [157]
CV	$[AuCl_4^-] = 1 \text{ mM}$	$[Tyramine] = 1 \text{ mM}$	10	~15 nm	Ref. [157]
CV	$[AuCl_4^-] = 0.2 \text{ mM}$	$[Tyramine] = 1 \text{ mM}$	12	~5 nm	Ref. [157]
CV	$[AuCl_4^-] = 1 \text{ mM}$	$[Tyramine] = 0.5 \text{ mM}$	12	~5 nm	Ref. [157]
CV	$[AuCl_4^-] = 1 \text{ mM}$	$[Tyramine] = 1 \text{ mM}$	12	~5 nm	Ref. [157]
IDPM $\Delta_{org}^{aq} \Phi = 0.123 \text{ V}$	$[AuCl_4^-] = 0.2 \text{ mM}$	$[Tyramine] = 1 \text{ mM}$	-	~7 nm (univocal shapes)	Ref. [158]
IDPM $\Delta_{org}^{aq} \Phi = 0.0440 \text{ V}$	$[AuCl_4^-] = 0.2 \text{ mM}$	$[Tyramine] = 1 \text{ mM}$	-	~60 nm (presence of nanorods)	Ref. [158]
IDPM $\Delta_{org}^{aq} \Phi = 0.123 \text{ V}$	$[AuCl_4^-] = 1 \text{ mM}$	$[Resorcinol] = 10 \text{ mM}$	-	~6 nm (univocal shapes)	Ref. [158]
IDPM $\Delta_{org}^{aq} \Phi = 0.0440 \text{ V}$	$[AuCl_4^-] = 1 \text{ mM}$	$[Resorcinol] = 10 \text{ mM}$	-	~45 nm (univocal shapes)	Ref. [158]

CV – Cyclic Voltammetry, IDPM – ion determining potential method

1.3.4. Carbon based materials at/near polarized liquid – liquid interface

Some effort has been done with regard to planar liquid – liquid interface modification with carbon based materials with examples emerging from synthesis¹⁵⁹, functionalization¹⁶⁰ or catalysis¹⁶¹ etc. and only few examples emerges from the use of carbon or/and carbon based material at the polarized liquid – liquid interface. Carbon materials were also used to form ‘semi modified’ ITIES and such examples are also given here.

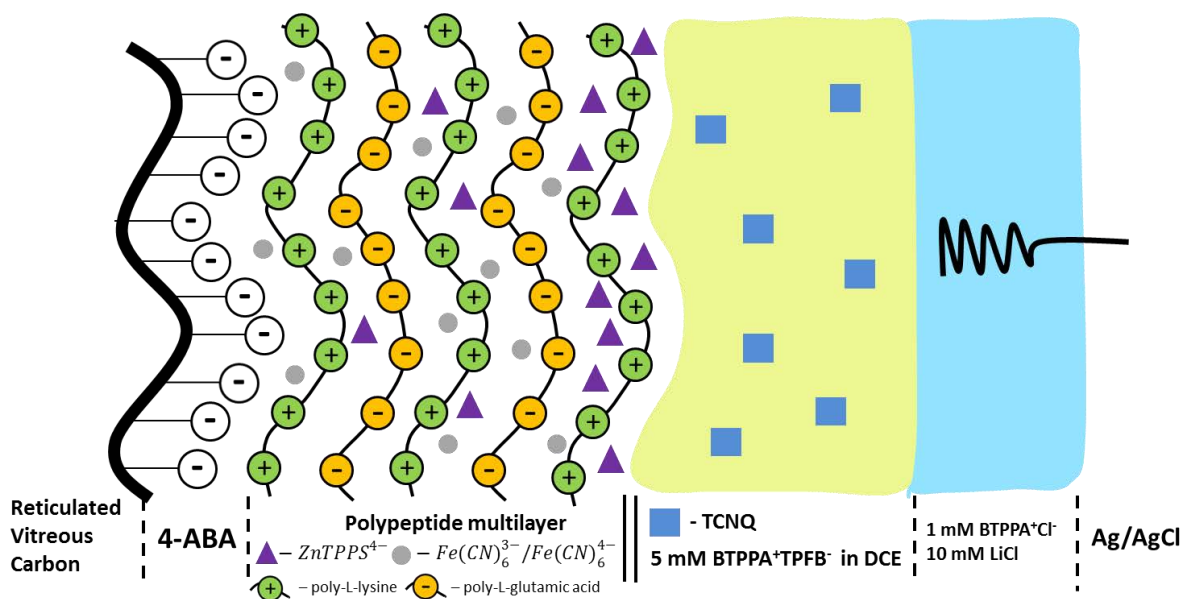


Figure 1.17. Scheme of 3D-ITIES composed from reticulated vitreous carbon modified with 4-ABA/polypeptide multilayer impregnated with ferri/ferrocyanide ions and photosensitizer (ZnTPPS⁴⁺) and the organic phase being the solution of electron acceptor (TCNQ) and 5 mM organic electrolyte. Abbreviations stand for: 4-ABA is the 4-aminobenzoic acid, TCNQ is 7,7',8,8'-tetracyanoquidimethane and ZnTPPS⁴⁺ is the zinc *meso*-tetrakis(*p*-sulfonatophenyl) porphyrin. Figure is adapted from ref.¹⁶²

Tan *et al.* used reticulated vitreous carbon sponge electrode to support the liquid – liquid interface and due to its high surface area packed in relatively small volume unit the whole concept was called 3D-ITIES.¹⁶² The idea is schematically shown on **Figure 1.17**. Carbon walls were first modified with 4-aminobenzoic acid (4-ABA) by the electrochemical oxidation. Next, a polypeptide multilayer was deposited on 4-ABA monolayer with a layer-by-layer deposition technique (the peptide solution, into which carbon modified with 4-ABA monolayer was immersed, was alternatively changed between poly-L-lysine and poly-L-glutamic acid). To show potential photovoltaic application, the carbon sponge was impregnated with aqueous solution of $K_4Fe(CN)_6$, $K_3Fe(CN)_6$ (as the electron transfer mediator) and photosensitizer molecule – zinc *meso*-tetrakis(*p*-sulfonatophenyl) porphyrin and a dried under the nitrogen flow. Next, such modified carbon sponge was immersed into the organic phase (dichloroethane) containing electron acceptor – 7,7',8,8'-tetracyanoquidimethane – and organic electrolyte.

Upon irradiation with the beam light (454 nm) the photocurrent associated with the electron transfer reaction between the dye entrapped in the polypeptide multilayer and the

electron acceptor in the organic phase gave about 8 times bigger value as compared with planar disc-glassy-carbon electrode modified in the same manner. Resulting photocurrent increase was associated with the high specific surface area of the carbon foam electrode. As mentioned by authors, the carbon material due to its high absorption could be replaced with other – transparent or reflective – electrodes to further increase a photovoltaic efficiency.

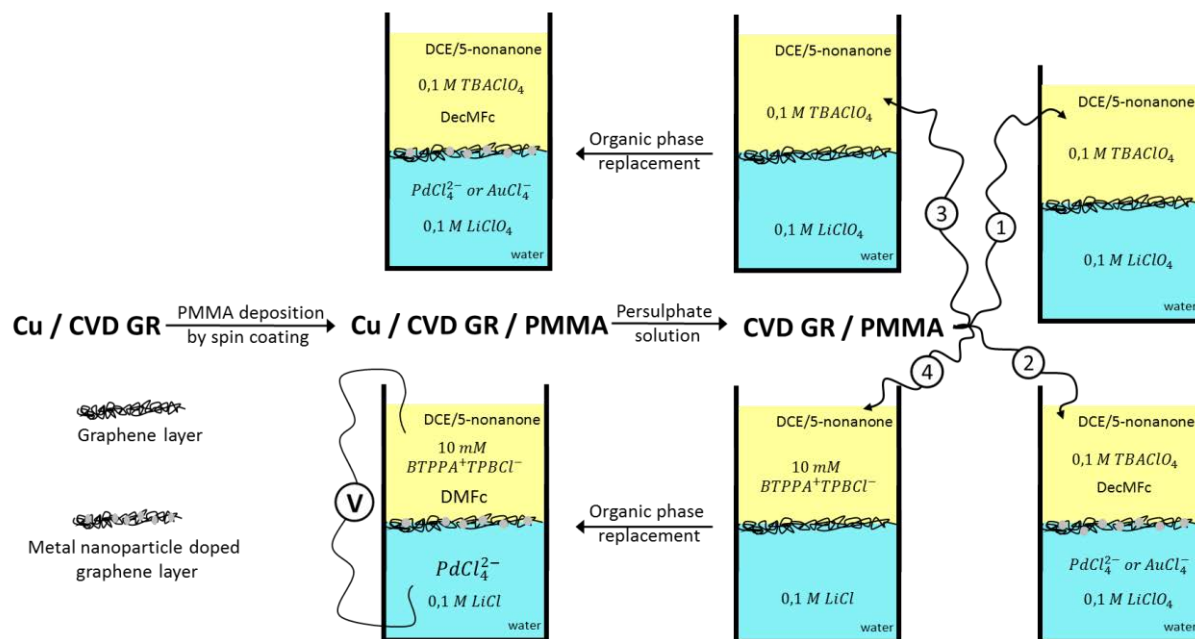
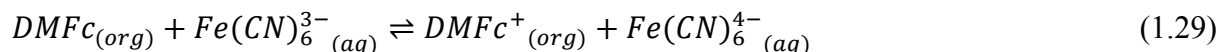


Figure 1.18. Scheme of the ITIES modification with a (doped)-graphene layer. The abbreviations stand for: CVD GR – chemical vapor deposited graphene; DMFc – 1,1'-dimethylferrocene, DecMfc – decamethylferrocene. Numbers from arrows correspond to different experimental synthetic approaches: (1) CVD GR deposition; (2) one step CVD GR/metal nanoparticles deposition; (3) two step CVD GR/metal nanoparticles deposition and (4) two step CVD GR/metal nanoparticles deposition under the potentiostatic control. Figure prepared on the basis of ref.¹⁶⁰

In another study, Dryfe et al. developed a method, where graphene adsorbed at the ITIES was doped with the Pd or Au nanoparticles.¹⁶⁰ The scheme on **Figure 1.18** shows the step-by-step experimental route. First, the chemical vapor deposited graphene (CVD GR) on the copper support was covered with a 100 nm layer of methyl methacrylate (PMMA) (using the spin coating technique). Next, the copper support was removed by etching in persulfate solution to yield the PMMA/CVD GR multilayer. The PMMA from PMMA/CVD GR once added to the organic phase (mixture between dichloroethane and 5-nonane) dissolves and release CVD GR which then spontaneously self-assembles at the ITIES (route (1) on **Figure 1.18**). Three different ways of making CVD GR doped metal nanoparticles were proposed: (i)

– marked as route (2), required the aqueous phase containing metal precursor species reduced with the electron donating DecMFC from the organic phase with the parallel CVD GR adsorption; (ii) route (3) implied the CVD GR deposition prior to metal precursor interfacial reduction and (iii) route (4) allowed the Pd nanoparticles deposition by potentiometric electron transfer control between DMFC from the organic phase and Pd metal precursor in the aqueous phase, also after CVD GR interfacial deposition. Depending on experimental approach different morphologies of the metal nanoparticles grown on the carbon scaffold were found – high distribution ranging from 40 to 300 nm for the (2) experimental route and narrow size distribution with the 20 – 40 nm size range for the (3) experimental route, both shown on **Figure 1.18**. The size of the electrochemically controlled deposition of Pd nanoparticles on the CVD GR modified ITIES was in the 50 – 100 nm range.

Recently communicated report from Dryfe and coworkers described the catalytic effect of few layer graphene and single wall carbon nanotubes modified ITIES on interfacial electron transfer reaction (between 1,1'-dimethylferrocene in the organic phase and ferricyanide in the aqueous phase).¹⁶³ The interfacial reaction for the electron transfer can be schematically written as:



The electron transfer reaction, in the presence of few layer graphene film at the ITIES gave rise to a higher faradaic current, which was attributed to the increase in the effective interfacial area. Similar catalytic effect was found for the carbon nanotubes (CNT) modified ITIES. Increase in electron transfer current in such case was attributed to the increase in surface active area and/or doping-charging effect of the CNT. It was also shown that Pd metal nanoparticles can be easily prepared on the carbon modified ITIES with the spontaneous or potential-induced electron transfer. The size of the particles, depending from the support, oscillated around 10 – 20 nm for CNT and 20 – 40 nm for graphene flakes.

The electrified liquid – liquid interface modified with carbon based material was developed for catalytic water splitting – hydrogen evolution reaction ($2H^+ + 2e^- \rightarrow H_2 \uparrow$). The two electron transfer reaction between the protons from the aqueous phase and the electron donor from the organic phase can be controlled with the interfacial Galvani potential difference. A recent article by Ge *et al.* has described the effect of graphene and mesoporous carbon doped with Mo₂S nanoparticles modified ITIES on interfacial proton

reduction catalysis.¹⁶⁴ The authors have shown that modification of the liquid – liquid interface separating tetrakis(pentafluorophenyl) borate anions in the aqueous phase (used as proton pump and potential determining ion) and electron donor – DecMFC – in the organic phase with the graphene doped MoS₂ leads to 40 fold increase in the hydrogen evolution rate and over 170 fold when mesoporous carbon was used as the conductive support. Similarly, 1000 fold increase in reaction rate was observed when the ITIES was modified with Mo₂C doped multiwalled carbon nanotubes under similar conditions.¹⁶⁵ The choice of carbon material as a scaffold for nanoparticles deposition is not surprising as (i) it exhibit the large dispersion of nanoparticles being the catalytic sites of the proton reduction reaction; (ii) it possess high specific surface area and (iii) the use of a carbon provides the interfacial region with the extra electrons.

1.3.5. Silica modified liquid – liquid interface

The following section is devoted to examples of the silica materials synthesized or deposited at/or in the close vicinity of the liquid – liquid interface. Silica, thanks to its attractive physicochemical properties (biocompatible, chemically inert, undergoes easy functionalization, allow the formation of multi-scale porous materials, insulator etc.) found applications in range of scientific directions: drug delivery systems,¹⁶⁶ multi-scale porous membranes,¹⁶⁷ supports for enzymes^{168,169} and proteins¹⁷⁰ immobilization, high-specific-surface-area sorbents or gas sensors¹⁷² – being only “the tip of the iceberg” among other examples. Much attention was pay during the last few decades to air – liquid¹⁷³ and liquid – solid^{98,174} interfaces modified with mesoporous silica. Insight into the field yielded to a development of range of methods allowing the morphological control and the design of the well-defined silica materials. Up-to-date, modification of the interface separating two immiscible liquids with the silica materials is restricted to the emulsion, microemulsions and over a few dozen examples emerging from the neat liquid – liquid interface, among which only few emerges from the ITIES modification. In following subsections attention is pay to the latter, which covers the three phase junction systems, the non-polarized planar liquid – liquid interfaces and finally the ITIES.

1.3.5.1. Three phase junction systems

Once the liquid – liquid interface is contacted with the solid electrode, the three phase junction system is formed. In principle, in such systems the electrochemical reaction at the solid support is followed by the ion transfer across the neighboring liquid – liquid interface. Three phase junction with one of the phases being a solid electrode modified with the silicate material was studied in the group of Opallo.¹⁷⁵ First report dealt with *ex situ* Au electrode modification with silicate films on the surface of which the small droplet of the hydrophobic redox liquid (t-butylferrocene) was placed and hereinafter was covered with the aqueous phase. Silica modification was performed in order to minimize transfer of relatively hydrophilic t-butylferrocenium cation (generated upon electrooxidation) to the aqueous phase. The best effect was observed when electrode was premodified with mercaptotrimethoxysilane. Electrochemically assisted Sol – Gel process employing the three phase junction was also reported¹⁷⁶ and is schematically shown on **Figure 1.19**. The ITO electrode crossing the interface between aqueous solution of sulphites ions and the nitrobenzene containing n-octyltriethoxysilane was modified with the silica positioned – almost completely – on the aqueous side of the liquid – liquid junction. The hydrolysis and condensation reaction were catalyzed by protons generated at ITO electrode according to the redox reaction:



The n-octyltriethoxysilane, once hydrolyzed, transfer across the liquid – liquid interface and condensed at the ITO electrode. The resulting stripe width ranges from 10 μm to 70 μm depending on the method used (cyclic voltammetry or chronoamperometry) and electrodeposition time. The stripe thickness was largest ~ 100 nm on the aqueous side of the interface.

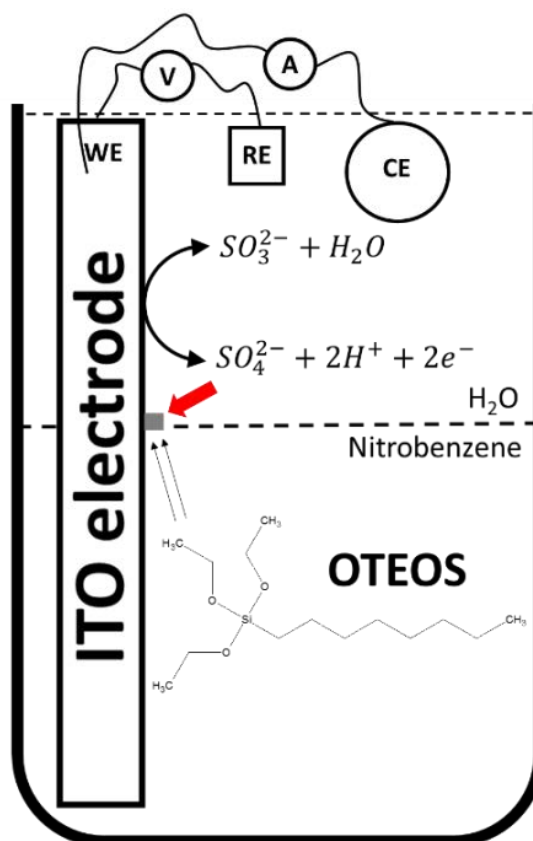


Figure 1.19. Set-up showing silica stripe formation at the three phase junction. Deposition place is indicated with red arrow. Protons were produced at the ITO on the aqueous side of the liquid – liquid interface with the conventional three electrode set up. OTEOS is n-octyltriethoxysilane. Scheme was adapted from ref.¹⁷⁶

1.3.5.2. Neat, non-polarized liquid – liquid interface *in situ* modification with silica materials

First reports dealing with silica synthesis at the planar liquid – liquid interface involved an acid-prepared mesostructures method.¹⁷⁷ This approach consists of the synthesis of silica materials at the interface between surfactant (structure directing agent) aqueous solution at pH adjusted to be considerably below the isoelectric point of silica species and the organic solvent – typically hexane, decane or methylene chloride – containing silica precursor. Self-assembly of the template and inorganic species at the oil/water interface follows $S^+ - X^- - I^+$ mechanism (where S^+ is the cationic surfactant, X^- is the halide anion and I^+ is the positively charge inorganic species), controlled by hydrogen-bonding interactions. The silica precursor is hydrolyzed at the oil/water interface. Hydrolyzed species, being more hydrophilic than hydrophobic, transfer to the aqueous phase and undergoes self-assembly

with abundantly present cationic surfactants. As the reaction time passes, the film grows towards aqueous side of the interface. Morphology of the film differs depending on the side of the interface; in the organic environment the silica film consisted of ball-shaped beads with diameters ranging up to 100 μm whereas the shapes from the aqueous site are much smaller and differentiated. Analogous experimental approach was employed at the oil/water interface to grow mesoporous silica fibers.^{178,179} The formation of desired fiber shapes requires the control of variety of factors: pH of the aqueous phase, the template and the precursor concentrations, nature of the organic phase and use of co-solvent (changing the kinetics of hydrolyzed silica species crossing the interface). Resultant silica-fibers with length up to 5 cm and diameters from 1 μm to 15 μm with high mesoporous quality (hexagonal arrangement and narrow pore size distribution, pores oriented parallel to the fiber axis and high specific surface area of 1200 m^2/g) were obtained. Regev *et al* studied the silica film formation at the heptane/water interface under acidic and basic conditions.¹⁸⁰ The aqueous phase contained CTACl and CTAB in acidic and basic media respectively. Counter phase was always the mixture between TEOS and heptane. Different morphology on both sides of the silica film was found; for acid media the synthesized film roughness on the aqueous side were found to be in the order of 50 nm, whereas for the organic side it was 3 nm (as measured with AFM). For silica films prepared from basic media it was found that both aging and curing time have an effect on film mesostructure: (i) aging times <6h results in poor order and undefined crystalline phase, (ii) aging times >6h generates cubic structure and leads to better crystalline structure and (iii) long curing times (>15h) led to a structure collapse.

Fabrication of ordered silica-based films at the liquid – liquid interface could also be obtained by silica spheres deposition. Example of such an approach was given by He *et al*.¹⁸¹ First the monodisperse SiO_2 spheres were modified with 3-(acryloyloxy)propyltrimethoxysilane (bearing C=C bond) and dispersed in aqueous phase containing benzoin ethyl ether (photo-initiator of polymerization). Liquid – liquid interface was constituted between dichloromethane and aqueous phase containing silica spheres and photo-initiator. The colloidal particles self-assembled at the liquid – liquid interface were bonded into the stable film by polymerization induced by UV irradiation. Self-assembly of SiO_2 spheres has led to well-ordered, mechanically stable film of one monolayer thickness for times starting from 30 min and silica spheres concentration up to 0.013%. Whitby *et al*. studied the effect of SiO_2 nanoparticles/surfactant composite on the liquid – liquid interface stabilization. Macroscopic systems reveal new set of information helping to understand the

phenomenon of the colloidal dispersion stabilized by solid nanoparticles – called Pickering emulsions. Two approaches have been employed: (i) silica nanoparticles and CTAB species were dispersed in the aqueous phase and contacted with hexane¹⁸² and (ii) silica nanoparticles dispersed in the aqueous phase were separated from hexane containing octadecylamine (ODA).¹⁸³ Adsorption of CTA⁺ at SiO₂ nanoparticles surface tune their properties and make them partially hydrophobic which facilitates their interfacial deposition. Rearrangement, immediately after deposition, of SiO₂/CTA⁺ layer was also observed and attributed to interaction among alkyl chains and/or organic phase. A second system (ii) is different. In the presence of ODA in the organic phase, three distinctive stages, for the increasing surfactant concentration were proposed. First, for low ODA concentrations the interface coverage was low and hence electrostatic (and probably hydrogen bonding) interactions were not sufficient enough to induce the SiO₂ adsorption. The partition of ODA between water – hexane and its adsorption at SiO₂ surface become visible close to the oil – water interface saturation with the surface active molecules. Silica nanoparticles ‘modified’ with ODA species started to adsorb at the liquid – liquid interface and changed its viscoelastic properties (higher interfacial tension values observed as compared with system in absence of silica nanoparticles). Finally at high ODA concentrations, the interface is fully occupied by the SiO₂–ODA spheres, which probably (no experimental evidences were given) self-assembly forming densely packed layer at liquid – liquid interface.

Approach dealing with the silica film generation at the liquid – liquid interface having anisotropic properties (also referred to as Janus properties) was first reported by Kulkarni *et al.*¹⁸⁴ Interface was constituted between ammonia aqueous solution and heptane containing methyltrimethoxysilane. Basic pH of the aqueous phase has led to the silica precursor hydrolysis and its interfacial condensation. Films were directly collected from the interface or supported with the porous material (suspended in the organic phase so that its bottom edge barely touched the aqueous phase) and cured in the oven. For the highest methyltrimethoxysilane/heptane molar ratio – 0.4 – the superhydrophobic properties of the silica film from the organic side of the interface (contact angle ~152°) were attributed to the high methyl group surface coverage and its morphology (thick film with roughness on organic site). Aqueous side of the film was hydrophilic as confirmed with the contact angles ~65°. The NH₄OH was found to have an effect on film grown and the wetting properties for concentration below 0.1 M. It seems that addition of cationic (CTAB) and anionic (SDS) surfactants at concentration >CMC to the aqueous phase does not change the wetting

properties of the organic-side of the silica film, and only CTAB slightly decreased the hydrophilicity of the aqueous side of the film (contact angle increased from 65° in the absence to 75° in the presence of CTAB). The presence of charged surfactants (especially CTAB) could have some additional mesoporous structure driving properties; however no experimental effort was made towards this direction. Further examples of silica films of Janus type generated at static liquid – liquid interface were studied by Biswas and Rao.¹⁸⁵ Films were grown at the toluene (containing silica precursor) – water (at acidic pH facilitating precursor hydrolysis) interface. Three silica precursors were used: tetraethoxysilane, hexadecyltrimethoxysilane and perfluorooctyltrimethoxysilane. On micrometer scale, organic side of the silica film had always rougher structure than its counter – aqueous side. Contact angle measurements have shown that the hydrophilicity of the aqueous side of the silica films stayed unaffected ($\sim 70^\circ$) for all three precursors. Contact angle on organic side of the silica films varied depending from the hydrophobic character of the precursor. Results indicated slight hydrophobicity for tetraethoxysilane-based organic-side (contact angle = 92°) as compared with very hydrophobic hexadecyltrimethoxysilane- and perfluorooctyltrimethoxysilane-based organic-sides of the films (contact angles = 140° and 146° respectively).¹⁸⁵ The compilation of different synthetic approaches leading to neat liquid – liquid interface modification with silica materials can be found in **Table 1.6**.

Table 1.6. Compilation of works dealing with silica material deposition at neat liquid – liquid interface.

Organic phase solvent	Silica source	pH of aq. phase	Template (if used)	Morphology and characteristics	Ref.
Decane	TEOS	Acidic	CTAB	Planar films. Hexagonal order of pores oriented perpendicularly to the film;	177
Hexane	TEOS, TPOS, TBOS	Acidic	CTAB	Silica fibers with mesopores ordered hexagonally and oriented parallel to fiber axis. Shape of the fibers depend from the precursor used;	178
Heptane	TEOS	Acidic	CTACl	Planar films with rougher aqueous-side and smoother organic-side;	180
Heptane	TEOS	Basic	CTAB	Planar films of MCM-41 and MCM-48 type, hexagonal and cubic order of pores;	180
Heptane	MTMS	Basic	CTAB, SDS	Planar films possessing Janus properties. Rough organic-side and smooth aqueous-side. Methyl groups oriented towards organic-side;	184
Toluene	TEOS HDTMOS PfOTMOS	Acid	-	Planar films possessing Janus properties. Hydrophobicity of organic side depends from precursor used and increase in order: TEOS > HDTMOS > PfOTMOS;	185
Dichloromethane	Monodisperse SiO ₂ spheres modified with 3APTMS	Neutral	-	Monolayer films build from monodispersed silica spheres (~300 nm in diameter);	181

TEOS – tetraethoxysilane, TPOS – tetrapropoxysilane, TBOS – tetrabutoxysilane, MTMS – methyltrimethoxysilica, HDTMOS – heksadecyltrimethoxysilane, PfOTMOS – pentafluorooctyltrimethoxysilane, 3APTMS – 3-(acryloyloxy)propyltrimethoxysilan

1.3.5.3. Electrified Interface between Two Immiscible Electrolyte Solutions modification with silica materials

The examples of the electrified liquid – liquid interface modification with the silica materials are basically based on *ex situ* and *in situ* approaches.

1.3.5.3.1. *Ex situ* modification

In recent years, Dryfe *et al.* published series of papers focused on *ex situ* modified ITIES with silicalite materials. In the pioneering work,¹⁸⁶ for the first time, they modified ITIES with inorganic material - namely non-polar zeolite (the zeolite membrane is schematically depicted on **Figure 1.20 A**). The *ex situ* modification employs material initially grown on mercury surface, which after proper treatment was cured to a glass tube using a silicone rubber. By interfacial modification authors were able to slightly increase the potential window as compared with the unmodified system. The size of the pinholes within the zeolite network allowed the size-selective ion transfer across the interface. Two different in size model ions were employed, this is TMA⁺ and TEA⁺. Cyclic voltammetry has shown that TMA⁺ (hydrodynamic radius 0.52 nm) transfer remain unaffected in the presence of zeolite membrane, whereas the transfer of the later ion (TEA⁺ with 0.62 nm in hydrodynamic radius) was suppressed. It has to be mention that the TMA⁺ backward transfer (from organic to aqueous phase) was accompanied by adsorption within the zeolite network, as indicated from the current drop and partial loss of reversibility. In the second approach¹⁸⁷ it was shown that zeolite framework modified ITIES can significantly increase the potential window. The key requirement is the use of background limiting cation and anion with the size exceeding the zeolite framework pores. This was obtained by employing tetrabutylammonium tetraphenylborate (TBA⁺TPB⁻) as an organic electrolyte. The value of standard transfer potentials for organic electrolyte ions were lower for cations and higher for anions as compared with the standard transfer potential of aqueous salt ions and hence the potential window – at the unmodified ITIES – was limited by supporting organic electrolyte ions transfer. The diameter of TPB⁻ (0.84 nm) is comparable to the pore diameter of silicalite (0.6

nm). The size of the pores in zeolite network prevented the organic electrolyte anion interfacial transfer and as a result, elongated the potential window, which finally was limited by the smaller inorganic aqueous electrolyte ions transfer. The silicalite membranes were immersed for ten minutes in the aqueous phase prior to each electrochemical measurement in order to saturate the interior of the pores with the aqueous solution. The hydrophobic character of silicates could enhance the organic phase penetration into zeolite framework, and hence the exact position of the interface remained unclear. To answer these doubts, Dryfe *et al.* studied facilitated ion transfer of alkali metals with 18-crown-6 ether and based on obtained electrochemical results they suggested that it is rather the aqueous phase which fills the silicalite pores. *Ex situ* zeolite modified ITIES size selective membrane can be complete with charge selectivity¹⁸⁸. The example given by Dryfe *et al.* concerns sodium zeolite-Y pressed with 10 tons of pressure and healed with tetraethoxy silane (TEOS) solution. Healing process was applied in order to eliminate inter-grain pathways between mechanically pressed zeolite crystals, which may constitute the route for analytes transfer. Resulting disks with 0.75 mm in thickness and 20 mm in diameter were used to support the liquid – liquid interface. Cyclic voltammetry results in the presence of zeolite-Y membrane have shown size selective exclusion of tetrabutylammonium cations whereas tetraethylammonium cations undergo reversible transfer. When BF_4^- and ClO_4^- were studied as the transferring ions (with diameter of ions smaller than diameter of pore entrance) no voltammetric response was observed. This result univocally indicated charge selective exclusion for negatively charged ions. The supporting electrolytes used in this study were LiCl and $BTPPA^+TPBCl^-$ in aqueous and organic phase respectively. Since the zeolite-Y membrane exhibit both size and charge sieving effect, the potential limits were elongated from a negative and a positive potential side. Broader potential window from less positive potential side has arisen due to size exclusion of $BTPPA^+$ transfer and charge barrier for Cl^- transfer across modified ITIES.

The increase in the potential window from more positive potential side is in agreement with the organic anion size and charge ($TPBCl^-$) being unable to cross the pores. Finally, with help of inductively coupled plasma optical emission spectrometry - used to calculate the concentration of TEA^+ in the zeolite-Y modified ITIES – and cyclic voltammetry, authors estimated apparent diffusion coefficient for TEA^+ within the membrane. The parameter was calculated based on Randles – Sevcik equation and ranged from $1.9 \cdot 10^{-8}$ to $3.8 \cdot 10^{-8}$ cm/s².

The ion transfer voltammetry at the ITIES modified with the zeolite Y can be also used to change the chemical properties of the silicalite material. The example include proton exchange with the sodium from the membrane framework immersed in an acidic solution¹⁸⁹.

Ex-situ, silica modified ITIES

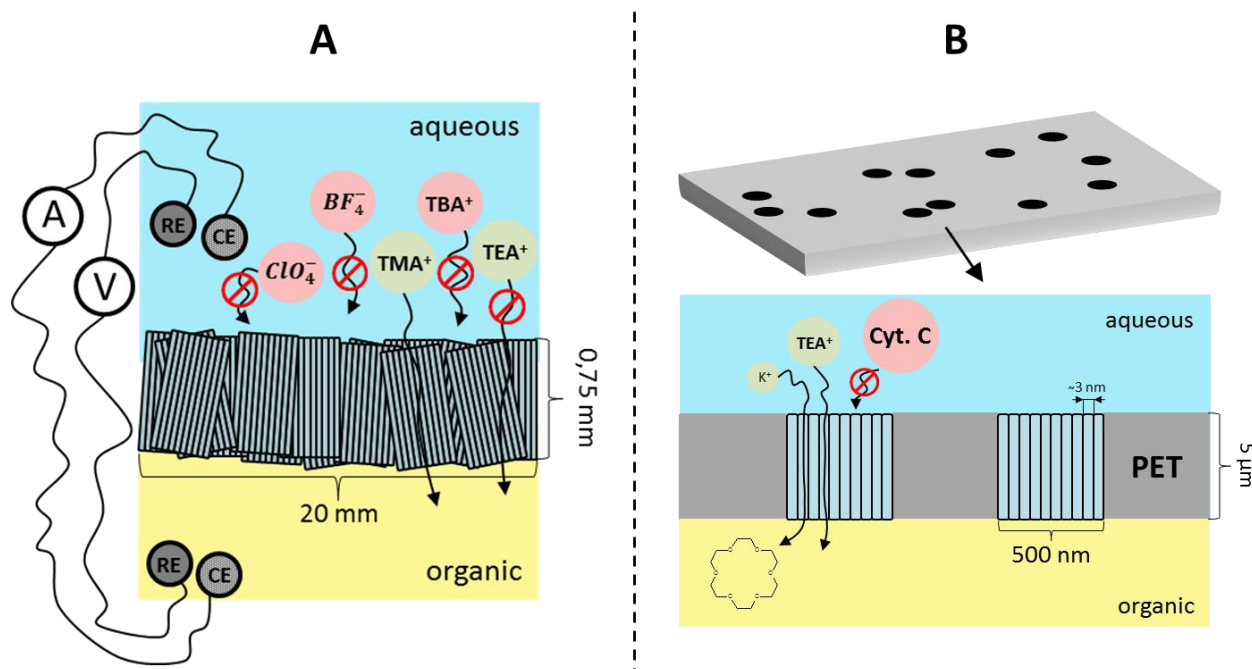


Figure 1.20. Schematic and simplified schemes for ex situ modified ITIES with silica materials. A – correspond to macroscopic ITIES modified with zeolite membrane used in size-selective voltammetric study¹⁸⁸ and B – is the polyethylene terephthalate (PET) membrane with randomly distributed pores modified with the aspiration induced infiltration method.¹⁹⁰

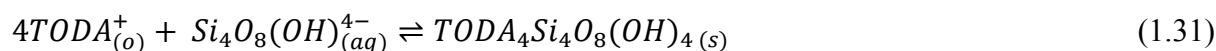
Another example, developed in the group of Chen,¹⁹⁰ emerges from *ex situ* modification of macroporous polyethylene terephthalate (PET) membrane with randomly distributed pores with 500 nm in diameter and 5 μm in height (see **Figure 1.20 B** for schematics). Silica deposition inside the pores was performed with the aspiration-induced infiltration method¹⁹¹ from the acidic solution containing CTAB and TEOS as template and precursor respectively. The as-prepared membrane was used to support liquid – liquid interface (ITIES separating 0.1 M KCl aqueous solution and 0.02 M BTPPA⁺TPB⁻ in DCE). Authors claimed that silica inside the PET macropores has formed channels directed along the pores. The average pore diameter was

estimated to be 3 nm (based on N₂ adsorption/desorption method), which is suitable for macromolecule sieving. Three molecules were employed to study the permeability of the silica modified macropores by ion transfer voltammetry: TEA⁺, K⁺ (with crown ether present in the organic phase) and a biomolecule, Cytochrome c. Especially the potassium did not encounter any resistance to mass transfer in the presence of silica membrane. TEA⁺ also gave rise to a signal which was partially hindered by a TPB⁻ transfer (application of species giving a wider potential window could improve interpretation of voltammetric data). No signal was detected for Cytochrome c, which size apparently exceeded the silica channels entrance dimensions and hence retained in the aqueous phase. Similar conditions were used for the folic acid detection.¹⁹² Analytical study allowed the characterization of the folic acid transfer across the silica modified PET membrane with and without CTAB species inside the silica channels. When the liquid – liquid interface was constituted between 10 mM NaCl_(aq) and 20 mM BTPPA⁺TPBCl_(org)⁻ in dichlorohexane, interfacial transfer of the folic acid was found to be better pronounced in the presence of CTAB among the silica network (phenomena attributed to the anion exchange process between bromides from CTAB and the folic acid). Presence of alkyl chains inside the silica channels changed the polarity of the interior of initially hydrophilic pores, which shifted the position of the interface from the pore ingress to its interior. To overcome this problem low molecular weight polyvinylchloride was used in order to gelified the organic phase. Such an approach, first stabilized the position of the interface and second, allowed the use of stripping techniques, which even further improved limit of detection of folic acid (from 100 μM for CTAB doped silica modified PET membrane for CV at water – dichlorohexane interface up to 80 nM for differential pulse stripping voltammetry technique for CTAB doped silica modified PET membrane at water – organogel interface).

1.3.5.3.2. *In situ* modification

In situ, electrochemically controlled silica film formation at the ITIES, was reported for the first time in 2003 by Mareček and Jänchenová.¹⁹³ Method has involved Sol-Gel process with template and precursor separated between the organic and the aqueous phase respectively.

During silica film formation – by cyclic voltammetry – the trimethyloctadecylammonium cation (TODA⁺) (used as a template and cationic part of organic electrolyte in parallel) was transferred to the aqueous solution of water glass containing Na₂O and SiO₂. The interfacial transfer was followed by the template and the precursor self-assembly reaction and finally silica film deposition at the liquid – liquid interface according to the following reaction:



$Si_4O_8(OH)_{(aq)}^{4-}$ represents predominant polynuclear silica species in experimental pH > 10, and hence proposed by authors reaction stoichiometry. Based on electrochemical results, the authors proposed a film formation mechanism. Polarization toward cathodic potential initiated TODA⁺ transfer from the organic to the aqueous phase facilitated by silicate ions. Next, the interaction of the template with the precursor took place in the aqueous phase, which resulted in a film deposition. Change in polarization direction resulted in positive peak attributed to back transfer of TODA⁺ to the organic phase and its replace by Na⁺ ions in a film texture. In their continuation work, the authors took protocol elaborated in their first report and doped silica material with platinum ions¹⁹⁴. For this purpose the $(NH_4)_2PtCl_4$ was added to the initial sol solution. The template transfer to the aqueous phase triggered synthesis of hybrid material at the DCE – water interface. However fundamental, these two works suffer from lack of quantitative analysis that could confirm e.g. replacement of template molecules with Na⁺ during reverse scan, confirmation of Pt particles presence among the silica framework or finally tangible evidence of synthesized films applications (only possible examples were given in the text). No additional effort was made towards evaluation of eventual mesoscopic morphology, which undoubtedly is of highest industrial and academic interest

Chapter II. Experimental part

The aim of the following part is to supply the reader with all the experimental, technical and instrumental details concerning this work. At the very beginning the full list of chemicals that have been used among this study is given. Next section describes the electrochemical set-ups, including: (i) the cell used to study the reaction taking place at the macroscopic ITIES, (ii) the cell and the membrane used for miniaturization and finally (iii) the system employed to probe local pH change induced by ion transfer and UV irradiation. The compositions of cells during electrochemical measurements as well as the information concerning preparation of the aqueous and the organic phase prior to silica interfacial deposition were included in separate section. Next are the information concerning instrumentation. This chapter is fulfilled with the set of step-by-step protocols dealing with the: (i) organic synthesis of chemicals prepared for the purpose of this work and (ii) preparation of the organic counter electrode as well as (iii) micro capillaries used to support the liquid – liquid interface.

2.1. Chemicals

The **Table 2.1** gives the full list of the chemicals that have been used in this work. For each chemical its name, abbreviation, source and function are given.

Table 2.1. Full list of chemicals used in this work

Aqueous and organic electrolytes						
Name	Additional information	Abbreviation	CAS registratory number	Molar mass g/mol	Source	Function
Bis(triphenylphosphoranyldiene) ammonium chloride	97%	BTPPA ⁺ Cl ⁻	21050-13-5	574.03	Aldrich	For organic electrolyte preparation
Potassium tetrakis(4-chlorophenylborate)	≥98%	K ⁺ TPBCl ⁻	14680-77-4	496.11	Fluka	For organic electrolyte

Chapter II. Experimental part

						preparation
Bis(triphenylphosphoranyldiene) ammonium tetrakis(4-chlorophenylborate)¹	-	BTPPA ⁺ TPBCl ⁻	-	995.59	Synthesized in this study	Organic phase electrolyte
Sodium chloride	≥98%	NaCl	7647-14-5	58,44	Prolabo	Aqueous phase electrolyte
Lithium chloride	≥99%	LiCl	7447-41-8	42.39	Aldrich	Aqueous phase electrolyte
Tetrabutylammonium tetrakis(4-chlorophenylborate)²	-	TBA ⁺ TPBCl ⁻	-	699.48	Synthesized in this study	Organic phase electrolyte
Template salts and silica precursors						
Cetyltrimethylammonium tetrakis(4-chlorophenylborate)³	-	CTA ⁺ TPBCl ⁻	-	786.01	Synthesized in this study	Template salt
Cetyltrimethylammonium bromide	≥99%,	CTAB	57-09-0	364.45	Acros Organics	Template
Tetraethoxysilane	98%	TEOS	74-10-4	208.33	Alfa Aesar	Silica precursor
(3-mercaptopropyl)triethoxysilane	>97%	MPTMS	4420-74-0	196.34	Fluka	Silica precursor
(3-azidopropyl)trimethoxysilane⁴	-	AzPTMS	-	157.29	Synthesized in this study	Silica precursor
(3-chloropropyl)trimethoxysilane	97%	3CITMS	2530-87-2	198.72	Alfa Aesar	AzPTMS precursor
Interfacial active species						
Tetramethylammonium chloride	≥99%	TMA ⁺ Cl ⁻	75-57-0	109.60	Fluka	Interfacial active compound
Tetraethylammonium chloride	≥99%	TEA ⁺ Cl ⁻	56-34-8	165.70	Fluka	Interfacial active compound
Tetrabutylammonium chloride	≥99%	TBA ⁺ Cl ⁻	214-195-7	277.92	Fluka	Interfacial active compound
4-octylbenzenesulfonic acid sodium salt	97%	4OBSA ⁻	6149-03-7	294.39	Fluka	Interfacial active compound
Poly(aminoamide) dendrimer generation 0	20% solution in methanol	PAMAM G.0	155773-72-1	516.68	Aldrich	Interfacial active

Chapter II. Experimental part

						compound
Poly(aminoamide) dendrimer generation 1	20% solution in methanol	PAMAM G.1	142986-44-5	1429.85	Aldrich	Interfacial active compound
Trimethylbenzhydrylammonium iodide⁵	-	PH ⁺ I ⁻	-	353.24	Synthesized in this study	Interfacial active compound
Trimethylbenzhydrylammonium tetrakis(4-chlorophenylborate)⁶	-	PH ⁺ TPBCI ⁻	-	683.35	Synthesized in this study	Interfacial active compound bearing photosensitive cation
Solvents						
1,2-dichloroethane	≥99%,	DCE	107-06-2	98.96	Sigma-Aldrich	Organic phase solvent
Decane	99%	-	124-18-5	142.28	Sigma-Aldrich	To change organic phase composition
Ethanol	Ethanol absolut	EtOH	64-17-5	46.07	Sigma-Aldrich	To change organic phase composition
Water	From milliQ system	H ₂ O	7732-18-5	18.02	-	Aqueous phase solvent
Other compounds						
Iron(III) chloride hexahydrate	99 – 102%	FeCl ₃ ·6H ₂ O	10025-77-1	270.30	Fluka	Ag/AgCl electrode preparation
Hydrochloric acid	1M, volumetric solution	HCl	7647-01-0	36.46	Riedel-de Haen	pH adjusting
Sodium hydroxide	pellets, pure	NaOH	1310-73-2	39.99	Riedel-de Haen	pH adjusting
Potassium hydroxide	Analytical reagent	KOH	1310-58-3	56.11	R.P. Normapur	For glass cell cleaning
Potassium bromide	-	KBr	7758-02-3	119.00	Sigma-Aldrich	For IR pellets

Aminodiphenylmethane hydrochloride	97%	ADPM	5267-34-5	219.71	Sigma-Aldrich	For PH ⁺ preparation
Iodomethane	99.5%	CH ₃ I	74-88-4	141.94	Sigma-Aldrich	For PH ⁺ preparation
Sodium carbonate	≥99.9%	Na ₂ CO ₃	497-19-8	105.99	Merck	For PH ⁺ preparation
Potassium iodide	99%	KI	7681-11-0	166.00	SDS	For PH ⁺ preparation
Sodium thiosulfate	≥99%	Na ₂ S ₂ O ₃	7772-98-7	158.11	Labosi	For PH ⁺ preparation
Dichloromethane	≥99.9%	CH ₂ Cl ₂	75-09-2	84.93	Carlo Erba Reagents	For PH ⁺ preparation

The chemicals synthesized in this study were prepared according to protocol available in section **1**– 2.5.1; **2** – 2.5.3; **3** – 2.5.2; **4** – Appendix II; **5** – 2.5.7 and **6** – 2.5.4.

2.2. Electrochemical set-ups

Different set-ups were used among this work and their descriptions are divided in agreement with the successive parts of the thesis i.e. macroscopic ITIES modification with the silica material, microscopic ITIES modification with the silica material and finally local pH changes at the ITIES induced by ion transfer and UV irradiation.

(i) Electrochemical cells supporting macroITIES

The custom made electrochemical cells used to study the electrochemical silica deposition at the macroscopic ITIES are presented on **Figure 2. 1**. The cells were custom made from glass tubes with inner diameters 12 mm (**Figure 2. 1 A**) and 19 mm (**Figure 2. 1 B**). The reference electrodes placed in the Luggin capillaries of each phase were Ag/AgCl wires whereas the counter electrodes were made from platinum mesh. The Ag/AgCl electrode was prepared by oxidation of silver wire in a saturated solution of FeCl₃. The aqueous counter electrode was platinum mesh spot welded to platinum wire. The organic counter electrode was the platinum

mesh spot welded to platinum wire which was isolated from both phases by glass tube (for protocol of preparation of the organic counter electrode please refers to **section 2.5.5**). During the measurement, the organic phase Luggin capillary was filled with the 10 mM BTPPA⁺Cl⁻ and 10 mM LiCl supporting aqueous solution. The cell with the smaller interfacial radius was used to study ion transfer reactions and interfacial silica deposition mechanism. The cell with the bigger interface diameter was equipped with a removable upper Luggin capillary and hence was used for the electrogeneration of large amounts of silica (several mg per synthesis). In the second case, during the interfacial deposition, the volume of the organic phase was diminished by placing inert glass boiling stones at the bottom of the cell.

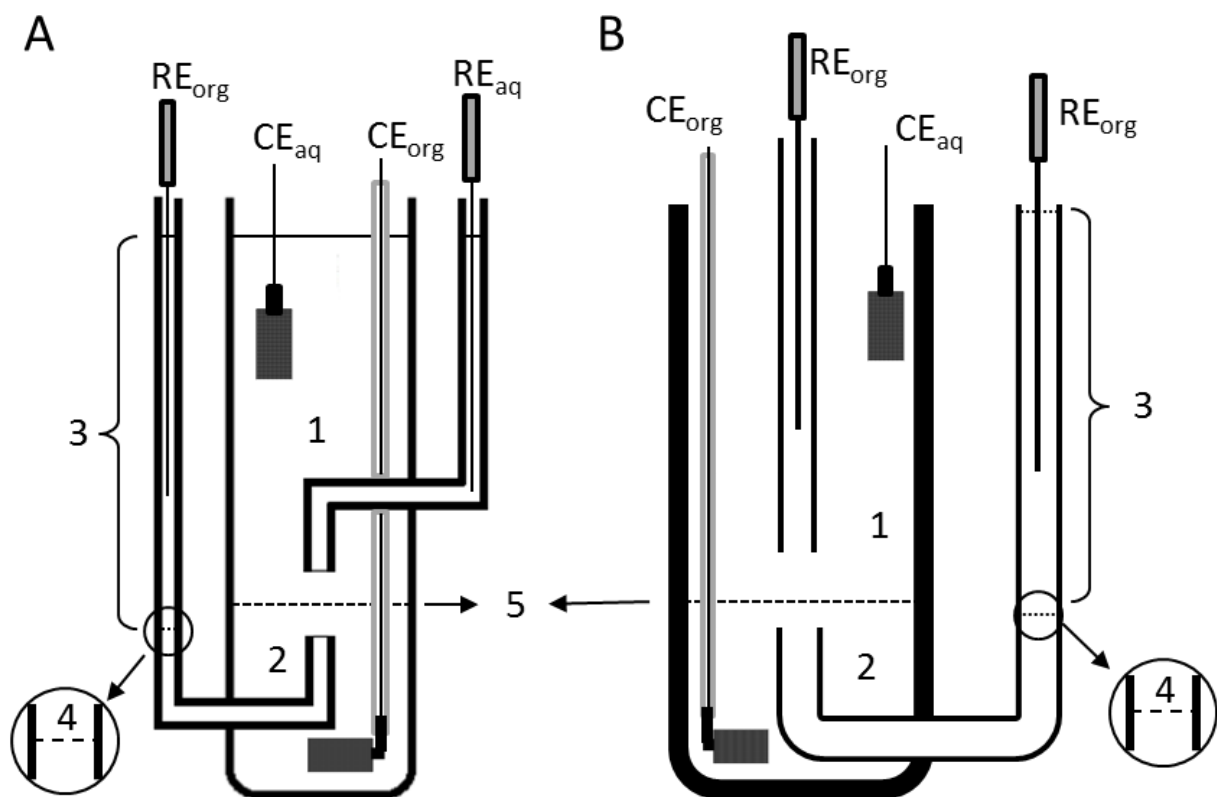


Figure 2.1. Four electrode electrochemical cells supporting the macroscopic liquid – liquid interface: A – with fixed Luggin capillaries and B – with removal upper Luggin capillary. The RE_{org} and RE_{aq} correspond to the organic and the aqueous reference electrodes respectively whereas the CE_{org} and CE_{aq} correspond to the organic and the aqueous counter electrodes respectively. The numbers stand for: 1 – the aqueous phase; 2 – the organic phase; 3 – supporting aqueous phase; 4 – is the liquid – liquid interface between higher density phase and the supporting aqueous phase and 5 is the ITIES. The interfacial surface area was 1.13 cm² for cell A and 2.83 cm² for cell B.

(ii) Electrochemical set-up supporting microITIES

The electrochemical cell used for electrochemical silica interfacial deposition study and electroanalytical evaluation of the silica deposits is shown on **Figure 2.2 A**. The cell consists of a simple glass vessel covered with a lid with three holes. The side places were occupied by platinum mesh counter electrode and Ag/AgCl reference electrode (prepared by Ag oxidation in the oversaturated solution of FeCl_3). The center hole was occupied by glass tube to the bottom

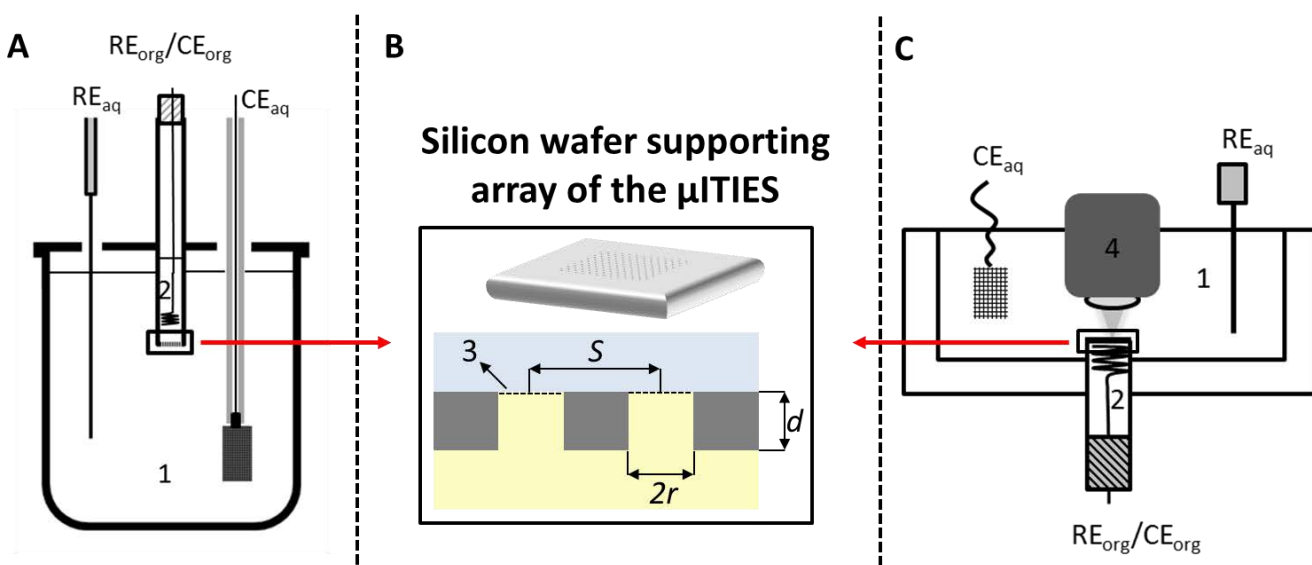


Figure 2.2. The electrochemical cells used for A - microITIES modification and electroanalytical study and C – for *in situ* Raman analysis of electrochemical silica deposition. B – is the silicon membrane used to support array of microITIES. Designation stands for: 1 – aqueous phase; 2 – organic phase; 3 – microITIES (r is the pore diameter, S is the pore center-to-center distance and d is the membrane thickness – 100 μm), 4 – is the objective used to focus laser beam. RE and CE stands for reference electrode and counter electrode respectively. Aq stands for aqueous whereas org for organic.

of which silicon wafer with array of microITIES was attached (silicon wafer was fixed to the glass tube using silicon acetate sealant from Rubson® (resistive to DCE)). The glass vessel was filled with the aqueous phase whereas the glass tube was filled with the organic phase. The silver wire acting as both organic reference and organic counter electrode was placed directly in the organic phase. Prior to contacting two phases, the organic phase was placed in the glass tube and it was left for one minute in order to impregnate the array of pores with the organic solution.

Once the silver wire was placed in the organic phase the upper hole of the glass tube was finely covered with the ParaFilm®. The set-up used to couple electrochemical silica deposition with the confocal Raman spectroscopy is shown on **Figure 2.2 C**. In this configuration the glass tube filled with the organic phase was placed in the bottom of a custom made PTFE vessel filled with the aqueous phase. The top side of the glass tube was finished with the silicon wafer bearing the array of microITIES. Down part of glass tube was closed with a silicone stopper in order to avoid the organic phase leakage. During the measurement laser spot was focused at the liquid – liquid interface using objective adopted to work in the liquid media. The electrodes were the same as for the cell shown on **Figure 2.2 A**.

Table 2.2. Characteristics of silicon wafers used to support the array of microITIES.

Design number	Pore radius / μm	Spacing / μm	Number of pores	Interfacial Surface area / cm^2
1	5	20	2900	2.28×10^{-3}
2	5	50	460	3.61×10^{-4}
3	5	100	110	8.64×10^{-5}
4	5	200	30	2.36×10^{-5}
5	10	100	120	3.77×10^{-4}

The silicon membrane supporting the array of microITIES (see **Figure 2.2 B**) was fabricated from a silicon wafer being a 4x4 mm square. The pores were patterned by UV-photolithography and pierced by a combination of wet and DRIE etches as described elsewhere.⁸³ The fabrication process has led to hydrophobic pore walls. The pores were therefore filled with the organic phase, presenting an array of inlaid microITIES. The characteristics of silicon wafers used in this work are shown in **Table 2.2**. The pore height was constant and for all wafers was 100 μm .

(iii) Electrochemical set-up used to study local pH change

For electrochemical study of PH^+ ion transfer the cell with the macroscopic ITIES (see **Figure 2. 1 A**) and microscopic ITIES (see **Figure 2.2 A**) were used. In some experiments single pore microITIES (see **section 2.5.7** for protocol of preparation) was used instead of silicon wafer membrane.

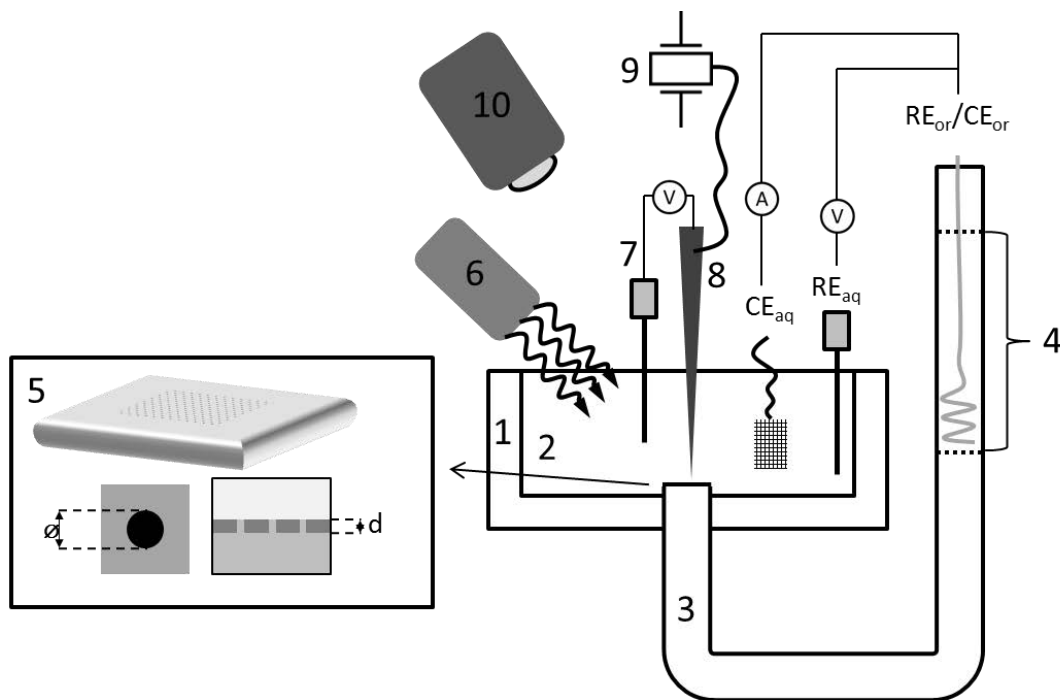


Figure 2.3. Set-up used during local pH measurement above the liquid – liquid interface supported with array of micrometer pores. The designations are as follows: 1 – PTFE cell, 2 – aqueous phase, 3 – the glassy tube filled with the organic phase and aqueous reference supporting electrolyte (4), 5 – the silicon wafer supporting array of microITIES (\varnothing is the pore diameter equal to $50\ \mu\text{m}$, and d is the membrane thickness – $100\ \mu\text{m}$), 6 – the source of UV irradiation, 7 – the double junction Ag/AgCl reference electrode, 8 – the iridium oxide modified platinum electrode, 9 – correspond to shear-force positioning and 10 – the CCD camera used for visualization. Electrochemistry at the liquid – liquid interface was controlled with the CE_{aq} – aqueous counter electrode (platinum mesh), RE_{aq} – reference counter electrode (Ag/AgCl) and $\text{RE}_{\text{org}}/\text{CE}_{\text{org}}$ – Ag/AgCl wire used as organic reference and counter electrode in one.

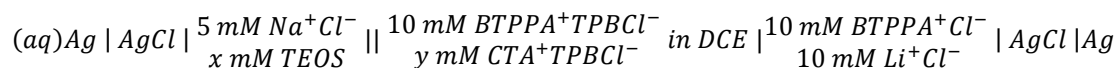
The local pH measurements induced by the PH^+ photodegradation above the liquid – liquid interface were studied using the set-up schematically shown on **Figure 2.3**. The liquid – liquid interface was supported with the silicon wafer bearing array of microITIES (eight pores, each having $50\ \mu\text{m}$ in diameter). The silicon wafer was fixed to the U-bended glass tube using

silicone sealant. Ion transfer was controlled with the four electrode configuration. Platinum mesh and Ag/AgCl were used as the counter aqueous and the reference aqueous electrodes respectively. The Ag/AgCl wire placed in the aqueous supporting electrolyte was used as the organic counter and reference electrode in one. Platinum micro disc electrode sealed in the glass capillary and modified with the iridium oxide was used for potentiostatic pH measurement (the Ag/AgCl with double junction was used a reference electrode). The pH probe positioning was performed with the shear force measurement. The electrode was situated above the pore in such a way that the distance between the surface of the wafer and the electrode tip was 1 μm . The UV irradiation source was directed toward interface using flexible optical fiber.

2.3. Composition of electrochemical cells. The aqueous and the organic phase preparation

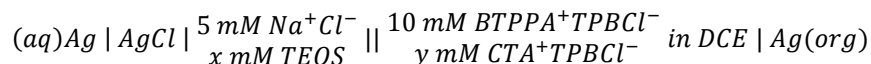
The electrochemical set-up, used for silica material electrodeposition at macroscopic ITIES, can be written as:

Cell 1:

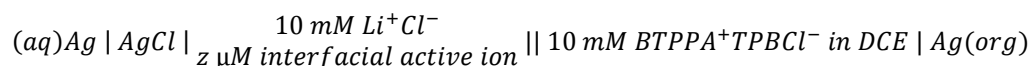


The electrochemical set-up used to study microITIES modification with silica deposits is shown on cell 2 configuration. MicroITIES modified with silica deposits were evaluated electrocatalytically using ion transfer voltammetry (analytes were the species being different in size, charge and nature) in the cell 3 configurations.

Cell 2:



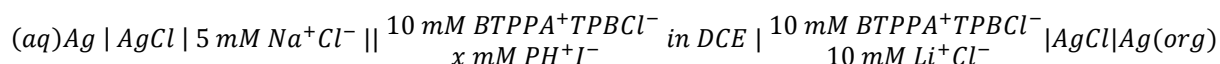
Cell 3:



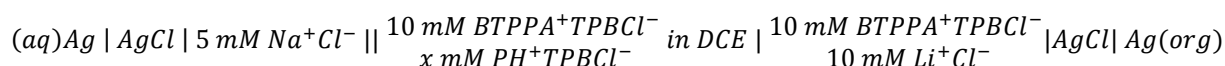
The various TEOS and CTA⁺ concentrations used in the above mentioned cells 1 and 2 were in the ranges $50 \text{ mM} \leq x \leq 300 \text{ mM}$ and $1.5 \text{ mM} \leq y \leq 14 \text{ mM}$, respectively.

In order to study local pH changes at the liquid – liquid interface induced by ion transfer and UV irradiation photo active compound (PH⁺) had to be synthesized (**see protocol in section 2.5.7**) and assessed electrochemically. Cell 4 and 5 were used in this regard:

Cell 4:

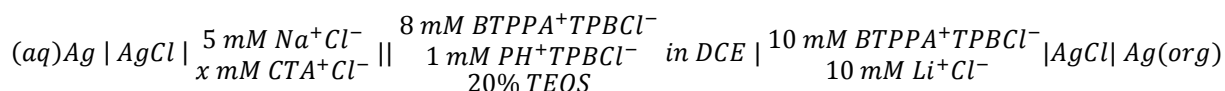


Cell 5:



Silica deposition triggered by local pH changes was performed in the cell 6 configuration. The $[CTA^+Cl^-]_{aq} = x \text{ mM}$ where $0.70 \text{ mM} \leq x \leq 2.02 \text{ mM}$.

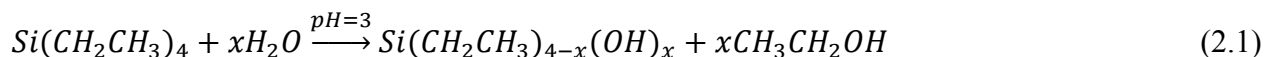
Cell 6:



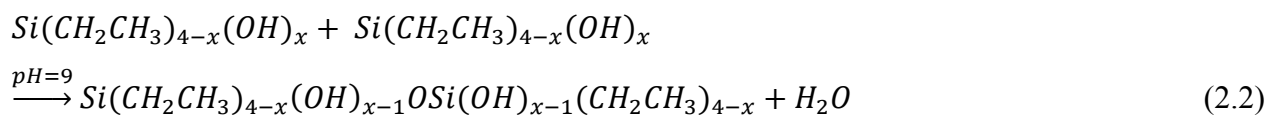
(ii) Composition of the aqueous and the organic phase during silica deposition induced by CTA⁺ ion transfer

Aqueous phase

During the interfacial silica electrodeposition the silica precursor – TEOS – was initially dissolved in the aqueous part of the liquid – liquid cell. Initially the TEOS was added to the 5 mM NaCl solution and the pH was adjusted to 3 in order to facilitate the hydrolysis reaction:



Such mixture, initially biphasic, was vigorously stirred for 1h until clear solution was obtained. Next the pH was increased to around 9 in order to facilitate condensation process.



The precursor solution prepared in such a manner was than directly transferred to the liquid – liquid electrochemical cell and constituted the higher density phase.

Organic phase

The organic phase used during interfacial electrochemical silica deposition was 1,2-dichloroethane solution of 10 mM BTPPA⁺TPBCl⁻ (prepared according to protocol from **section 2.6.1**) and x mM CTA⁺TPBCl⁻ (prepared according to protocol from **section 2.6.2**). The organic phase was the lower density phase of the liquid – liquid cell.

(ii) Composition of the aqueous and the organic phase during silica deposition induced by local pH change

The composition of two immiscible phases during silica material interfacial deposition triggered by local pH change was inversed as compared with previous experiments. This means that precursor was initially dissolved in the organic phase whereas template species were in the aqueous phase. The organic phase composition, 20% TEOS solution in DCE, was unchanged among all experiments. The aqueous phase was x mM CTA⁺Br⁻ solution (for x = 0.70; 1.38 and 2.02 mM) in 5 mM NaCl.

2.4. Instrumentation

Electrochemical measurements – All electrochemical measurement from chapter III and IV were performed with a **PGSTAT 302N** (Metrohm, Switzerland) with the four electrode configuration. Potentiostat was controlled by NOVA software. In chapter V the liquid – liquid interface was polarized using **PalmSens EmStat³⁺** potentiostat with the PalmSens Differential Electrometer Amplifier allowing the application of four electrode configuration. Palmsens potentiostat was controlled by PStTrace software.

Small Angle X-ray Scattering – SAXS measurements were performed with the **SAXSee mc²** apparatus from Anton Paar.

Profilometry based on shear force measurement – shearforce detection was done with two piezoelectric plates attached to the pulled borosilicate glass capillary and connected to a lock-in amplifier (**7280 DSP LOC-IN-AMPLIFIER**).

Nitrogen adsorption-desorption – isotherms were obtained at $-196\text{ }^{\circ}\text{C}$ over a wide relative pressure range from 0.01 to 0.995. The volumetric adsorption analyzer was **TRISTAR 3000** from Micromeritics. The samples were degassed under vacuum for several hours at room temperature before nitrogen adsorption measurements. The specific surface area was calculated with the BET (Brunauer, Emmett, Teller) equation.

X-ray Photoelectron Spectroscopy – analysis was performed with the **KRATOS Axis Ultra X-ray spectrometer** from Kratos Analytical. The apparatus was equipped with the monochromated $\text{AlK}\alpha$ X-ray source ($h\nu = 1486.6\text{ eV}$) operated at 150 W.

Fourier transform Infra-red Spectroscopy – IR spectra were recorded in transmission mode using the KBr pellets as a support for a sample. The **Nicolet 8700 apparatus** was used for this purpose.

Transmission Electron Microscope – the TEM micrographs were recorded with the **CM20 apparatus** (Philips, Netherlands) at an acceleration voltage 1 kV.

Scanning Electron Microscope – the SEM micrographs were obtained using a **Philips XL30** (with acceleration voltage equal to 1 kV), without any sample metallization.

Confocal Raman spectroscopy – **Horiba Jobin Yvon T64000** spectrometer equipped with a nitrogen cooled CCD detector with a green laser light (the wavelength was 532 or 514 nm) was used to collect Raman spectra. The irradiance was measured in air at 100 kW cm^{-2} and was estimated to have the same value in the aqueous phase. No laser heating in the aqueous phase was observed.

UV irradiation – the irradiation source was HXP 120-UV lamp from Kubler Codix. The apparatus was equipped with the flexible optical fiber.

Local pH measurement – High impedance **potentiometer Kethley 6430** was used in all potentiometric pH measurements. The double junction Ag/AgCl was used as a reference electrode. pH probe was the Pt microelectrode modified with iridium oxide. The pH probe calibration was conducted prior and after measurements in buffered solutions at pH 7 and 4.

Ion chromatography – the analysis was performed with **882 Compact IC Plus from Metrohm** equipped with IC conductivity detector.

High Pressure Liquid Chromatography – chromatograms were recorded using **Waters 501 HPLC pump** and **Waters 486 Tunable Absorbance detector**. The column was RP 18C 100-4.6 mm from Chromolith® performance.

^1H NMR – all spectra were recorded with a **Bruker 200 MHz** spectrometer at 298 K.

UV-Vis spectroscopy – all UV-Vis spectra were recorded in quartz cuvettes with **Cary 60 UV-Vis** spectrometer from Agilent Technologies

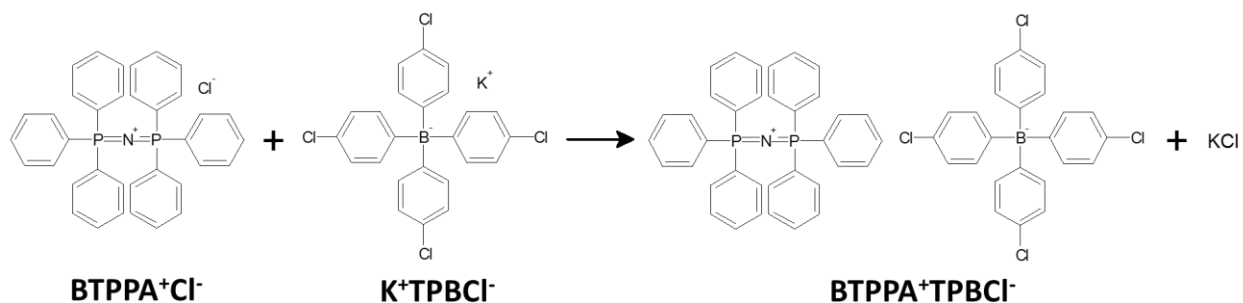
Mass spectroscopy – **MicroTOFq** spectrometer from Bruker was used. The ESI (electrospray ionization) source was in positive mode. The scan was performed between 50 up to 1200 m/z. The capillary was set at 4500 V. The end plate offset was -500V.

2.5. Protocols

Inseparable part of this work was organic synthesis, miniaturization and electrodes preparation. All step-by-step protocols describing these aspects are arranged together in the following sections.

2.5.1. Preparation procedure of $\text{BTPPA}^+\text{TPBCl}^-$

Bis(triphenylphosphoranyliene)ammonium tetrakis(4-chlorophenylborate) ($\text{BTPPA}^+\text{TPBCl}^-$) - organic electrolyte salt, was prepared according to the following metathesis reaction:



Preparation involves few stages:

1. 1.157 g of $\text{BTTPA}^+\text{Cl}^-$ and 1.000 g of K^+TPBCl^- were dissolved in 10 ml and 20 ml of 1:2 mixture of $\text{H}_2\text{O}:\text{MeOH}$ respectively. Solution of $\text{BTTPA}^+\text{Cl}^-$ was added drop-wise to a vigorously stirring solution of K^+TPBCl^- resulting in a white precipitate.
2. The reaction was continuously stirred at 4°C for 48h. After this time, solvent was filtered under vacuum for about 30 min. Reaction product was transferred to dry beaker and placed in a desiccator overnight. Beaker was covered with an aluminum foil to prevent light induced decomposition of the product.

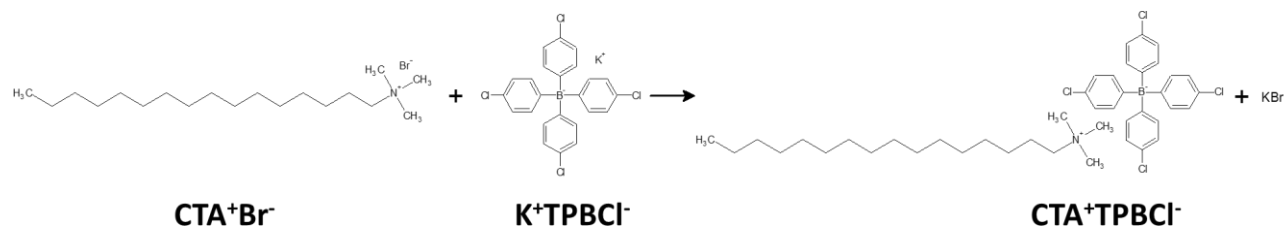
3. Next step was to dissolved $\text{BTPPA}^+\text{TPBCl}^-$ in acetone and then filtered under gravity using paper filter. Vessel with the filtrate was covered with Parafilm® in which small holes were made to allow evaporation of acetone.
4. Depending on volume of acetone used, evaporation takes up to few days. Resulting $\text{BTPPA}^+\text{TPBCl}^-$ gives rectangular crystals as it is shown on **Figure 2.4**. Afterwards, crystals were rinsed with 1:1 Acetone:H₂O mixture, filtered under vacuum and stored overnight in desiccator.
5. The resulting $\text{BTPPA}^+\text{TPBCl}^-$ was stored in refrigerator in the vessel covered with an aluminum foil preventing from light exposure.



Figure 2.4. $\text{BTPPA}^+\text{TPBCl}^-$ crystals after acetone evaporation.

2.5.2. Preparation procedure of $\text{CTA}^+\text{TPBCl}^-$

Cetyltrimethylammonium tetrakis(4-chlorophenylborate) ($\text{CTA}^+\text{TPBCl}^-$) – surfactant template salt soluble in organic phase was prepared according to following metathesis reaction:

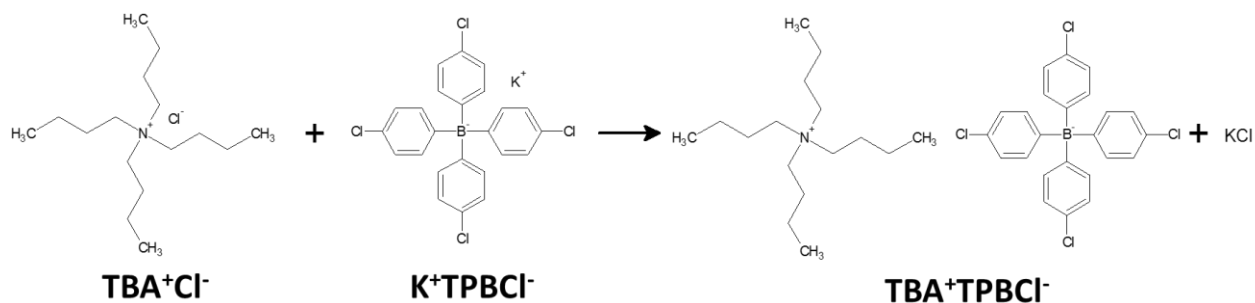


Preparation involves few stages:

1. Equimolar amounts of CTA^+Br^- (0.800 grams) and K^+TPBCl^- (1.089 gram) were weighted and dissolved in 5 ml and 10 ml of 1:2 mixture of $\text{H}_2\text{O}:\text{MeOH}$, respectively. Then solution of CTA^+Br^- was added drop-wise to a vigorously stirring solution of K^+TPBCl^- . The product of reaction - white precipitate - was then left under stirring in the fridge for 48h.
2. After this time suspension was filtered under vacuum and then dried overnight in desiccator.
3. Dry $\text{CTA}^+\text{TPBCl}^-$ was dissolved in acetone and was filtered under gravity using paper filter. The beaker containing $\text{CTA}^+\text{TPBCl}^-$ was covered with the Parafilm® and placed under the fume hood. Small holes were made in Parafilm® to allow acetone evaporation.
4. Recrystallized $\text{CTA}^+\text{TPBCl}^-$ is very dense and viscus liquid residual at the bottom of the beaker. In the last stage, the product was dissolved in dichloroethane and moved to the volumetric flask in order to calculate its concentration (beaker was weighted with and without $\text{CTA}^+\text{TPBCl}^-$).
5. The solution was stored at 4°C .

2.5.3. Preparation procedure of TBA⁺TPBCl⁻

Tetrabutylammonium tetrakis(4-chlorophenylborate) (TBA⁺TPBCl⁻) – salt of interfacially active model cation – TBA⁺ - soluble in the organic phase, was prepared according to following metathesis reaction:

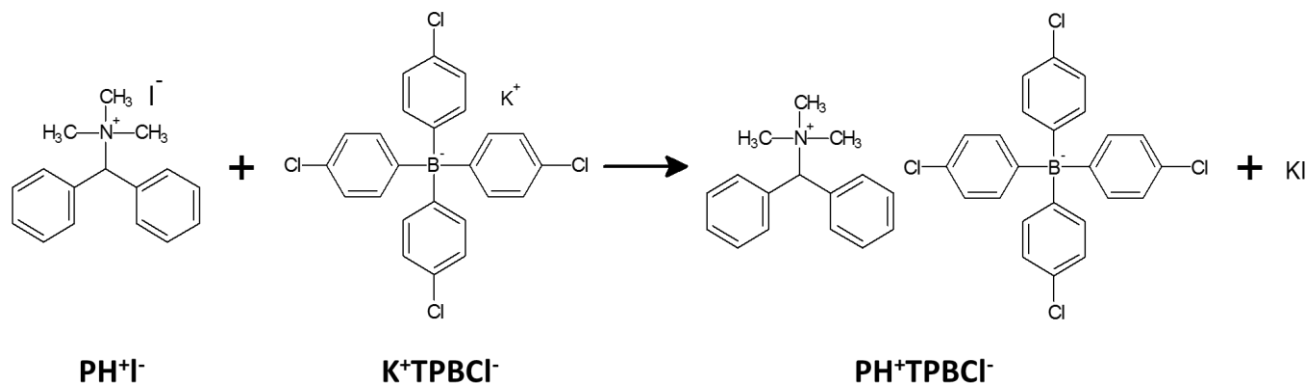


Preparation involves few stages:

1. Equimolar amount of TBA⁺Cl⁻ (0.500 grams) and K⁺TPBCl⁻ (0.893 grams) were dissolved in 10 ml and 20 ml of 1:2 mixture of H₂O:MeOH respectively. Solution of TBA⁺Cl⁻ was added drop-wise to a vigorously stirring solution of K⁺TPBCl⁻ resulting in white precipitate.
2. The reaction was continuously stirred at fridge for 48h. After this time solvent was filtered out under vacuum for about 30 min. Reaction product was transferred to dry beaker and placed in desiccator overnight.
3. Next step was to dissolved TBA⁺TPBCl⁻ in acetone and then filtered under gravity using paper filter. Vessel with the filtrate was covered with Parafilm® in which small holes were made to allow the acetone evaporation.
4. Recrystallized TBA⁺TPBCl⁻ (small, powder-like crystals) was transferred to the vessel and stored at 4°C.

2.5.4. Preparation procedure of PH⁺TPBCl⁻

Trimethylbenzhydrylammonium tetrakis(4-chlorophenylborate) (PH⁺TPBCl⁻) – photoactive compound organic salt, was prepared according to following metathesis reaction:



Preparation involves few stages:

1. Equimolar amounts of PH⁺I⁻ (0.500 grams) and K⁺TPBCl⁻ (0.740 grams) were dissolved in 10 ml and 20 ml of 1:2 mixture of H₂O:MeOH respectively. Solution of PH⁺I⁻ was added drop-wise to a vigorously stirred solution of K⁺TPBCl⁻ resulting in white precipitate.
2. The reaction was continuously stirred at fridge for 48h. After this time the solvent was filtered under vacuum for about 30 min.
3. In order to purify the product from KI, it was rinsed three times with distilled water (iodides detection was performed with HPLC in order to follow effectiveness of KI removal – see **Figure 2.5**). Each time 10 ml of water was shaken together with the PH⁺TPBCl⁻ and then it was centrifuged (15 minutes with 5000 rpm).
4. Free from KI reaction product was transferred to dry beaker and placed in desiccator overnight.

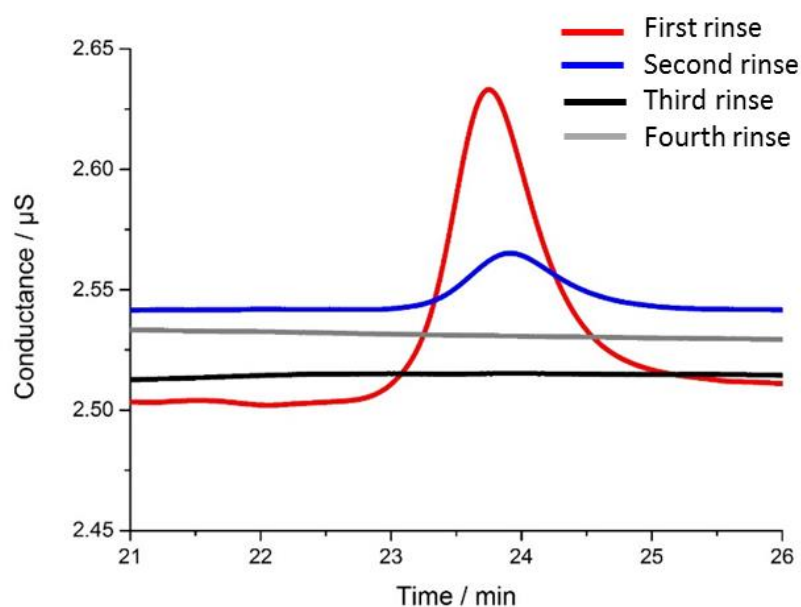


Figure 2.5. The ion chromatography detection of iodides after four successive reaction product ($\text{PH}^+\text{TPBCl}^-$) rinsing with distilled water.

5. Next step was to dissolve $\text{PH}^+\text{TPBCl}^-$ in acetone and then filter it under gravity using paper filter. Vessel with the filtrate was covered with Parafilm® in which small holes were made to allow the acetone evaporation.
6. Recrystallized $\text{PH}^+\text{TPBCl}^-$, being a viscous liquid, was dissolved in dichloroethane and transferred to a volumetric flask. The mass of the $\text{PH}^+\text{TPBCl}^-$ was taken as a result of mass subtraction of beaker with and without photoactive compound product. Solution was stored in the fridge.

2.5.5. Protocol of organic counter electrode preparation

Borosilicate glass capillary, as an inert material, was used to protect interior of the electrode from both solutions (the organic and the aqueous phase). Preparation of organic counter electrode requires:

- Platinum mesh and platinum wire attached to each other by spot welding (**Figure 2.6 A**);
- 10 cm length borosilicate capillary with inner diameter – 1.16 mm and outer diameter – 2.00 mm. Capillaries were from Sutter Instruments Company (**Figure 2.6 B**);
- Dual-component conductive epoxy – Epotek H20S from Epoxy technology (**Figure 2.6 C**);
- Copper-tinned contact wire. From Rowan Cable Products (**Figure 2.6 D**).
- Silicon sealant – Rubson®;
- Blade and elastic isolation;
- Pump (**Figure 2.7 C**) and Bunsen burner (**Figure 2.7 D**);

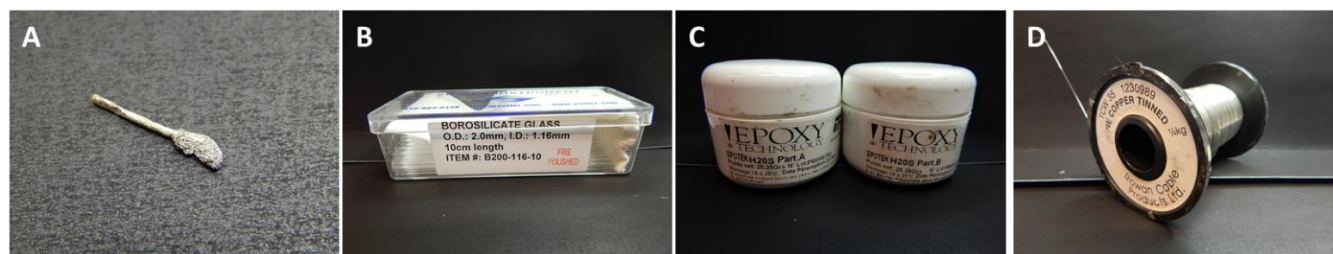


Figure 2.6. Components used for the organic counter electrode preparation: A – platinum mesh fixed to platinum wire, B – borosilicate capillaries, C – dual-component conductive epoxy and D – copper-tinned contact wire.

Step-by-step electrode preparation protocol can be described as follows:

1. First, the platinum mesh has to be welded around the platinum wire. Next, as it is shown on **Figure 2.7 B**, the platinum wire was placed inside the borosilicate capillary. The second side of the glass capillary was connected to the hose (**Figure 2.7 A**), which has led to the pump.

2. The glass around the platinum wire was gently melted above the Bunsen Burner. Heating was slowly started from the mesh side and the capillary was progressively inside the flame. Attention had to be paid since capillary can easily collapse above the platinum wire closing the capillary. If so, step two has to be repeated.

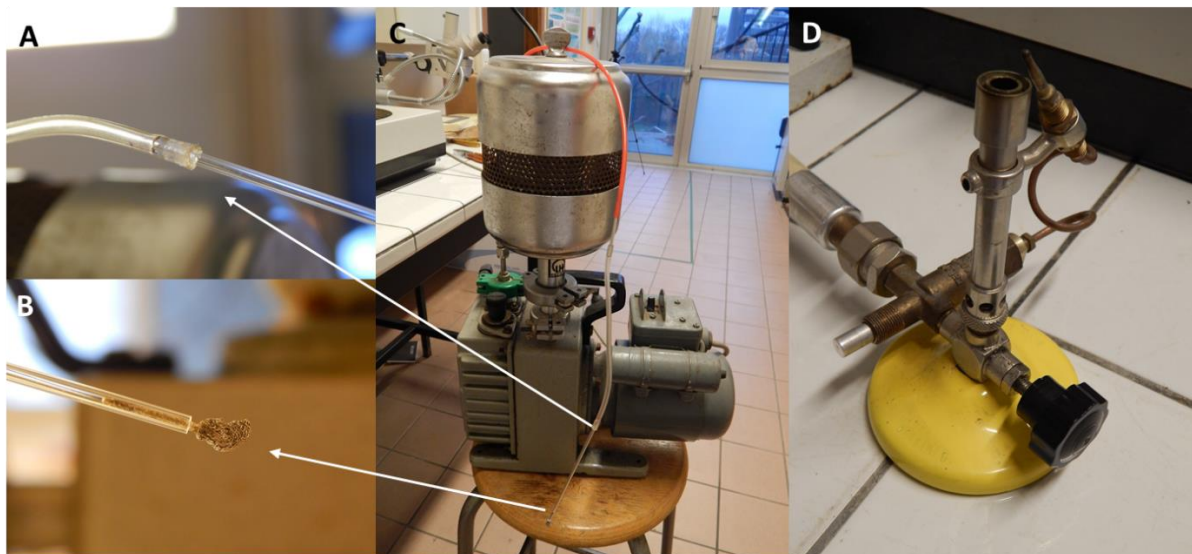


Figure 2.7. Trapping the platinum wire inside the glass capillary was performed with the pump (C) under the Bunsen burner (D). One side of capillary was attached to the pump hose (A) whereas the platinum mesh and wire occupied second side (B).

3. Once platinum mesh and wire are securely fixed to the capillary (**Figure 2.8 B**) the conductive resin has to be placed just above the wire (**Figure 2.8 C**). Syringe with long needle can be used for this purpose. First uptake some resin inside the needle and then presses it out to the capillary.



Figure 2.8. Successive steps of electrode preparation. A – Platinum mesh and wire inserted into the capillary, B – glass melted around the platinum wire and C – conductive resin placed above the wire.

4. The ~15 cm copper-tinned (for electric contact) wire was placed inside the glass capillary until it touched the conductive resin. To speed up curing time of resin capillary was put in the oven at 130°C for few hours.
5. Once resin is cured, the electrode was taken out from the oven and its interior was filled with the silicon sealant (once again using syringe with the thicker needle possible). Finally, elastic isolation was placed on top of the electrode in order to secure the contact wire. Ready electrode is depicted on **Figure 2.9**.



Figure 2.9. Platinum mesh based counter organic phase electrode.

2.5.6. Single pore microITIES protocol of preparation

Greater part of this thesis belongs to miniaturization. Reproducible procedure of preparation of the single pore capillaries supporting miniaturized liquid – liquid interface is described in here. Preparation of single pore microITIES requires:

- borosilicate glass capillaries with filament (outer diameter 1.56 mm and inner diameter 0.75 mm) from SUTTER INSTRUMENT®;
- gold wire with fixed diameter (in case of this work the diameter was 25 or 50 μm);
- 10 ml of *aqua regia* solution (mixture between concentrated hydrochloric acid and nitric acid in 3 to 1 v/v ratio respectively);
- Pump, vertical capillary puller and external power supply shown in **Figure 2.10** as **A**, **B** and **C** respectively.

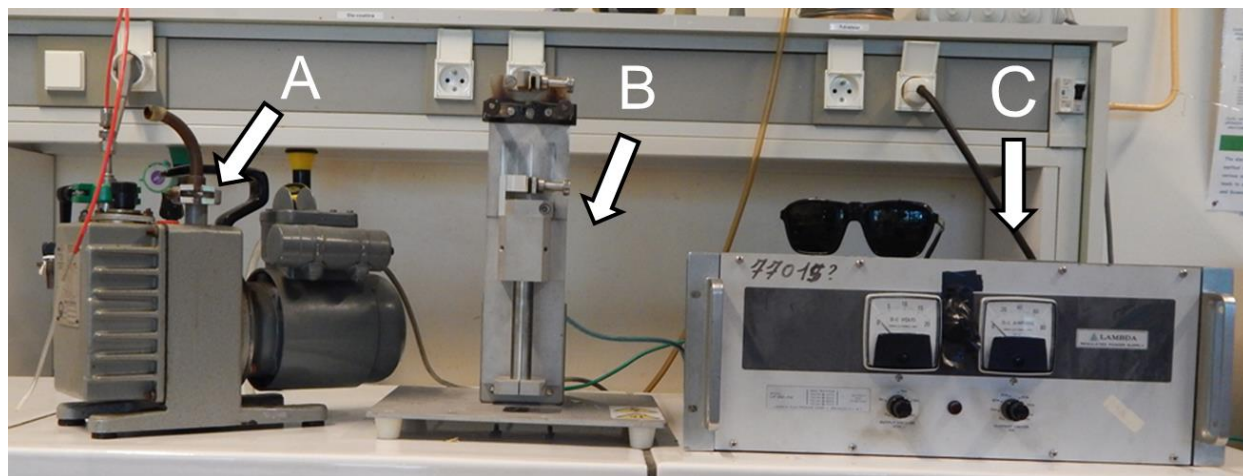


Figure 2.10. Set-up used to prepare the single pore microITIES capillaries. A – is the pump, B – is the vertical capillary puller and C – is the external power supply.

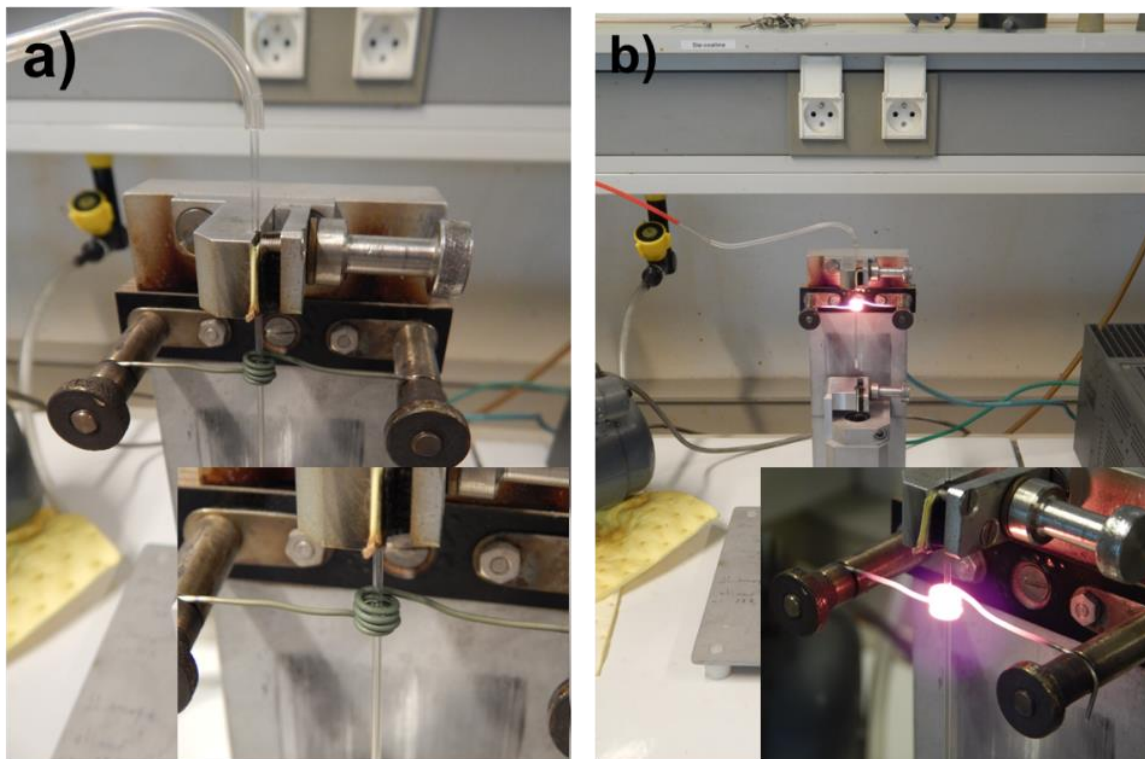


Figure 2.11. The vertical capillaries puller was used to close the capillary in the middle and to melt the gold wire into the glass. a) shows the capillary placed in the nickel/chrome wire ring before current passage and b) after current was passed through the wire.

The single pore microITES preparation can be divided into few steps:

1. Initially, the borosilicate glass capillary has been closed in the middle. To do so, one end of the capillary was clogged with the Parafilm® and then the capillary has been placed vertically with the opened end directed upwards so that its half-length was placed in the middle of the ring made from several scrolls of the nickel/chrome 80/20 wire (**Figure 2.11 a**). Using external power supply the current was passed through the wire *ipso facto* increasing the temperature in the vicinity of the capillary (**Figure 2.11 b**), which in turn decreased the glass velocity. Next, the hose from the pump was attached to the top of the capillary and under vacuum the walls in the heating region were collapsed, closing the capillary in the mid-length (**Figure 2.12 b**).
2. Next step was to place short piece of gold wire (3-5 mm, $\varnothing = 25$ or $50 \mu\text{m}$) just above the collapsed part of the capillary. The gold wire was melted into the glass in the same

manner as the capillary was closed. The capillary was then turned up-side-down and second piece of the gold wire was melted into glass as it is shown on **Figure 2.12 c**.

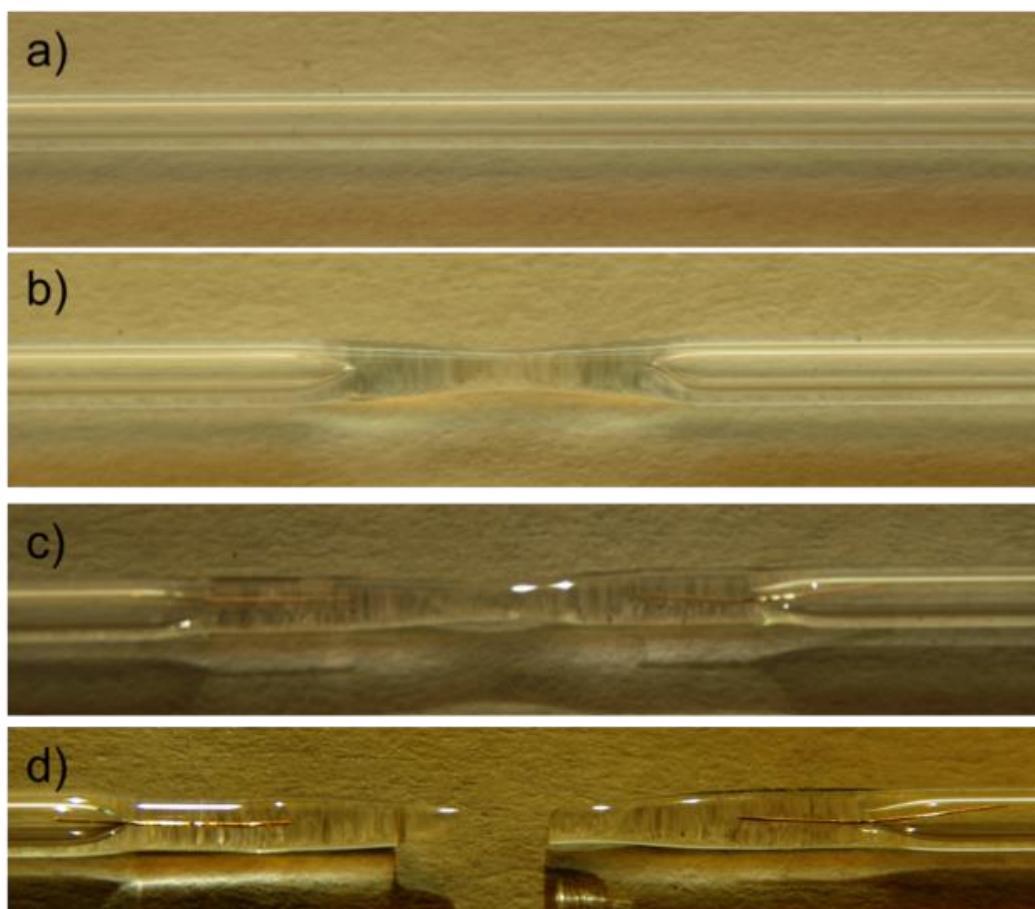


Figure 2.12. a) Borosilicate glass capillary before closing the mid-length, b) with collapsed walls closing the capillary in the middle c) the 50 μm gold wires melted into the glass on double side of the capillary mid-length and d) the capillary splitted into two pieces, each contained gold wire.

3. Subsequently the capillary was cut with the diamond knife in the mid-length (**Figure 2.12 d**). Two resulting pieces have been polished (initially with 250 granulation sand paper) in order to remove redundant layer of glass (**see Figure 2.13 b**) up to the gold wire. The polishing was repeated three more times with the decreasing - 1000, 2500 and 4000 - granulation of sand paper in order to smooth the surface as it is shown on **Figure 4 c**. The photo of polishing set-up can be found in **Figure 2.13 a**.

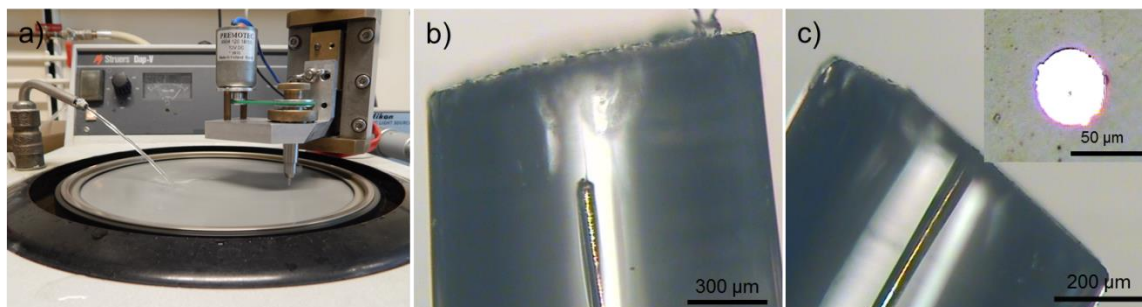
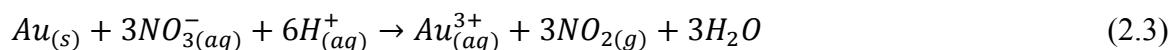


Figure 2.13. a) The polishing set-up used in this protocol, b) the capillary with the excess of glass above the gold wire and c) the capillary after polishing with four different sand papers (gold wire diameter was 50 μm).

- The gold from the glass was removed by placing the capillary overnight into the beaker containing *aqua regia*. The gold etching has to be hold under the fume hood due to the toxic nitrogen dioxide evolution during the reaction:



- On the following day, remains of *aqua regia* inside the capillary were carefully removed by rinsing them few times with distilled water. Obtained micropores, which will support the liquid – liquid interface, are presented in **Figure 2.14**.

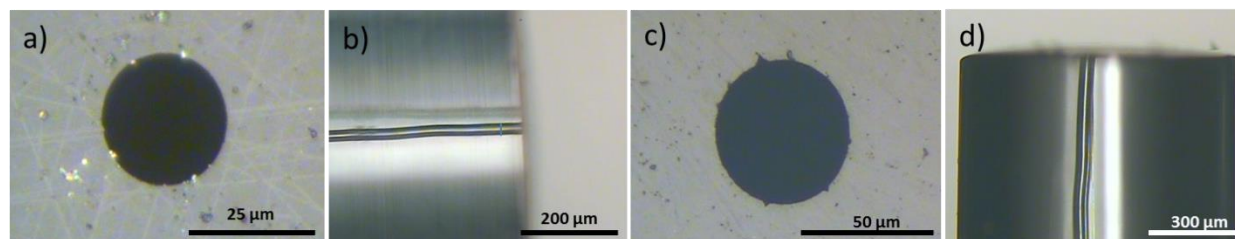
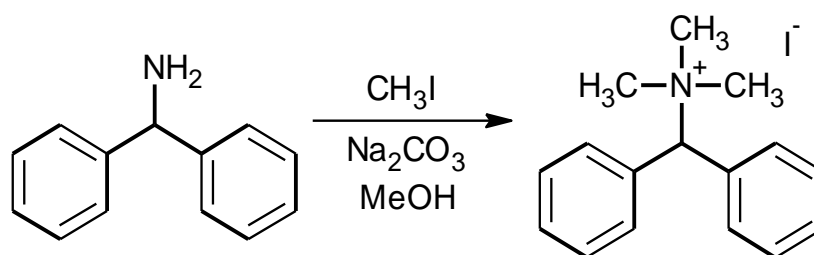


Figure 2.14. Optical microscope images recorded after gold removal. Images a) and b) correspond to the pore with 25 μm in diameter, whereas c) and d) to the pore with 50 μm in diameter. a) and c) are top view, b) and d) are the side view of the single pore capillary.

2.5.7. Protocol of preparation of trimethylbenzhydrylammonium iodide

The protocol was adapted from a previous study.² The amide group of aminodiphenylhydrochloride is nucleophilic center, which is methylated with methyl iodide in order to form quaternary amine. The overall reaction of methylation can be schematically written as:



The protocol of preparation can be divided into few stages:

1. First, the solvent – 100 ml of methanol, was placed into the round-bottom two neck flask and was deoxygenated for 30 minutes by passing the nitrogen through the solution (top neck was clogged with the cap, whereas the side neck was covered with turn-over Flang stopper through which two needles were placed, first as a nitrogen inlet and second as nitrogen outlet).
2. The following reagents: 1g of aminodiphenylmethane hydrochloride, 3.85g of anhydrous sodium carbonate and 2.26 ml of iodomethane were added to the flask containing methanol.

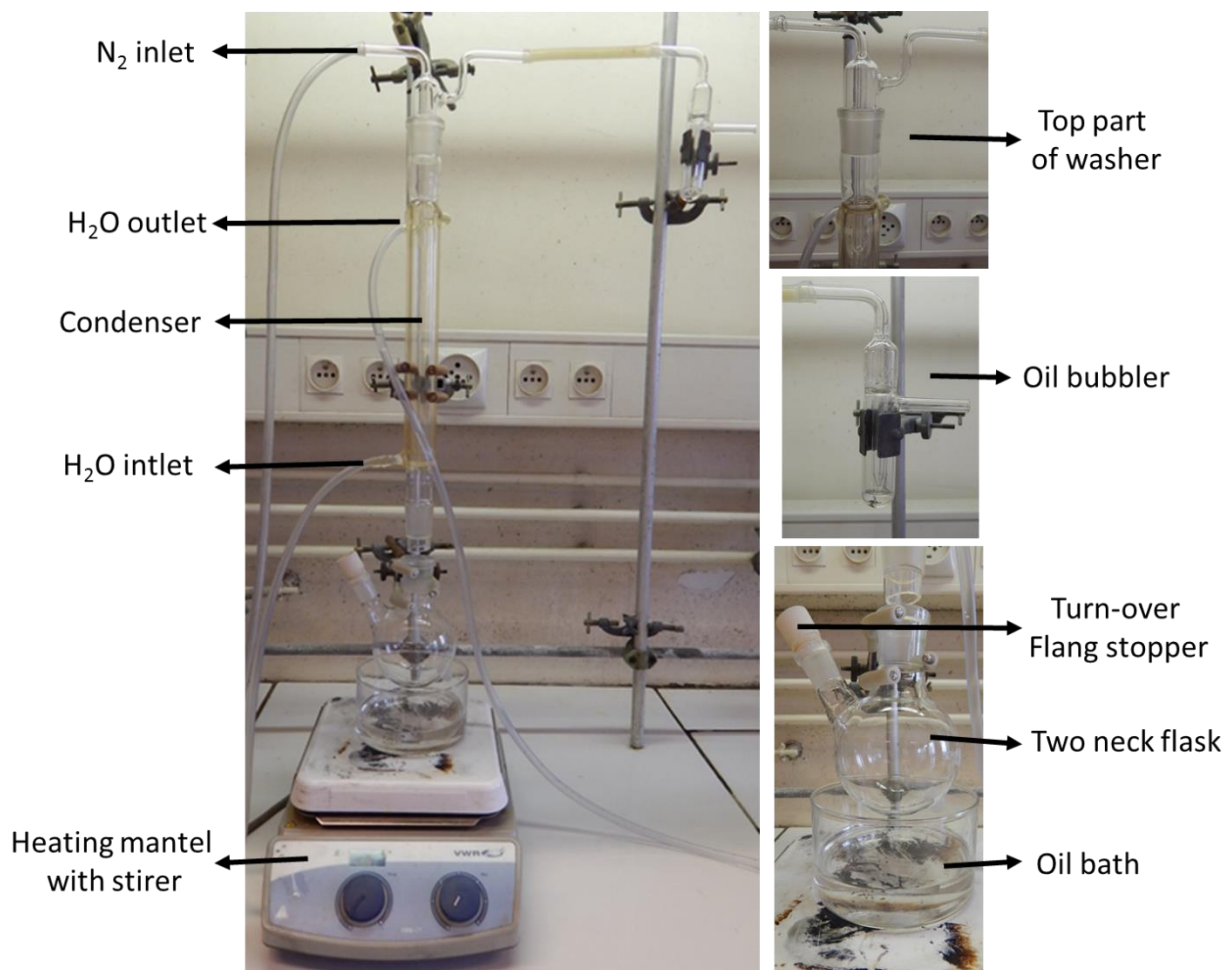


Figure 2.15. Reflux set-up used for synthesis of trimethylbenzhydrylamonium iodide.

3. The solution was refluxed for 24 hours under nitrogen. Set-up constructed for this purpose is shown on **Figure 2.15**. The round-bottom flask was placed in the oil bath with the temperature set to be 60°C. Top neck of the flask was connected with the condenser. Reaction was carried out under inert gas atmosphere. N₂ inlet was supplied from top part of condenser. Gas bubbler filled with silicon oil was employed to monitor the N₂ flow.
4. After 24 hours, once the mixture cooled down to room temperature, 30 ml of 1M sodium thiosulfate was added and then mixture was stirred for 15 minutes. Insoluble part of reaction mixture was gravity filtered with paper filter. 10 grams of potassium iodide was added and the reaction mixture was stirred for another 15 minutes.

5. Further purification step was completed in separatory funnel. The reaction mixture was shaken with 50 ml of H₂O and 50 ml of dichloromethane. Organic phase was collected. Extraction was repeated two more times with 50 ml dichloromethane each time.
6. Dichloromethane was reduced under vacuum with rotary evaporator shown on **Figure 2.16**.
7. Obtained product was recrystallized from acetone.

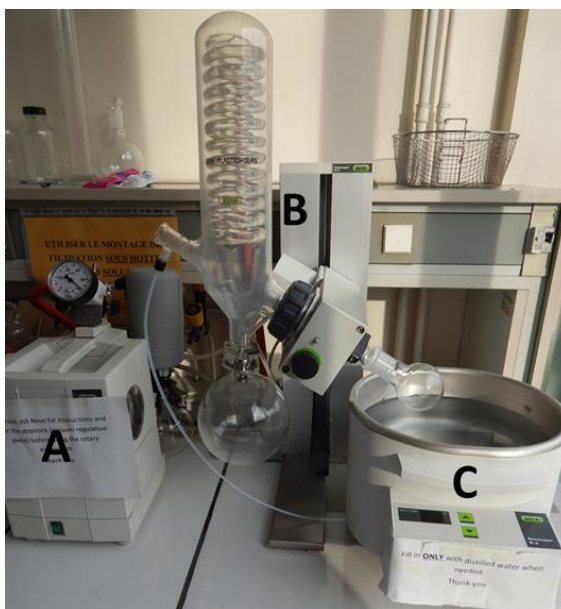


Figure 2.16. Distillation under vacuum set-up. A – the pump, B – rotary evaporator and C – heating bath filled with distilled water.

Chapter III. Templated Sol – Gel process of silica at the electrified liquid – liquid interface

Under proper conditions the liquid – liquid interface can be polarized and used as a well understood electro chemical device (the equations developed for the electrochemistry of solid electrodes are applicable at the ITIES). From an electroanalytical point of view the electrified liquid – liquid interface brings several advantages over the solid electrodes: (i) it is self-healing, which eliminates the problems concerning electrode surface polishing; (ii) it has an interface deprived from defects up to a molecular level; (iii) the detection is not restricted to reduction and oxidation reaction but can arise from simple interfacial ion transfer reaction; (iv) it has good sensitivity and finally (v) reasonable limits of detection down to nM level for miniaturized systems. The ITIES can be used for determination of number of ionic analytes ranging from inorganic molecules^{30,196} to organic compounds including the species which are biochemically important.¹⁹⁷ Chiral detection was also reported at the ITIES.^{198,199} In spite of number of qualities the detection at the ITIES still suffer from poor selectivity, which until today is restricted to the use of ionophores (discussed in the **section 1.1.2.2**) or *ex situ* zeolite modifiers (discussed in the **section 1.3.5.3.1**). For solid electrodes it was shown many times that the surface modification can significantly improve their selectivity. Recently the Sol – Gel process of silica attracted a lot of attention for an electrochemical conductive electrode modification since under proper conditions, in the presence of structure driving agents called templates, the formation of highly ordered structures oriented normal to the electrode substrate – even with complex geometry – was easy to control.^{3,4} The optimal conditions requires the hydrolysis of TEOS – silica precursor species – at the acidic pH equal to 3 in the presence of cationic CTA⁺ surfactants – used as a template – and

supporting electrolyte, for TEOS/CTA⁺ molar ratio equal to 0.32. The condensation process of silica, cylindrical CTA⁺ micelles formation and silica scaffold generation were triggered simultaneously by the application of sufficiently low potential at which an electrochemical reduction of H⁺ and H₂O has led to OH⁻ evolution and subsequently local pH increase.

The first reports dealing with the *in situ* electrified liquid – liquid interface modification with silica materials emerge from the group of Marecek^{193,6} (discussed with more details in the **subchapter 1.3.5.3.2**). The study, however fundamental, requires further investigation hence any effort was made towards: (i) morphological evaluation of electrogenerated deposits – which probably exhibited some degree of mesostructure; (ii) additional experimental work supporting silica deposit formation mechanism and (iii) experimental examples for any possible applications of mesoporous material at the liquid – liquid interface. Consequently, the *in situ* modification of the liquid – liquid interface with silica materials is still unexplored and poorly studied field of science.

This study aims to investigate deposition of mesoporous silica material at the macroscopic liquid – liquid interface. By coupling the electrochemistry at the ITIES with the Sol-Gel process of silica (in the presence of structure driving agents) the liquid – liquid interface can be easily modified. To do so, the precursor species were hydrolyzed in the aqueous phase and separated from the organic template solution by liquid – liquid interface. The silica material formation was controlled by electrochemical transfer of positively charged template species from the organic to the aqueous phase. Number of experimental parameters e.g. initial concentration of template and precursor, polarity of the organic phase or experimental time scale were investigated. Electrochemical information extracted during interfacial silica deposition allowed the proposal of possible deposit formation mechanism. The detailed description of electrogenerated silica material was performed with a number of qualitative, structural and morphological studies. The ultimate goal of this work is to construct well characterized molecular sieves that could be used to improve selectivity of electroanalytical sensors employing the liquid – liquid interface.

3.1. Results and discussion

3.1.1. Electrochemical study

The CV recorded in the absence of CTA^+_{org} and $TEOS_{aq}$ is shown on **Figure 3.1** with a dashed line. No ion transfer occurred in the available potential window which is limited by the background electrolyte transfer ($Cl^-_{org \rightarrow aq}$ at the less positive potential and $TPBCl^-_{aq \rightarrow org}$ at the more positive potential side). The addition of cationic surfactant salt to the organic phase – CTA^+TPBCl^- – (see **Figure 3.1** red solid line) resulted in the irreproducible current spikes also known as the electrochemical instability – the phenomena known to occur at the electrified liquid – liquid interface in the presence of surface active species, which is discussed in more detail in **section 1.1.4**.

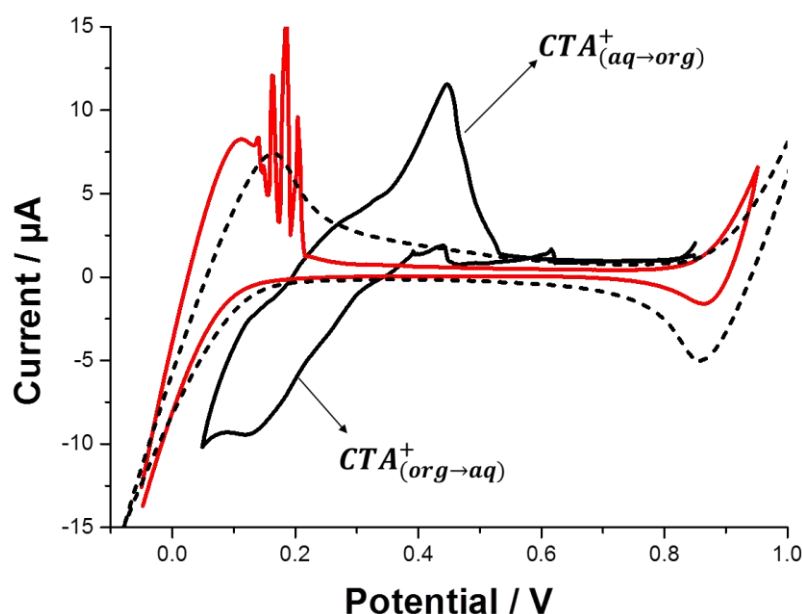


Figure 3.1. Cyclic voltammograms recorded in Cell 1. Black solid line was recorded in the presence of TEOS ($x = 50$ mM) and in the presence of CTA^+ ($y = 1.5$ mM); Black dashed line was recorded in the presence of organic and aqueous supporting electrolytes (x and $y = 0$ mM) and red solid line correspond to voltammogram recorded in the absence of TEOS ($x = 0$ mM) in the aqueous phase and in the presence of CTA^+ in the organic phase ($y = 14$ mM). Scan rate = 5 mV/s.

The adsorption of CTA^+ ions destabilized the interface and caused the current spikes close to the Galvani transfer potential of CTA^+ species. Once $[CTA^+] = 1.5 \text{ mM}$ and $[TEOS] = 50 \text{ mM}$ were present in the organic and the aqueous phase respectively, CV shown on **Figure 3.1** as black solid line was recorded. The interface was polarized from +900 mV down to +50 mV on the forward scan. A negative peak evolution was observed at around +100 mV only if both components – CTA^+ and TEOS – were present in the electrochemical cell and hence it was attributed to CTA^+ transfer probably assisted by hydrolyzed TEOS species. No silica deposit formation was found when the electrochemical cell was left for 16h at open circuit potential at room temperature, which is in an agreement with the report from Faget *et al.* who did not observe any silica deposit formation at the non-polarized liquid – liquid interface until the heating at 150°C for 2 – 10 h was employed.⁷ **Figure 3.2** shows the proposed mechanism of CTA^+ transfer followed by interfacial silica deposit electrogeneration. It was assumed that at the beginning of the polarization (see **Figure 3.2 scheme 1**) the interface was covered with the monolayer of CTA^+ ions. Forward polarization has led to negative current increase at around +100 mV attributed to $CTA^+_{org \rightarrow aq}$ transfer (see **Figure 3.2 scheme 2**). The presence of CTA^+ in the aqueous phase (see **Figure 3.2 scheme 3**) has a dual role: (i) surfactants interact between each other and form liquid crystal phase which act as ‘mold’ for condensing silica species and (ii) CTA^+ is a catalyst in the Sol-Gel process of silica due to electrostatic interactions between negatively charged hydrolyzed TEOS species and positive charge of surfactant hydrophilic head. On the reverse scan, the back transfer of positively charged CTA^+ micelles with the condensed silica took place (see **Figure 3.2 scheme 4**). The positive peak with its center at around +400 mV ended with an abrupt current drop (see **Figure 3.2 scheme 5**) was attributed to the adsorption process of CTA^+ ions in the silica framework and their partial back transfer to the organic phase. Further polarization did not induce any changes in the current characteristic and only capacitance current was recorded (see **Figure 3.2 scheme 6**). The charge transferred to the aqueous phase during one cyclic voltammogram recorded at a sufficiently low scan rate (5 mV/s) was enough to generate a white layer of silica deposit at the liquid – liquid interface. Similar deposits were reported for the tetraoctadecylammonium transfer (initially dissolved in the DCE phase) to the aqueous phase in the presence of liquid glass.⁵

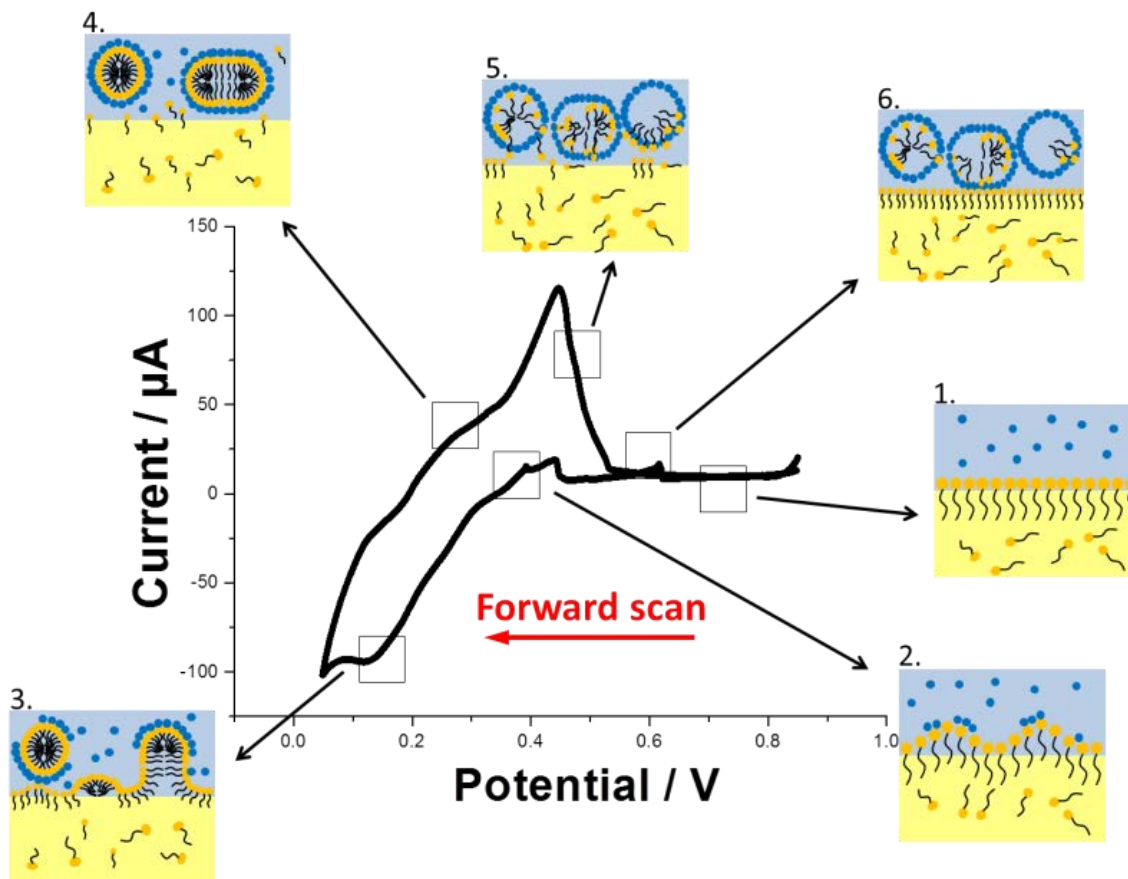


Figure 3.2. Schematic representation of the silica deposit formation mechanism. Forward scan is indicated with the red arrow. $[CTA^+]_{org} = 1.5 \text{ mM}$; $[TEOS]_{aq} = 50 \text{ mM}$; Scan rate = 5 mV/s

Charge associated with the transfer of CTA^+ was found to be dependent from the aqueous phase pH as it is shown on **Figure 3.3**. Each point from the curve is the average of the five last (from fifteen consecutive voltammetric cycles) positive peak charges. The charge under the reverse peak was observed to obtain maximum values for the pH = 9-10 at which the existence of polynuclear species – $Si_4O_6(OH)_6^{2-}$ and $Si_4O_8(OH)_4^{4-}$ – is predominant in the aqueous phase. At the pH = 11 and < 9 mononuclear species are dominant and hence as a consequence the net negative charge is not sufficient to facilitate the $CTA^+_{org \rightarrow aq}$ transfer. Based on this result the pH of the aqueous phase during interfacial silica electrogeneration was kept at around 9.5.

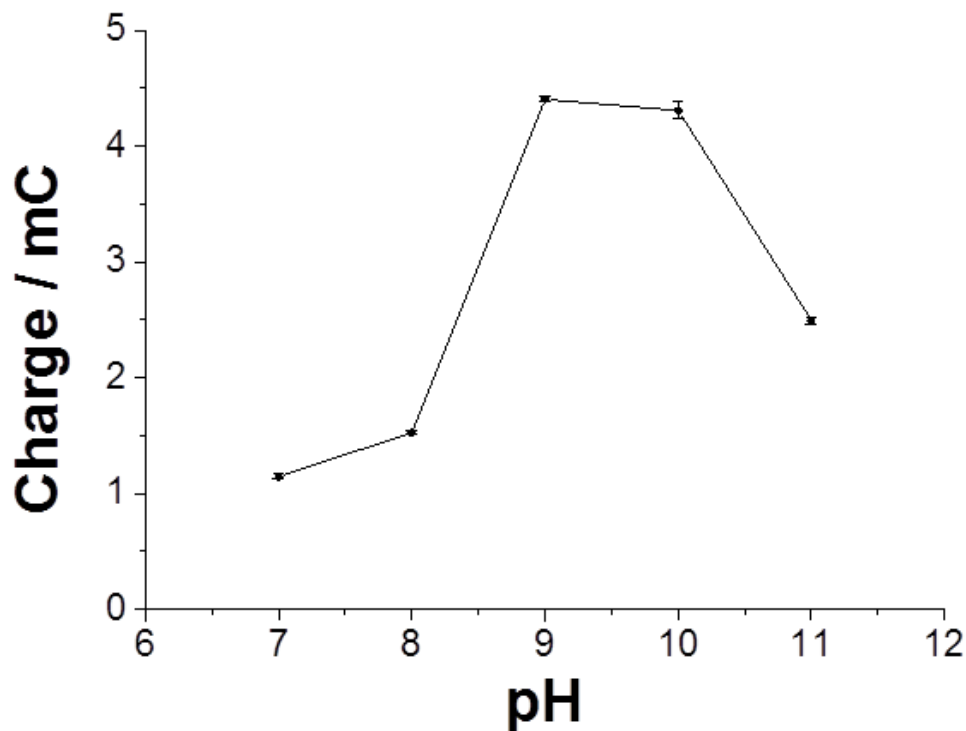


Figure 3.3. The charge of the forward cyclic voltammetry scan recorded in the presence of $[\text{CTA}^+]_{\text{org}} = 3$ mM and $[\text{TEOS}]_{\text{aq}} = 300$ mM as a function of pH. The error bars are the standard deviation of the last five values of fifteen consecutive runs.

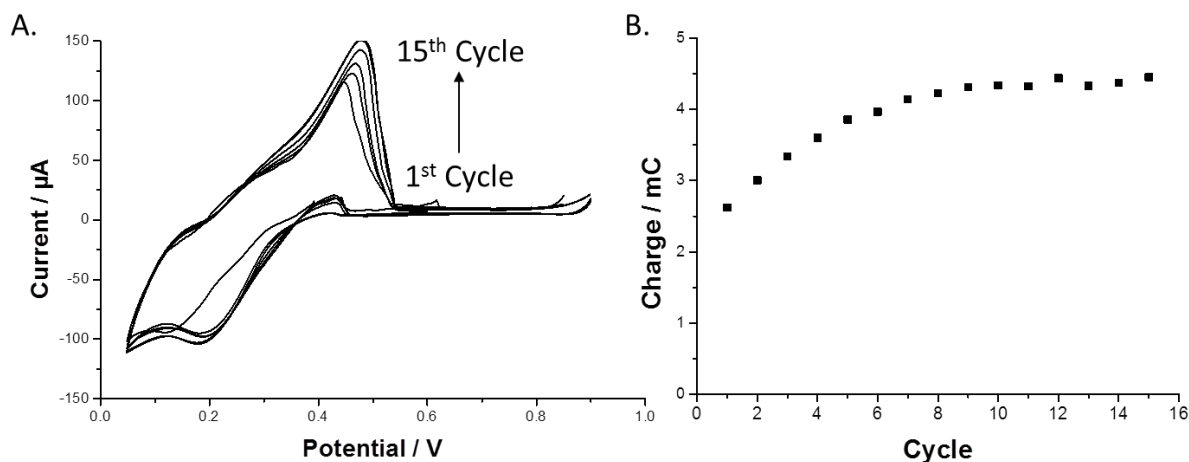


Figure 3.4. A – Cyclic voltammograms recorded for the 1st, 2nd, 3rd, 5th, 10th and 15th cycle in the presence of $[\text{TEOS}]_{\text{aq}} = 50$ mM and $[\text{CTA}^+]_{\text{org}} = 1.5$ mM. B – Correspond to reverse peak charge as a function of number of cycles. Scan rate = 5 mV/s. pH of the aqueous phase was 9.5.

The influence of repetitive cycling on the current – potential characteristics and the charge above the reversed peaks are shown on **Figure 3.4 A and B** respectively (pH of the aqueous

phase was 9.5). From **Figure 3.4 A** it is clear that after first cycle the transfer potential of $CTA_{org \rightarrow aq}^+$ is slightly shifted towards more positive values, probably due to a local increase in the net negative charge arising from the silica species undergoing condensation followed by deposition. Increase in the reversed peak height was observed, usually until 8th cycle whereas for the forward peak its shape was rather unchanged after first cycle. On **Figure 3.4 B** the charge above the reverse scan was plotted in function of number of cycles. Apparently the charge associated with the $CTA_{aq \rightarrow org}^+$ back transfer increased approximately up to 8th cycle and reaches a plateau. The global concentration of the CTA^+ in the organic phase remained unchanged as the charge under the forward peak remained constant between second and fifteenth scan.

For higher surfactant concentration the destabilization of the interface induced by CTA^+ interfacial adsorption was manifested by current spikes – also known as electrochemical instability – usually appearing on the first voltammogram recorded during silica deposition. On **Figure 3.5 A** cyclic voltammograms represents the first cycle recorded for 3 mM (black curve) and 14 mM CTA^+ (red curve) in the organic phase. The current spikes appeared in both cases however were much more pronounced for the higher surfactant concentration. Interestingly, the presence of silica deposits stabilized the interfacial region as the current spikes did not occur up to the last fifteenth cycle in both cases (see **Figure 3.5 B**).

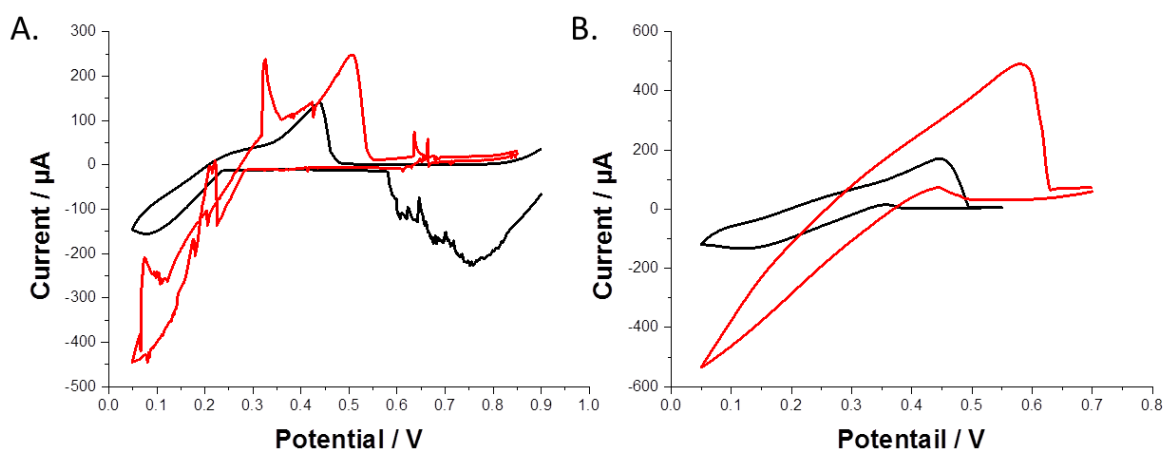


Figure 3.5. Cyclic voltammograms showing the influence of interfacial silica deposit formation on the electrochemical instability. A – Cyclic voltammograms for the 1st scan; B – Cyclic voltammograms for the 15th scan. Red line correspond to $[CTA^+]_{org} = 3$ mM, black line correspond to $[CTA^+]_{org} = 14$ mM. $[TEOS]_{aq} = 50$ mM. Scan rate = 5 mV/s.

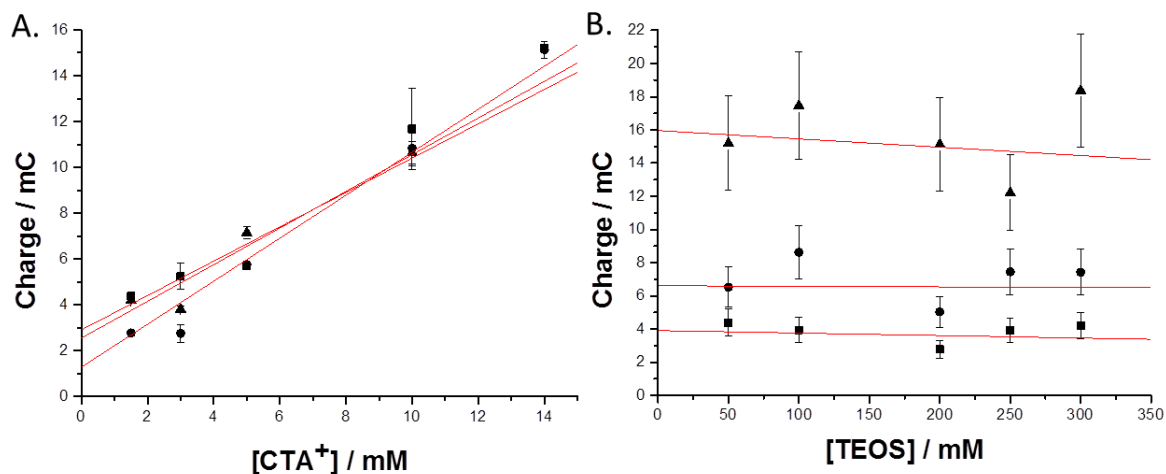


Figure 3.6. Influence of $[CTA^+]_{org}$ – A and $[TEOS]_{aq}$ – B on the reverse peak charge for: A – 1.5 mM (■), 5 mM (●) and 14 mM (▲) $[TEOS]_{aq}$; and B – 50 mM (■), 200 mM (●) and 300 mM (▲) $[CTA^+]_{org}$. The points and the error bars (standard deviations) were calculated from the last five cycles of the fifteen repetitive voltammetric runs.

Subsequent parameter studied was the influence of the $[CTA^+]_{org}$ and $[TEOS]_{aq}$ on the electrochemical response of the system recorded during silica electrodeposition. **Figure 3.6 A** represents the average charge of the last five points recorded during fifteen subsequent cycles (as it is shown for instance on **Figure 3.4 B**) for different constant $[TEOS]_{aq}$ and varied $[CTA^+]_{org}$. For **Figure 3.6 B** the $[CTA^+]_{org}$ was kept constant and the $[TEOS]_{aq}$ was changed. These two figures indicate that the limiting factor for the interfacial silica deposit formation is the CTA^+ transfer since: (i) the reverse peak charge increased linearly from 1.5 mM up to 14 mM $[CTA^+]_{org}$ regardless of $[TEOS]_{aq}$ and (ii) the reverse peak remained constant for increasing $[TEOS]_{aq}$ and constant $[CTA^+]_{org}$.

3.1.2. Characterization of silica deposits electrogenerated at the ITIES

For further characterization the silica material was electrogenerated in the electrochemical cell supporting the liquid – liquid interface possessing the largest surface area (see **Figure 2. 1 B**). After electrodeposition the ITIES was modified with the silica film being a gel phase – not fully condensed silica matrix. In order to obtain solid silica it has to be cured. To do so, the silica deposits were collected (using microscope cover slip immersed in the cell prior to electrolysis) and stored overnight in the oven at 130°C. Silica deposits were prepared under different initial synthetic conditions, which include: the effect of $[\text{TEOS}]_{\text{aq}}$ and $[\text{CTA}^+]_{\text{org}}$, the polarity of the organic phase and the method used for electrolysis. Samples prepared in such way could then be used for further characterization. IR spectroscopy and XPS were used to study chemical functions of the silica deposits. BET analysis allowed evaluation of the silica porosity after the calcination (removal of organic residues from inside the pores induced by thermal oxidation). Finally, the SAXS and TEM were employed as a tool to study the structural properties of the silica.

3.1.3. Spectroscopic analysis

Characteristic IR spectrum recorded for the silica deposit electrogenerated at the ITIES using surfactant template is shown on **Figure 3.7**. The peaks attributed to the vibrations of silica network are localized at 1080 cm^{-1} – intense band arising from Si-O-Si asymmetric stretching mode, 790 cm^{-1} – arising due to symmetric stretching of Si-O-Si and 480 cm^{-1} – attributed to Si-O bond rocking. The small peak observed at around 1200 cm^{-1} was described in the literature as an overlap of asymmetric stretching modes of Si-O-Si bond.⁸ The broad band from about 3100 cm^{-1} up to 3750 cm^{-1} corresponds to both: terminal -O-H stretching mode present inside the silica walls and absorbed of adsorbed water molecules. The additional contribution to -O-H can be also found as a peak around 1630 cm^{-1} , which arises from its bending vibration mode.^{9,10} Finally, IR spectroscopy was also used to track remaining surfactant species. The CTA^+ molecules were tracked by two characteristic peaks situated at 2925 cm^{-1} – attributed to asymmetric CH_2 stretching vibrations and at 2850 cm^{-1} – arising as a reason of CH_2 symmetric stretching vibrations. Also the peak at around 1480 cm^{-1} could inform about the presence of alkyl chains as

it corresponds to C-H bending vibration, although it is not clearly pronounced on the recorded spectrum.⁸ The presence of template molecules in the silica framework was in agreement with the voltammetric results, which have indicated that the interfacial transfer of CTA^+ was irreversible and its reverse transfer was accomplished with the adsorption process. The absorption of aromatic rings from the cationic part of organic electrolyte was observed as a peak with very weak intensity at around 3060 cm^{-1} (see inset of Figure 3.7).¹¹ The organic electrolyte cation presence could be due to the residuals from the organic phase evaporation most probably collected together with the silica deposit from the liquid – liquid interface. However, as it will be shown in one of the following chapters, this was not the case since organic electrolyte ions were also incorporated in a silica deposit formation.

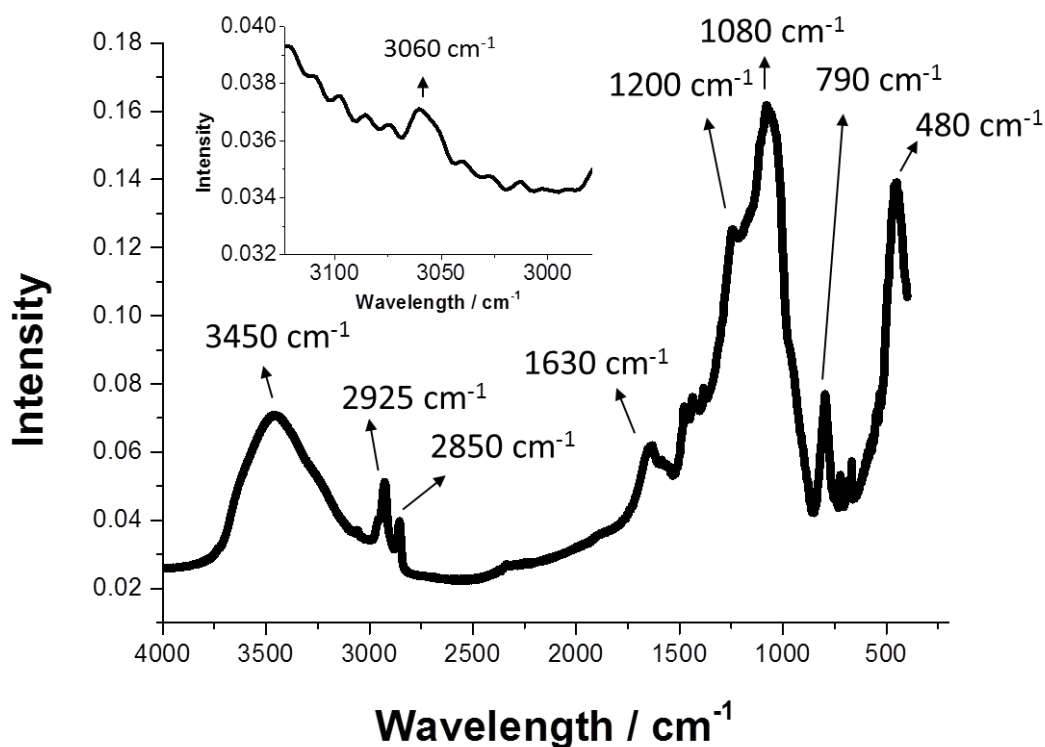


Figure 3.7. Infra-red spectrum of silica deposit prepared for following template and silica precursor concentrations: $[\text{CTA}^+]_{\text{org}} = 14\text{ mM}$ and $[\text{TEOS}]_{\text{aq}} = 300\text{ mM}$. The most significant wavenumbers are indicated with the arrows.

X-Ray Photoelectron Spectroscopy (XPS) measurements were performed in order to prove the formation of silica as well as to study the contribution of other attractions between the atoms. A typical XPS spectrum for the silica deposit synthesized at the ITIES (for $[\text{CTA}^+]_{\text{org}} = 10$

mM and $[\text{TEOS}]_{\text{aq}} = 300 \text{ mM}$) is shown on **Figure 3.8 A**. A series of peaks corresponding to Na_{1s} , O_{1s} , N_{1s} , Cl_{2s} , P_{2p} , Si_{2p} and C_{1s} were detected. The presence of peaks arising from Na_{1s} and Cl_{2s} are most probably due to remaining aqueous supporting electrolyte residuals, although some charge balancing of terminal OH^- inside the pores by Na^+ cannot be excluded. Another source of Cl^- anions is the TPBCl^- – anionic part of organic electrolyte – which apparently was also present in the sample. The BTTPA^+ traces could be followed with the P_{2p} signal. The possible explanation of two hydrophobic ions that were present in the sample is not straightforward since some residuals could have been collected together with the organic phase during silica deposit collection. The SiO_2 formation can be confirmed on the basis of **Figure 3.8 B** (presence of Si-O bond) and **D** (presence of Si-O-Si bond). Nitrogen deriving from surfactant species was also present. The C-O bond from **Figure 3.8 C** suggests that TEOS molecules were not fully hydrolyzed and some Si-O-C may still remain in the sol solution.

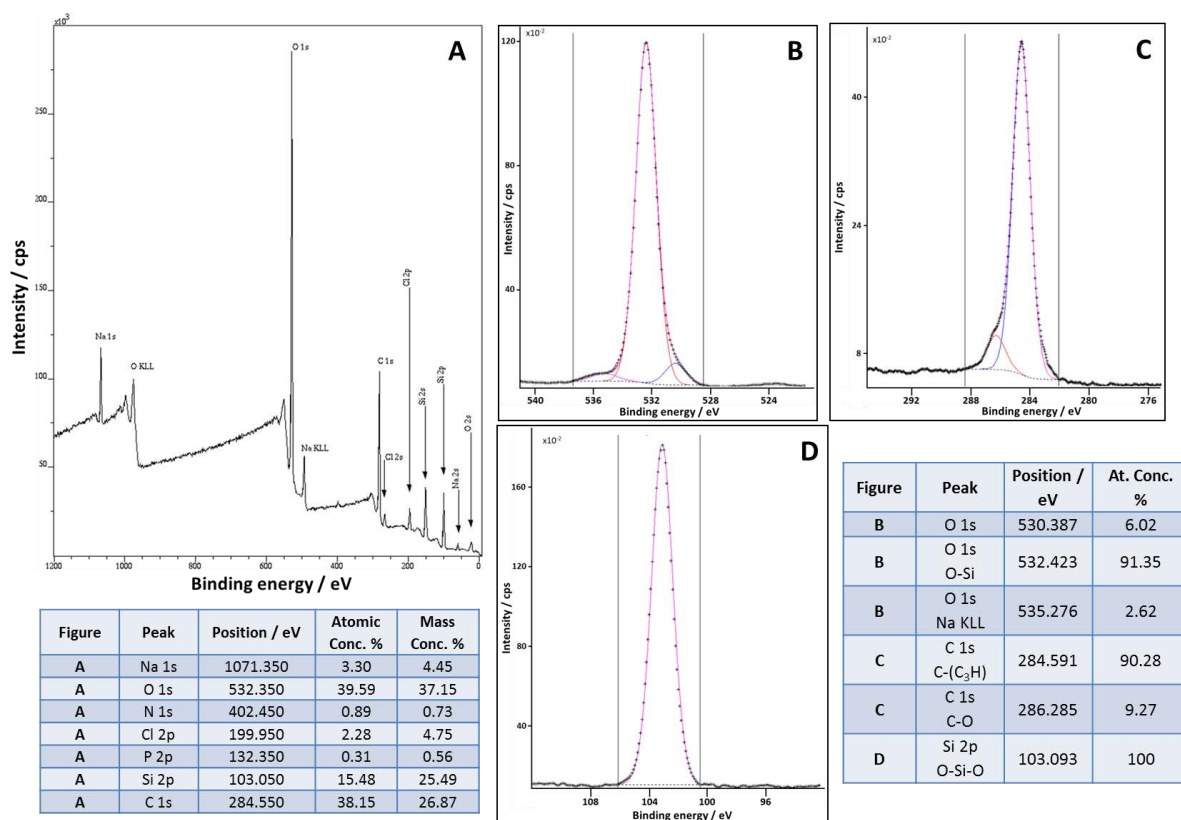


Figure 3.8. XPS spectra of the silica deposit prepared for: $[\text{CTA}^+]_{\text{org}} = 10 \text{ mM}$ and $[\text{TEOS}]_{\text{aq}} = 300 \text{ mM}$. A – spectrum in the full range; B – spectrum in the region of O_{1s} ; C – spectrum in the region of C_{1s} and D – spectrum in the region of Si_{2p} . The tables are correlated with the spectra.

3.1.4. BET analysis

The results of nitrogen adsorption-desorption isotherm for the silica deposit electrogenerated at the liquid – liquid interface are displayed on **Figure 3.9**. The curve marked with the squares corresponds to the silica deposit that was cured in the oven at 130°C overnight. The second plot, marked with the circles, was recorded after calcination at 450°C for 30 min. Clearly, after calcination, the pores filled with the organic species are released since the specific surface area increased from 194 m²/g up to 700 m²/g. The curve recorded after calcination took the shape of type IV isotherm¹² with two capillary condensation steps: the first at $p/p_0 = \sim 0.4$ and the second at $p/p_0 = \sim 0.7$ (which was also present for the sample before calcination). The first step is characteristic for the mesoporous materials with relatively small pore – the pores dimensions were calculated to be around 7 nm. The step at $p/p_0 = \sim 0.7$ indicated that synthesized silica exhibit second degree of mesoporosity which is around 1 μm.

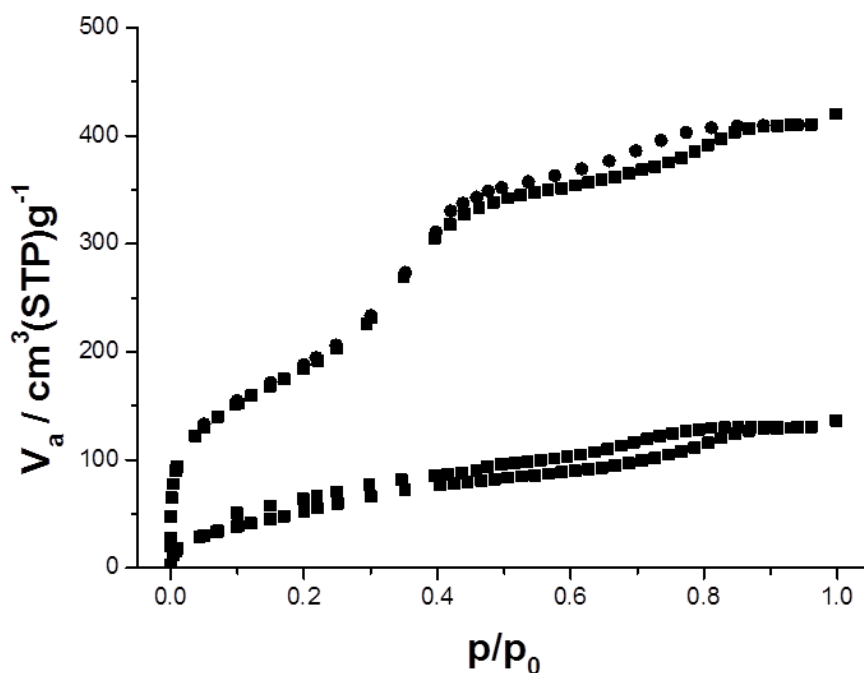


Figure 3.9. Nitrogen adsorption-desorption of the silica deposit prepared using $[\text{CTA}^+]_{\text{org}} = 14 \text{ mM}$ and $[\text{TEOS}]_{\text{aq}} = 300 \text{ mM}$ before (squares) and after (circles) calcination (heat treatment was performed at 450°C for 30 min).

3.1.5. Morphological characterization

SAXS analysis was employed to study structural parameters of silica deposits. Broad peak in the SAXS patterns suggested the presence of ‘worm-like’ structure (especially visible for **Figure 3.10 A blue curve**).¹³ This level of order confirms the template (CTA^+) transfer from the aqueous to the organic phase, where it self-assembles with TEOS molecules and results in the silica modified ITIES. **Figure 3.10 A** shows the structural properties of the silica deposits prepared for different $[\text{CTA}^+]_{\text{org}}$ (5 mM – black curve, 10 mM – red curve and 14 mM – blue curve) while the $[\text{TEOS}]_{\text{aq}}$ was kept constant (300 mM). The peak intensity increased with the increasing $[\text{CTA}^+]_{\text{org}}$ and the pore center-to-center distance (being the $2\pi/q$ where q is the wavelength of the peak center) decreased from 5.7 nm ($[\text{CTA}^+]_{\text{org}} = 5$ mM) to 4.8 nm ($[\text{CTA}^+]_{\text{org}} = 10$ mM) down to 4.5 nm ($[\text{CTA}^+]_{\text{org}}$). It was already shown that the $[\text{CTA}^+]_{\text{org}}$ influenced the charge transfer during the voltammetric silica deposition and hence was the limiting factor during the silica formation. The $[\text{CTA}^+]_{\text{org}}$ was directly related with the CTA^+ concentration in the aqueous diffusion layer once CTA^+ was transferred from the organic to the aqueous phase. The critical micelle concentration (CMC) in water for CTA^+Cl^- is 1.4mM.¹⁴ The concentration of CTA^+ in the aqueous diffusion layer is more likely to be above the CMC for the higher $[\text{CTA}^+]_{\text{org}}$ and hence results in better structuration of the silica deposit. When $[\text{CTA}^+]_{\text{org}}$ was kept constant (14 mM) and $[\text{TEOS}]_{\text{aq}}$ was decreased from 300 mM down to 50 mM the small increase in the pore center-to-center distance (from 4.5 nm to 4.9 nm) was observed. It was concluded that $[\text{TEOS}]_{\text{aq}}$ impact on the silica deposit formation is not as important as it was shown for $[\text{CTA}^+]_{\text{org}}$. The nature and the polarity of the organic phase were found to have a great influence on the structure of the deposits as it is shown on **Figure 3.10 B**. The concentration of the CTA^+ and TEOS were kept constant for all three samples. The presence of 30% of decane (**black curve Figure 3.10 B**) in the organic phase resulted in very weak response and the pore center-to-center distance around 6.1 nm. Interestingly, the addition of 20% of ethanol (**blue curve Figure 3.10 B**) to the organic phase has led to the formation of still broad however clear response; with a pore center-to-center distance of 3.8 nm (the alcohols are known to affect the structure of silica prepared by Sol-Gel process in the presence of CTA^+ as structure driving agents).¹⁵ The discrepancy of the pore center-to-center distance calculated from SAXS pattern and from the

BET analysis (pore diameter was found to be 7 nm) can be attributed to the sample broad pore dimensions distribution.²⁰⁸

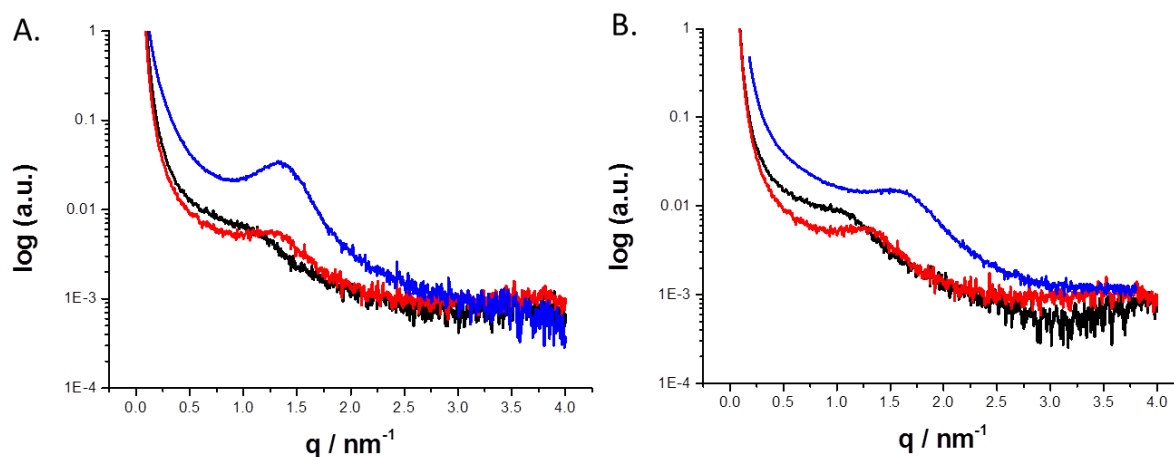


Figure 3.10. Variation of SAXS pattern recorded for silica deposits electrogenerated at the ITIES. A – correspond to silica deposits synthesized under different $[\text{CTA}^+]_{\text{org}}$ (black – 5 mM, red – 10 mM and blue – 14 mM) and constant $[\text{TEOS}]_{\text{aq}} = 300 \text{ mM}$; B – correspond to organic phase different polarity (black – 30% decane / 70% DCE, red – 100% DCE and blue 20% ethanol / 80% DCE) the $[\text{CTA}^+]_{\text{org}} = 10 \text{ mM}$ and the $[\text{TEOS}]_{\text{aq}} = 300 \text{ mM}$. All samples were prepared by cyclic voltammetry.

The set of TEM micrographs for silica deposits prepared under different conditions are shown on **Figure 3.11**. All images confirmed the presence of ‘worm-like’ type of pores and the mesoporous character of the material. Preparing the silica deposits by chronoamperometry apparently has little impact on their structure as there are no significant differences (see TEM images from **Figure 3.11 A and B**) between the silica deposits prepared by cyclic voltammetry. Also the pore center-to-center distance calculated from SAXS patterns show very small discrepancy (4.6 nm for chronoamperometry and 4.8 nm for cyclic voltammetry).

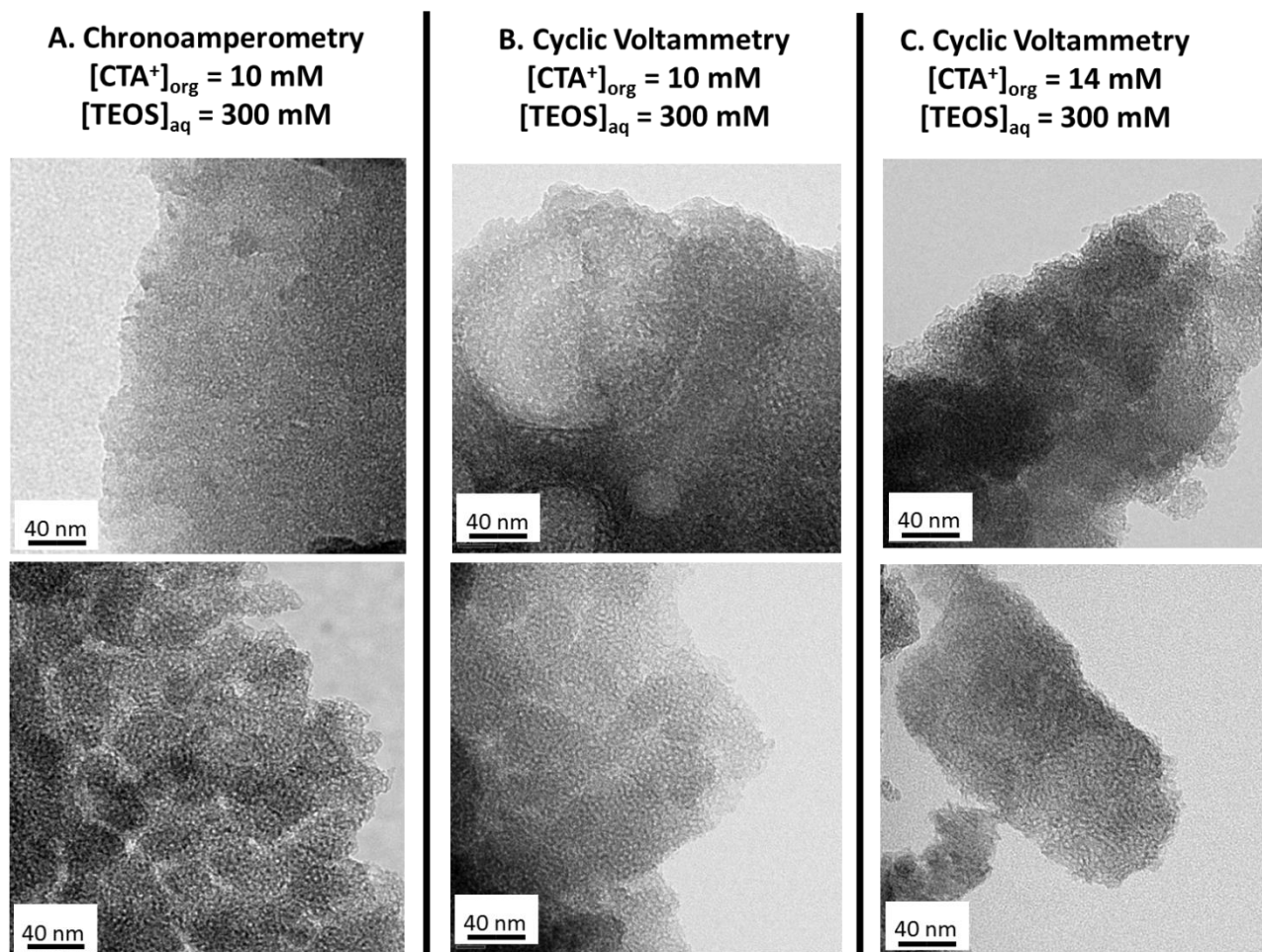


Figure 3.11. TEM images of silica deposits prepared by both cyclic voltammetry and chronoamperometry. The initial composition of two phases is indicated as the headlines of each column.

3.2. Conclusion

The macroscopic liquid – liquid interface electrochemical modification with silica material structured with the cationic surfactant – being the surface driving agent – was studied. It has been shown that silica deposits can be formed only in the presence of both, silica precursor in the aqueous phase and positively charged surfactant template in the organic phase. This indicates that the CTA^+ ion transfer was facilitated by negative charge of polynuclear TEOS species hydrolyzed in the aqueous phase. The shape of voltammetric response has suggested the interfacial adsorption process of CTA^+ , as abrupt drop in current was always observed on the reverse peak. Moreover, it was concluded that the formation of silica at the ITIES is limited by

$[\text{CTA}^+]_{\text{org}}$, as the charge above the reverse peak was increasing linearly with its concentration (varying $[\text{TEOS}]_{\text{aq}}$ did not affect the charge transfer). Silica deposits were also found to stabilize the liquid – liquid interface as the electrochemical instability was not observed after deposition.

Electrochemical deposition was followed by the silica collection, curing and finally its characterization. With spectroscopic methods, the formation of Si-O-Si bond was confirmed. Additionally the presence of template species could be followed by IR spectroscopy as two vibrational modes of symmetric and asymmetric stretching of CH_2 bonds were found. The organic electrolyte was also found to be present in the silica deposits. Although most probably some organic phase solution was collected together with the deposit its participation in silica formation cannot be excluded.

Thermal treatment at 450°C for 30 min was enough to calcinate the organic residues from inside the silica pores. The BET isotherm confirmed the presence of mesostructure. The pore symmetry was found to be of ‘worm like’ structure as concluded from broad peak presence in the SAXS patterns and from TEM micrographs. The pore center-to-center distance, depending on the experimental conditions applied during silica deposit synthesis, ranged from 3.8 nm up to 6.1 nm.

Silica generated at the liquid – liquid interface requires further treatment in order to support and cure the silica material for further application in electroanalysis. This is not feasible at the macroscopic ITIES and as a consequence silica has to be supported in a way which will allow its synthesis, processing and finally reuse in the liquid – liquid configuration. To do so, the liquid – liquid interface was miniaturized and modified with the silica material using conditions elaborated at the macroscopic ITIES as it is shown in the following chapter IV. Results described in this chapter are also available in the **Electrochemistry Communications**, 2013, **37**, 76 – 79.

Chapter IV. Silica electrodeposition using cationic surfactant as a template at miniaturized ITIES

In the following chapter, the liquid – liquid interface was miniaturized through silicon chips supporting an array of pores. Electrodeposition of silica material at the microITIES was performed with the protocol developed at the macroITIES (described in chapter III). Application of the membrane supporting array of microITIES allowed the mechanical stabilization of silica deposits. The electrochemical deposition process, silica deposits morphological study, spectroscopic characterization, *in situ* spectroscopic study of silica formation and finally electroanalytical evaluation of silica deposits were investigated in a series of experiments that are described in following subchapters.

4.1. Electrochemical and morphological study of silica deposits at the array of microITIES

The supported microITIES allowed an easy and straightforward silica deposition. The silicon chips (mesoporous membrane of array of pores prepared by lithography) have additionally served as the support for silica deposits, which after electrogeneration have kept their mechanical stability and hence further characterization and reuse in electroanalysis was possible. In the following subchapters, parameters such as the concentration of template ions in the organic phase and precursor species in the aqueous phase, time scale of the experiment or the influence of geometry of the array of microITIES used to support the liquid – liquid interface on the silica deposit formation were evaluated based on cyclic voltammetry (CV) results. Morphological study, performed with SEM and profilometry based on shear force measurement allowed the morphological characterization of silica deposits. The effect of calcination was studied with Raman spectroscopy and ion transfer voltammetry.

4.1.1. Surfactant-template assisted Sol-Gel process of silica at the microITIES

Typical CV recorded at the microITIES membrane design number 3 (**Table 2.2**) during silica deposit formation is marked on **Figure 4.1** with a black curve. The deposition was performed with $[CTA^+]_{org} = 14 \text{ mM}$ and $[TEOS]_{aq} = 50 \text{ mM}$ in the cell 2 at 5 mV/s. Red curve from **Figure 4.1** corresponds to blank CV recorded in **cell 2** in the absence of template and precursor in the aqueous and the organic phase respectively. During silica electrogeneration the interface was polarized from +600 mV down to -100 mV on the forward scan (the polarization direction was chosen with agreement to the positive charge of cationic template species, which in order to trigger silica condensation reaction, had to be transferred from the organic to the aqueous phase). As it is shown on **scheme 1** on **Figure 4.1**, it was assumed that at the beginning of the polarization the liquid – liquid interface was uniformly covered with the CTA^+ monolayer and the current was only measured due to interfacial double layer charging. The $CTA^+_{org \rightarrow aq}$ has started at around +100 mV. The local concentration of CTA^+ in the aqueous diffusion profile zone should exceed its CMC (it was reported to be 1.4 mM for CTAB)²⁰⁶ in order to form spherical and positively charged micelles. The presence of positive charge at the edge of micellar spheres catalyzes the condensation of the TEOS precursor around the template species, resulting in silica material formation (see **scheme 2** on **Figure 4.1**). The sigmoidal shape of the negative peak suggest that the $CTA^+_{org \rightarrow aq}$ was not limited by linear diffusion inside the pore of the silicon wafer, which should be the case in here (the shape of the negative response will be discussed in the following section). The polarization was reversed at -100 mV. Going towards more negative values would force the transfer of first $Cl^-_{aq \rightarrow org}$ followed by $BTPPA^+_{org \rightarrow aq}$. During the reverse scan the CTA^+ was expected to back transfer towards the organic phase. The formation of the characteristic positive peak at around +260 mV terminated with the abrupt drop in current has suggested adsorption process of CTA^+ among the silica network (drop in current informs that there are no more charges to transfer).

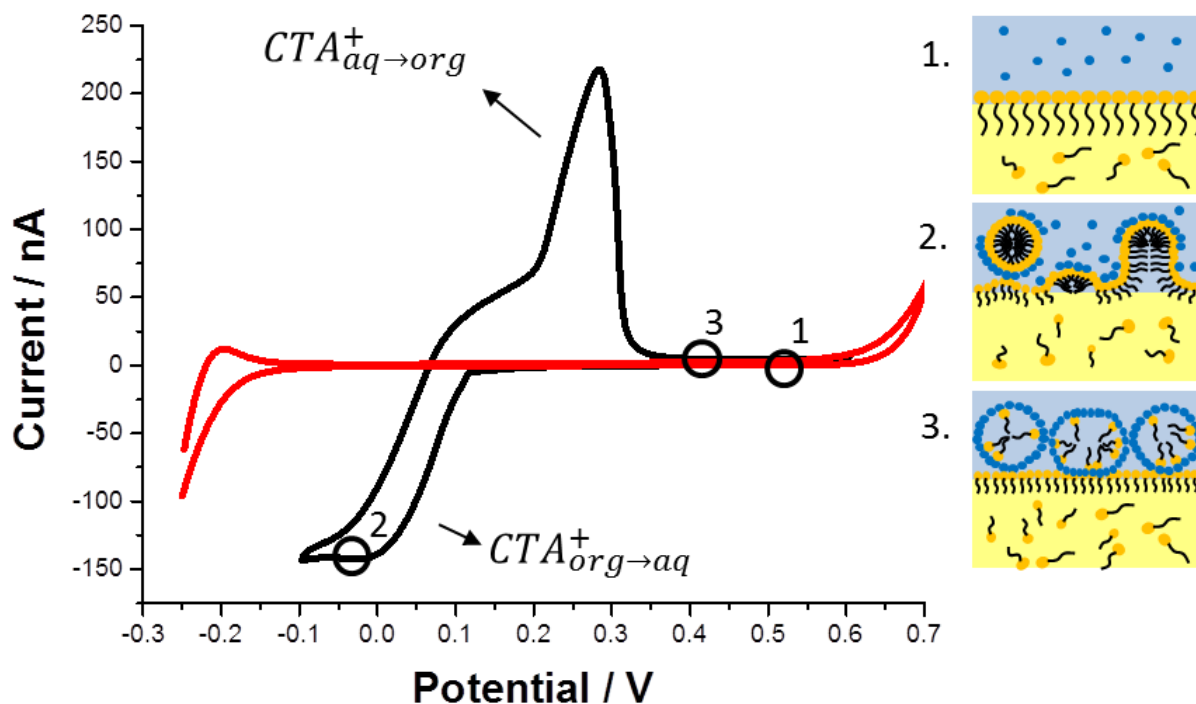


Figure 4.1. Typical cyclic voltammogram recorded during the formation of silica deposit. The microITIES membrane was design number 3. The CV was recorded in cell 1 (black line) for $[TEOS]_{aq} = 50$ mM and $[CTA^+]_{org} = 14$ mM. A blank cyclic voltammogram was recorded in cell 1 (red line), without TEOS and CTA^+ . The schemes on the right illustrates the different stages of the silica deposition: 1. Formation of the monolayer at the beginning of polarization; 2. Transfer of $CTA_{org \rightarrow aq}^+$ followed by micelles formation and silica condensation; 3. Partial backward transfer of CTA^+ to the organic phase and silica deposition.

The information extracted from the shape of a reverse peak confirms the participation of the CTA^+ species in the silica material formation on the aqueous side of the liquid – liquid interface and has indicated that the back transfer is not a diffusion-limited process. After one cycle, the array of microITIES is completely covered with the silica material as it is shown on **scheme 3** on **Figure 4.1**.

4.1.1.1. Factors affecting silica deposition at the array of microITIES

In the following part the influence of the parameters such as: (i) template and precursor initial concentrations, (ii) the time scale of the experiments – i.e. scan rate influence – and (iii) the different geometries of array of the micropores supporting the liquid – liquid interface on the silica material deposition are discussed.

4.1.1.1.1. Influence of $[CTA^+]_{org}$ and $[TEOS]_{aq}$

The silica deposits are being formed only when CTA^+ is transferred from the organic to the aqueous phase containing silica precursor – hydrolyzed TEOS. It is not surprising that composition of both contacting phases is likely to affect the deposition process. CVs recorded during interfacial silica material formation for $[TEOS]_{aq} = 50$ mM and $[CTA^+]_{org} = x$ mM where $1.5 \text{ mM} \leq x \leq 14 \text{ mM}$ can be found on **Figure 4.2 A**. When $[CTA^+]_{org}$ was kept constant (14 mM) and $[TEOS]_{aq}$ was increased from 50 mM up to 300 mM, CVs shown on **Figure 4.2 B** were recorded. To study the influence of $[CTA^+]_{org}$ and $[TEOS]_{aq}$, the deposition conditions were chosen in such a way that each pore was independent of each other. The membrane design number 3 (see **Table 2.2**) (100 μm center-to-center distance was enough to avoid the overlap of radial diffusion layer) and moderate scan rate (5 mV/s) were employed for this purpose. When $[TEOS]_{aq}$ was kept constant and $[CTA^+]_{org}$ was increased from 1.5 mM up to 14 mM the linear increase of the negative peak current was observed – arising from $CTA^+_{org \rightarrow aq}$ (as it is shown in insert of **Figure 4.2 A**). This reaction is the rate-determining step. The characteristics of the positive peaks are different. Faradaic current associated with the CTA^+ back transfer has grown up to $[CTA^+]_{org} = 5$ mM and level off for higher concentrations (see **Figure 4.2 A**). Such behavior can be explained in the following manner: the formation of silica deposits assisted by surfactant template for low $[CTA^+]_{org}$ has involved most of the CTA^+ species transferred to the aqueous phase and hence low current recorded during backward transfer was expected. Higher $[CTA^+]_{org}$ has resulted in much thicker silica deposit formation, which acts as a physical barrier

for the CTA^+ returning to the aqueous phase. When $[CTA^+]_{org}$ was kept constant and $[TEOS]_{aq}$ was increased from 50 mM up to 300 mM no significant changes in the current response and the shape of CVs were observed. The only difference was a shift in the potential transfer of $CTA^+_{org \rightarrow aq}$ towards more positive values (100 mV) for higher $[TEOS]_{aq}$. This was not surprising since the concentration of the negatively charged hydrolyzed TEOS species in the aqueous phase was increased by a factor of 6, which promotes the transfer of $CTA^+_{org \rightarrow aq}$ at higher potential values.

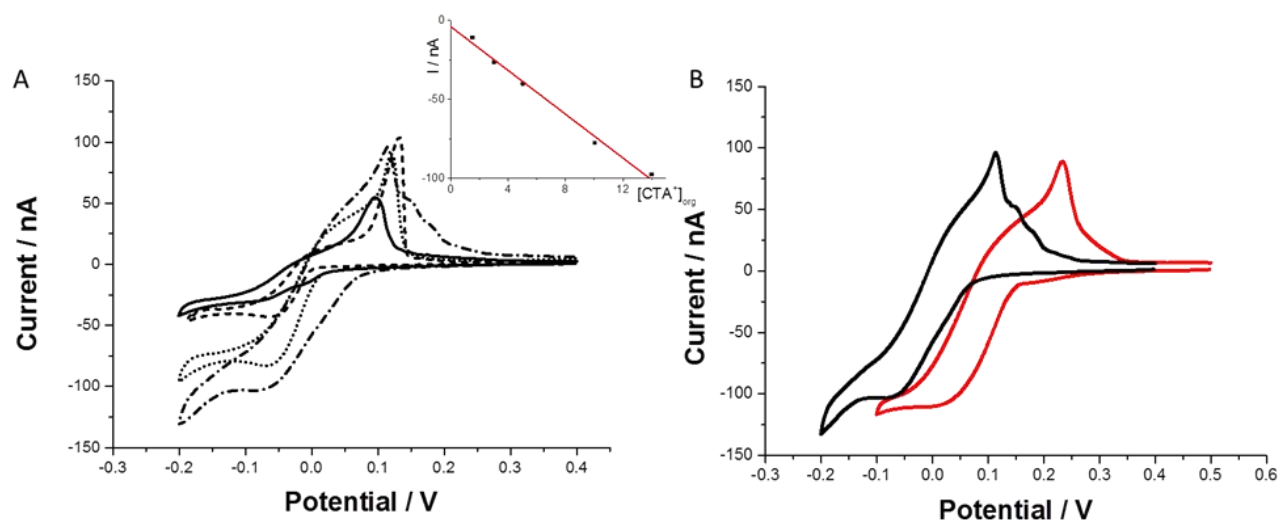


Figure 4.2. A – Cyclic voltammograms recorded during silica deposits formation for $[TEOS] = 50$ mM and $[CTA^+] = 3$ mM (solid line), 5 mM (dashed line), 10 mM (dotted line) and 14 mM (dash - dot line). Linear dependency of the negative peak current versus CTA^+ concentration for the constant $[TEOS]_{aq}$ can be found as an insert. B – Cyclic voltammograms recorded for $[CTA^+] = 14$ mM and $[TEOS]_{aq} = 50$ mM (black curve) and 300 mM (red curve). microITIES membrane design was number 3. Scan rate in all cases was 5 mV/s.

These findings indicate that the $[CTA^+]_{org}$ is the limiting factor for the silica deposits formation reaction and $[TEOS]_{aq}$ has no influence on the reaction rate (in contrary to the mesoporous silica films at the solid electrodes derived from the surfactant assisted Sol-Gel process of silica).^{97,98}

4.1.1.1.2. Influence of the pore center-to-center distance

For the micro electrode arrays or the microITIES arrays the shape of the current – potential curves and the limiting currents are highly affected by the center-to-center distance (noted as spacing factor, S) between two micro electrodes or microITIES. Change in the spacing factor allows the control of the planar and radial diffusion contributions affecting the mass transfer of the ions. Davies and Compton⁸⁴ have divided microdisc arrays into four main groups based on their geometrical size with respect to the size of diffusion zones: (i) $\delta < r$, $\delta < S$; (ii) $\delta > r$, $\delta < S/2$; (iii) $\delta > r$, $\delta > S/2$ and (iv) $\delta > r$, $\delta \gg S$, where r is the pore radius, δ is the diffusion zone radius and S is the pore center to center distance (see

Figure 4.3 for schemes with corresponding designations for the array of microITIES). For each group, they have proposed voltamperometric current response characteristics for a charge transfer reaction,: (i) linear diffusion leading to clear peak, (ii) radial diffusion leading to steady state wave, (iii) slight overlap of the diffusion profiles leading to a slight peak to clear peak and (iv) total overlap of the diffusion profiles giving a clear peak, from which only group (ii) does not follow scan rate dependency.⁸⁴

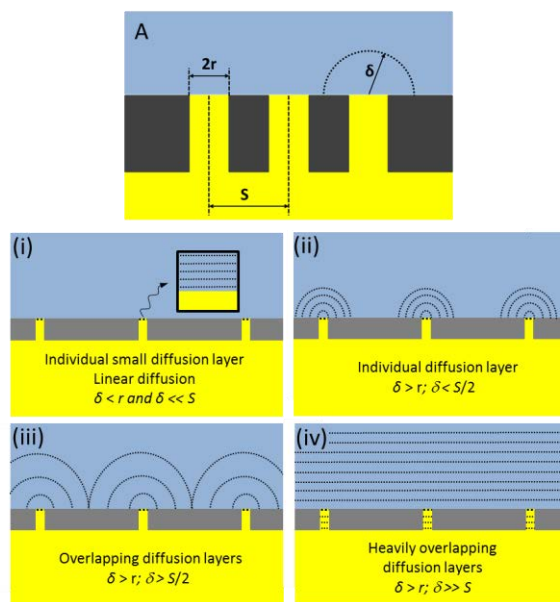


Figure 4.3. Schematic representation of microITIES arrays with different diffusion zones. Scheme A shows the geometrical parameters of the membrane supporting microITIES: r – is the pore radius, S – is the pore center-to-center distance or in other words spacing factor and δ – is the diffusion layer thickness.

Schemes from (i) to (iv) are different groups of the microITIES arrays divided with respect to the size of diffusion zones.

The terminology proposed by Compton and Davis can be applied to describe the results obtained during silica deposits formation at an array of microITIES supported with different membranes (design number 1, 2, 3 and 4 were used – see **Table 2.2**) with constant pore radius ($r = 5 \mu\text{m}$) but various spacing factor ($20 \mu\text{m} \leq S \leq 200 \mu\text{m}$). The schemes on

Figure 4.3 show diffusion layer profiles from the aqueous side of the liquid – liquid interface but they can be also applied by analogy for the organic side of the liquid – liquid interface. On **Figure 4.4** the CVs curves have been presented as current density *versus* potential in order to take into account the fact that the number of pores within the array supporting microITIES, consequently their total surface area, varies for each design.

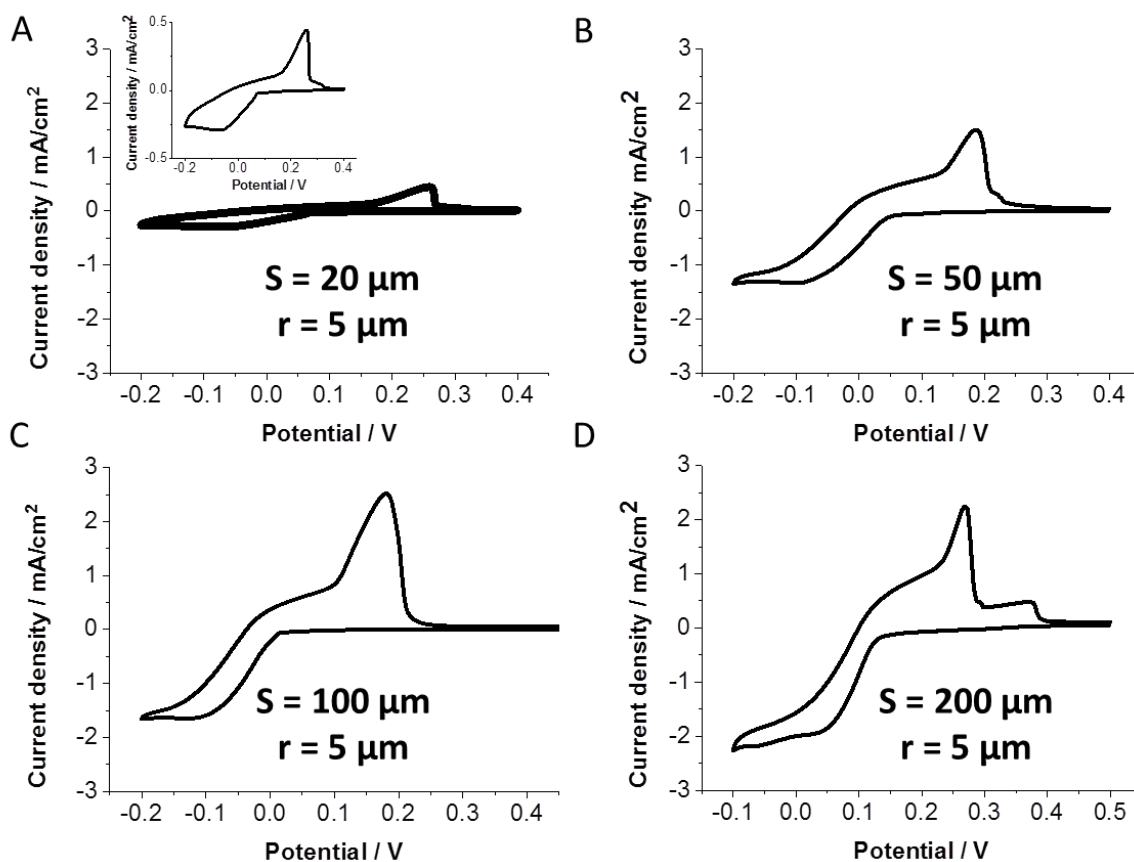


Figure 4.4. Variations of current density in function of the applied potential recorded during silica deposits formation at the membranes supporting the array of microITIES with different spacing factors

(indicated as S on each graph). Membrane design numbers were A – 1, B – 2, C – 3 and D – 4. Potential scan rate was 5 mV/s in all cases. $[\text{CTA}^+]_{\text{org}} = 14 \text{ mM}$; $[\text{TEOS}]_{\text{aq}} = 50 \text{ mM}$.

The increase in spacing from 20 μm (**Figure 4.4 A**) up to 200 μm (**Figure 4.4 B**) has led to dramatic increase in the current densities along with significant change in the shape of the negative peak response, shifting from peak-like (**Figure 4.4 A**) to wave-shaped (**Figure 4.4 C and D**). Change in the peak shape can be ascribed to distinct diffusional regimes. Using the nomenclature proposed by Compton and Davis⁸⁴ and based on shapes of current density – potential curves, one can attribute membrane number 1 to group (iii) or (iv), whereas membrane number 3 belongs probably to the borderline between group (ii) and (iii). Since the low spacing factor was manifested by slight peak, the condition $\delta > S/2$ has to be met. On the contrary, the steady-state wave has indicated that $\delta < S$ in case of high spacing factor. The current density – potential curve recorded at the membrane design number 2 gave rise to a wave with a slight-peak on the forward signal, which means that δ was still larger than half of the pore center-to-center distance (see **Figure 4.4 B**). Due to high spacing factor, the CV response (on the forward scan) recorded at the membrane design number 4 (**Figure 4.4 D**) – steady-state wave as $S \gg \delta$ – was similar with the membrane design number 3 (see **Figure 4.4 C**). The unaffected shape of the backward peak on scan reversal has indicated a non-diffusion limited process since its shape was not affected by the diffusion regimes. Moreover, for lower spacing factor, the larger current densities have been observed due to enhanced mass transfer governed by a radial diffusion (i.e., as also observed for arrays of ultramicroelectrodes)^{209,210} whereas almost total overlap (for the membrane design number 1 where the pore center-to-center distances is of the same order of magnitude as the pore size) has led to the linear diffusion profile on the organic side of the ITIES and as a result has lowered the ion flux crossing the interface (**Figure 4.4 A**). Occasionally some deviations from the current characteristics of the positive peak (after abrupt drop in current) were observed (clearly visible on **Figure 4.4 D**). This was most probably due to entrapped CTA^+ species, with a higher energy required for back transfer to the organic phase.

4.1.1.1.3. Influence of the scan rate

Figure 4.5 A illustrates the influence of the scan rate on the current-potential curves recorded during interfacial silica deposition at the membrane design number 3. Both the current intensity and the shape of CV curves were found to vary, with negative peak evolving from slight

peak to wave and to bigger peak when increasing the potential scan rate. These observations can be rationalized by analyzing the diffusion layer profile for each case. A prerequisite is to know the diffusion coefficient of the transferring species (i.e., CTA^+). Apparently, this value is not available but one can reasonably get an estimation of it from the literature data available for the closely related octadecyltrimethylammonium chloride (ODTM) compound (only 2 more CH_2 moieties in the alkyl chain with respect to CTA^+). The diffusion coefficient in the aqueous phase for ODTM was found to be around $0.66 \times 10^{-6} \text{ cm}^2 \text{ s}^{-1}$ as determined by pulse gradient spin-echo NMR.²¹¹ Taking into account the difference in alkyl chain length between ODTM and CTA^+ – two carbon atoms – and the change in medium viscosity – from 1.002 cP (at 20°C)²¹² for aqueous phase to 0.85 cP (at 20°C)²¹² for DCE – then one would expect D_{CTA^+} to be slightly higher than D_{ODTM} . Consequently, a D_{CTA^+} value is expected to be around reasonable value of $1 \times 10^{-6} \text{ cm}^2 \text{ s}^{-1}$. From such D_{CTA^+} value, one can estimate the diffusion layer thickness at various scan rates on the basis of the following equation:

$$\delta = \sqrt{2D_{\text{CTA}^+} t} \quad (3.1)$$

The estimated thicknesses of diffusion layers of CTA^+ for each scan rate are thus roughly: 630 μm for 0.1 mV/s, 200 μm for 1 mV/s, 90 μm for 5 mV/s, and 63 μm for 10 mV/s. The diffusion layer from the organic side of the liquid – liquid interface can be considered as:

$$\delta = \delta_l + \delta_{nl} \quad (3.2)$$

where δ_l is the linear diffusion inside the pores of the membrane and δ_{nl} correspond to diffusion zone on the pore ingress from the organic side. For the highest scan rate – 10 mV/s – the diffusion layer thickness, δ_l , is less than the membrane thickness – $d = 100 \mu\text{m}$ – (**see scheme (i) on Figure 4.5**) and hence the transfer inside the pore was limited only by linear diffusion (resulting in peak like response). In this case, not enough CTA^+ species were transferred from the organic to the aqueous phase and no silica deposit formation was observed (verified with the profilometry based on shear force measurements). Consequently, all CTA^+ species transferred to the aqueous phase on the forward scan were transferred back to the organic medium on scan reversal, as supported by forward and reverse charge transfer of similar magnitude (**see Figure**

4.6). Decreasing potential scan rates down to 5 and 1 mV/s has led to diffusion layer thicknesses increasing from almost equal (i.e., 90 μm for 5 mV/s) to much larger (i.e., 200 μm for 1 mV/s) than the membrane thickness, leading to sigmoidal-shaped current responses on forward scan (yet with an additional residual and very slight peak at 5 mV/s). The origin of such wave is due to the prolongation in diffusion layers profiles (forming hemispherical diffusion zones at the pores entrance from the organic side of the interface due to fulfillment of $S/2 > \delta_{nl}$ condition, see schemes (ii) on **Figure 4.5**). In addition, the local changes in the interfacial properties as a result of growing silica deposit also play a role in the evolution of CV curves, as one can expect some additional resistance to mass transport through the interface in the presence of a silica deposit. This is notably the case of 1 mV/s scan rate (see scheme (iii) on **Figure 4.5**) for which long

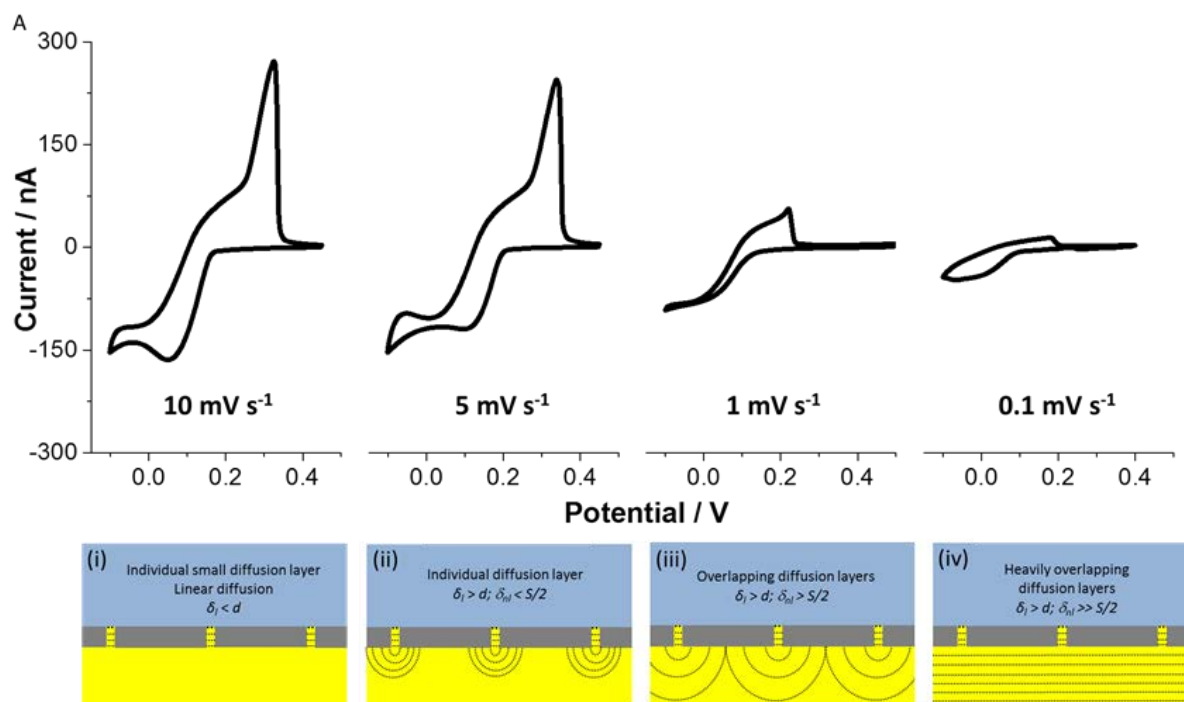


Figure 4.5. A - Cyclic voltammograms recorded in the presence of $[\text{CTA}^+]_{\text{org}} = 14 \text{ mM}$ and $[\text{TEOS}]_{\text{aq}} = 50 \text{ mM}$ at various scan rates at the microITIES design number 3. Schemes on the bottom of the figure correspond to diffusion layer profiles proposed for each scan rate: B – 0.1 mV/s; C – 1 mV/s; D – 5 mV/s and E – 10 mV/s. δ_l – is the diffusion layer thickness inside the pore, δ_{nl} – is the diffusion layer thickness outside the pores in the organic phase, d – is the pore diameter and S – is the spacing factor (100 μm). Pore radius (r) was 5 μm .

experimental times would cause an increase in δ_{nl} exceeding half of the pore center-to-center distance ($S/2$) on the basis of the estimated δ value (i.e., 200 μm in this case), leading to the overlap of radial diffusion zones, which should have a peak-like response. The fact that it is not happening here and that a sigmoidal response was obtained is attributed to the restricted transfer of CTA^+ across the interfacial synthesized silica material (apparent diffusion values for the overall process have to be lower than those in solution at an unmodified liquid-liquid interface). Actually, much longer experimental times were necessary (for instance, that corresponding to a potential scan rate as low as 0.1 mV/s) to get conditions of total diffusion overlap (see scheme (iv) on **Figure 4.5**).

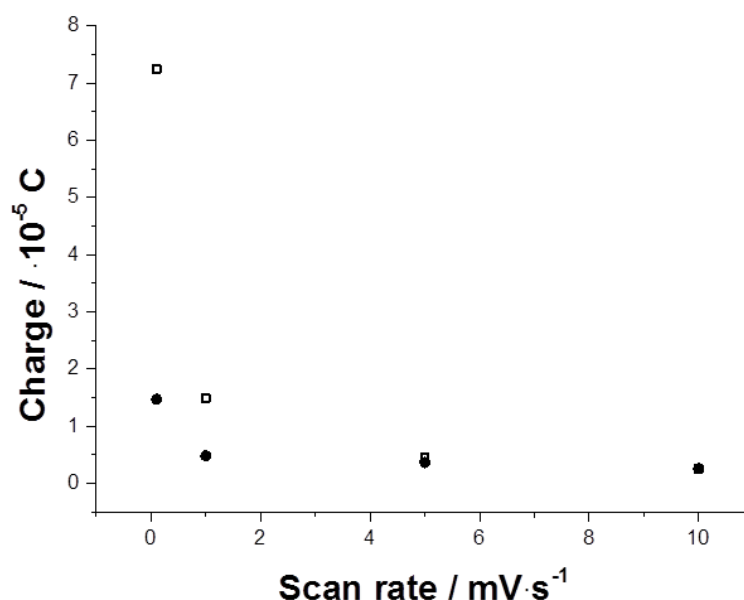


Figure 4.6. The charge for forward (empty squares) and reverse (filled circles) processes recorded during silica deposits formation versus scan rate.

In this case, the $\text{CTA}_{org\rightarrow aq}^+$ transfer was limited by linear diffusion below the pores, which becomes the limiting factor, leading to a peak-shaped voltammogram. The large difference between the charge passed through the microITIES during forward and reverse scan indicates that a significant part of CTA^+ species transferred to the aqueous phase has been involved in the formation of silica deposits, as trapped inside the mesostructure, and thus are no longer available for back transfer to the organic phase on scan reversal (see **Figure 4.6**).

4.1.2. Morphological study

The morphology of the silica deposits generated at arrays of microITIES under various conditions was analyzed by SEM and profilometry (based on shearing force measurement). Micrographs and profilometry images concern deposits generated using the same composition of solutions ($[\text{TEOS}]_{\text{aq}} = 50 \text{ mM}$ and $[\text{CTA}^+]_{\text{org}} = 14 \text{ mM}$), but different supporting silicon membranes and distinct deposition conditions (potential scan rates and number of cycles as well as the deposition method). The data are presented in **Figure 4.7** under the form of side views of single pore (row a) and pore arrays (row b), and mapping profilometry (row c). The first observation is that the silica deposits are always formed on the aqueous side of the liquid–liquid interface. A second point is the good quality of the deposits, which have been formed uniformly on all pores, and their crack-free appearance after surfactant removal (images were recorded after calcination at 400°C) suggests a good mechanical stability. When using the same support (microITIES number 2), keeping constant the scan rate (5 mV/s), but increasing the number of cycles from half scan (first column) to 3 scans (second column), one can notice an increase in both the deposit height (from $1.7 \mu\text{m}$ to $3.4 \mu\text{m}$) and the deposit diameter (from $14 \mu\text{m}$ to $15.7 \mu\text{m}$). Also, there was no significant difference in the deposit diameter between samples prepared from half and whole potential cycle, showing only an increase in the deposit height from $1.7 \mu\text{m}$ up to $2.7 \mu\text{m}$, consistent with the lengthened duration of more negative potentials application. All these results have confirmed that the electrochemically-induced $\text{CTA}^+_{\text{org} \rightarrow \text{aq}}$ transfer was indeed at the origin of the surfactant-templated silica self-assembly process. However, the deposit height growth was not directly proportional to the number of CV cycles, most probably due to increased resistance to $\text{CTA}^+_{\text{org} \rightarrow \text{aq}}$ transfer in the presence of much thicker deposits. A more effective way to get massive silica material deposition at the microITIES was to slow down the potential scan rate (which also requires the use of a silicon membrane with larger pore spacing to avoid overlap of the radial diffusion profiles). This is shown on part 3 of **Figure 4.7** for the modification of membrane design number 3 by one scan at 0.1 mV/s , leading to much thicker deposits ($13.1 \mu\text{m}$ in height and $33.1 \mu\text{m}$ in diameter). Since the generated deposits were massive as compared with

other experiments, they were likely to be more affected by calcination and can suffer from some losses (see, e.g., one deposit missing on the bottom left of part 3b on **Figure 4.7**).

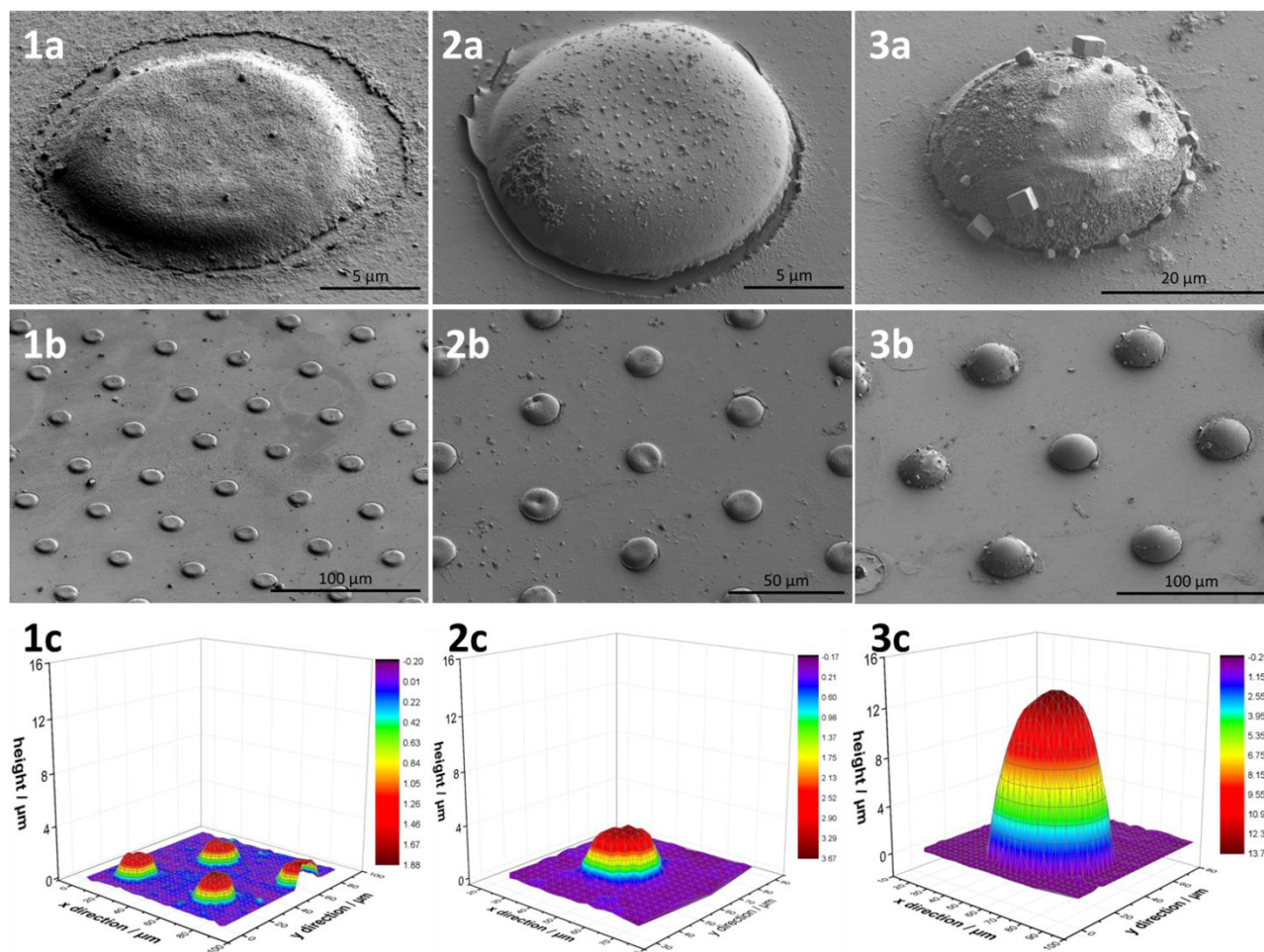


Figure 4.7. SEM micrographs and 3D profilometry mapping based on shear force measurements obtained for various microITIES membranes modified with silica deposits. The rows correspond to three different points of views: (a) side view on single pore recorded by SEM, (b) side view on array of modified interfaces recorded by SEM and (c) modified interface mapping made by profilometry. The columns divide the images depending on synthesis initial conditions: (1) deposits prepared by one linear scan voltammetry (half CV scan) at 5 mV/s using microITIES number 2; (2) deposits prepared by three successive CV scans at 5 mV/s using microITIES number 2; and (3) deposits prepared by one CV scan at 0.1 mV/s using microITIES number 3. Polarization direction was always from anodic to cathodic potential direction.

Another way to control the generation of silica deposits was the use of constant-potential amperometry (i.e., chronoamperometry) instead of linear sweep or cyclic voltammetry. Too short experiment times (5-10 s) did not lead to any silica material formation. Then, the amount of deposited material was found, as expected, to increase with the potentiostatic step duration (for

example 50 s deposition time led to deposits with 3.7 μm in height and 14.9 μm in diameter), while extending the electrosynthesis up to 200 s enabled the formation of massive deposits, with 8.4 μm in height and 18.6 μm in diameter. As for deposits prepared by cyclic voltammetry, their shape was also found to change from rather flat to hemispherical when increasing the charge passing across the interface contributing thereby to larger amounts of silica material deposited at the microITIES. Finally, the variation in shape of the silica deposits resembles to an image of the evolution of the diffusion layer profiles (on the aqueous side of the interface): short deposition times corresponds to mainly linear diffusion limitations, yet with some radial contribution at the macropore edges, while longer experiments are governed by radial diffusion control. This is quantitatively illustrated on **Figure 4.8** where the deposit height, h , was plotted as function of the difference between deposit and pore radii, $r_d - r_p$. At the beginning of the deposition process $h \approx r_d - r_p$, corresponding to a rather flat morphology, while subsequent growing has led to more hemispherical shape with h values likely to rise up to $2 \times (r_d - r_p)$. Finally, more massive deposits were characterized by preferential lateral growth ($h < 2 \times (r_d - r_p)$). On the other hand, it is also possible that the liquid – liquid micro-interfaces displacement under charge transfer,²¹³ which could affect the deposit internal geometry, seems to be minimal here. SEM images for detached membranes (see **Figure 4.9 A and B**) indeed suggest that the silica deposits are filled inside and rather flat at the bottom.

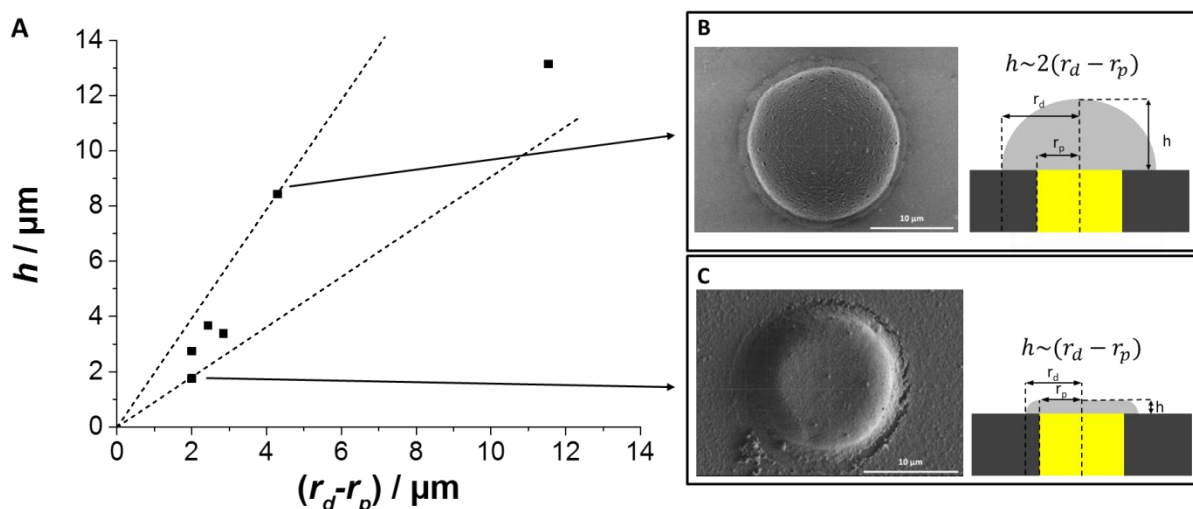


Figure 4.8. A - Deposit height versus the difference between deposit and pore radii for materials prepared either by cyclic voltammetry or chronoamperometry. The schemes on the right (SEM micrographs and corresponding drawings) correspond to two ‘extreme’ cases indicated with the

arrows. B – correspond to the silica deposits prepared with chronoamperometry ($E = -0.15$ V, $t = 200$ s, membrane design number 4) and C – correspond to the silica deposits prepared by cyclic voltammetry (5 mV/s, half cycle, membrane design number 3).

Another point, yet minor, to mention from the morphological analysis is the presence of cubic spheres on some silica deposits (see, e.g., image 3a on Figure 4.7), which are the sodium chloride crystals arising from residual background electrolyte back transfer from organic to aqueous phase. This phenomenon is similar to that reported by Silver *et al.*²¹⁴, on the basis of protein crystallization experiments at liquid – liquid interfaces. This means that the electro-assisted generation of silica material could be also suitable to the entrapment of proteins in the silica matrix (sol-gel silica is indeed known to enable encapsulation of proteins)²¹⁵ as an effective way to immobilize biomolecules at liquid – liquid interfaces. Finally, a very thin additional silica layer covering the whole silicon membrane (including silica deposits) can be also evidenced from SEM pictures (see micrographs 1a and 2a in Figure 4.7). This arises most probably from some evaporation induced condensation of TEOS and silica deposition even if each electrosynthesis experiment was followed by careful rinsing with distilled water.

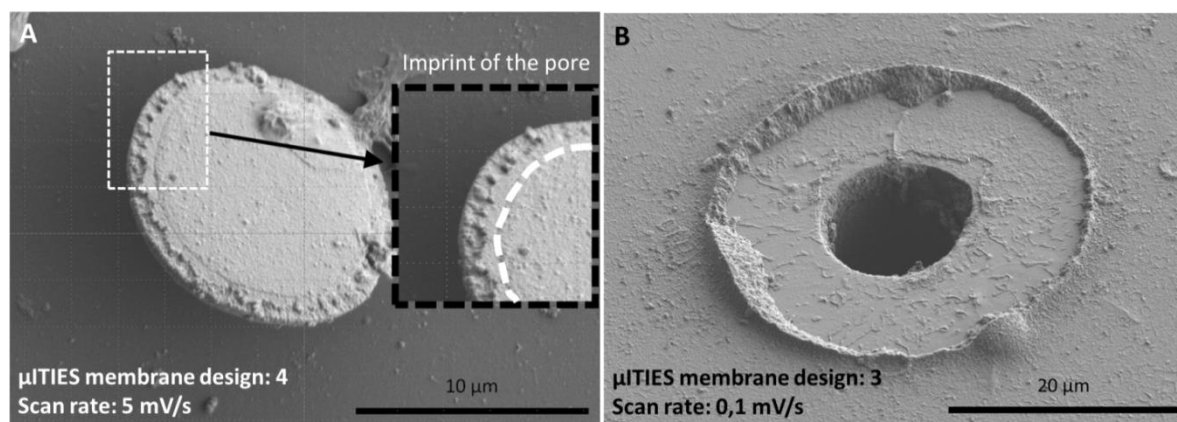


Figure 4.9. A – SEM image of the silica deposit turned upside down. Inset shows the zoom of the deposit with the dashed white line indicating the imprint of the pore supporting the liquid – liquid interface. B – is the SEM micrograph for the pore from which the silica deposit has been removed. In both cases the silica deposition was performed with one cyclic voltammetry cycle for $[CTA^+]_{org} = 14$ mM and $[TEOS]_{aq} = 50$ mM. Membrane design and the scan rate are indicated on the micrographs.

The ‘worm like’ shape of the pores among the silica deposits generated at the macrosopic liquid – liquid interface (confirmed by TEM and SAXS) were also found to present in the silica deposits at the microITIES as it is shown with TEM micrographs on the **Figure 4.10**.

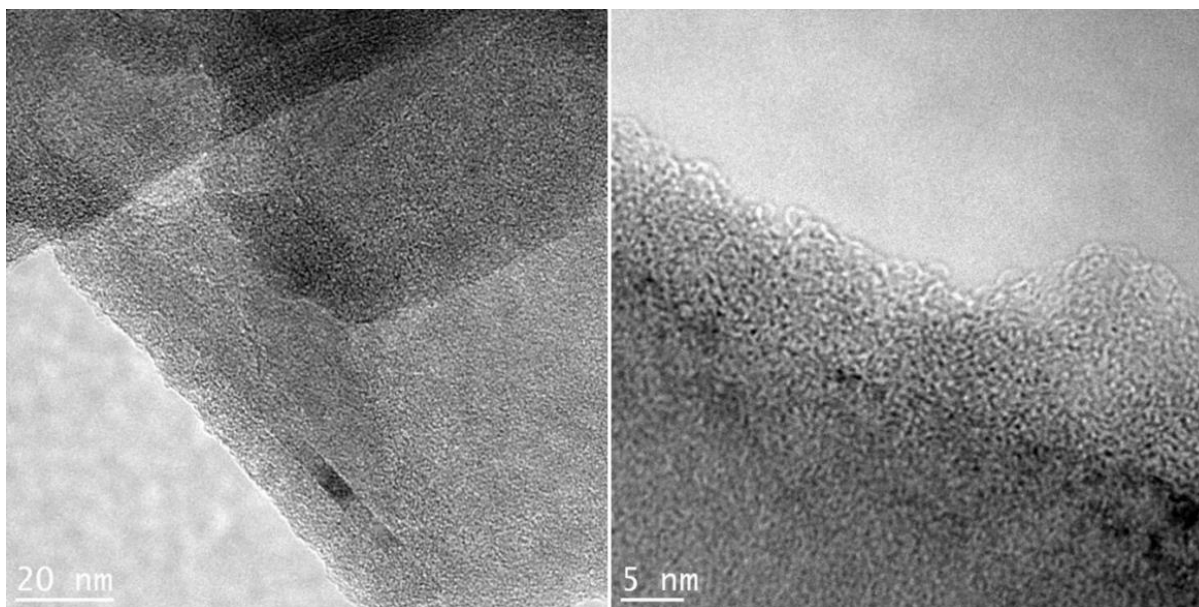


Figure 4.10. The TEM micrographs for the silica deposits electrogenerated for $[CTA^+]_{org} = 14$ mM and $[TEOS]_{aq} = 50$ mM. The scan rate was 5 mV/s. Deposition was performed at membrane design number 4 with one cycle.

4.1.3. Spectroscopic and electrochemical characterization of deposits

Confocal Raman spectroscopy was first used to evidence the formation of a silica network at microITIES. It has been performed after thermal treatment of the deposits (24h storage at 130°C followed by 30 min at 400°C) to be able to detect the characteristic vibrational modes of silica without being disturbed by large signals arising from the organic matter expected to be present in the same spectral region (see **Figure 4.11**). In addition to the narrow and intense band at 520 cm^{-1} due to the vibration mode characteristic of the silicon wafer support, one can notice a broad band from 375 cm^{-1} to 500 cm^{-1} attributed to the Si–O–Si vibrational mode, and a single band at 710 cm^{-1} suggesting the presence of terminal Si–OH groups. This strongly supports the formation of silica.

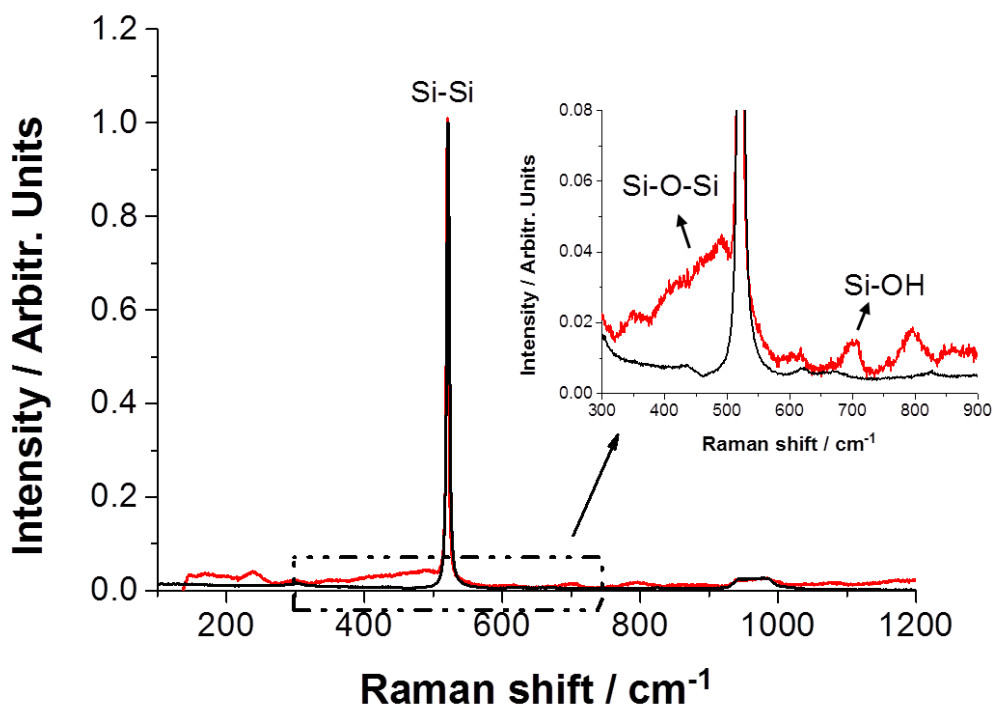


Figure 4.11. Raman spectra for silicon membrane (black line) and silica deposit after calcination (red line). The enlargement of the spectra in the 300 – 800 cm⁻¹ region corresponds to the frequencies of vibration of silica bonds. Spectra were normalized to the Si-Si peak.

Raman spectroscopy can be also used to characterize the organic species that have been incorporated into the silica material during formation of the deposits, as well as to check the effectiveness of their removal upon calcination. This is shown on **Figure 4.12 B**, where the broad and intense signal located in the region 2760 – 3020 cm⁻¹ region, corresponding to the –CH₂– stretching mode of the long alkyl chain of CTA⁺ species,²¹⁶ confirms the presence of the surfactant template in the material. This signal disappears almost completely after heat treatment, indicating the successful calcination of the organic template. From **Figure 4.12 B**, one can also notice a broad signal of weak intensity at 3060 cm⁻¹, which can be ascribed to the C-H stretching mode of aromatic rings, which are present in the organic electrolyte (BTPPA⁺TPBCl⁻), suggesting that some of these cations have been co-encapsulated in the silica material in addition to the surfactant template. This is best shown on **Figure 4.12 A**, where the typical signature of BTPPA⁺TPBCl⁻ is seen via the bands located in the 600 to 1800 cm⁻¹ region²¹⁷ (for instance the

peak at around 1000 cm^{-1} is due to the vibration of the aromatic rings).²⁰³ After calcination, all these bands disappeared, which indicates the complete removal of this organic electrolyte from the deposits. One can also notice from **Figure 4.12 A** two broad peaks of weak intensity in the region from 1250 to 1750 cm^{-1} , which appeared upon calcination, representing actually the D and G bands of traces of amorphous carbon arising from thermal decomposition of the organic molecules.²¹⁸ These results support that the mesopore channels have been liberated from most of their organic content, even if the quantitative analysis of the porosity by the classical gas adsorption method was not possible due to the too low amount of available material (too small deposits).

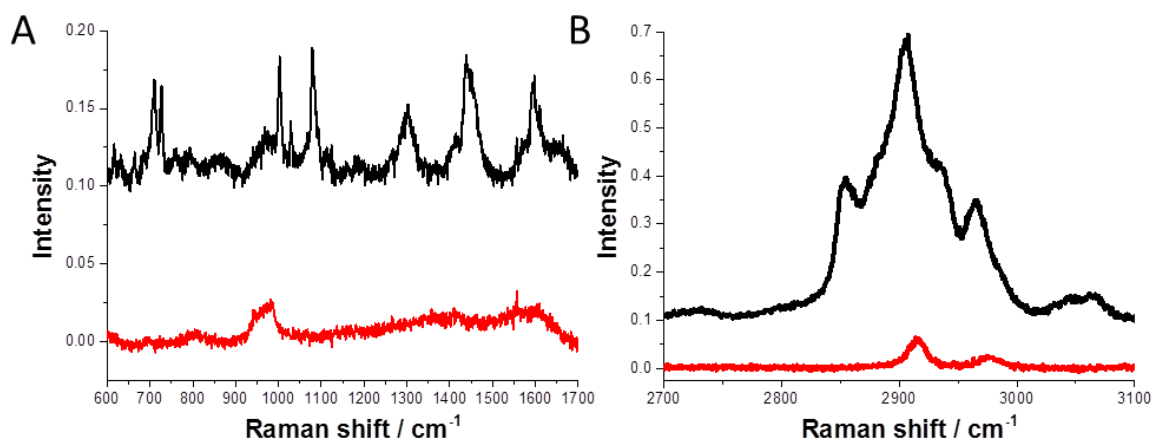


Figure 4.12. Two different vibrational ranges of RAMAN spectra recorded for silica deposit before (black curve) and after (red curve) calcination.

The effect of calcination was observed with ion transfer voltammetry (see **Figure 4.13**). Silica deposits employed here were obtained by CV for the following conditions: $[\text{TEOS}]_{\text{aq}} = 50\text{ mM}$; $[\text{CTA}^+]_{\text{org}} = 14\text{ mM}$; potential scan rate 5 mV/s ; 2 subsequent cycles at the membrane design number 3, and then, calcinated at 400°C after 24h storage at 130°C . The blank CV recorded only in the presence of supporting electrolytes before calcination (**Figure 4.13 A – black curve**) is characterized by a high capacitive contribution, which is significantly lower after heat treatment (**Figure 4.13 B – red curve**), suggesting an effective removal of organic species from the silica material. This is also evidenced by the appearance of a broad signal in the region

of $Cl_{aq \rightarrow org}^-$,²¹⁹ indicating possible interfacial transfer of the residual products of organic species decomposition.

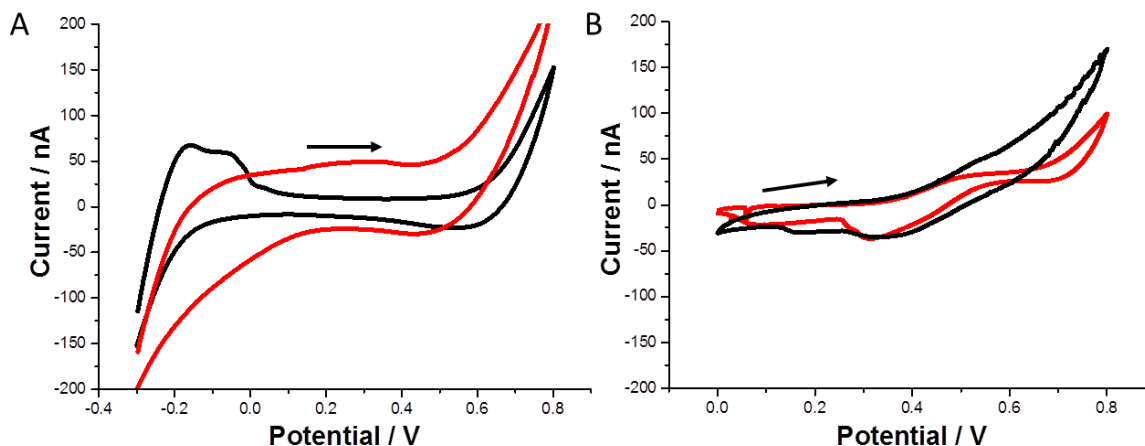


Figure 4.13. A – blank cyclic voltammograms and B – voltammetric transfer of $[TMA^+]_{aq} = 70.9 \mu M$ before (red line) and after (black line) calcination. microITIES membrane design number was 3. Silica deposits were electrogenerated by CV (2 cycles at 5 mV s^{-1} , $[CTA^+] = 14 \text{ mM}$ and $[TEOS] = 300 \text{ mM}$).

In order to better evaluate the permeability of μ ITIES modified with silica deposits before and after calcination, a model interfacial active cation was employed. The transfer of $TMA^+_{aq \rightarrow org}$ through the microITIES modified with the silica deposits was clearly observed after removal of the surfactant template (**Figure 4.13 B – red curve**), confirming good permeability of the mesoporous silica deposits, whereas negligible transfer (possible hindering effect of capacitive current cannot be excluded) occurred before calcination (**Figure 4.13 B – black curve**). The corresponding CV curve was characterized by a sigmoidal wave when transferring from the aqueous to the organic phase and a peak-like response on scan reversal (due to the restricted amount of TMA^+ for back transfer). The absence of significant $TMA^+_{aq \rightarrow org}$ transfer prior to template removal also confirms the good quality of the deposits and the fact that all – or the greatest part of – the macropores of the silicon membrane have been successfully modified with the silica deposits.

4.1.4. Conclusion

Miniaturized liquid – liquid interface supported by an array of micropores can be easily modified with the mesoporous silica deposits with the surfactant assisted Sol-Gel process of silica. The experimental time scale – i.e. scan rate – was shown to have a great effect on the voltammetric characteristics recorded during deposition as well as on the shape of the silica deposits, which tend to grow towards the bulk of the aqueous phase taking the shape of the diffusion layer profile of CTA^+ on the aqueous side of the liquid – liquid interface. The spacing factor between two neighboring pores in the different microITIES geometrical arrays was also shown to affect deposition process. The rate limiting properties of CTA^+ found at macroscopic ITIES were also confirmed with miniaturized system. With TEM the mesoporous character of the silica was confirmed. The effect of calcination – removal of organic species blocking the interior of the pores – was followed by confocal Raman spectroscopy and ion transfer voltammetry of TMA^+ . The system optimized in this section can be used for further evaluation in electroanalysis as it will be shown in **section 4.4** of following chapter. The results for this section can be also found in **Langmuir**, 2014, **30**, 11453 – 11463.

4.2. *In situ* confocal Raman spectroscopy study of interfacial silica deposition at microITIES

In general, electrochemistry at the ITIES allows the estimation of thermodynamic, kinetic and charge transfer parameters, but precise quantitative information about the interfacial region has to be supported by other methods, especially when very precise molecular information of the system is required. Spectroscopic methods (both linear and non-linear techniques) can be coupled to electrochemistry at the ITIES.²²⁰ At the liquid – liquid interface the biggest difficulty is the separation of the signal originating from the bulk from the signal originating from the interfacial region. This can be overcome by fulfilling the condition of total internal reflection.²²⁰ The first studies of interfacial processes by spectroelectrochemistry were made using linear techniques, which include UV-visible volt- and chronoabsorptiometry,^{221,222,223} volt- and chronofluorimetry^{224,225} or reflectance spectroscopy.²²⁶ In contrast, non-linear techniques (sum frequency spectroscopy and second harmonic generation) have provided information about the molecular structure of the liquid – liquid interface as they are surface specific.¹⁹ Confocal Raman microspectrometer can also be used to focus the analysis at the interface and provide useful interfacial information. A Raman spectroscopy with a spatial resolution of 0.5–1 mm has been used to investigate electron transfer reaction at solid microelectrode arrays.^{227,228} Raman spectroscopy has also been used for the characterization of reactions occurring at the neat liquid – liquid interface.^{217,229,230,231,232,233} Interfacial reaction²²⁹ or metallic nanoparticle self-assembly^{230,231,232,217} at the liquid–liquid interface were also reported to be monitored by Raman spectroscopy. However, the investigation of reactions at the liquid–liquid interface controlled by electrochemical means has scarcely been studied. Indeed, it was only recently that surface enhanced Raman scattering was used to study the potential dependent agglomeration of silver nanoparticles at the water – 1,2-dichloroethane (DCE) interface.²¹⁷ More recently, the interfacial transfer of ferriox ion and heterogeneous electron transfer between dimethylferrocene (from the organic phase) and hexacyanoferrate (II/III) anions (from the aqueous phase) were followed by confocal Raman spectroscopy.²³⁴ The electrodeposition of gold nanoparticles formed at a three-phase junction was also investigated by surface enhanced Raman spectroscopy.¹¹¹

In the present work, an experimental set-up was developed to couple electrochemical measurements at the ITIES with Raman confocal microscopy. The association of electrochemistry and Raman techniques at microscopic liquid – liquid interfaces allows the collection of complementary data for the mechanism involved in the electrochemically assisted generation of surfactant-templated silica material at such interfaces. The incident laser was focused on both macroscopic and microscopic interfaces to allow the recording of Raman spectra at open circuit potential and upon application of interfacial potential differences. Finally, the changes in interfacial molecular composition of microITIES were studied during the formation of silica deposit. **Figure 4.14** shows the molecular composition of two immiscible phases during silica electrogeneration.

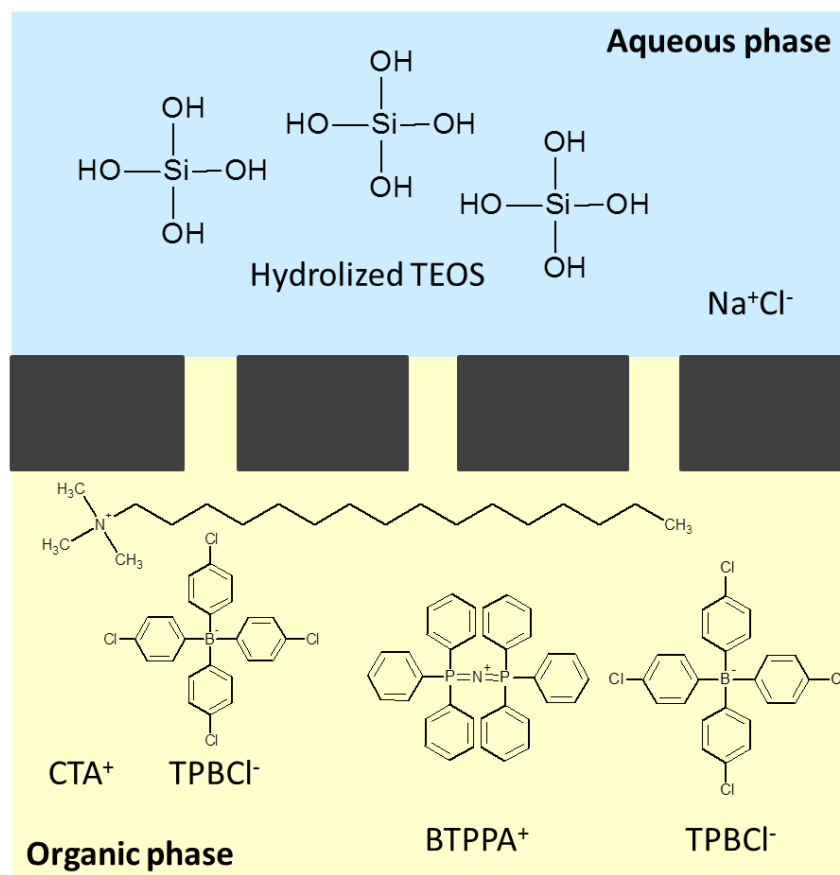


Figure 4.14. Composition of the aqueous and the organic phase during electrochemical silica deposition at array of microITIES.

4.2.1. Raman spectroscopy analysis of the liquid – liquid interface at open circuit potential

Figure 4.15 shows the different Raman spectra recorded at the interface formed between a 5 mM NaCl aqueous solution and DCE in the absence (**Figure 4.15 a**) and in the presence of 10mM BTPPA⁺TPBCl⁻ (**Figure 4.15 b**), of 10mM BTPPA⁺TPBCl⁻ and 14 mM CTA⁺TPBCl⁻ (**Figure 4.15 c**) and 53 mM CTA⁺TPBCl⁻ (**Figure 4.15 d**) in the organic phase. Prior to spectrum collection, the laser was focused on the macroscopic liquid – liquid interface. Spectrum (a) from **Figure 4.15** was recorded at the liquid – liquid interface with pure DCE as the organic phase. The series of peaks obtained correspond to the peaks obtained for the Raman spectrum of pure DCE recorded in solution in the macroscopic cell (see spectra A on **Figure 4.16**). The peaks at 653 and 673 cm⁻¹ can be assigned to the C–Cl stretching modes of the gauche conformer, whereas the peak at 753 cm⁻¹ arises from the C–Cl Ag stretching mode of the trans conformer.²³⁵

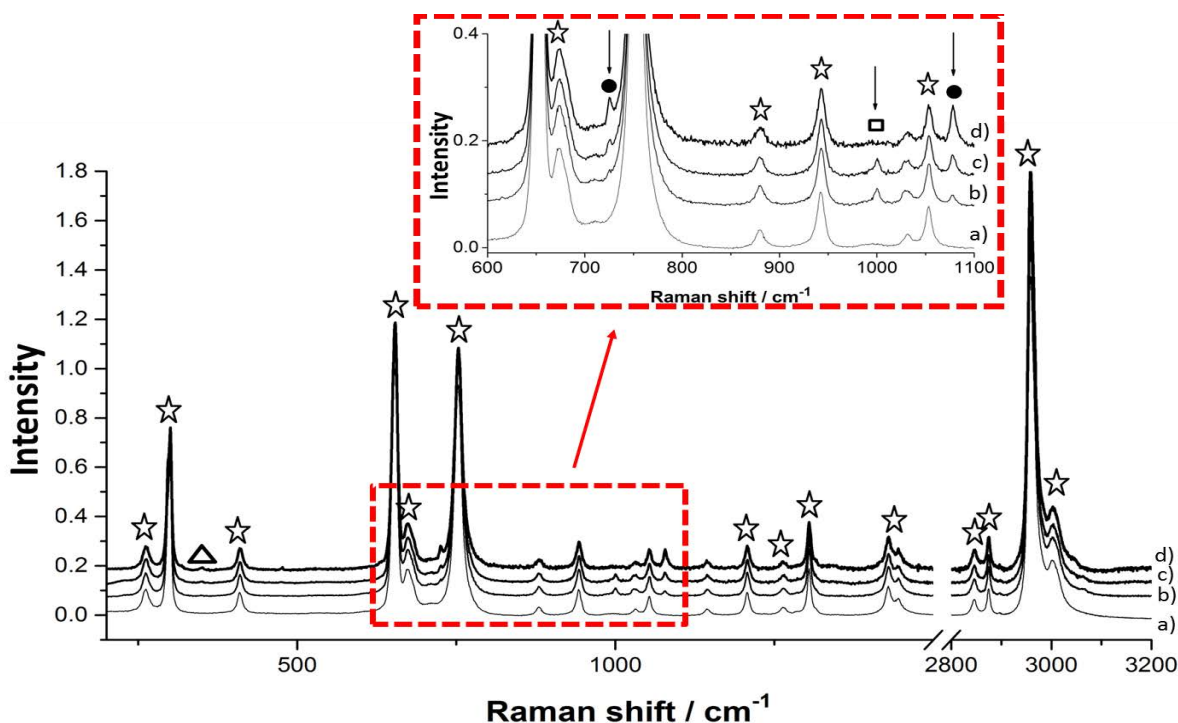


Figure 4.15. Raman spectra recorded at open-circuit potential at the macroscopic liquid – liquid interface constituted between 5 mM NaCl aqueous solution and: a) DCE, b) 10 mM BTPPA⁺TPBCl⁻ in DCE, c) 10 mM BTPPA⁺TPBCl⁻ and 14 mM CTA⁺TPBCl⁻ in DCE and d) 53 mM CTA⁺TPBCl⁻ in DCE. Raman bands marked with (□) were assigned to BTPPA⁺, with (●) to TPBCl⁻, with (☆) to DCE and (Δ) to CTA⁺. All spectra were normalized to the band at 2987 cm⁻¹.

Additionally, the chloromethyl group gives two overlapping peaks at around 3034 cm^{-1} (weak intensity) assigned to the antisymmetric CH_2 stretching mode and 2987 cm^{-1} (very strong intensity) assigned to the corresponding symmetric stretching mode.²³⁶ When the organic electrolyte was added to the organic phase, three additional peaks were observed (see inset of **Figure 4.15**) at 725 , 1000 and 1078 cm^{-1} . The peak at 725 cm^{-1} was probably due to the aromatic C–Cl vibration and arose from the presence of the anion of the organic electrolyte. The origin of the peak at 1000 cm^{-1} was ascribed to the presence of the aromatic rings of BTPPA^+ (also found elsewhere)²¹⁷ and can be therefore treated as a trace of the organic electrolyte. The peak at 1078 cm^{-1} can be assigned to the vibration of the aryl–Cl bond present only in the TPBCl^- .

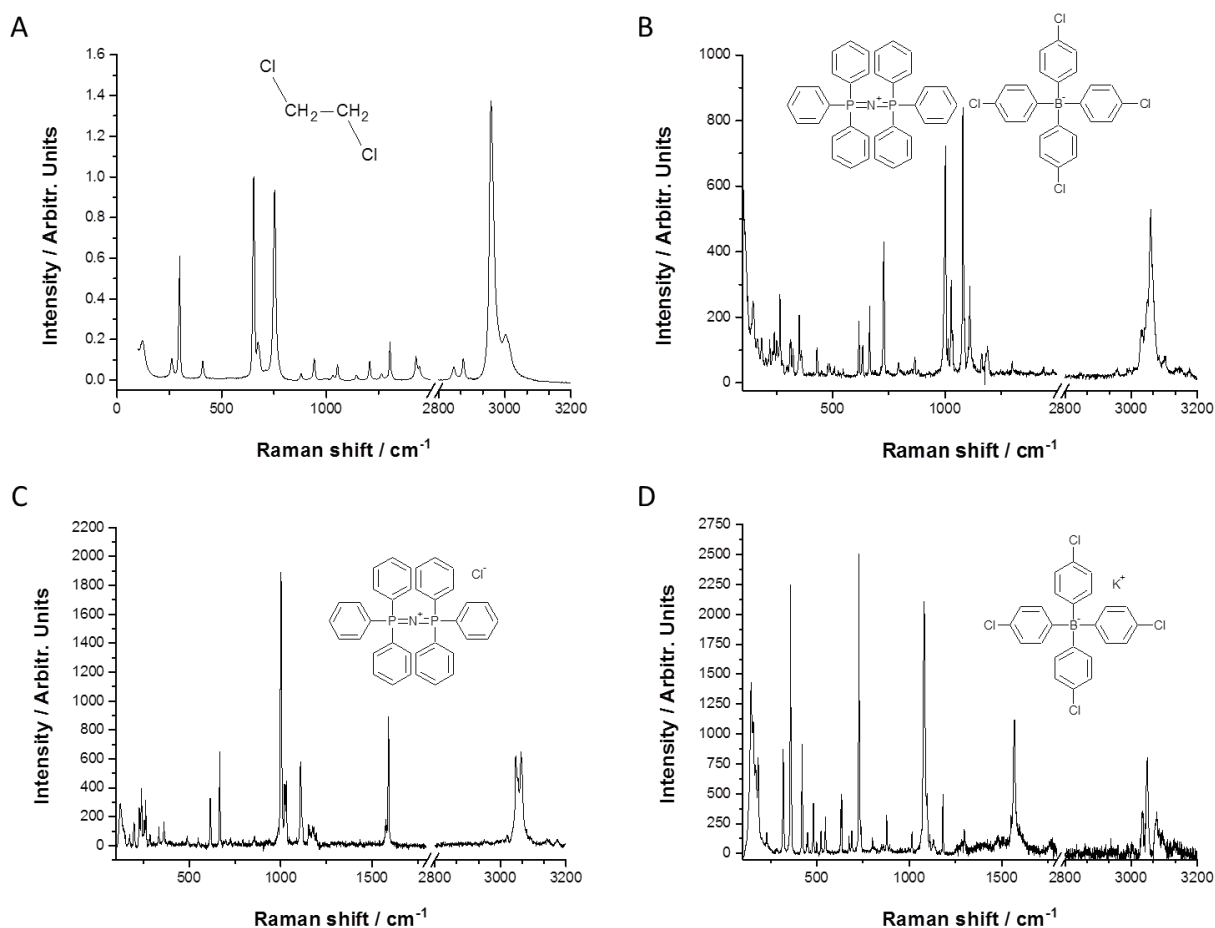


Figure 4.16. Raman spectra recorded for a) DCE, b) $\text{BTPPA}^+\text{TPBCl}^-$, c) $\text{BTPPA}^+\text{Cl}^-$ and d) K^+TPBCl^- .

These observations were in good agreement with the Raman spectra of the powders of the organic electrolyte $\text{BTPPA}^+\text{TPBCl}^-$ (spectra **B** on **Figure 4.16**) of $\text{BTPPA}^+\text{Cl}^-$ (spectra **C** on

Figure 4.16) and of the K^+TPBCl^- (**spectra D on Figure 4.16**). The intensity of both peaks at 725 and 1078 cm^{-1} has increased with the concentration of $\text{CTA}^+\text{TPBCl}^-$ in the organic phase (see **inset of Figure 4.15**), confirming the correct attribution of these peaks to the vibrations related to TPBCl. The intensity of the peak at 1000 cm^{-1} attributed to BTPPA^+ , remained constant upon addition of 10 mM $\text{CTA}^+\text{TPBCl}^-$ in the organic phase and then dropped for 53 mM $\text{CTA}^+\text{TPBCl}^-$ in the organic phase, suggesting that the attribution of a vibrational mode of BTPPA^+ was correct. Addition of $\text{CTA}^+\text{TPBCl}^-$ to the organic electrolyte solution also gave rise to another peak at 349 cm^{-1} , which could be attributed to low-frequency deformation modes of CTA^+ alkyl chains.²⁰³ These experiments demonstrated that the organic electrolyte and surfactant ions remained in the organic phase at open-circuit potential.

4.2.2. Ion transfer followed by Raman spectroscopy

Previous works have demonstrated that the application of a negative potential difference can cause a displacement of the interface with ingress to the aqueous phase.^{213,237} The influence of polarization potential on the position of the interface was then investigated by recording Raman spectra under various negative interfacial potential differences can be found on **Figure 4.17** (see **Figure 4.17 A** for full spectra and **B** for spectral region of interest) to ensure that variations of Raman peak intensities are due to ion transfer rather than displacement of the interface. Prior to spectrum collection, the laser spot was focused at the microITIES under open circuit potential (see dashed curve on **Figure 4.17 A and B** for recorded spectrum). Then, the interfacial potential difference was held for times sufficiently long (which was typically 4 minutes) to collect a full Raman spectrum from 200 to 3200 cm^{-1} . Spectra were normalized to the silicon peak at 520 cm^{-1} (arising from photons scattered by the silicon membrane). The interfacial potential difference was varied from -200 mV down to -800 mV. At these potentials, BTPPA^+ ions were transferred from the organic phase to the aqueous phase as demonstrated on the blank CV shown on **Figure 4.17 D**. Three types of behaviour were observed corresponding to the different molecules present in the solution. As the interface is polarized at more negative potentials, all bands (653, 673, 753,

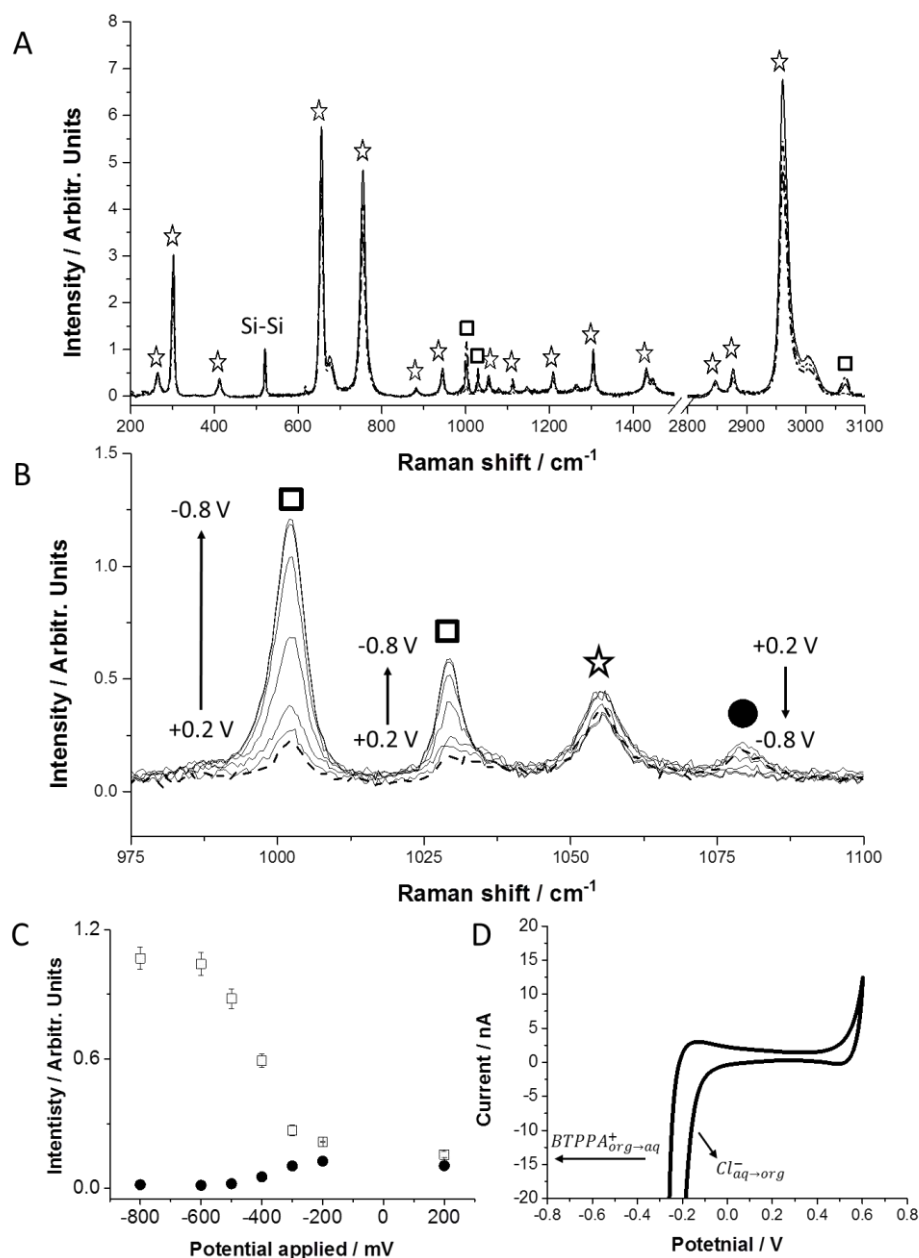


Figure 4.17. A – full Raman spectra and B – Raman spectra in the region from 975 cm^{-1} to 1100 cm^{-1} recorded at the microITIES between 5 mM NaCl aqueous phase solution and $10\text{ mM BTTPA}^+\text{TPBCl}$ organic phase solution under different negative polarization. For A and B dashed line corresponds to Raman spectrum recorded at open circuit potential. Dotted line from A was recorded under negative polarization potential at -300 mV whereas the solid was recorded at -800 mV . The spectra from B were recorded from $+200\text{ mV}$ up to -800 mV . C – shows the peak intensity (after normalization to 520 cm^{-1}) in function of applied potential – empty squares correspond to the peak at 1002 cm^{-1} while filled circles can be attributed to the peak at 1078 cm^{-1} (in that case error bars are too small to notice); open circuit potential was 200 mV ; Raman peaks marked with (\square) were assigned to BTTPA^+ , with (\star) to DCE and with (\circ) to TPBCl. D – is the blank voltammogram recorded prior to spectra collection with the scan rate equal to 5 mV/s .

2847, 2877, 2961 and 3005 cm^{-1}) assigned to the vibrational modes of DCE decreased in intensity, which would confirm that the organic phase did not ingress to the aqueous phase (**Figure 4.17 A**). This is supported by the increase of the band intensity at 1002 and 1029 cm^{-1} related to BTPPA⁺ ions (**Figure 4.17 C – open squares**). Indeed, more and more BTPPA⁺ ions were transferred as the interfacial potential difference became more and more negative (i.e., from 200 mV down to -800 mV). Furthermore, at such negative interfacial potential difference, the transfer of anions from the organic side of the interface (TPBCl⁻) was not expected. The band intensity at 1078 cm^{-1} drop as the interfacial potential difference varied (**Figure 4.17 C – filed black circles**). These experiments demonstrated that the variations in Raman spectra were due to ion transfer caused by the application of a negative interfacial potential difference. The displacement of the liquid – liquid interface was excluded.

4.2.3. Interfacial silica deposition followed by Raman spectroscopy

The electrochemically assisted assembly of surfactant-templated silica at the microITIES was followed by Raman spectroscopy. A Raman spectrum was first recorded at open circuit potential (ocp = +200 mV) and it showed all the characteristic vibration bands reported on **Figure 4.18**. After this control experiment, the interfacial potential difference was linearly swept (at 5 mV/s) from +600 mV down to -100 mV and the potential was held at -100 mV while a second Raman spectrum was recorded. Next the potential was swept back from -100 mV to +600 mV where a third Raman spectrum was recorded while holding the potential at +600 mV; the same operation was repeated once more to get the 4th and 5th Raman spectra, which are shown on **Figure 4.18 A** for three distinct spectral regions (**Figure 4.18 B** shows the potential values at which Raman spectra were recorded). After the first potential scan, molecular composition of the liquid – liquid interface has changed and the spectrum obtained became much more complex than at OCP. The arrows on **Figure 4.18** indicate the evolution of the particular peaks upon repetitive scans; with some of the intensities increasing with the number of scans while others drop down. The region from 2800 to 3100 cm^{-1} showed the most dramatic variations upon voltammetric

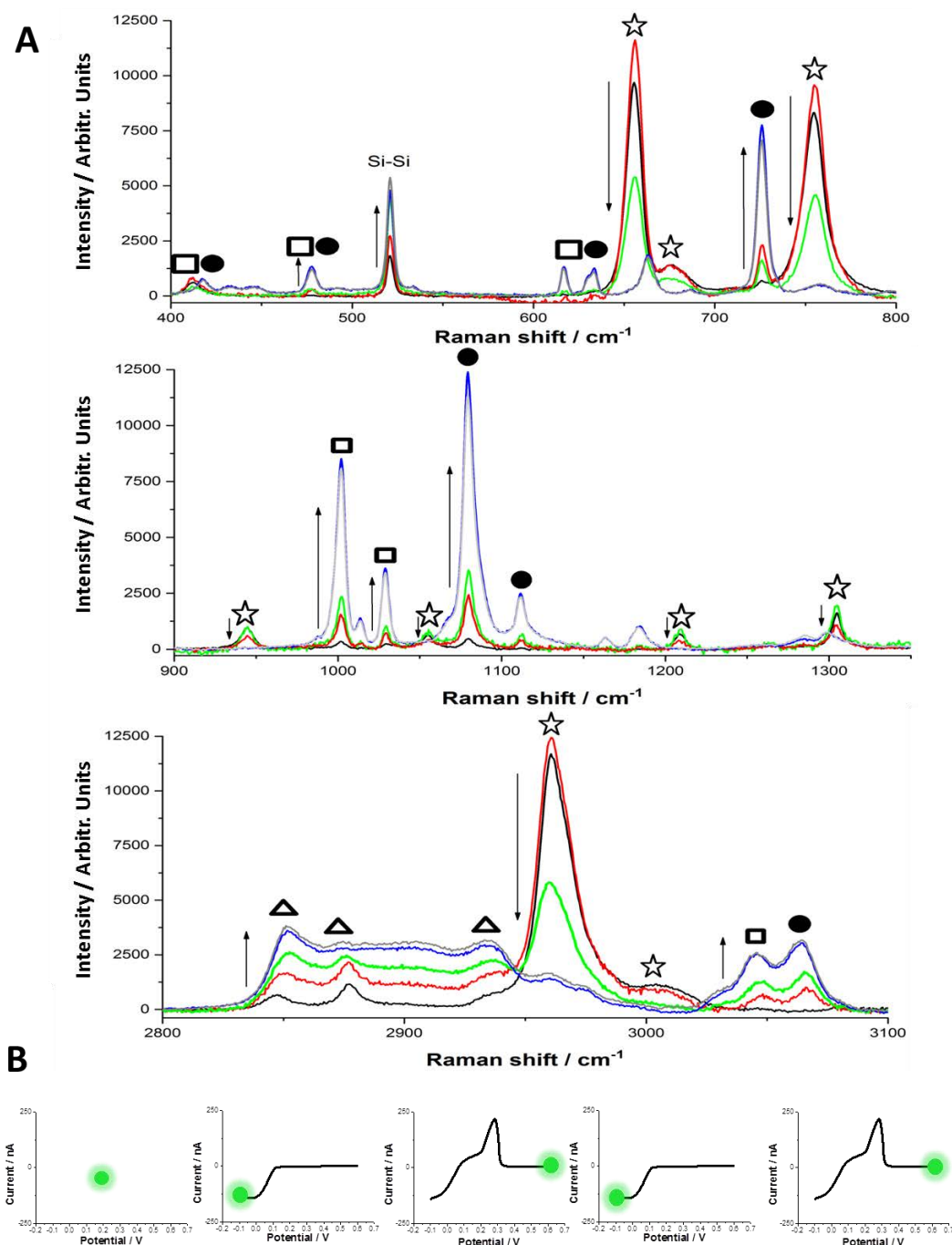


Figure 4.18. A – Raman spectra recorded during *in situ* silica material formation at the microITIES in three different spectral regions. Arrows on the graphs indicate the direction of peak evolution, whereas the colors correspond to the order of spectra collection (1st - black, 2nd - red, 3rd - green, 4th - blue and 5th - grey). The Raman spectrum collection was performed alternately with ion-transfer linear sweep voltammetry as it is shown schematically in part B of the graph. Raman bands marked with (\square) were assigned to BTPPA⁺, with (\bullet) to TPBCl, (\star) to DCE and (Δ) to CTA⁺.

cycling. This region corresponds to the C–H stretching modes, which originated from either DCE, BTPPA⁺, TPBCl⁻ or CTA⁺ ions. The presence of CTA⁺ after the first scan was confirmed by the vibrational contribution from its long alkyl chains, in particular, CH₂ symmetric stretching at 2851 cm⁻¹, CH₃ symmetric stretching at 2874 cm⁻¹ and CH₃ asymmetric stretching mode at 2935 cm⁻¹.

Additionally, BTPPA⁺ and TPBCl⁻ ions gave rise to two overlapping bands from 3025 to 3080 cm⁻¹. The band centered at 3044 cm⁻¹ originated most probably from BTPPA⁺ and arose from the five aryl C–H bonds in the aromatic rings, whereas the latter at 3064 cm⁻¹ can be assigned to monosubstituted aromatic rings as in the case of the chlorophenyl substituent in TPBCl⁻. The other peaks associated with BTPPA⁺ at 1002 and 1025 cm⁻¹ and with TPBCl⁻ at 1078 and 1115 cm⁻¹ also increased. If the growth of characteristic peaks assigned to CTA⁺ vibrational modes was expected, the increase of those related to the ions of the organic phase electrolyte was more surprising, however possible since the silica material is known to be an attractive adsorbent for coadsorption between CTA⁺ and species containing aromatic rings.²³⁸ Indeed, the spectra presented on **Figure 4.18** had shown that these ions were barely visible at open circuit potential. Furthermore, peak intensities of the vibrational modes of BTPPA⁺ were not growing before a potential difference of -300 mV was reached, whereas TPBCl⁻ did not transfer at all at such a negative interfacial potential difference (see **Figure 4.17 C**). A possible explanation to such an increase in the intensity of the bands characteristic of these two compounds is that they can be trapped in the silica-surfactant matrix, which is being formed by self-assembly between condensing TEOS and CTA⁺ transferred to the aqueous phase, via favorable electrostatic interactions (i.e., between the TPBCl⁻ anions and CTA⁺ cations, and between BTPPA⁺ cations and the negatively charged silica surface). Such a hypothesis was notably supported by previous observations made for CTA⁺ based mesoporous silica materials for which the final composition implied the presence of ionic species in addition to the presence of the surfactant and silica.^{239,240}

Unfortunately, no direct *in situ* evidence of the interfacial silica material formation was found, since no band for the Si–O–Si vibrational mode has been observed during the acquisition time used in *in situ* experiments. This might be due to the fact that longer acquisition times were required to observe the Si–O–Si vibrational mode in the 450 to 500 cm⁻¹ region¹⁸⁵ for silica

deposits and if existing here, this signal was too weak to be visible with respect to the other ones or to the noise of the Raman spectra. Another point was that the condensation kinetics for sol-gel-derived silica is usually rather slow (i.e., low condensation degree for the material generated in the synthesis medium, as pointed out from *in situ* NMR experiments),^{241,242} and required subsequent heat treatment to achieve a high degree of crosslinking of the silica network. Actually, the observation of the silica vibration band for a silica deposits electrogenerated at the microITIES was possible, but only after calcination at 400 °C for 30 minutes (see **Figure 4.11**).

Another indirect evidence of silica formation can be seen by following the evolution of the Si-Si band at 520 cm⁻¹ (see **Figure 4.18 A**). Indeed, mesoporous materials (e.g. mesoporous silica) can serve as a waveguide for light.²⁴³ The amount of the silica material generated at the microITIES grew with the number of scans, and hence disturbed the system by guiding laser photons through the silica deposits to the silicon wafer supporting the microITIES. The waveguide phenomenon (due to elastic light scattering by the silica formed) was observed as the increase in Si-Si band intensity. The same phenomenon could be responsible for the disappearance of all bands originating from DCE once silica is being formed at the liquid – liquid interface.

The Raman shifts of the particular molecular contributions used to describe all recorded spectra from this work are summarized in the **Table 4.1**.

Table 4.1. Summary of the bands observed in the different Raman spectra

Molecule of interest	Raman shift frequency ²⁰³ /cm ⁻¹	Band assignment ²⁰³	Description ²⁰³
CTA ⁺	3000 – 2840	-CH ₂ - and -CH ₃ stretching	Strong and characteristic bands
	2962 ± 10	-CH ₃ Antisymmetric stretching	Strong intensity and characteristic frequencies
	2926	-CH ₂ - Antisymmetric stretching	Strong in Raman
	2872 ± 10	-CH ₃ symmetric stretching	Strong intensity and characteristic frequencies
	2853	-CH ₂ - Symmetric stretching	Often overlapped with CH ₃ in anti-symmetrical region
	1470 – 1440	-CH ₃ Antisymmetric bending	Medium intensity
	1470 – 1340	CH ₂ and CH ₃ bending	Not necessarily visible in Raman spectra

	1465	Scissoring (bending) mode	
	1305 – 1295	-(CH ₂) _n - in phase twisting mode	Medium – strong intensity in Raman
BTPPA⁺	3100 – 3000	Aromatic ring in C-H stretching region	
	1600 – 1000	Five aryl C-H bonds (in aromatic)	
	1500 – 1141	P=N	
	1130 – 1090	P-(Ph) ₃	Weak in Raman
	1010 – 990	Aromatic rings	Very strong in Raman
	1000 – 700	C – H bending	
TPBCl⁻	3070 – 3030	C-H of substituted benzenes	One strong band
	1620 – 1585	Mono- and disubstituted benzene	The two quadrant stretch components give rise to two bands. When benzene is substituted with Cl the bands will occur at lower limit.
	1590 – 1565		
	1083	Aryl-Cl in chlorobenzene	For phenyl group on para this band is seen in the 1130 – 1190 cm ⁻¹ region. From m to s in Raman
	420 – 390	Mono and parasubstituted benzenes	Very weak Raman band
DCE	3030 ²⁴⁴	-CH ₂ antisymmetric stretching	
	2987 ²⁴⁴	-CH ₃ symmetric stretching	
	730 – 710 ²⁴⁴	Cl-(CH ₂) _n -Cl stretching mode of the trans conformer	
	657 ²⁴⁴	CH ₃ -CH ₂ -Cl stretching mode of the gauche conformer	

4.2.4. Conclusions

The confocal Raman spectroscopy with the spatial resolution around 1 μm allowed the study of molecular changes at the miniaturized ITIES induced by electrochemically driven ion transfer and silica deposition reactions. Ion transfer of cationic part of supporting electrolyte of the organic phase – BTPPA⁺ – induced by negative polarization, could be followed by confocal Raman spectroscopy after a precise assignment of each typical band (based on data available in the literature and series of reference measurements). The high spectral resolution of usual Raman spectrometers and the sharpness of Raman peaks were of strong help in this regard. Raman

spectroscopy also offers the opportunity to monitor vibrational modes in the aqueous phase, which is more difficult in infrared absorption spectroscopy (though not impossible using dedicated techniques like attenuated total reflection sampling (ATR)). The confocal microscope also enabled to finely localize the liquid – liquid interface, which was mandatory in this kind of study. Besides, compared to non-linear optical techniques like second harmonic or sum-frequency generation, the laser irradiance can be low enough to avoid any disturbance of the fragile interface during the formation of the silica deposits. No direct evidence was found for Si-O-Si formation during *in situ* silica formation study with Raman spectroscopy (it was already shown before that such band can be found for cured deposits). Silica formation was confirmed indirectly as the interfacial molecular characteristics have changed dramatically upon interfacial polarization in the presence of template molecules in the organic phase and silica precursor in the aqueous phase. Additionally, it was found that organic supporting electrolyte is also involved in the silica formation mechanism as the signals arising from its vibrational mode were also present in recorded Raman spectra. This experimental set-up developed in this work could be also used to follow the *in situ* functionalization of silica deposits via the co-condensation of silanes and organosilanes. The results from this part of work can be also found in **Phys.Chem.Chem.Phys.**, 2014, **16**, 26955 – 26962.

4.3. Electrochemical evaluation of microITIES modified with silica deposits

In the following section the silica deposits electrogenerated at the liquid – liquid interface supported with the membrane design number 3 (30 pores, each having 5 μm in radius, for more details refer to **Table 2.2**) are evaluated with the ion transfer voltammetry. Interfacially active ions of different charge, size and nature: (i) three different in size tetraalkylammonium cations, (ii) single charged anion and (iii) two generations – G0 and G1 – of PAMAM dendrimers were employed for this purpose. The silica deposition was performed with one voltammetric cycle at 5 mV/s for $[\text{CTA}^+]_{\text{org}} = 14 \text{ mM}$ and $[\text{TEOS}]_{\text{aq}} = 50 \text{ mM}$ (see **Figure 4.4 C**). Modified with silica silicon membranes were then calcinated at 450°C for 30 min.

4.3.1. Blank experiment before and after modification

Figure 4.19 shows the blank CVs recorded before and after modification of the microITIES array with the silica deposits. The potential region was scanned from more negative to more positive potentials on the forward scan as indicated on **Figure 4.19** with the dotted arrow. The potential window was determined by the transfer of the supporting electrolyte ions dissolved in each phase, which resulted in a current rise on both sides of CV. There was no significant impact of the silica deposits on the potential window width. At the negative end, the potential window was limited by the transfer of Cl^- , which crosses the interface at a higher potential than BTTPA^+ ions. Indeed, previous studies have shown that the Galvani potential for Cl^- is $\Delta\Phi^{1/2} = -530 \text{ mV}$,^{21,245} whereas the Galvani potential for BTTPA^+ is $\Delta\Phi^{1/2} = -700 \text{ mV}$.²⁴⁵ The peak observed at $\Delta\Phi = -450 \text{ mV}$ was then attributed to the back-transfer of Cl^- from the organic to the aqueous phase, whose diffusion was confined inside the microITIES pores and hence was linear. At the positive end of the potential window, the transfer was limited by the transfer of anions of the organic electrolyte salt. Indeed, the absence of a peak on the reverse scan has suggested a radial diffusion in the aqueous phase, which would correspond to the back transfer of TPBCl^- from the aqueous to the organic phase. Unfortunately, the Galvani standard

potential for the transfer of TPBCl⁻ has never been determined²⁴⁵ and one can only assume that it is lower than the one for Li⁺ which is $\Delta\Phi^{1/2} = +580$ mV.²⁴⁶

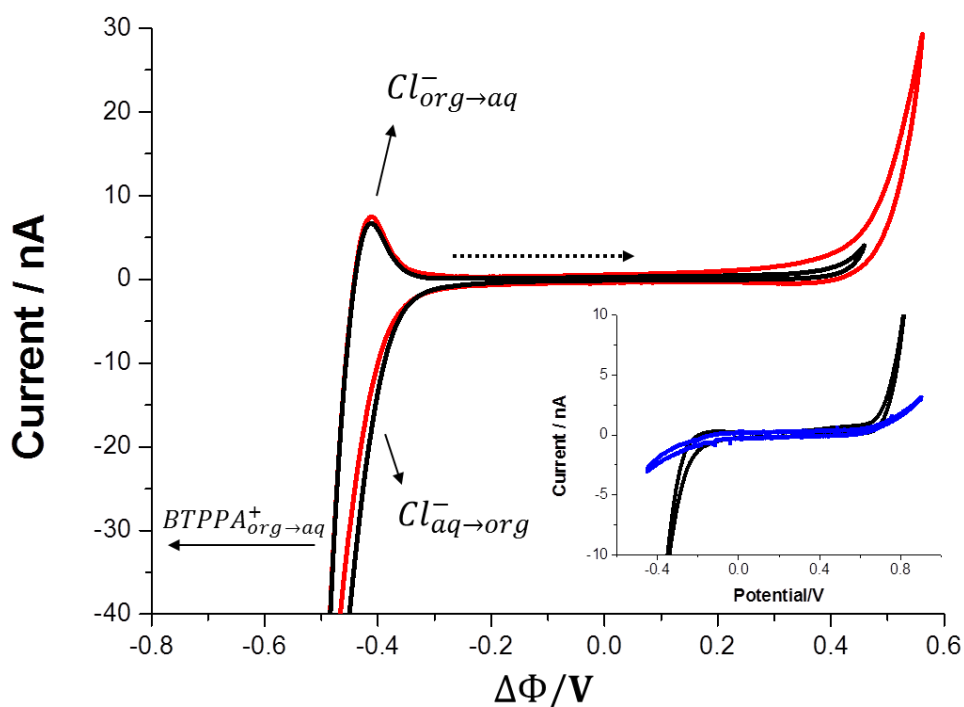


Figure 4.19. CV recorded only in the presence of supporting electrolytes (10 mM LiCl in the aqueous phase and 10 mM BTPPA⁺TPBCl⁻ in the organic phase) before – black line – and after – red line – modification with silica deposits. The insert is the CV recorded in the absence of the aqueous supporting electrolyte before – black line – and after – blue line – modification. Scan rate was 10 mV/s. Dotted arrow indicates the direction of polarization on the forward scan.

4.3.2. Single charge ion transfer before and after modification

Electrochemical behavior in the presence of silica deposits of three tetraalkylammonium cations of different sizes (TMA⁺, TEA⁺ and TBA⁺) – see **Figure 4.20 A** – and of the negatively charged 4OBSA⁻ – see **Figure 4.20 B** – were first studied. The electrochemical behavior of each analyte was investigated in the absence (black curves) and in the presence (red curves) of silica deposits at the microITIES. All ions were initially present in the aqueous phase at concentration

of 56.8 μM , and the forward polarization was selected in agreement with the charge of transferring species (towards positive potentials for tetraalkylammonium cations and towards negative potentials for 4OBSA⁻). The shape of cyclic voltammograms for all four species showed a sigmoidal forward signal – in agreement with hemispherical diffusion zone from the aqueous side of the interface – and a reverse peak like response – indicative for linear diffusion limitation inside the microITIES pore channels filled with the organic phase. The voltammograms are shown on the Galvani potential scale, based on the peak transfer of Cl⁻.

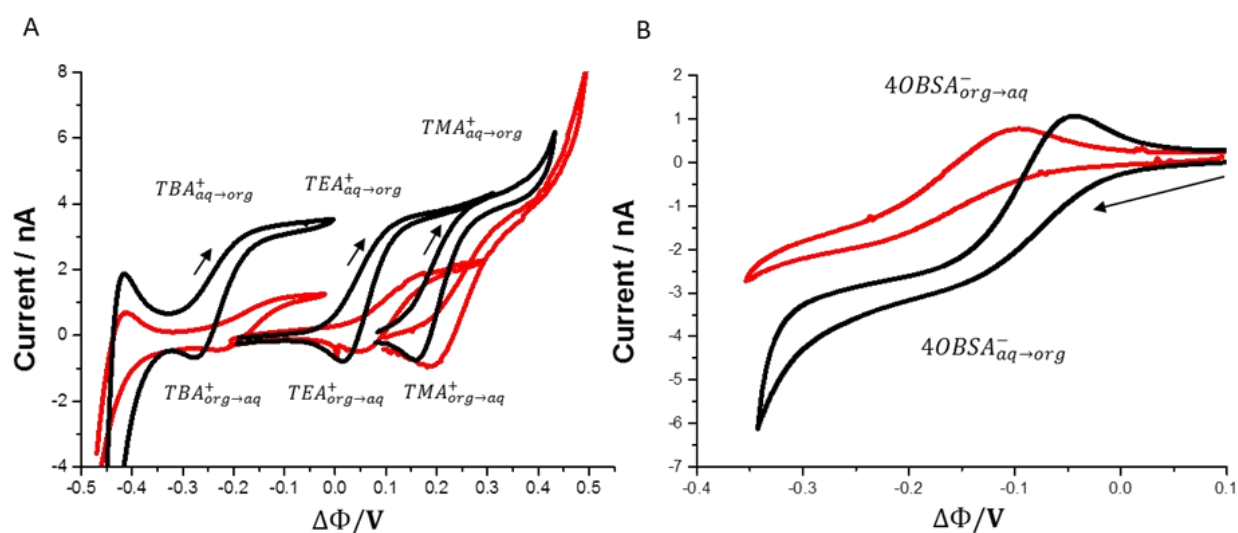


Figure 4.20. CVs of four different ions crossing the interface in the absence (black curves) and in the presence (red curves) of silica deposits at the array of microITIES. A – shown the transfer of three different in size cations (starting from left): TBA⁺, TEA⁺ and TMA⁺. B – is the transfer of negatively charged 4OBSA⁻. Arrows indicate direction of polarization on the forward scan. The concentration of each ion was 56.8 μM and the scan rate was 10 mV/s.

The presence of silica deposits has an impact on both the ion transfer potential and current intensity. For all four ions studied here, the presence of silica deposits at the microITIES has made the transfer more difficult, as an ion transfer potentials were shifted negatively by 22 mV for TMA⁺, 26 mV for TEA⁺, 46 mV for TBA⁺ and by 50 mV for 4OBSA⁻. Based on the potential shift the difference of the Gibbs Energy of transfer, $\delta\Delta G$, could be estimated:

$$\delta\Delta G = \Delta G_{\text{before modification}} - \Delta G_{\text{after modification}} \quad (3.3)$$

Where $\Delta G_{\text{before modification}}$ is the Gibbs energy of transfer in the absence of silica deposits and $\Delta G_{\text{after modification}}$ is the Gibbs energy of transfer in the presence of silica deposits. ΔG is governed with the following equation:

$$\Delta G = -zF\Delta\Phi \quad (3.4)$$

On **Figure 4.21** the variation of Gibbs energy of ion transfer was plotted as a function of the ion hydrodynamic radius. For cations of the tetraalkylammonium series, the shift in Gibbs energy of transfer became larger as the hydrodynamic radius grew. This is to be expected as the diffusion of larger cations through the mesopores of the silica deposits might be more impeded than the smaller cations. The Gibbs energy of transfer for the anion 4OBSA^- was also higher after modification than before indicating that the transfer had become even more difficult.

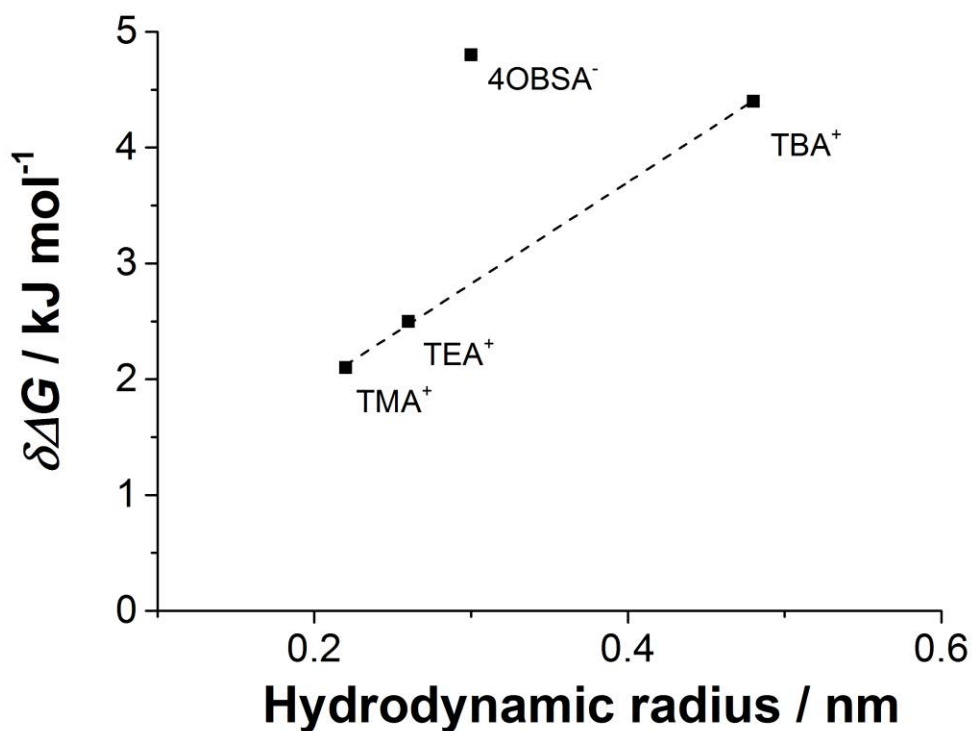


Figure 4.21. Variation of the difference of Gibbs energy of transfer before and after microITIES modification with silica deposits vs the hydrodynamic radius (see **Table 4.2** for values) of the single charged species.

The difference was higher than any of the cations tested, even larger than TBA^+ , whose hydrodynamic radius is almost twice bigger ($r_{h\ 4OBSA} = 0.30\ nm$ and $r_{h\ TBA} = 0.48\ nm$).²⁴⁷ In spite of similar hydrodynamic radii, the behaviors of TEA^+ ($r_h = 0.28\ nm$ ²⁴⁷) and $4OBSA^-$ were quite different with a shift of $2.5\ kJ\ mol^{-1}$ for TEA^+ and $4.8\ kJ\ mol^{-1}$ for $4OBSA^-$. A similar trend was observed for the ion transfer current with a drop caused by the interface modification: 59% for $4OBSA^-$ and 48% for TEA^+ . This behavior can be attributed to electrostatic repulsion between negative net charge of silica surface (arising from the presence of deprotonated terminal OH groups located on the edge of silica walls as the point of zero charge is 2)²⁴⁸ and anionic $4OBSA^-$.

4.3.3. Multicharged ion transfer before and after modification

Dendrimers are the second family of species studied in this work. Large multi-charged species are giving complex electrochemical response at ITIES, which varies with the dendrimer generation. They can undergo either interfacial adsorption⁵³ or ion transfer^{50,53}. Furthermore, PAMAM dendrimers at electrified liquid – liquid interface were employed as encapsulating agents for smaller porphyrin molecules²⁴⁹ or molecular organic dyes.²⁵⁰ Complex behavior of dendrimer-guest molecular association studied with cyclic voltammetry coupled with spectroscopic methods indicated that ion transfer reaction is accomplished with interfacial adsorption process – well pronounced by rapid current drop on the reverse peak.²⁴⁹ **Figure 4.22** shows the electrochemical behavior of PAMAM dendrimers generation 0 (G0) (**Figure 4.22 A**) and generation 1 (G1) (**Figure 4.22 B**) before (black lines) and after (red lines) modification. The voltammograms are shown on the Galvani potential scale, based on the internal reference – peak transfer of Cl^- (despite such peak is not present on the graphs shown, the correction was made in regard to blank CV recorded prior to each experiment). Both PAMAM dendrimers ($28\ \mu M$) and the model ion TEA^+ ($42\ \mu M$) were initially present in the aqueous phase to facilitate the comparison. CVs from **Figure 4.22 A and B** before modification had the same characteristics, independent of the generation of PAMAM dendrimer studied. A first sigmoidal wave rose at $+44\ mV$ corresponding to the non-diffusion limited transfer of $TEA^+_{aq \rightarrow org}$. The second sigmoidal wave originated from $PAMAM_{aq \rightarrow org}$ transfer, which was partially masked by organic electrolyte

anion transfer – $TPBCl_{org \rightarrow aq}^-$. On the reverse scan, back transfer of PAMAM dendrimers resulted in a peak response followed by diffusion limited back transfer of $TEA_{org \rightarrow aq}^+$.

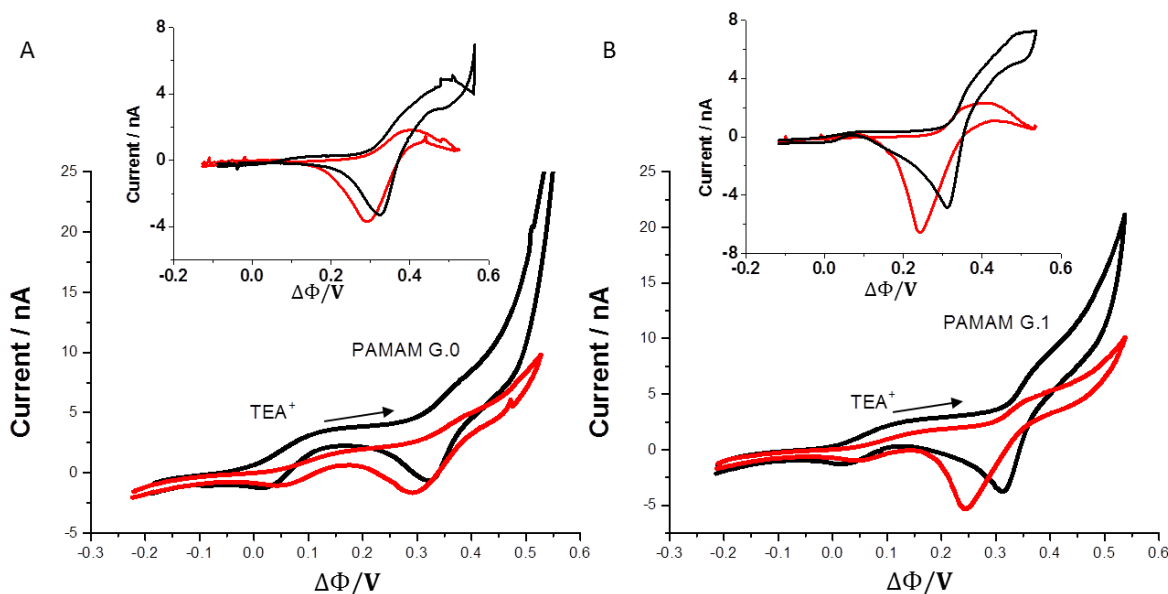


Figure 4.22. Cyclic voltammograms illustrating the transfer of A – PAMAM generation G0 and B – PAMAM generation G1 dendrimers in the absence (black line) and the presence (red line) of silica deposits. The concentrations are $[TEA^+]_{aq} = 42 \mu\text{M}$ and $[PAMAM\ G0\ or\ G1]_{aq} = 28 \mu\text{M}$. Scan rate was $10\ \text{mV s}^{-1}$. Black, solid arrows indicate the direction of polarization during forward scan. Inserts are the CVs after background subtraction.

Prior to interfacial modification, both dendrimers (G0 and G1) underwent a simple ion transfer reaction, which is also the case at the macroscopic ITIES.⁵⁰ Modification of the microITIES with silica has led to the following results : (i) a lower forward current for both dendrimers, which was slightly more pronounced for PAMAM G1 (51% of loss on the forward current as compared with a 29% loss on the forward current for PAMAM G0); (ii) a shift in forward and reverse transfer potentials towards more negative potentials, which was in contrast to the series of tetraalkylammonium cations and (iii) the shape of back transfer peak for PAMAM G0 was unaffected after modification and hence a diffusion-limited peak was observed suggesting that the transfer current is due to an interfacial transfer reaction. The characteristics of PAMAM G1 behavior are more complex as the peak shape was changed. These phenomena (i, ii, and iii) may have two origins. First, on the forward scan, ion transfer can be affected by electrostatic interaction between positively-multi-charged dendritic molecules and negative net charge of silica (terminal OH groups inside the mesopores), which has led to charge screening and resulted

in lower current. Second, the peak on the reverse scan (especially visible for PAMAM G1) was probably affected by adsorption process since additionally to the negative peak potential shift the current drop was more rapid and the separation between forward and reverse signal increased from 64 mV to 114 mV (factors that are a fingerprint of macromolecules exhibiting adsorption behavior at ITIES)^{53,249–251}. In the case of PAMAM G1 adsorption, facilitated transfer of the organic electrolyte counter ion cannot be excluded and may give some additional portion of faradaic current on forward scan, as it was shown for proteins^{55,56} and synthetic dendrimers⁵³ studied at the ITIES.

4.3.4. Electroanalytical properties of microITIES modified with silica deposits

Figure 4.23 and **Figure 4.24** have three columns: a) CVs recorded before modification; b) CVs recorded after modification and c) corresponding calibration curves. The rows on **Figure 4.23** can be ascribe to 1 – TMA⁺; 2 – TEA⁺ and 3 – TBA⁺, whereas on **Figure 4.24** to 4 – 4OBSA⁻; 5 – PAMAM G0 and 6 – to PAMAM G1. As already noticed, modification caused the decrease of the faradaic current evidenced for each of studied ions. On the forward scan, the sigmoidal wave current increased linearly for the three tetraalkylammonium cations and 4OBSA⁻ over the whole concentration range studied. This was observed in the presence and in the absence of silica deposits. This behavior was different for multi-charged species. The forward transfer current reached a plateau for the higher concentrations of dendrimers (see **calibration curves on Figure 4.24 5c and 6c**). The analytical parameters of each ion (sensitivity, limit of detection and apparent diffusion coefficients within the silica deposits) in the presence and in the absence of silica at microITIES were extracted from these calibration curves (**Table 4.2**). The theoretical calibration curve (see **solid line on Figure 4.23 and Figure 4.24 in column c**) was calculated with the equation expressing the limiting current in presence of hemispherical diffusion zone:

$$i_{lim} = 4nrz_iDFC_i \quad (3.5)$$

where n is the number of microITIES in the array ($n = 30$), r is the microITIES radius ($r = 5 \mu\text{m}$), z_i is the charge of the species transferred, F is the Faraday constant ($96485 \text{ C} \cdot \text{mol}^{-1}$) and C_i is concentration. Theoretical calibration curves in the absence of silica deposits were fitted using

eq. 3.5 with diffusion coefficients taken from other studies (exception was 4OB S A $^-$ for which diffusion coefficient was extracted from linear fit of experimental calibration curve (red dashed line on **Figure 4.24 4c**). Berduque et al. have shown that the electrochemical behavior of PAMAM dendrimers G0 and G1, is characteristic of multiply charged species.⁵⁰ However, they demonstrated that the charge transferred is lower than the theoretical charge.

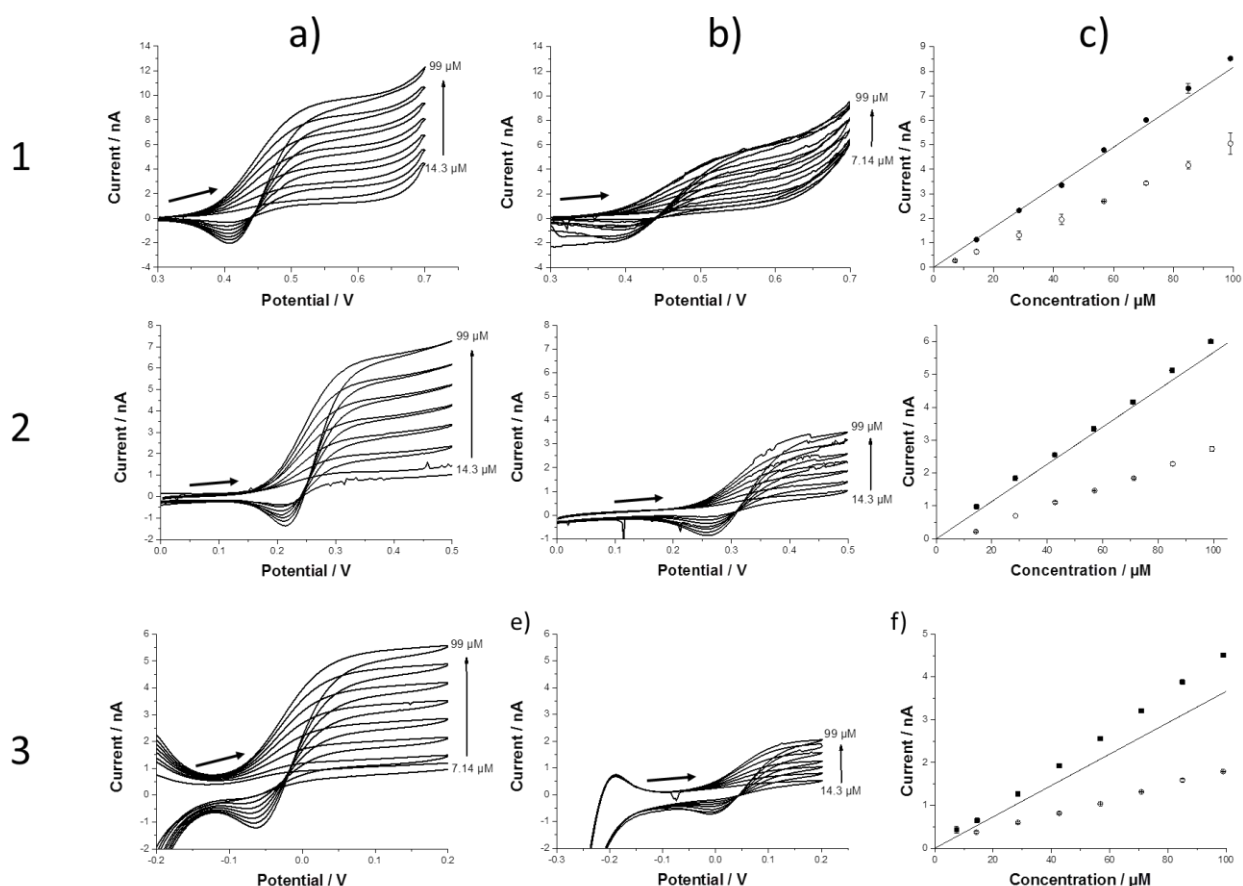


Figure 4.23. Data correspond to TMA $^+$ (row 1), TEA $^+$ (row 2) and TBA $^+$ (row 3). Cyclic voltammograms for different interfacial active ion concentrations recorded before modification are shown in column a, whereas their voltammetric behavior after modification is depicted in column b. Column C represent the calibration curves before modification (black squares), after modification (empty circles) and theoretical values calculated using eq. (3.5) (solid line). Error bars, however present are smaller than the size of the points. Arrows indicate the direction of polarization during forward scan. Scan rate was 10 mV/s.

There is a good correlation between the sensitivity calculated from the slope of theoretical fitting using Eq. (3.5) and the sensitivity measured experimentally before modification, S_0 , for TMA $^+$, TEA $^+$, and to a lesser extent for TBA $^+$ and PAMAM G0 and G1.

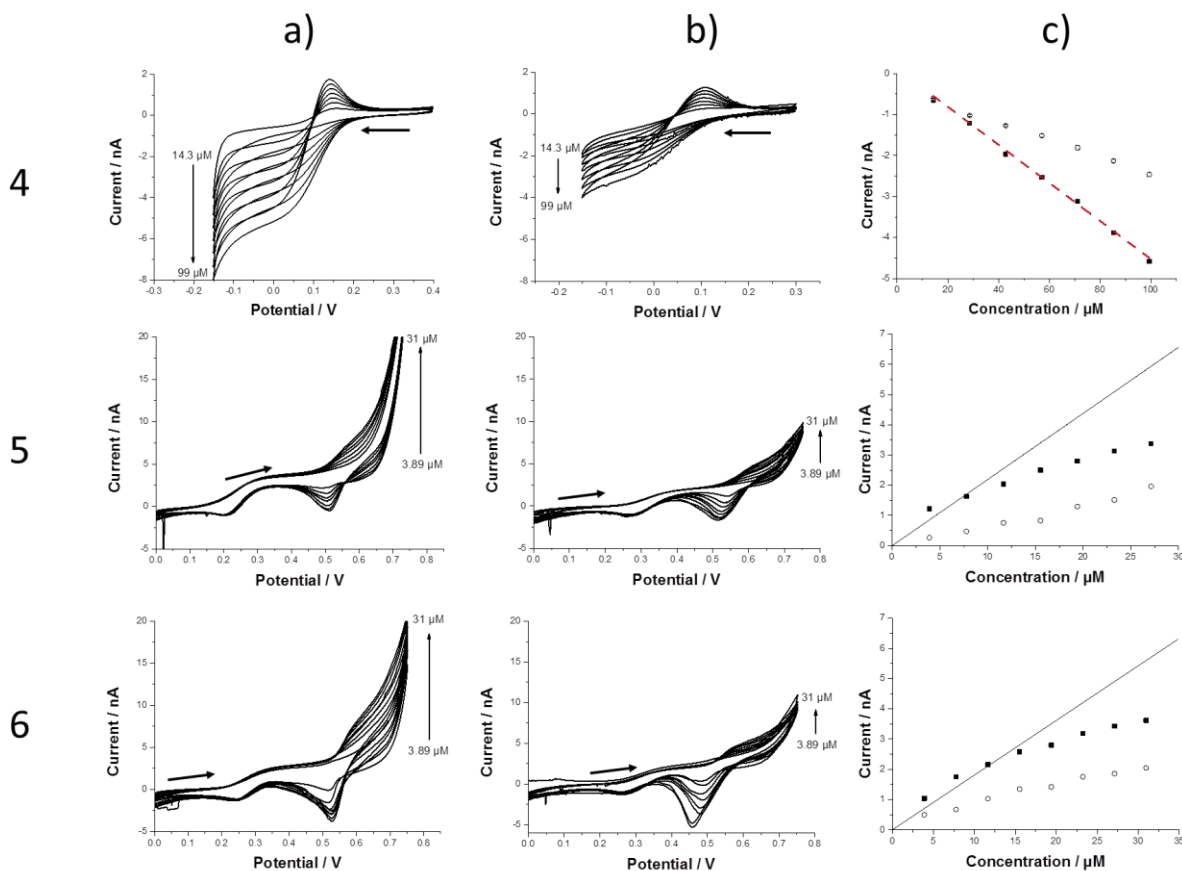


Figure 4.24. Continuation of **Figure 4.23**. Data correspond to 4OBSA⁻ (row 4); PAMAM G.0 (row 5) and PAMAM G.1 (row 6). The remaining description is identical with **Figure 4.23**.

The impact of the interface modification on the sensitivity, S , is shown for the different ions studied as a function of the product of their charge, z_i , and their diffusion coefficient, D_i (**Figure 4.25**). For single charge species, the impact of the interface modification on the sensitivity ratio S/S_0 (S_0 is the sensitivity before modification) was lower for the smaller ion TMA⁺ than for the larger TBA⁺. A similar trend was observed for dendrimers where the impact on the sensitivity ratio was greater for PAMAM G1 than for PAMAM G0. The sensitivity of the larger molecule (PAMAM G1) was more affected than the one of the smaller molecule (PAMAM G0). Nevertheless, the S/S_0 is higher for both these multiply-charged molecules than for single charged ions. This can be explained by stronger interactions between the negatively charged silica walls and the multiple charges of PAMAM dendrimers.

The limit of detection (LOD) was calculated from the linear fit of equation:

$$LOD = \frac{3.3SD}{s} \quad (3.6)$$

where SD is the standard deviation of the intercept and S is the sensitivity. LODs for the ions studied before microITIES modification are in the μM range, with the exception of TBA^+ in the sub- μM range. The modification with mesoporous silica did not impact significantly the LODs since their value remained rather in the same range (see **Table 4.2**).

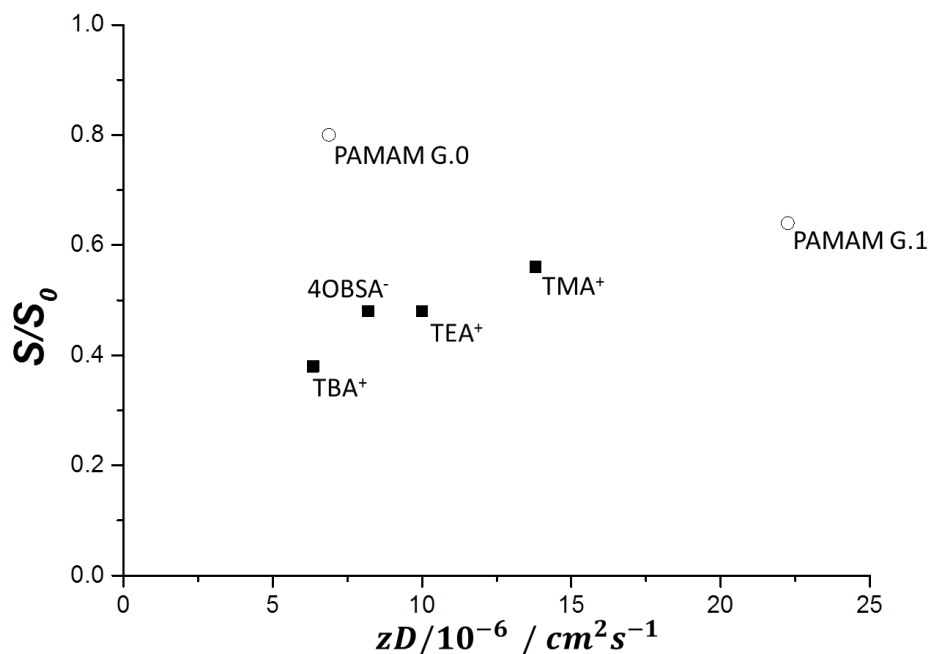


Figure 4.25. Sensitivity ratio, S/S_0 , as a function of zD for 4OBSA^- , TBA^+ , TEA^+ and TMA^+ PAMAM G0 and PAMAM G1.

According to **eq. (3.5)**, the difference in sensitivity before and after modification can be explained by an impeded diffusion of charge species through mesoporous silica, leading to apparent diffusion coefficients, D'_i , that are lower than the diffusion coefficients of species in the bulk solution. From linear fit of calibration curves for modified microITIES using **eq. (3.5)**, the D'_i for all studied species was extracted, assuming that the microITIES radius remained unchanged in the presence of silica deposits (deposits are flat at the bottom and preferably filled with the aqueous phase). The D'_i calculated for all ions are shown in **Table 4.2**. 40% drop in D'_i

for TMA⁺ and 50% drop for TEA⁺, TBA⁺ and 4OBSA⁻ were observed in the presence of silica deposits. These estimations correlate with previous studies. The diffusion coefficient of TEA⁺ within zeolite Y modified ITIES (with the aperture diameter of 7.4 Å) was two order of magnitude lower than in the aqueous phase.¹⁸⁸ TEM images showed that the mesopores dimensions of silica material from this work was significantly larger than zeolite Y and hence the effect on D'_i is considerably smaller as on the diffusion coefficient through zeolite Y.

Table 4.2. The structural and electroanalytical data for six different in size, charge and nature species employed in this work.

Ion transferred	r_h / nm	$D_i \cdot 10^{-6} / \text{cm}^2 \cdot \text{s}^{-1}$	$D'_i \cdot 10^{-6} / \text{cm}^2 \cdot \text{s}^{-1}$	z_i	Sensitivity / nA·mM ⁻¹			LOD / μM**	
					$S_{theor.}$	S_0 (R ²)	S (R ²)	BM	AM
TMA ⁺	0.22 ²⁴⁷	13.8 ²⁵²	8.5	+1	81.6	87.4 (>0.999)	49.0 (0.999)	1.91	0.82
TEA ⁺	0.26 ²⁴⁷	10.0 ± 0.4 ²⁵²	5.0	+1	56.7	57.4 (>0.999)	28.8 (0.998)	0.47	3.82
TBA ⁺	0.48 ²⁴⁷	6.4 ± 0.3 ²⁵²	3.1	+1	36.6	45.2 (>0.999)	17.4 (0.997)	0.07	5.32
4OBSA ⁻	0.30*	8.2**	3.8	-1	n/a	-46.4 (0.998)	-22.1 (0.992)	3.88	2.78
PAMAM G0	0.70 ²⁵³	3.4*	2.6	2 ⁵⁰	87.6	94.2 (0.989)	74.9 (0.986)	2.41	3.82
PAMAM G1	0.55 ⁵³	4.5 ⁵³	0.9	5 ⁵⁰	129	91.6 (0.961)	58.6 (0.977)	4.90	3.70

r_h is the hydrodynamic radius, D_i is the aqueous diffusion coefficient, D'_i is the apparent diffusion coefficient determined experimentally, z_i is the charge, S_{theor} correspond to the theoretical sensitivity based on Eq. (3.6), S_0 correspond to the sensitivity at a bare microITIES and S to the sensitivity at a modified microITIES, BM to before modification and AM to after modification. *Calculated from the Stokes Einstein relationship, $r_h = \frac{k_B T}{6\pi\eta D}$, where k_B is the Boltzmann constant ($1.3807 \cdot 10^{-23} \text{ m}^2 \cdot \text{kg} \cdot \text{s}^{-2} \cdot \text{K}^{-1}$), T is the temperature (293 K), η is the aqueous phase viscosity (0.89 cP) and D is the diffusion coefficient ($\text{cm}^2 \cdot \text{s}^{-1}$). **Calculated from calibration curve fit based on equation describing limiting current at array of microITIES (eg. (3.5)).

4.3.5. Conclusion

Arrays of microITIES were modified with silica deposits based on electrochemically driven surfactant (CTA⁺) assisted Sol – Gel process with TEOS as a silica precursor species. The electrodeposition and morphological study was done and is described in **section 4.2** of this chapter. Silica deposits were characterized by ion transfer voltammetry of six different in size, nature and charge analytes: TBA⁺, TEA⁺, TMA⁺, 4OBSA⁻ and PAMAM G0 and G1. The transfer peak currents observed for the transfer of all species were lowered and the transfer peak

potentials were shifted depending on the nature of studied analyte in the presence of silica deposits at the ITIES. Increase in size of tetraalkylammonium cations has led to a greater current drop and potential shift (from finely affected TMA⁺ to clearly changed TBA⁺). In case of 4OBSA⁻ both, the current drop and $E_{1/2}$ shift were attributed to both size and charge effects. The electrochemical behavior of multi-positively-charged dendrimers in the presence of silica deposits was attributed to the electrostatic interaction with negatively charged silica net. Furthermore, microITIES modification affects differently the electroanalytical parameters (sensitivity, LOD and apparent diffusion coefficient) Depending on the size of the species transferred, suggesting the future possibility of selective ion transfer using microITIES modified with functionalized mesoporous silica. The results of this section were published in **Electrochimica Acta** doi:10.1016/j.electacta.2015.01.129.

Chapter V. Local pH change at the ITIES induced by ion transfer and UV photolysis

The anodic oxidation of water allows the generation of H^+ which can act as a catalyst in the Sol-Gel process of silica leading to uniform and compact film formation at the electrode surface.²⁵⁴ The silica film formation from hydrolyzed alcoxysilane species can be also conducted under high pH values – easily feasible by cathodic water reduction.²⁵⁵ Such approach can be extended to TiO_2 electro-assisted deposition,²⁵⁶ $SiO_2 - TiO_2$ ²⁵⁷ or SiO_2 – conducting polymers²⁵⁸ formation as the electrode modifiers. The electro-assisted (at cathodic potential facilitating OH^- evolution) Sol – Gel process of silica generated in the presence of structure driving agents has led to the formation of well-ordered and oriented normal to the electrode surface mesoporous films.^{97,239} Such properties are of paramount interest in electroanalysis since well-defined mesostructure can act as the molecular sieve, which in case of silica, can be additionally modified with number of functionalities.¹⁰²

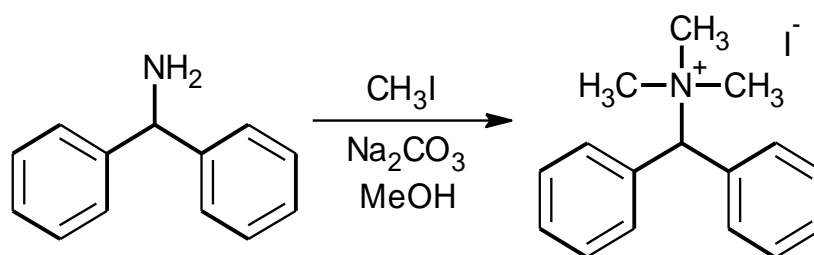
The approach where the H^+ or OH^- generated at the ITIES can indirectly trigger modification of the liquid – liquid interface has never been studied before. Indeed during the interfacial modification with polymer¹⁵³ or polymer-Au NPs¹⁵⁶ the generation of protons as a reaction side product was reported however not evidenced experimentally. The application of interfacially and photo active species (in polymer science such species are known as photobase²⁵⁹ or photoacid²⁶⁰ generators) which photolysis may lead to change in the pH could be applied to trigger pH sensitive reaction as for instance Sol – Gel process of silica.

In this work the trimethylbenzhydrylammonium (PH^+) cation was first synthesised¹⁹⁵ and then used as the interfacially and photoactive ion which photolysis has led to the local pH decrease. First, the PH^+ electrochemical behavior was studied at macro- and microITIES. The

photolysis of the PH^+ was performed with the UV irradiation and it was followed by electrochemistry, HPLC and mass spectroscopy. Interestingly the transfer and subsequent photolysis of PH^+ was not the only source of the pH change. The side reaction at the counter electrode was found to occur – reduction of water at negative interface polarization potentials has led to an increase in pH. The local pH measurement had to be performed in order to separate the pH increase occurring at the aqueous counter electrode from the pH change occurring at the ITIES. To do so the Pt microdisc electrode modified with an iridium oxide (as the pH electrode)^{261,262} was used to probe the pH above the microITIES. Finally, the local pH change was used to trigger the interfacial silica deposition in the liquid – liquid interface configuration where precursor (TEOS) was initially dissolved in the DCE whereas template (CTA^+Br^-) in the aqueous phase.

5.1. Synthesis and characterization of trimethylbenzhydrylammonium iodide

Trimethylbenzhydrylammonium iodide (PH^+I^-) was prepared from aminodiphenylmethane (ADPM) according to the following schematic reaction:¹⁹⁵



Scheme 5.1. Methylation reaction of aminodiphenylmethane

The methylation of primary amine with methyl iodide has led – under proper conditions – to quaternary amine. Detailed protocol of preparation can be found in **section 2.5.7 of chapter II**. The proton NMR spectra for both: ADPM and PH^+I^- can be found on **Figure 5.1** as spectra **a** and **b** respectively. Three characteristic resonances (**Figure 5.1 a**) were attributed to the ADPM

protons. The resonance at around 9.2 ppm, marked with A, corresponds to the protons at the amine group. The multiple peaks from 7.3 to 7.6 ppm, marked as B, are due to the phenyl rings

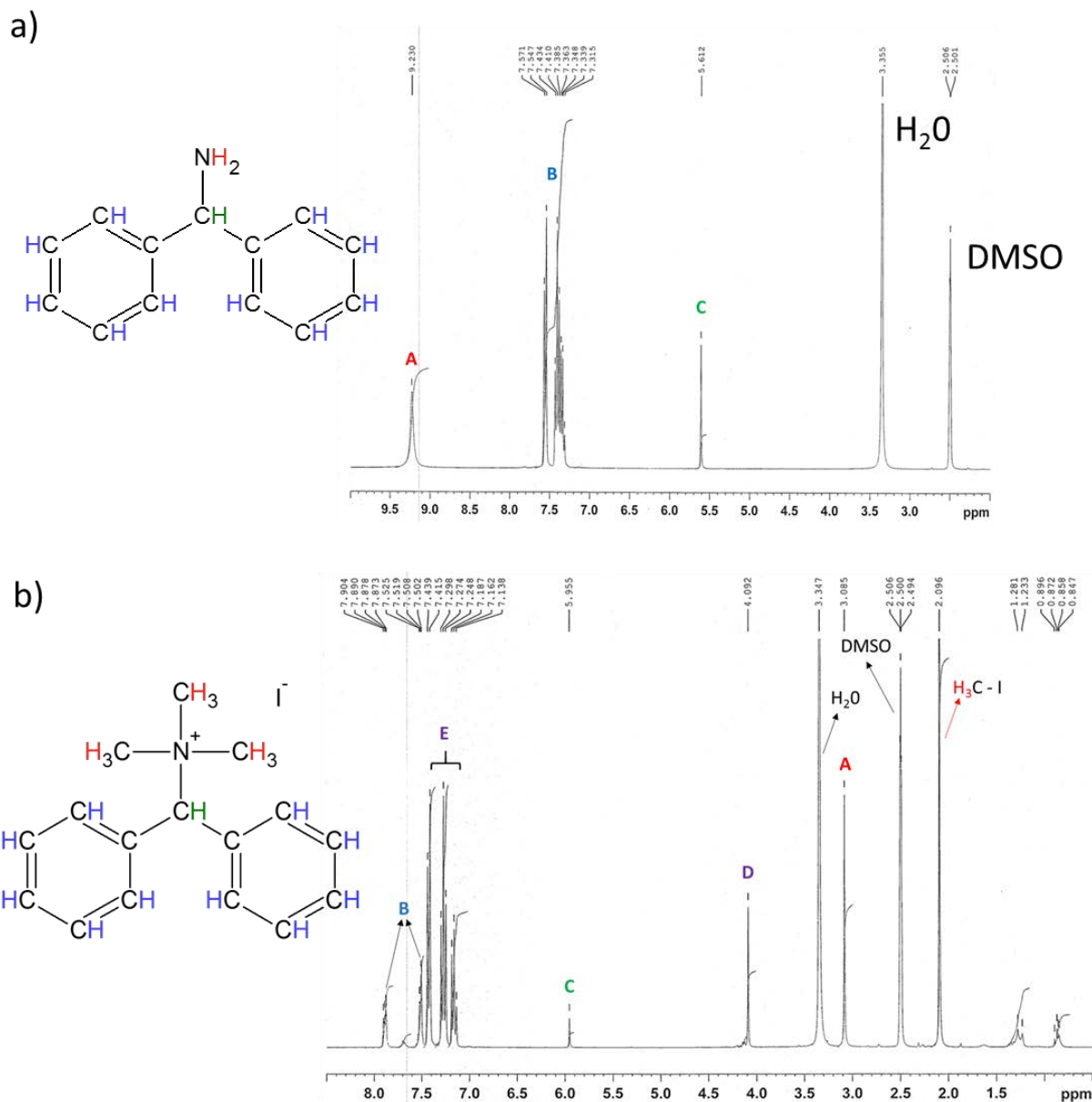


Figure 5.1. Proton NMR spectra for a) ADPM and b) PH^+T . Studied molecules were dissolved in DMSO. Spectra were recorded in the 300 MHz spectrometer.

protons whereas the resonance at around 5.6 ppm is the singlet from the methyl protons. The integration yields: A – 2.93H; B – 10.31H and C – 1H and agrees with number of protons from three distinctive environments. The spectra on **Figure 5.1 b** was recorded for PH^+T in DMSO.

Spectral information allowed the following statements: (i) disappearance of resonance at 9.2 ppm confirms the absence of amine group, and hence the consumption of starting substrate; (ii) the resonances corresponding to PH^+ are marked as A at around 3.1 ppm – methyl group protons at quaternary nitrogen, B at around 7.9 ppm and 7.5 ppm – protons at aromatic substituents – and C at around 6.0 ppm corresponding to proton at methane groups. Integration of the peaks yields: A – 9.5H, B – 10.32H and C – 1H and correlates with the number of protons from three different proton environments in PH^+ molecule; (iii) resonances at D (around 4.1 ppm) and E (in the region from 7.1 to 7.4 ppm) are most probably due to the side reaction products or arise as the reason of the photolysis of PH^+ that might occur during the synthesis and (iv) resonance at 2.1 ppm probably arise from the methylene iodide protons (still present in the post-reaction mixture).

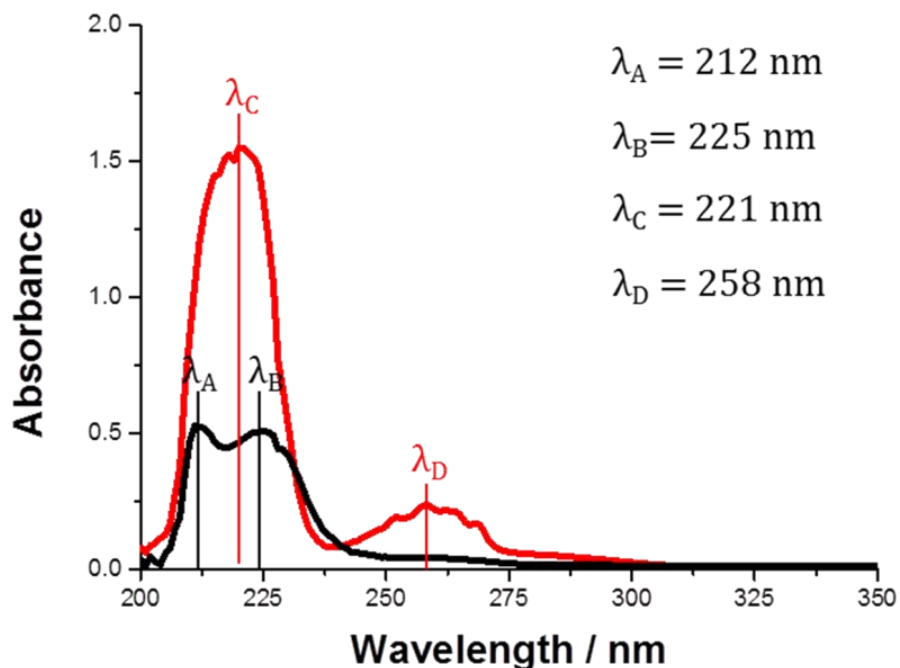


Figure 5.2. UV-Vis spectra for 437 μM PH^+ in ethanol (black line) and diphenylmethanamine in ethanol (red line).

The disappearance of primary amine group of the ADPM after methylation reaction was also confirmed with the UV-Vis spectroscopy. **Figure 5.2** reveals two spectra: marked with black line for PH^+ and red line for ADPM. For both molecules, the existence of two electron-donating

phenyl substituents results in broad absorption bands with the maximum absorption peaks at $\lambda_C = 221$ nm for ADPM and $\lambda_A = 212$ nm and $\lambda_B = 225$ nm for $\text{PH}^+\Gamma$. For the ADPM, the presence of pair of unbounded electrons at the nitrogen atom of primary amine group additionally gave rise to the second, well separated band with the maximum absorption at $\lambda_D = 258$ nm. The disappearance of this absorption band after methylation reaction confirms the formation of ammonium group.

Raman spectra shown on **Figure 5.3** were recorded for the $\text{PH}^+\Gamma$ (black line) and ADPM (red line). Methylation reaction can be followed in the spectral region from 2700 to 3200 cm^{-1} . The presence of methyl groups was confirmed based on the vibrational modes of symmetric CH_3 stretching – see region marked as A – and antisymmetric CH_3 stretching – see region marked as B – both clearly present after the methylation reaction. A series of peaks in the region C arose from aromatic C–H vibrations of two phenyl substituents.

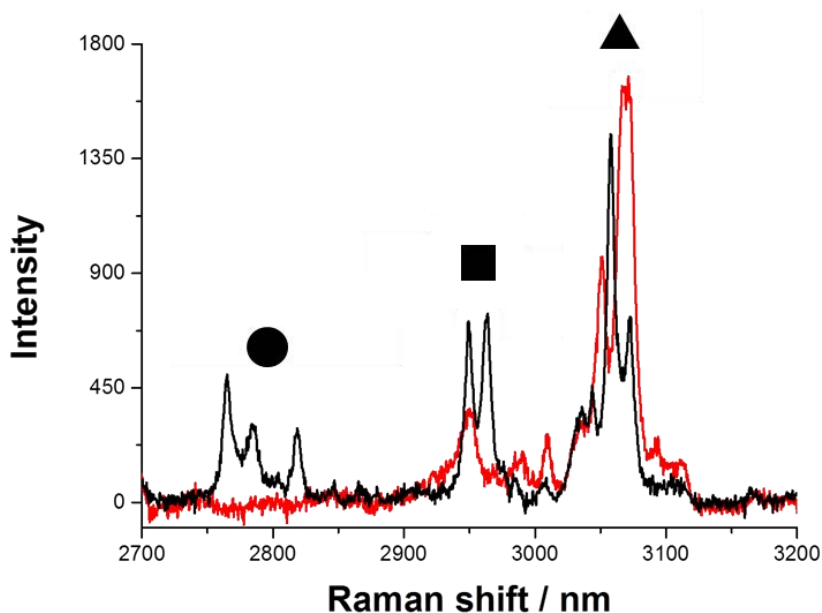


Figure 5.3. Raman spectra in the region from 2700 to 3200 cm^{-1} . Bands correspond to: ● – symmetric CH_3 , ■ – antisymmetric CH_3 and ▲ aromatic C–H vibrational modes respectively. Black line correspond to $\text{PH}^+\Gamma$ whereas red line to ADPM.

The electrochemical behavior of $\text{PH}^+\Gamma$ (see **Figure 5.4 a**) was studied at the single pore glass capillary supporting microITIES – for protocol of preparation refer to **section 2.5.6 in chapter II**. The pore diameter was 25 μm and the interior of the capillary was silanized prior to

the experiments in order to prevent the leakage of the organic phase during the measurements. The CV marked with a dashed line was recorded in the **cell 5** for $x = 0$ mg/mL and corresponds to a blank voltammogram. The solid curve was recorded in the presence of post-synthesis mixture containing the PH^+T (0.5 mg/mL) in the organic phase. The direction of polarization (from more positive to less positive potential) was chosen in agreement with the positive charge of PH^+ initially present in the organic phase. Two signals arise among the available potential window: (i) the couple of peaks with $E_{1/2}$ equal to around +200 mV were attributed to PH^+ transfer. The forward peak centered at around +160 mV suggests the direction of transfer of the interfacially active species from the organic to the aqueous phase (linear diffusion for the applied scan rate was only present inside the capillary filled with the organic phase – **Figure 5.4 (c)**) and along with the negative value of current, It indicates that the transferring species were positively charged.

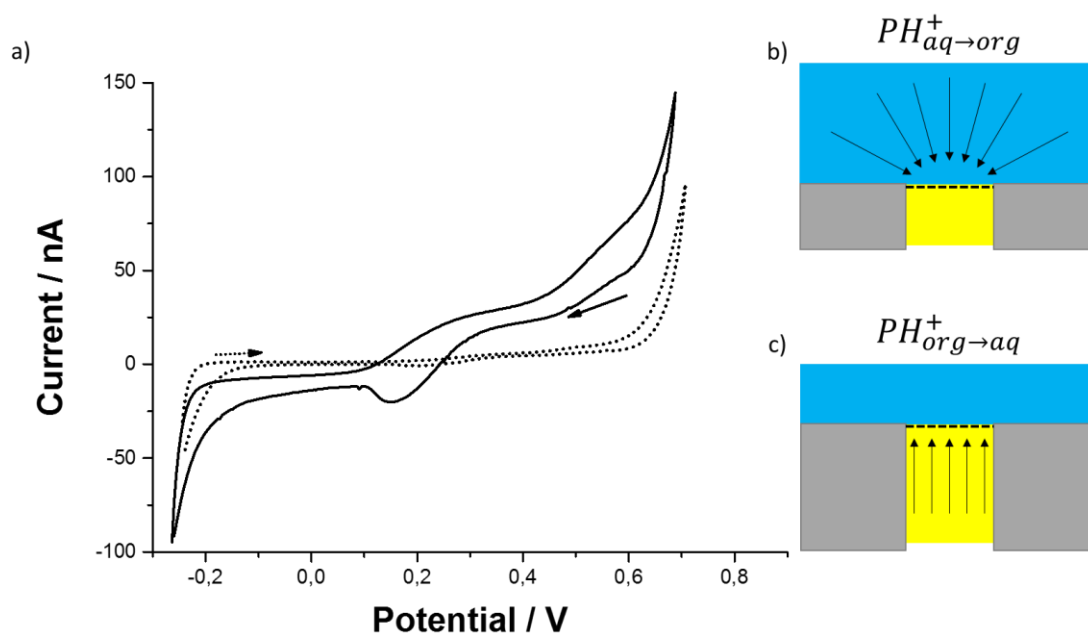
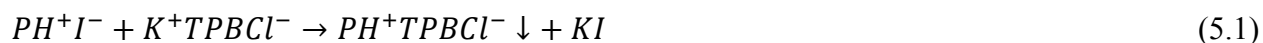


Figure 5.4. Cyclic voltammograms recorded at single pore microITIES. Dashed line represents to blank CV. Solid line corresponds to 0.5 mg/ml post-synthesis mixture containing PH^+T dissolved in the organic phase. The arrows indicate the direction of polarization on the forward scan. Scan rate was 5 mV/s. Schemes b) and c) correspond to radial diffusion from the aqueous side of the interface and linear diffusion from the organic side of the interface respectively.

The $PH_{aq \rightarrow org}^+$ back transfer forms the wave like signal which is expected for non-diffusion limited mass transfer governed by the hemispherical diffusion layer on the aqueous side of the liquid – liquid interface (see **Figure 5.4 (b)**). (ii) A second pair of signals at a positive potential, partially masked by the background electrolyte transfer (the potential window is limited by $TPBCl_{org \rightarrow aq}^-$ transfer), were attributed to the transfer of the side reaction product(s) rather than $I_{org \rightarrow aq}^-$ transfer. It is because the standard half wave potential expressed in the Galvani potential scale ($\Delta_{org}^{aq} \phi_{1/2}$) for iodide is $-340 \text{ mV}^{1,21,245}$ and hence I^- would be expected to cross the interface at the more negative side of the potential window. Unfortunately, showing the potential scale as the standard Galvani potential difference is not possible since no internal reference was present in the system. Moreover, for the signal with $E_{1/2}$ at around $+550 \text{ mV}$ it was also difficult to study the effect of capillary geometry on the shape of the signal itself since it is partially masked with the background electrolyte transfer and hence the charge of the transferring specie remains unknown. The presence of undesirable species transferring on the positive side of the available potential window required further processing, hence the PH^+ was precipitated from the post-synthesis mixture with $TPBCl^-$ (please refer to **section 2.5.4 in chapter II** for protocol of PH^+TPBCl^- preparation):



After filtration, the white precipitate was rinsed four times with 50 mL of distilled water (the flask containing PH^+TPBCl^- and 50 mL of H_2O was place in the ultrasound bath for 10 min each time). After sonification each sample was centrifuged. Next, the aqueous phase was collected from above the solid PH^+TPBCl^- and analyzed by the ion chromatography.

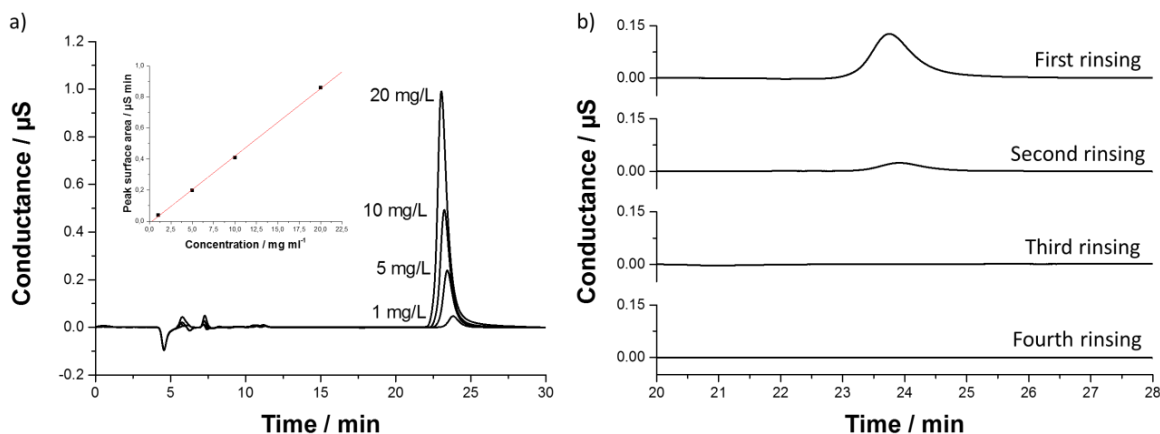


Figure 5.5. Ion chromatography used for iodides detection. a) Chromatograms for known concentrations of aqueous solutions of potassium iodide (insert corresponds to a calibration curve), b) chromatograms for water used for iodides extraction for four subsequent purification steps after $\text{PH}^+\text{TPBCl}^-$ metathesis reaction. The eluent used was the aqueous solution of 3.2 mM Na_2CO_3 and 1 mM NaHCO_3 . In all cases the background was subtracted for better data presentation.

The concentration of iodides in each sample was calculated based on the calibration prepared prior to the experiment – refer to **Figure 5.5 (a)**. **Figure 5.5 (b)** shows the chromatograms for four samples after subsequent rinsing in the region of iodides retention time peak. After first rinsing the iodides concentration was equal to 3.07 mg/mL and dropped to 0.74 mg/mL after second rinsing. No iodides were detected after third and fourth rinsing. Based on this result three rinsing steps were adopted for iodides removal after the metathesis reaction.

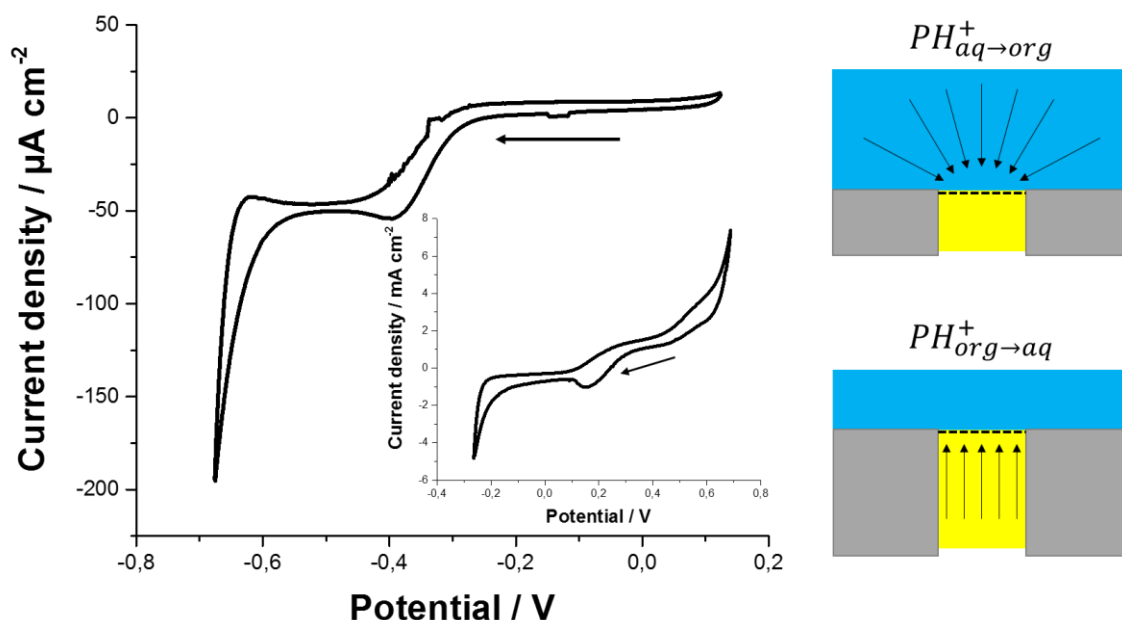


Figure 5.6. The current density versus potential recorded for 1 mM $\text{PH}^+\text{TPBCl}^-$ initially present in the organic phase at array of microITIES (8 pores each having 50 μm in diameter). Insert is the current density versus potential for PH^+T before metathesis reaction (recorded at single pore microITIES with diameter equal to 25 μm). The schemes represent the radial diffusion from the aqueous side of the interface and linear diffusion inside the pore filled with the organic phase. Solid arrows indicate the direction of polarization during forward scan. Scan rate was 10 mV/s.

The fulfilment of the metathesis reaction was finally confirmed with the ion transfer voltammetry. **Figure 5.6** shows the current density versus potential recorded at array of microITIES (8 pores, each having 50 μm in diameter being separated from each other by the distance of 500 μm) for 1 mM $\text{PH}^+\text{TPBCl}^-$ initially present in the organic phase. The metathesis reaction has led to a disappearance of the signals at the positive off-end of the potential window (clearly visible on the CV shown as an insert of **Figure 5.6** which was recorded before metathesis reaction). The presence of the pair of signals with $E_{1/2}$ at +350 mV, as well as their geometry (peak like on the forward – linear diffusion inside the pore – and wave like on the reverse scan – radial diffusion on the pore ingress) confirms the occurrence of the PH^+ interfacial transfer.

5.2. Electrochemical characterization of PH^+ transfer at macroITIES

Figure 5.7 A shows the CVs recorded in the cell with macroscopic liquid – liquid interface. The curve marked with the dashed line represents a blank voltammogram recorded only in the presence of supporting electrolytes (5 mM NaCl in the aqueous phase and 10 mM $\text{BTPPA}^+\text{TPBCl}^-$ in the organic phase). The curve marked with the solid line was recorded in the **cell 5** for $x = 330 \mu\text{M}$. The polarization direction, based on the charge of PH^+ , was from a more positive to a less positive potential during forward scan. For the concentration studied, PH^+ starts to transfer from the organic to the aqueous phase at around +350 mV, reaching maximal current ($-67.5 \mu\text{A}$) for the peak at +220 mV. On the reverse scan, the back transfer peak center was found at +350 mV with a height of $64.7 \mu\text{A}$. The half-wave transfer potential ($E_{1/2}$) for the PH^+ is +300 mV. CVs for different concentration of PH^+ in the organic phase (from $50 \mu\text{M}$ to $832 \mu\text{M}$) are overlaid and shown on **Figure 5.7 B**. The linear increase of current on the forward scan in function of the concentration is shown as an inset of **Figure 5.7 B**. The increasing peak separation for higher analyte concentrations is common at liquid – liquid interface and might arise from the system resistivity likewise from PH^+ partial interfacial adsorption.

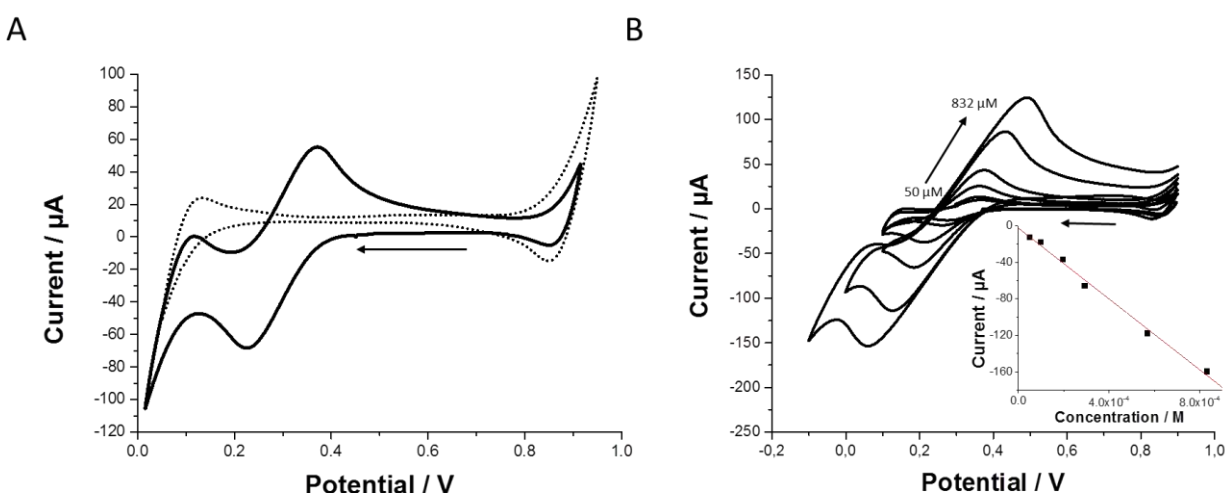


Figure 5.7. A – Cyclic voltammogram in the absence (dotted line) and presence (solid line) of $330 \mu\text{M}$ $\text{PH}^+\text{TPBCl}^-$ in the organic phase. B – Cyclic voltammograms for different concentration of $\text{PH}^+\text{TPBCl}^-$ in the organic phase: $123,4 \mu\text{M}$; $470 \mu\text{M}$; $1,01 \text{ mM}$; $2,02 \text{ mM}$ and $2,82 \text{ mM}$. Insert shows the current of the

forward peak versus concentration of the PH^+ . Solid arrows indicate the direction of polarization during forwards scan. Scan rate was 10 mV/s.

The scan rate dependence for 50 μM PH^+ was also studied and the results are shown on **Figure 5.8 A**. The ratio between forward and reverse peak currents was in the range between 1.03 for 5 mV/s up to 1.09 for 25 mV/s and is very close to 1 among all studied scan rates and together with the forward and reverse peak current center to center distance equal to 54 mV (very close to the 59 mV for monocharged species) the PH^+ transfer reaction can be classified as a reversible process. The square root from the scan rate versus current for the forward and reverse peak is shown on the **Figure 5.8 B**. A linear relationship was found over a range of scan rates (5 mV/s to 25 mV/s) and the diffusion coefficient (D) was calculated from the slope of the $I_p/v^{1/2}$ based on Randles-Sevcik equation:

$$I_p = (2.69 \times 10^5) z^{3/2} A D^{1/2} C v^{1/2} \quad (5.2)$$

where z is the charge, A is the interfacial surface area (2.83 cm^2) and C is the concentration ($50 \times 10^{-9} \text{ mol/cm}^3$). The obtained value of $6.91 \cdot 10^{-6} \text{ cm}^2/\text{s}$ is of the same order of magnitude as interfacially active species having similar hydrodynamic radius.¹ The behavior of PH^+ at the polarized ITIES can be classified as ‘common’ for known mono-charged quaternary ammonium cations. Its interfacial transfer can be easily controlled with electrochemical methods as for instance cyclic voltammetry, which in parallel can be used as an analytical detection method.

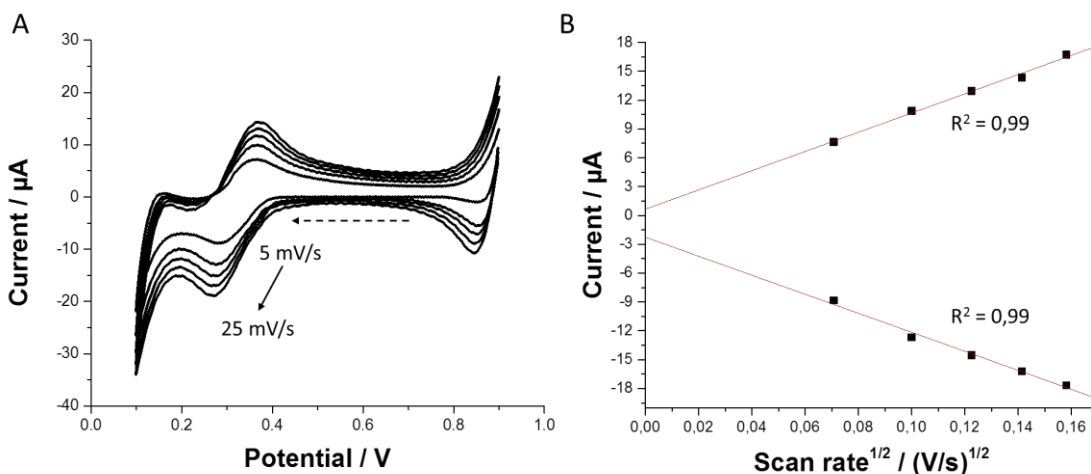
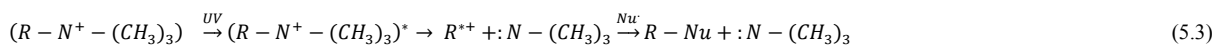


Figure 5.8. A – Cyclic voltammograms recorded for PH^+ interfacial transfer (concentration $50 \mu\text{M}$) initially present in the organic phase at different scan rates (from 5 to 25 mV/s every 5 mV/s). B – Correspond to the positive and negative peak current versus square root from the scan rate. R^2 is the coefficient of determination of linear fitting. Dashed arrow shows the direction of the polarization during a forward scan.

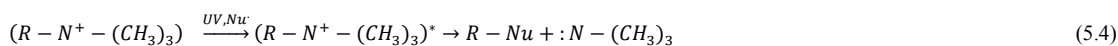
5.3. Study of photodecomposition of PH^+ species

Depending on the environment (in the presence or in the absence of nucleophiles in the liquid media) the photolysis reaction can result in three most probable mechanisms:¹⁹⁵

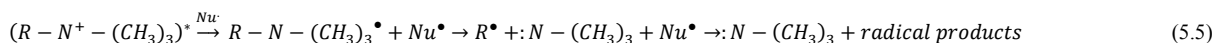
(1) Photo $\text{S}_{\text{N}}1$



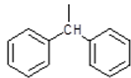
(2) Photo $\text{S}_{\text{N}}2$



(3) Single electron transfer (SET)



The abbreviations stand for:

UV – for Ultraviolet, Nu – for nucleophile and R – for 

First mechanism (photo S_N1) is expected to give tertiary amine ($:N - (CH_3)_3$) and a carbocation that reacts with the nucleophile and gives $R - Nu$ products. Photo S_N2 leads to a tertiary amine and $R - Nu$ through the formation of the intermediate. In the single electron transfer (SET) mechanism the electron from the nucleophile is excited by the UV irradiation and can transfer to the aromatic system of the quaternary ammonium cation. The resulting radical is then dissociated into the benzhydryl radical and the tertiary amine. When the photolysis of PH^+ cations carrying I^- or $TPBCl^-$ as the counter ion was studied in water or EtOH photo S_N1 mechanism was considered to take place (polar protic solvent favor S_N1 mechanism). In the case of the photolysis reaction which was taking place in DCE – SET mechanism was very probable.¹⁹⁵

PH^+ photolysis products were studied by HPLC. **Figure 5.9 A** is the reference chromatogram recorded for EtOH. Chromatogram from **Figure 5.9 B** was recorded for PH^+I^- dissolved in EtOH without any irradiation. Peak at 0.57 min correspond to the solvent (EtOH), whereas the peak at 12.28 min was attributed to PH^+ species. In the second approach the UV irradiation was coupled with the electrochemistry at the liquid – liquid interface. **Figure 5.9 C** correspond to the chromatogram recorded for the aqueous phase collected from above the organic phase after 50 min of chronoamperometric ($E = +150$ mV) $PH^+_{org \rightarrow aq}$ transfer with simultaneous UV irradiation. The series of peaks up to 3 min and an intense peak at 3.14 min were observed and attributed to the products of photo decomposition. Very weak peak was also recorded at around 12.95 min and originates from remaining PH^+ ions. **Figure 5.9 D** correspond to the reference chromatogram – for the aqueous phase from the liquid – liquid system being applied to identical conditions as in case of chromatogram from **Figure 5.9 C** in the absence of PH^+TPBCl^- .

Photolysis of PH^+ in the aqueous solvent has led to the formation of benzhydryl carbocation. The stability of carbocation in the nucleophilic (aqueous) solvent should be relatively weak and hence formation of alcohol is expected (less probable adjuncts are also possible for instance: benzhydryl chloride). The peak at around 3.14 min was assigned to the resulting benzhydrol (see **Figure 5.9 C**) and was confirmed by the injection of pure benzhydrol into the chromatographic column. Trace of undecomposed PH^+ can also be seen as very weak

signal at around 12.95 min. The peaks recorded up to around 3 min were assigned to the products of organic electrolyte decomposition and subsequent partition to the aqueous phase since a similar set of peaks was recorded during the blank experiment shown on **Figure 5.9 D** (the chromatogram was recorded for the aqueous phase collected after 50 min of chronoamperometric polarization at +150 mV in the absence of $\text{PH}^+\text{TPBCl}^-$ in the organic phase with simultaneous irradiation).

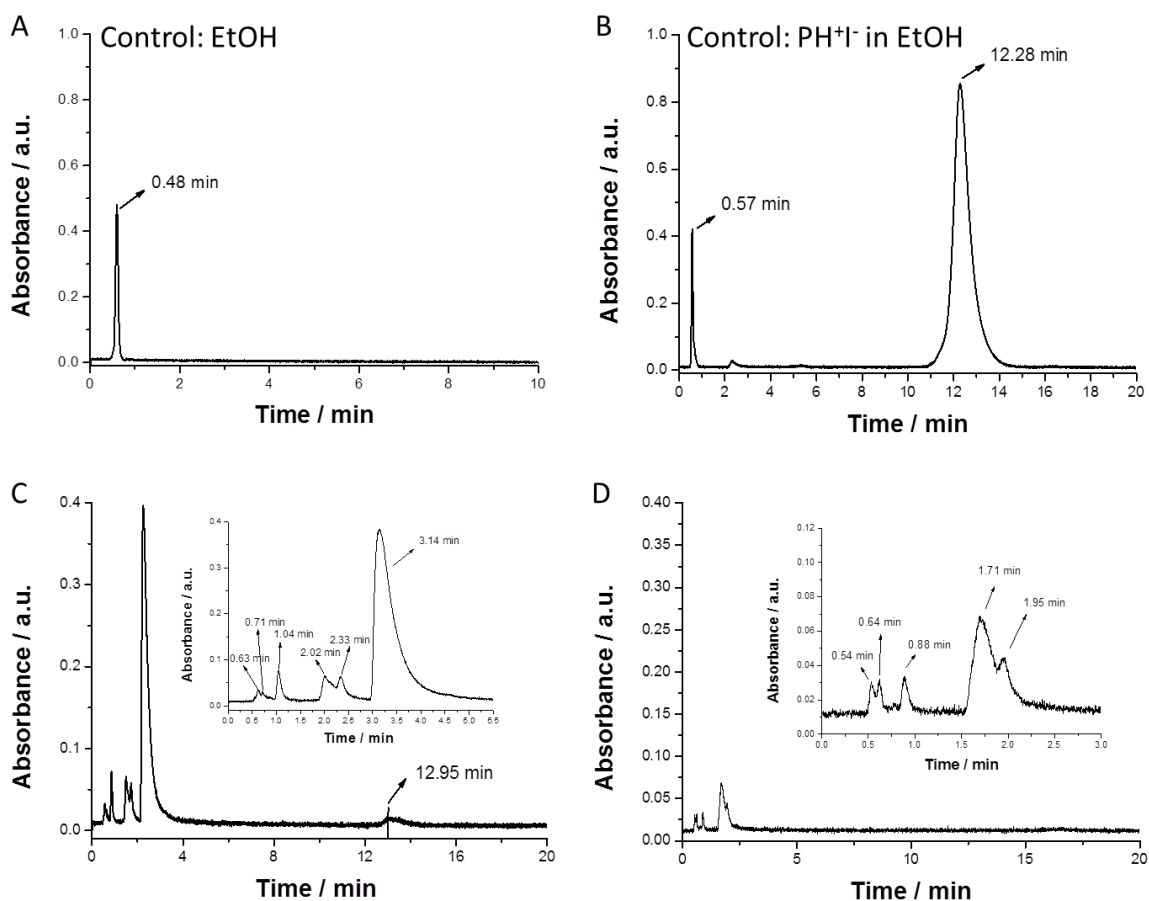


Figure 5.9. Chromatograms recorded during photodecomposition study of PH^+ cations: A – pure EtOH; B – 100 μM PH^+I^- in EtOH; C – aqueous phase collected from the liquid – liquid cell after 50 min of chronoamperometric transfer ($E = 0.15$ V) of PH^+ from the organic to the aqueous phase with simultaneous UV irradiation and D – the aqueous phase collected from the liquid – liquid cell under condition applied in part A in the absence of $\text{PH}^+\text{TPBCl}^-$ in the organic phase. Mobile phase flow rate was 3 ml/min. The wavelength of detector was 220 nm.

Photolysis of PH^+ could also be followed by cyclic voltammetry as shown in **Figure 5.10**. The liquid – liquid cell was under open circuit potential during irradiation and CVs were recorded before and after 40 min of irradiation. The current decrease on the forward and reverse peak induced by continuous UV irradiation suggests degradation of interfacially active PH^+ species in the organic phase. The forward and reversed peak currents has decreased from $i_f = 129.6 \mu\text{A}$ and $i_r = 131.4 \mu\text{A}$ before irradiation down to $i_f = 69.3 \mu\text{A}$ and $i_r = 44.5 \mu\text{A}$ after 40 min of UV irradiation. Interestingly the available potential window has been narrowed as a large background current was recorded at the positive end of potential scale. This increase observed can be attributed to proton ion transfer. The origin of the increased concentration of protons is discussed the following section.

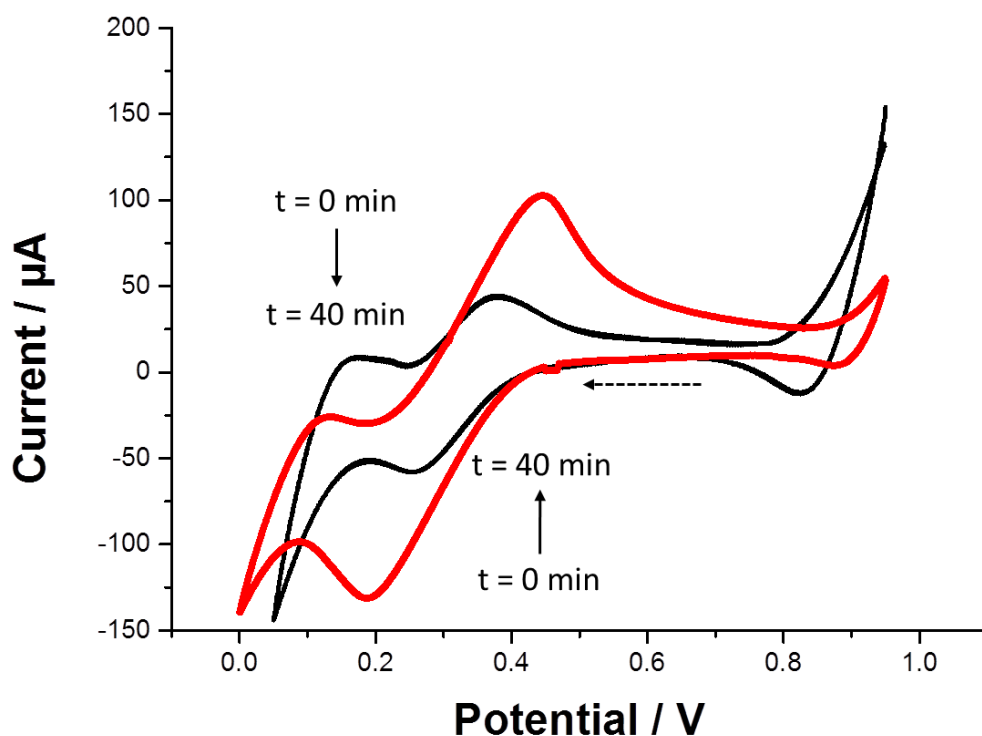


Figure 5.10. Cyclic voltammogram recorded for 1.01 mM $\text{PH}^+\text{TPBCl}^-$ initially present in the organic phase is marked with red line. Black curve was recorded after 40 minutes of UV irradiation. Solid arrows show the current decrease caused by irradiation. The direction of polarization is indicated with dashed arrow. Scan rate was 10 mV/s.

Mass spectroscopy was employed in order to study the content of the aqueous phase after $\text{PH}_{org}^+ \rightarrow aq$ electrochemical transfer and subsequent UV irradiation. For this purpose, the volume

of the aqueous phase in the electrochemical cell was decreased in order to increase final concentration of PH^+ species. After 60 min of chronoamperometric polarization (at $E = +150$ mV) the aqueous phase was transferred to a separate vessel, which thereafter was irradiated with UV light for another 60 minutes. A sample was injected to a mass spectrometer and the loop was cleaned with methanol for which the spectrum was recorded (presence of sodium chloride in the aqueous phase significantly increased noise to signal ratio of the mass spectrometer). The obtained mass spectrum is shown on **Figure 5.11**. The peak with the highest relative abundance at the m/z equal to 167.0860 a.m.u. was attributed to the benzhydryl cation

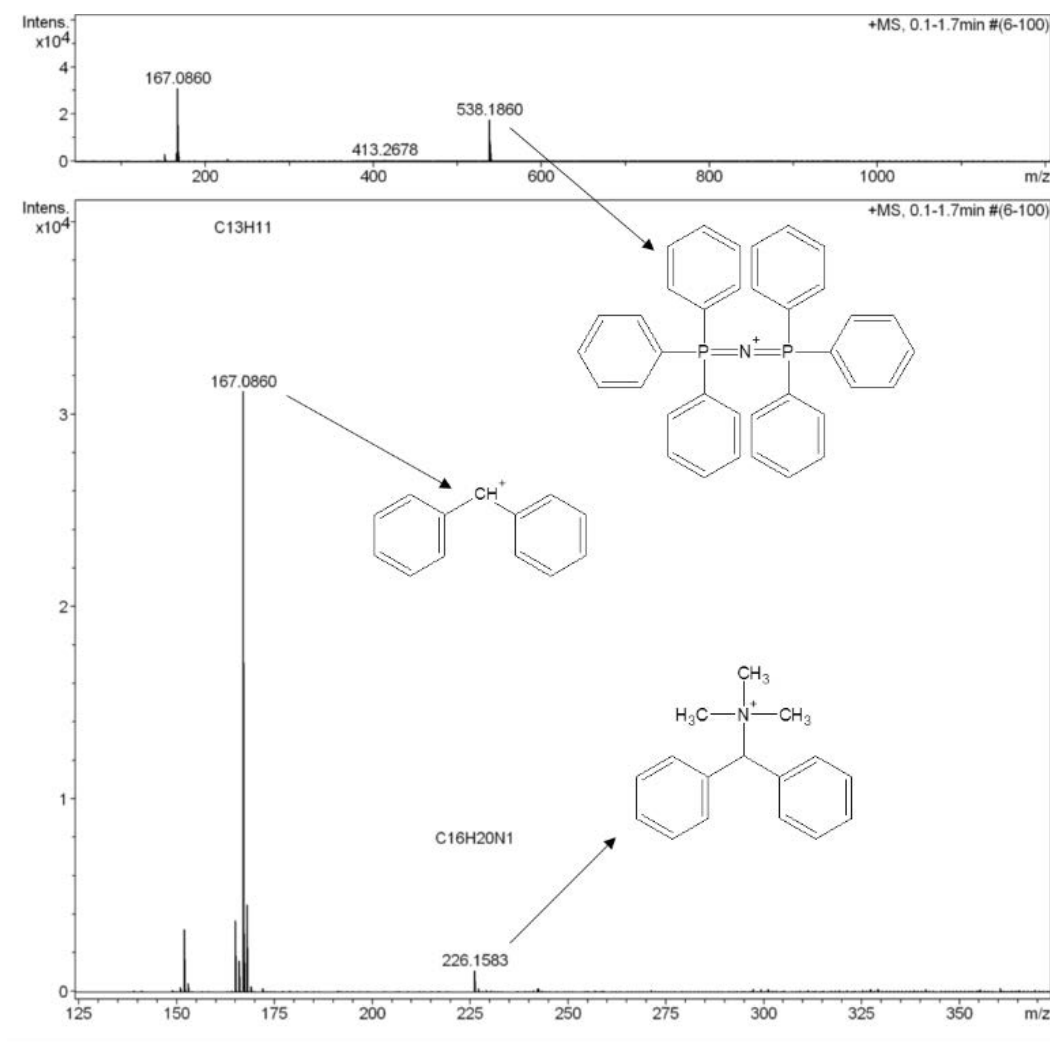


Figure 5.11. Mass spectrum recorded for aqueous phase after 60 min of chronoamperometric $\text{PH}_{org}^+ \rightarrow aq$ followed by 60 min UV irradiation. Initial $[\text{PH}^+\text{TPBCl}] = 1$ mM.

arising probably from benzhydrol (ionization has occurred in the mass spectrometer). The weak signal at m/z at 226.158 a.m.u. arise from traces of non-photodissociated PH^+ species. The presence of the signal at m/z at 538.186 a.m.u. with surprisingly high relative abundance – due to BTPPA^+ species which presence in the aqueous phase should be rather negligible – arise as a result of the way how the sample was injected to the spectrometer. As mentioned above it was recorded for the MeOH solution used to clean the loop from the residual molecules from the previous, aqueous sample. The solubility of the BTPPA^+ is much greater in MeOH and as a consequence gives strong signal.

The photodecomposition was confirmed and followed with three different techniques: cyclic voltammetry indicating disappearance of interfacially active species in the organic phase upon UV irradiation; chromatography which allowed the separation of photolysis products and finally mass spectroscopy aiming to study the nature of the aqueous phase photolysis products.

5.4. Local pH change induced by electrochemical transfer and photodecomposition of PH^+ species

To study the effect of PH^+ photodecomposition on the aqueous phase pH, the PH^+ species were transferred by electrochemistry to the aqueous phase with subsequent UV irradiation. First pH measurements were performed with the standard pH meter. pH increase was observed, however not due to photoelectrochemistry but as a reason of side reaction on the counter aqueous electrode – water reduction ($2\text{H}_2\text{O} + 2e^- \rightarrow \text{H}_2 + 2\text{OH}^-$). The effect of negative polarization on the aqueous phase pH was further studied and the results are shown on **Figure 5.12**. For each point, the ITIES was held at corresponding potential for 150 seconds (red circles) and 420 seconds (black squares). Apparently the pH of the aqueous phase stays unaffected up to 0 V. The pH jump due to OH^- electrogeneration at the aqueous counter electrode was observed at around -100 mV and reaches plateau for potentials < -200 mV. The pH change around the counter electrode was additionally detected with the pH indicator – phenolphthalein – added to the aqueous phase during voltammetric cyclic in the presence of $\text{PH}^+\text{TPBCl}^-$ in the organic phase.

The fuchsia cloud – indicating the pH increase – around the counter aqueous electrode starts to be visible once the +100 mV was reached on the forward scan. The interface polarization towards the less positive potential caused the increase of fuchsia cloud. On reverse polarization the fuchsia cloud was seen up to +300 mV until it became blurred away and disappeared. No change in color was detected in the vicinity of the liquid – liquid interface neither in the absence nor in the presence of UV irradiation coupled with the $PH_{org \rightarrow aq}^+$ transfer.

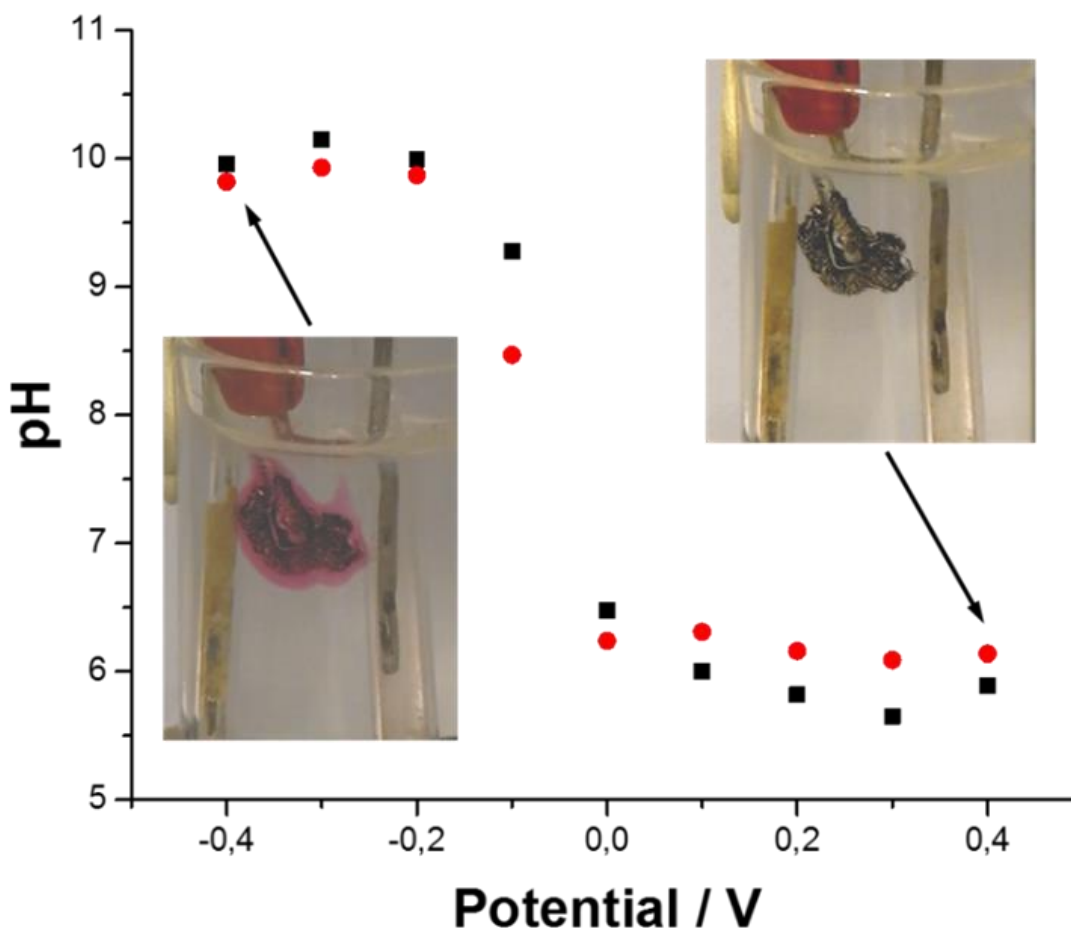


Figure 5.12. Changes of the aqueous phase bulk pH induced by the side reaction at platinum mesh counter electrode. pH for each point was measured after 150 seconds (red circles) and 420 seconds (black squares) of chronoamperometric polarization at given potential. pH at OPC before polarization was 5,73 for (red circles) and 5,83 for (black squares). Photos indicate the change in color of phenolphthalein around the platinum electrode.

The masking effect caused by the side reaction at the aqueous counter electrode highlighted the need to measure the pH locally. The set-up used for this purpose can be found on

Figure 2.3 in **section 2.2**. The liquid – liquid interface was supported with the array of pores, each having 50 μm in diameter, and hence the local pH measurements in the micrometer scale had to be performed. Several possible pH probes could be employed in this regard. Examples include: (i) microelectrodes modified with neutral carrier-based ion-selective liquid-membrane,²⁶³ (ii) the two-dimensional semiconductor pH probe,²⁶⁴ (iii) the antimony-antimony oxide electrodes²⁶⁵ or (iv) electrodes modified with iridium oxide.^{261,262} Especially the last example is worthy of note. Iridium oxide modified electrodes exhibit Nernstian behavior, are stable over long time periods, have a pH operating range from 2 to 12 and they are cheap as compared with iridium microwires. One of the methods of preparation is an electrodeposition from the alkaline iridium (III) oxide solution. Such an approach was employed in this work to modify Pt microdisc electrodes. Modification with iridium oxide was performed with 10 subsequent voltammetric scans (see **Figure 5. 13 A**) at scan rate of 50 mV/s between 0 V and +1300 mV – versus silver wire reference electrode.

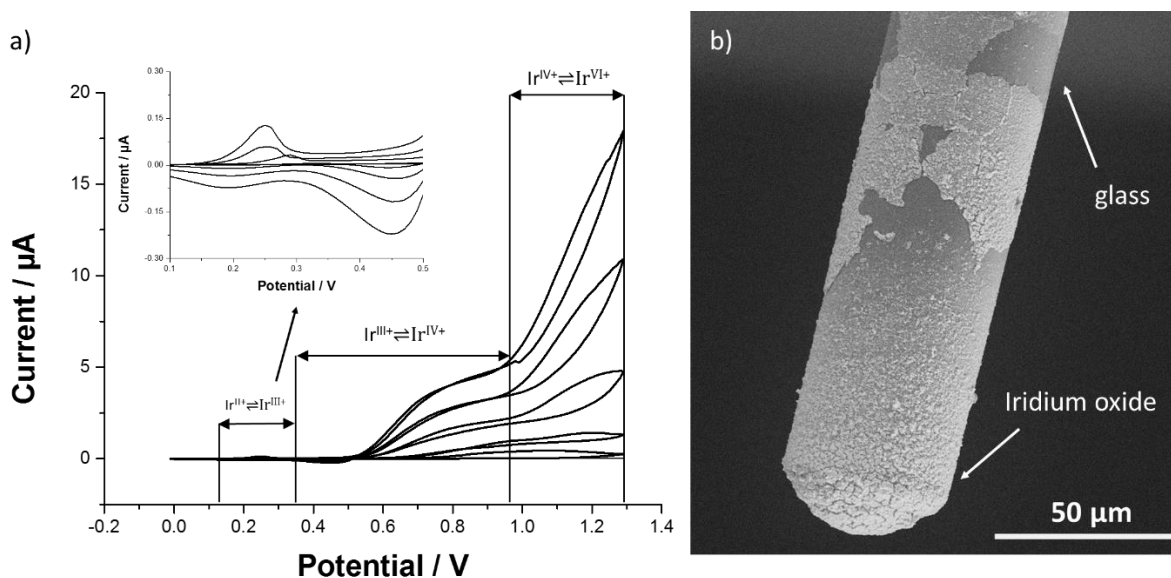


Figure 5. 13. a) Cyclic voltammograms recorded during the electrodeposition of iridium oxide at Pt microelectrodes, b) is the SEM image of the corresponding modified electrode.

On the forward scan, the electrode was polarized towards an anodic potential. Three pairs of signals corresponding to different oxidation states of iridium can be distinguished: (i) $E_{1/2}^1$ of 220 mV due to $\text{Ir}^{II+} \rightleftharpoons \text{Ir}^{III+}$ redox couple, (ii) $E_{1/2}^2$ at around 0.63 V originating from the $\text{Ir}^{III+} \rightleftharpoons \text{Ir}^{IV+}$ redox couple and (iii) the signal on the positive extreme of the potential window arising

from $Ir^{IV+} \rightleftharpoons Ir^{V+}$ reaction. The overall electrochemically induced reaction for the deposition of iridium oxide for the $E > +1200$ mV can be schematically written as:²⁶¹

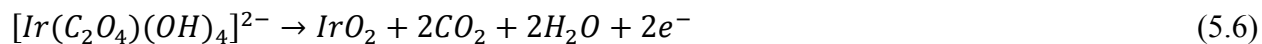


Figure 5. 13 B shows the SEM image of the Pt microdisc electrode modified under conditions described above. The amount of the iridium oxide deposit significantly exceeds the electroactive surface area of the Pt microdisc electrode sealed inside the glass; nonetheless its size still does not emerge from the scale limiting local measurements. Moreover, the pH dependent potential for the electrodes with greater amount of the deposited iridium oxide was more likely to be stable.

Ion transfer voltammetry allowed the control of PH^+ transfer to the aqueous phase where it was exposed to UV irradiation. The product of the photolysis, reactive carbocation, underwent the reaction with the aqueous media which in turn has affected the aqueous phase pH (in the vicinity of the liquid – liquid interface). To verify this finding the potentiometric pH measurements were performed with the iridium oxide modified Pt microdisc electrode performed above the liquid – liquid interface. The results are shown on **Figure 5.14**. The precise electrode position was control by shear force.²⁶⁶ Prior to and after the experiments, the pH probe was calibrated in two buffer solutions with pH equal to 4 and 7 (see the insert of **Figure 5.14**). The pH of the aqueous phase (5 mM NaCl solution) in the bulk was measured at 7.4. Next, the pH probe was situated 1 μ m above the liquid – liquid interface and the polarization was held at +150 mV (potential low enough to transfer $PH_{org \rightarrow aq}^+$ and high enough to avoid significant water reduction at the aqueous counter electrode) without any irradiation. No pH change, equal to around 6, was detected. Next, the polarized interface was subjected to simultaneous irradiation. The pH started to decrease after the first 5 minutes of transfer and irradiation and drop after 25 minutes. After 50 minutes the measured pH was around 1, which exceeded the working range of the iridium oxide modified electrode and the measurement is no longer reliable. The pH measured in the bulk solution after the experiment was around 7.5 and was similar to the value recorded prior to changes in the chemical composition of the aqueous phase.

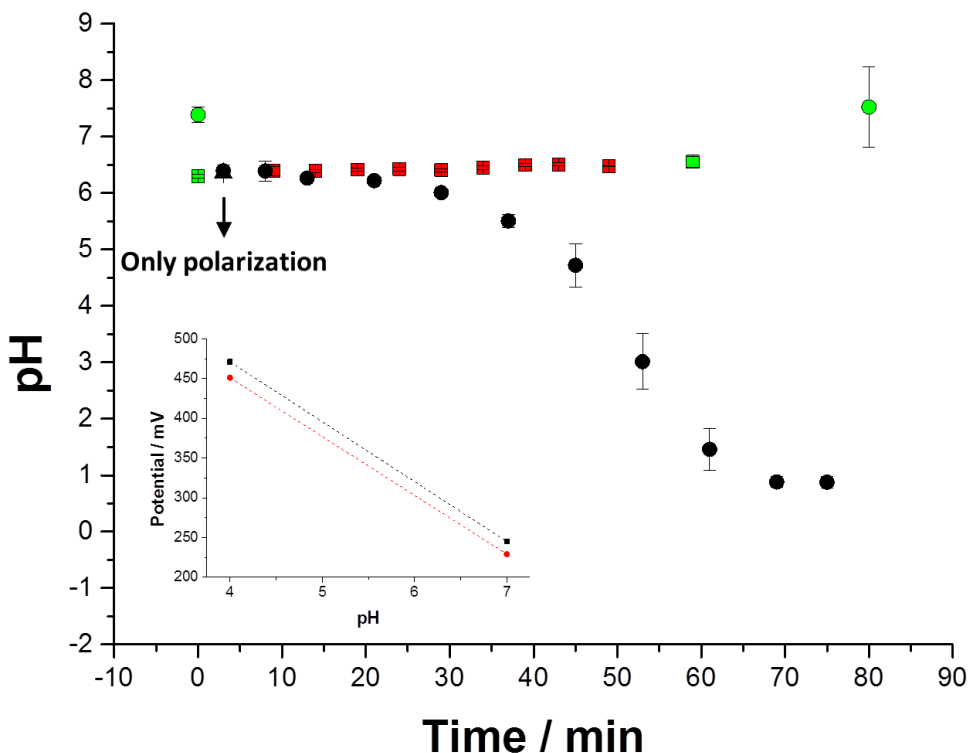
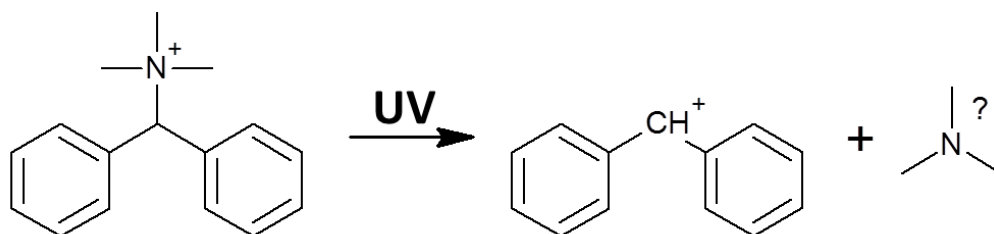


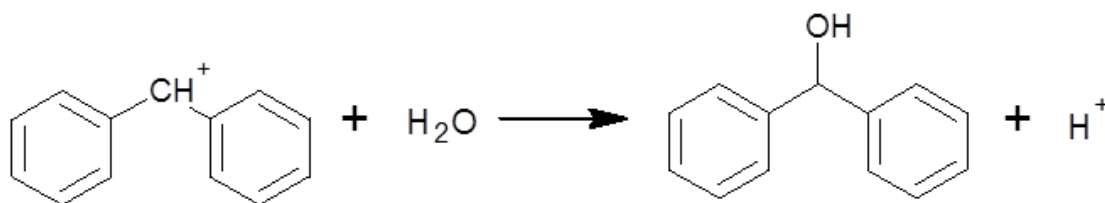
Figure 5.14. Local pH measurements in function of experimental time. Black circles correspond to the pH measurements 1 μm above the ITIES in the presence of 1 mM $\text{PH}^+\text{TPBCl}^-$ in the organic phase during $\text{PH}_{org \rightarrow aq}^+$ transfer and simultaneous UV irradiation (with the exception of the first point recorded 1 μm above the ITIES in the absence of irradiation). Red squares were recorded under identical conditions in the absence of $\text{PH}^+\text{TPBCl}^-$ in the organic phase. Green symbols correspond to the pH measurements in the bulk aqueous phase performed before and after local pH measurements. Insert correspond to the calibration curves recorded before (black points) and after (red point) experiment with the $\text{PH}^+\text{TPBCl}^-$ in the organic phase.

Based on previous findings it can be concluded that the UV irradiation of the PH^+ in the aqueous phase resulted in carbocation formation as shown **Scheme 5.2**:



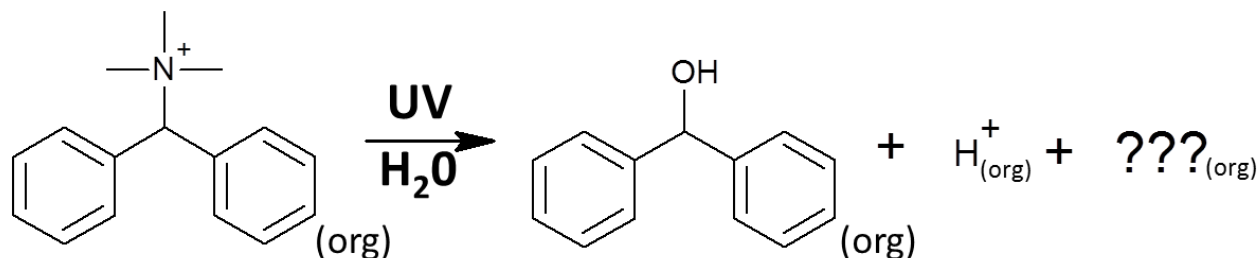
Scheme 5.3. The reaction of PH^+ photolysis.

No experimental evidence was found to support the formation of the trimethylammonium and hence it is possible that under the harsh conditions employed (high intensity of UV irradiation) the reactive nitrogen radicals underwent the recombination reaction with either the organic electrolyte salt or dichloroethane molecules dissolved in the aqueous phase. The carbocation formed in the aqueous phase upon PH_{org}^+ transfer and irradiation is expected to react with water:



Scheme 5.4. The reaction between carbocation and water molecules.

This is causing the local pH decrease as the protons are released during the reaction shown on **Scheme 5.4**. Photodecomposition of the PH^+ in the organic phase can also occur (see **Figure 5.10**). The carbocation formed in the DCE is expected to preferentially react with the traces of water dissolved in the organic phase as its stability is higher in chlorinated organic solvents.²⁶⁷



Scheme 5.5. Possible photolysis reaction of PH^+ in the DCE.

The exact nature of species marked with $???(org)$ was not studied and it can be only assumed that these arise from the nitrogen radical reactions which transfer to the organic phase. The $\Delta_{org}^{aq} \Phi_{H^+}^0$ at the DCE – water interface is 549 mV^1 and hence for the applied conditions (the potential was

hold at +150 mV $PH_{org \rightarrow aq}^+$) its transfer to the aqueous phase ($H_{org}^+ \rightarrow H_{aq}^+$) took place. The transfer of protons from the organic to the aqueous phase additionally increases their concentration above the liquid – liquid interface. Due to complexity of the system and the limitation of iridium oxide modified electrodes (working pH range is from 2 to 12) the local pH measurement can be only used to point out the change of pH. To confirm that the pH change is induced only by the PH^+ photodecomposition in the aqueous phase and does not arise from photodecomposition products of the organic electrolyte a control experiment in the absence of PH^+TPBCl^- in the organic phase was performed (see red squares on Figure 5.14). No pH change was observed among the studied experimental time once the pH probe was placed 1 μ m above the liquid – liquid interface, which potential was held at +150 mV with simultaneous UV irradiation.

The pH changes observed above the liquid – liquid interface are significant enough to induce the hydrolysis and condensation reaction of TEOS and hence such system was employed in this regard as it is shown in the following section.

5.5. Silica deposition induced by local pH decrease

The silica deposition at the electrified liquid – liquid interface can be triggered by electrochemical transfer of cationic surfactant – template – species from the organic phase to the aqueous phase containing already hydrolyzed silica precursor. The template can act as the catalyst for silica condensation reaction and as structure driving agent in one. The neat liquid – liquid interface can be also modified with the silica deposit in the ‘reversed system’ where the precursor is dissolved in the organic phase contacted with the acidic or basic aqueous phase.^{185,176} In order to induce porosity of the silica interfacial deposit, template – usually cationic surfactant – can be added to the aqueous phase.¹⁷⁷ A similar approach was used in this work. The only difference was the pH of the aqueous phase, which instead of being a fixed value (adjusted before the liquid – liquid interface was formed) was controlled with electrochemical transfer of $PH_{org \rightarrow aq}^+$ with simultaneous UV irradiation. **Figure 5.15** shows the CVs recorded at an array of microITIES (a) and macroITIES (b) separating the 8 mM $BTTPA^+TPBCl^-$ in 20% TEOS in DCE

and 5 mM NaCl aqueous solution in the absence and in the presence of CTA^+Br^- in the aqueous phase.

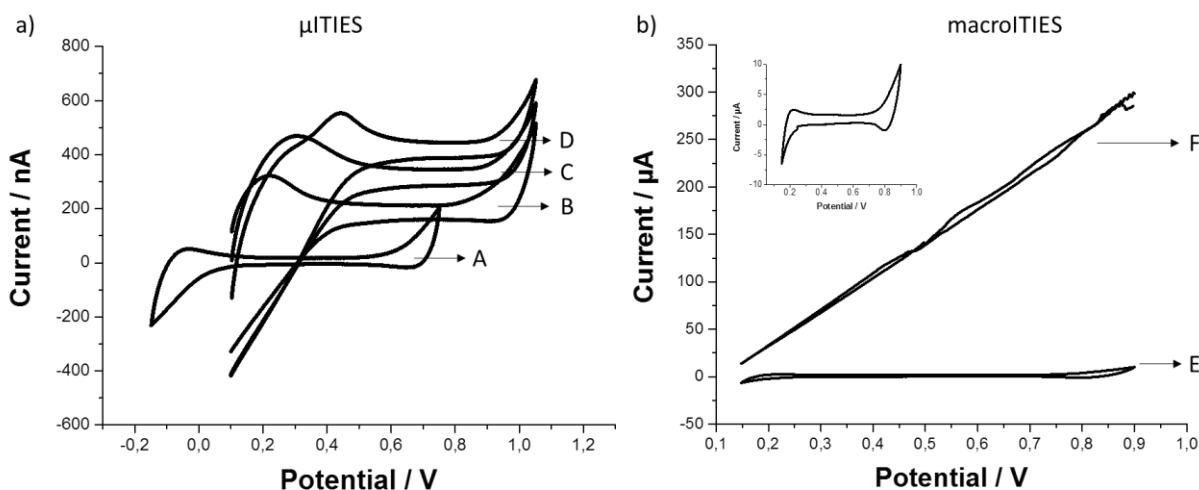


Figure 5.15. a) Cyclic voltammograms recorded at the array of microITIES (8 pores, 50 μm in diameter each). (A) correspond to blank system (8 mM $\text{BTPPA}^+\text{TPBCl}^-$ in 20% TEOS in DCE and 5 mM NaCl) which aqueous phase was further enriched by (B) 0.70 mM, (C) 1.38 mM and (D) 2.02 mM CTA^+Br^- . b) Cyclic voltammograms recorded in macroscopic cell supporting ITIES. (E) is the blank (8 mM $\text{BTPPA}^+\text{TPBCl}^-$ in 20% TEOS in DCE and 5 mM NaCl), which can be also found in the insert, whereas (F) additionally contained 1 mM CTA^+Br^- in the aqueous phase.

The CVs recorded at macroscopic ITIES in the presence of 1 mM CTA^+Br^- in the aqueous phase and TEOS in the organic phase (see **Figure 5.15 (b)**) has led to system destabilization and only resistance was recorded. No silica deposit formation was observed since under such conditions the hydrolysis of TEOS at the liquid – liquid interface is very slow. CVs recorded at microITIES (see **Figure 5.15 (a)**) showed that the interface is mechanically stable up to 2.02 mM CTA^+Br^- (this was the highest concentration studied) in the aqueous phase as compared with the macroscopic system. The only difference observed was the shift of the whole voltammogram towards more positive potential values and evolution of the peak limiting the potential window on the negative side of potential scale – probably arising from $\text{CTA}^+_{aq \rightarrow org}$ transfer.

In order to trigger silica deposition the local pH of the aqueous phase above the liquid – liquid interface was decreased by PH^+ transfer from the organic phase (the potential of the ITIES

was held at +150 mV for 60 minutes) with simultaneous UV irradiation. Photolysis of PH^+ has indirectly led to proton generation which catalyzes the hydrolysis reaction of silica from the organic phase.

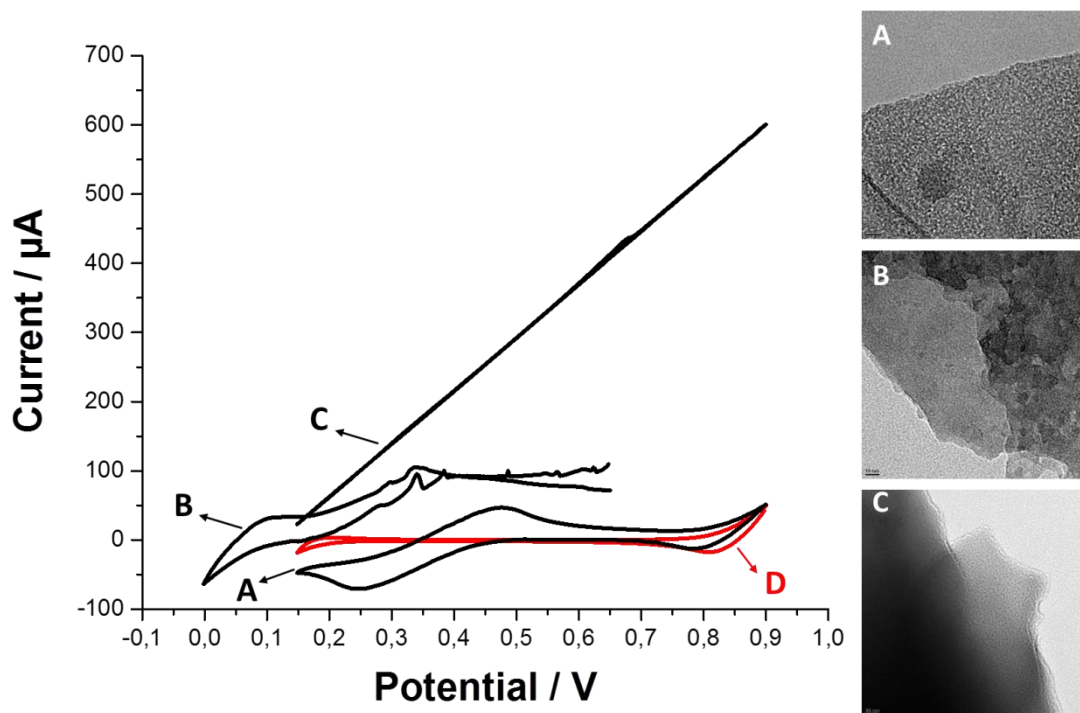


Figure 5.16. Cyclic voltammograms recorded at the macroscopic liquid – liquid interface. Red curve correspond to blank solution 8 mM $\text{BTPPA}^+\text{TPBCl}^-$ in 20% TEOS in DCE and 5 mM NaCl. Remaining black curves were recorded at the ITIES whose organic phase additionally contained 500 μM $\text{PH}^+\text{TPBCl}^-$ whereas the aqueous phase was enriched with 0 mM (A), 0.5 mM (B) and 2 mM (C) CTA^+Br^- in the aqueous phase. The TEM micrographs correspond to the silica deposits whose deposition was conducted under the condition indicated by corresponding CVs.

Figure 5.16 shows the voltammograms recorded prior to local pH change and silica deposition. As it was already shown on **Figure 5.15 (b)** the presence of cationic surfactants in the aqueous phase destabilizes the macroscopic liquid – liquid interface. In the presence of 0.5 mM CTA^+Br^- (curve B on **Figure 5.16**) in the aqueous phase the voltammogram shift and some current fluctuation were observed whereas only resistive current was recorded for 2 mM CTA^+Br^- (curve C on **Figure 5.16**). To trigger the silica deposition the interface was held at $E = +150$ mV for 60 min with simultaneous irradiation in the presence and in the absence of CTA^+ in the aqueous phase. Subsequently the cell was left for 12 hours. After this time the silica deposits were

collected and cured at 130°C for 16 hours. The morphological analysis was performed with the TEM imaginary. The ‘worm like’ structures were observed for all three samples even without CTA⁺ in the aqueous phase (see A – TEM image on **Figure 5.15**). This finding suggest that a spontaneous formation of mesopores could take place in here as it was already shown to occur for aluminosilicate materials prepared via Sol-Gel process.²⁶⁸

5.6. Conclusion

In this work, the interfacially active quaternary ammonium cation (trimethylbenzhydrylammonium – PH⁺) being sensitive to UV irradiation was synthesized and characterized electrochemically. The photodecomposition of the PH⁺ in the protic solvents was studied and the formation of benzhydrol in the aqueous phase, as one of the products of photolysis, was confirmed. The PH⁺ was then employed to locally affect the pH of the aqueous phase since its transfer can be controlled by electrochemical means whereas the irradiation leads to its decomposition followed by reactions which affect aqueous protons concentration. Due to the water reduction taking place at the aqueous counter electrode, the pH change of the aqueous phase could not be followed with the conventional pH measurement. Iridium oxide modified Pt microdisc electrodes were used to study the change of the pH at the local scale and the results have shown that the PH⁺ transferred and photodecomposed in the aqueous phase increase proton concentration. This experimental set-up was then used to modify the liquid – liquid interface with silica material. The results included in this chapter are planned to be published in **Electrochimica Acta** journal.

6. General conclusions

English version

The main focus of this thesis was the modification of electrified liquid – liquid interface with silica material to form molecular sieves. In general the silica deposition was performed via the Sol – Gel process in the presence of soft template. Deposition was controlled by electrochemistry at the ITIES. Two categories of the ITIES were employed for this purpose: (i) macroscopic ITIES created in a conventional four electrode electrochemical cell and (ii) microITIES under the form of an array of pores or single microscopic pore capillary.

The macroscopic ITIES was first employed to study the silica deposition mechanism. Cationic surfactant – CTA^+ – was used as a template and a catalyst for the silica formation, initially dissolved in the organic phase (10 mM $BTPPA^+TPBCl^-$ solution in dichloroethane). Silica precursor – TEOS – was hydrolyzed in the aqueous phase (at pH = 3) and it was thus separated from the template species. The transfer of CTA^+ was controlled with interfacial polarization and was only observed in the presence of hydrolyzed silica in the aqueous phase – this type of reaction is known as facilitated ion transfer. The silica formation was triggered once CTA^+ cations were transferred to the aqueous phase – the formation of spherical micelles catalyzes the condensation reaction and act as a template which structure the silica deposits. General conclusions were made regarding the macroscopic ITIES modification:

1. The CTA^+ transfer reaction was irreversible as the characteristic for adsorption current drop (associated to backward $CTA^+_{aq \rightarrow org}$ transfer) was found on the cyclic voltammograms;
2. The silica deposit is being formed at the liquid – liquid interface after one voltammetric cycle run at 5 mV/s;
3. Charge being back transferred to the organic phase increase for the first few cycles and becomes constant which indicated that the interfacial region was ‘saturated’ with the negative charge of condensing silica facilitating the $CTA^+_{aq \rightarrow org}$ transfer;

4. The limiting factor of the silica deposit formation is the $[\text{CTA}^+]_{\text{org}}$ and its concentration in the diffusion layer on the aqueous side of the liquid – liquid interface;
5. $[\text{TEOS}]_{\text{aq}}$ was not affecting the CTA^+ transfer in the studied concentration range (from 50 mM up to 300 mM);
6. The aqueous phase pH, governing the formation of polynuclear silanol species, was found to be optimal in the pH range from 9 to 10.

Moreover, the macroscopic ITIES has served for the silica deposit generation for further characterization. In order to cure the silica deposits collected from the liquid – liquid interface they were stored overnight in the oven at 130°C. Set of characterization techniques was employed, suggesting that:

1. The silica formation was confirmed. Further spectroscopic (infra-red) investigation indicated the presence of the CTA^+ among the silica network (as expected) and traces of organic electrolyte ions;
2. XPS indicated that TEOS was not totally hydrolyzed since C-O bond was detected. Furthermore, based on XPS results it was assumed that some charge balancing between negatively charged OH^- groups (present inside the silica pores) and Na^+ can occur;
3. The mesostructure of silica deposit was confirmed and the pore center-to-center distance depending on the polarity of the organic phase and $[\text{CTA}^+]_{\text{org}}$ concentration was in the range between 3.7 up to 7 nm;
4. The pores among the silica deposits are of ‘worm like’ shape as evidenced with the broad peak on SAXS patterns and directly on the TEM micrographs;

Once the silica deposit electrogeneration was optimized at the macroscopic ITIES, the miniaturization of the liquid – liquid interface was performed. The membrane used to support ITIES was a silicon wafer with array of microscopic pores (with the radius ranging from 5 μm up to 10 μm) arranged in honeycomb. Miniaturization has improved the electroanalytical parameters of the system (lower limit of detection due to lower capacitive current and better sensitivity arising from higher mass transfer) and additionally allowed the formation of mechanically stable silica deposits – which were further characterized and evaluated. The study concerning silica electrodeposition at the array of microITIES can be summarized as follows:

1. The current – potential characteristics affected by asymmetric diffusion profile on the both sides of the liquid – liquid interface did not correspond to the simple ion transfer reaction recorded during silica formation;
2. The shape of the forward peak (arising from $CTA_{org \rightarrow aq}^+$ transfer) depended on scan rate (diffusion layer thickness on the organic side of the liquid – liquid interface) and membrane design used (the pore center-to-center distance). Generally saying, the process was diffusion limited once the transfer was governed by linear diffusion inside the pores of the silicon wafer (for scan rate > 10 mV/s) and by overlaid diffusion layer on the ingress to the pores from the organic phase (for scan rate < 0.1 mV/s). Overlap of the diffusion profiles on the organic side of the liquid – liquid interface was also observed for the membranes supporting the pores with low spacing factor;
3. Silica deposits always grow towards the bulk of the aqueous phase. They are formed on the ingress to pore from the aqueous side of the interface, are flat on the bottom and are filled with the silica inside (which excludes any possible interface movement during deposition);
4. The shape of the silica deposits correspond to hemispherical diffusion layer of CTA^+ in the aqueous phase: for short experimental times they were flat at the top and rounded on the sides whereas longer experimental time has led to the hemispherical ‘cups’ formation;
5. The blocking effect of the organic species present inside the pores of silica deposits was confirmed by ion transfer voltammetry;
6. Calcination allowed the removal of organic species from inside the mesopores. Empty mesostructure was permeable for the analytes.

The *in situ* insight of the polarized ITIES with confocal Raman spectroscopy (the dimension of the miniaturized liquid – liquid interface required the application of local characterization technique) allowed the study of different molecular contributions. Two phenomena were followed: (i) interfacial ion transfer reaction and (ii) electrochemically controlled interfacial silica deposit formation. In general, the information extracted during this work reveals the following:

1. The negative polarization affected the molecular composition of the liquid – liquid interface as the Raman signals corresponding to $BTPPA^+$ and $TPBCl^-$ increased and decreased respectively;

2. No interface movement was detected since the set of Raman bands attributed to DCE have remained unchanged independently from the potential applied;
3. The molecular composition of the liquid – liquid interface during silica formation has changed dramatically after first half of the voltammetric cycles.
4. The strong signals from the CTA^+ , BTPPA^+ and TPBCl^- were found during the electrodeposition. The intensity of the signal tend to grow with the number of voltammetric cycles;
5. *In situ* study of silica deposition did not evidenced Si-O-Si bond formation. Nevertheless the silica presence was confirmed after electrogenerated material was cured thermally. Long acquisition time was employed for this purpose.

The ion transfer voltammetry of five different in charge, size and nature analytes were finally employed to electroanalytically evaluate the array of micro ITIES modified with silica deposits (modified under optimal conditions elaborated during previous study). Following observations were made:

1. The ion transfer was affected in the presence of silica deposits for all five analytes studied;
2. The change of the Gibbs energy of transfer for three different in size tetraalkylammonium cations before and after the modification was observed to be greater for the largest TBA^+ as compared with the slightly affected TMA^+ . The positively and mono charged analytes with the greater size required more energy to transfer across liquid – liquid interface modified with the silica deposits;
3. The transfer of negatively charged 4OBSA^- was also studied and it was found that the interfacial modification has increased the Gibbs energy of transfer in the same manner as for larger TBA^+ cation. This behavior was attributed to the electrostatic repulsion between negatively charged anion and OH groups located inside the silica pore walls;
4. The electrochemical behavior of PAMAM dendrimers at the modified liquid – liquid interface was found to be different from tetraalkylammonium cations. Firstly, the $E_{1/2}$ for both dendrimers was shifted towards less positive potential which means that the presence of silica deposits decreased the amount of energy required to trigger the transfer. Secondly, the fingerprints of adsorption for bigger PAMAM molecule – generation 1 –

were found in the presence of silica deposits. Both phenomena were attributed to the electrostatic interactions between positive charge of dendrimers and negative net charge of silica framework;

These observations clearly indicate that the presence of silica deposits at the ITIES affects the electrochemical behavior of different analytes in different manner suggesting that the ultimate goal of this work – sieving properties – are entirely possible. Further evaluation of liquid – liquid interface modified with silica material could be performed with the larger molecules as for instance: larger PAMAM dendrimers or biomolecules. Assessment of silica deposit with the permeability coefficient (which can be extracted from information collected with SECM) would be of highest interest. Some effort was made towards this direction (**see section 7.1**) however further study is needed.

The silica electrogeneration was performed on the aqueous side of the liquid – liquid interface and its morphology was governed by the hemispherical diffusion of CTA^+ . Interesting properties could be obtained if interior of the pore, where transfer is limited only by linear diffusion, could be modified in the same manner. Confined geometry inside the miniaturized pores can differently affect the morphology of the silica deposits and consequently their sieving properties. The selectivity of the ITIES modified with silica deposits can be also improved by chemical functionalization. Sol – Gel process allows the permanent introduction of the organic groups to the silica framework on the route of co-condensation between organosilanes with alkoxysilanes. Some preliminary results concerning functionalized silica interfacial deposition can be found in **section 7.2**.

First approach dealing with the liquid – liquid interface modification with the silica material was based on the controlled electrochemical transfer of template molecules from the organic phase to the silica precursor containing aqueous phase. The local change of the pH at the liquid – liquid interface is the second way of triggering silica deposition (the hydrolysis and condensation reactions are pH sensitive). The photosensitive and interfacially active cation – trimethylbenzhydrylammonium (PH^+) – was employed to change the pH above the liquid – liquid interface on its aqueous side. The conclusions for this part of the thesis are:

1. Electrochemical transfer of $PH_{org \rightarrow aq}^+$ with simultaneous UV irradiation has led to the formation of reactive carbocation (which reacts with water and forms benzhydrol) and releases a proton;
2. The overall pH of the aqueous phase was also affected by the water reduction taking place at the counter aqueous electrode;
3. The local pH measurements (performed above the liquid – liquid interface with the iridium oxide modified Pt microdisc electrodes) have shown that the interfacial pH is decreasing once PH^+ species are transferred and photodecomposed in the aqueous phase;
4. The local decrease in the pH was shown to catalyze the silica hydrolysis followed by condensation (in this configuration silica precursor – TEOS – was dissolved in the organic phase whereas the template – CTA^+ – was present in the aqueous phase) and resulted in silica deposit formation;
5. Miniaturization was found to mechanically stabilize the liquid – liquid interface in the presence of CTA^+ species (dissolved in the aqueous phase) which have destabilized macroscopic ITIES;
6. The mesostructure formation was poor and the worm like structures were present even when silica was deposited in the absence of CTA^+ in the aqueous phase.

Further study is needed to improve the mesostructure properties of synthesized material. The factor which affects the structuration of silica is the CTA^+ concentration. Conducting electrochemical study at the macroscopic ITIES in the presence of high $[CTA^+]_{aq}$ was impossible and hence miniaturization has to be employed (the microITIES was mechanically stable up to $[CTA^+]_{aq} = 2.02$ mM, higher concentrations were not investigated). The interfacial silica deposition can be also triggered by the local pH increase. In order to control this process electrochemically, interfacially active species (initially present in the organic phase) has to be functionalized with the basic center, for instance nitrogen atom with a lone electron pair. The electrochemically controlled transfer of the base to the aqueous phase will increase the pH which can trigger the silica deposition (**see section 7.3**).

Version Française

L'objectif principal de cette thèse concerne la modification de l'interface liquide – liquide par voie électrochimique. Ainsi, un matériau de silice a été utilisé dans le but de former une tamis moléculaire. En général, la déposition de silice a été effectuée par procédé Sol - Gel en présence des molécules connues en tant que 'templates'. La déposition a été contrôlée par électrochimie à l'interface liquide – liquide. Pour cela, deux catégories de d'ITIES (interface between two immiscible electrolyte solutions) ont été utilisées: (i) une interface liquide – liquide macroscopique créés dans une cellule électrochimique avec quatre électrodes et (ii) une l'interface liquide – liquide de dimension microscopique sous le forme d'une interface unique ou d'un réseau de micro-interfaces.

Dans un premier temps, l'interface liquide – liquide macroscopique a été utilisée pour étudier le mécanisme de déposition de silice. Pour cela, un tensioactif cationique – CTA^+ , initialement dissous dans une solution de $BTPPA^+TPBCl^-$ à 10 mM dans du dichloroéthane, a été utilisé à la fois en tant que 'template' et catalyseur lors de la formation de silice. Ensuite, un précurseur de silice – TEOS – a été hydrolysé dans la phase aqueuse (pH = 3) constituée de 5 mM NaCl. Après hydrolyse, le pH de la phase aqueuse a été augmenté jusqu'à 9 afin de promouvoir la formation d'espèces silanol polynucléaires. Un transfert de CTA^+ de la phase organique vers la phase aqueuse a été contrôlé par polarisation interfaciale et observé par présence de silice hydrolysé dans la phase aqueuse. Ce type de réaction est connu comme le transfert d'ions facilité. La formation de silice a été déclenchée une fois que les cations CTA^+ ont été transférés dans la phase aqueuse. Ainsi, la formation de micelles sphériques catalyse la réaction de condensation et agit comme la matrice qui structure les dépôts de silice. Les conclusions générales correspondant à la modification de l'interface liquide – liquide macroscopique sont les suivantes:

1. Caractéristique baisse de courant en voltampérométrie cyclique pendant le transfert retour ($CTA^+_{aq \rightarrow org}$) et indique que le transfert était irréversible et que CTA^+ a été piégé dans le matériau de silice;
2. Le matériau de silice est formé à l'interface liquide – liquide déjà après un cycle voltampérométrique effectué à 5 mV/s;

3. L'augmentation de charge au transfert arriéré ($CTA_{aq \rightarrow org}^+$) a été observé pour les premier cycles. La charge calculée pour les cycles suivants devient constante. Ces observations peuvent témoigner que la zone interfaciale est saturée par des espèces de silanol polynucléaire;
4. La formation de dépôts de silice a été limitée par $[CTA^+]_{org}$ et sa concentration dans la couche de diffusion du côté de la phase aqueuse de l'interface liquide – liquide;
5. L'intervalle de concentration de TEOS étudié, c'est-à-dire de 50 mM à 300 mM n'a pas affecté le transfert de CTA^+ ;
6. Un pH optimal pour la formation l'espace de silanol polynucléaire a été trouvé entre 9 et 10.

De plus, l'interface liquide – liquide macroscopique a permis de générer un dépôt de silice pour sa caractérisation ultérieure. Les dépôts de silice qui ont collectées de l'interface liquide – liquide, ils ont été stockés pendant une nuit dans un four à 130 ° C. Ensemble de techniques de caractérisation a été employé, ce qui suggère que:

1. La formation d'une liaison de silice (Si-O-Si) a été confirmée. Des études par méthodes spectroscopiques (infra-rouge) ont indiqué la présence de CTA^+ et de traces d'ions d'électrolyte organique dans le matériau de silice;
2. Des analyses par XPS ont indiqué que le TEOS n'a pas été totalement hydrolysé car une liaison C-O a été détectée. De plus, en se basant sur ces résultats XPS, on suppose qu'un équilibrage de charge entre des fonctions OH^- chargées négativement (présentes à l'intérieur de pores de la silice) et des ions Na^+ positifs peut se produire;
3. La mésostructure de dépôt de silice a été confirmée et une distance de centre à centre pour les pores en fonction de la polarité de la phase organique et de la concentration du CTA^+ dans cette phase organique $[CTA^+]_{org}$ ont été dans entre 3,7 et 7 nm;
4. Des analyses par SAXS et par imagerie MEB ont confirmé la présence de structures connues dans la littérature comme 'vermiculaires'.

Une fois que l'électrogénération de dépôt de silice a été optimisée à l'interface liquide – liquide macroscopique, la miniaturisation a été effectuée. L'ITIES microscopique a été supportée avec une plaquette de silicium dont la matrice des pores (le rayon était dans la gamme entre 5 et 10 μm) situé en arrangement hexagonal, prépare par lithographie. La miniaturisation a amélioré

certaines des paramètres électroanalytiques. D'une part, la limite de détection a baissé grâce à un courant capacitif. De l'autre part, un transport de masse plus élevé a permis d'améliorer la sensibilité du système. La déposition de silice à l'interface liquide – liquide miniaturisée a été étudiée et les conclusions suivantes ont été faites:

1. Les courbes courant – potentiel enregistrées lors de la formation de silice n'ont pas correspondu à une réaction simple de transfert d'ions;
2. La forme du sommet de polarisation en avant (résultant du transfert $\text{CTA}_{\text{org} \rightarrow \text{aq}}^+$) dépendait de la vitesse de balayage (épaisseur de la couche de diffusion sur le côté de la phase organique de l'interface liquide - liquide) et de la membrane de silicium utilisée (la distance de centre à centre entre les deux pores). En général, la réaction de transfert de $\text{CTA}_{\text{org} \rightarrow \text{aq}}^+$ était limitée par diffusion une fois que le transfert a été régi par diffusion linéaire à l'intérieur des pores de la membrane de silicium (à vitesse de balayage > 10 mV/s) et quand de couche de diffusion superposée sur l'entrée des pores du côté de la phase organique (à vitesse de balayage $< 0,1$ mV/s). Une superposition des profils de diffusion du côté de la phase organique a également été observée pour la membrane de silicium ayant un faible facteur d'espacement entre les pores;
3. Les dépôts de silice croissent toujours vers la phase aqueuse. Ils sont formés à l'entrée des pores à partir du côté de la phase aqueuse. Les dépôts sont plats en le fond et sont remplis par la silice à l'intérieur (ce qui exclut tout mouvement possible de l'interface pendant le procédé de déposition);
4. La forme des dépôts de silice correspond à la couche de diffusion hémisphérique du CTA^+ qui transfère vers la phase aqueuse: pour les expériences courtes, les dépôts étaient plats en haut et arrondies sur les côtés et hémisphériques, pour les expériences longues;
5. L'effet de blocage des espèces organiques présentes à l'intérieur des pores de dépôts de silice a été confirmée par voltamétrie de transfert d'ions;
6. La calcination a permis l'oxydation des espèces organiques à l'intérieur des mésopores. La mésosstructure vide était perméable pour les analytes.

La dimension de l'interface liquide – liquide miniaturisée a nécessité l'application d'une technique de caractérisation locale. Pour cela, une méthode de spectroscopie Raman confocale a été utilisée et a permis l'étude des différentes contributions moléculaires. Ainsi, deux

phénomènes ont été suivis: (i) la réaction interfaciale de transfert d'ions et (ii) la formation de dépôts de silice à l'interface contrôlée par voie électrochimique. En général, les informations suivantes ont été extraites de ce travail:

1. Une polarisation négative a affecté la composition moléculaire de l'interface liquide - liquide parce que les signaux Raman correspondant au BTPPA^+ ont augmenté et ceux du TPBCl^- ont diminué;
2. Aucun mouvement de l'interface n'a été détecté pendant la polarisation de l'interface : l'ensemble des bandes Raman attribués au DCE sont resté inchangées indépendamment du potentiel appliqué;
3. La composition moléculaire de l'interface liquide - liquide pendant la formation de silice a changé brusquement après la première moitié du cycle voltamétrique ;
4. Les signaux forts provenant du CTA^+ , du BTPPA^+ et du TPBCl^- ont été trouvés au cours de l'électrodéposition. L'intensité du signal a une tendance à augmenter avec le nombre de cycles voltammétriques;
5. Les études *in situ* de la déposition de silice n'ont pas prouvé la formation de liaisons Si-O-Si. Néanmoins, la présence de silice a été confirmée après le durcissement thermique du matériau.

La voltampérométrie de transfert de cinq ions qui différaient en charge, en taille et en nature a finalement été utilisée pour évaluer les dépôts de silice par voie électroanalytique (la membrane de silicium a été modifiée avec les conditions optimales élaborées lors de l'étude précédente). Les observations suivantes ont été réalisées:

1. Le transfert d'ions a été influencé en présence de dépôts de silice pour les cinq analytes étudiés;
2. La variation de l'énergie de Gibbs de transfert pour trois cations différents de tétraalkylammonium avant et après la modification a été observée à être supérieure pour la plus grande TBA^+ par rapport légèrement affectée TMA^+ . Ceci témoigne que le transfert des analytes mono chargé (positivement) avec la taille plus grande nécessite plus d'énergie pour transférer à travers de l'interface liquide - liquide modifiée avec les dépôts de silice;
3. Le transfert de 4OBSA^- chargé négativement a été également étudié : la modification a augmenté l'énergie de Gibbs de transfert de la même façon que pour un cation le plus grand

(TBA⁺). Ce résultat a été attribué aux répulsions électrostatiques entre des anions chargés négativement et des groupes -OH situés à l'intérieur des pores de la silice;

4. Le comportement électrochimique des dendrimères PAMAM à l'interface liquide – liquide miniaturisée et modifiée par dépôts de silice a été différent par rapport à celui des cations de tétraalkylammonium. Tout d'abord, le $E_{1/2}$ pour les deux dendrimères a été déplacé vers un potentiel moins positif ce qui signifiait que la présence de dépôts de silice a diminué la quantité d'énergie nécessaire pour déclencher le transfert. D'autre part, l'adsorption pour la plus grande molécule - PAMAM génération 1 – a été observée en présence de dépôts de silice. Ces deux phénomènes ont été attribués aux interactions électrostatiques entre des charges positives des dendrimères et un charge nette négative de matériau de silice;

Ces observations indiquent clairement que la présence de dépôts de silice à l'interface liquide – liquide miniaturisée affecte le comportement électrochimique de différents analytes de manière différente. Ceci suggère que l'objectif ultime de ce travail de thèse - propriétés de tamisage – est tout à fait possible. Une évaluation plus poussée de l'interface liquide - liquide modifiée avec du matériau de silice pourrait être réalisée avec des molécules plus grandes telles que par exemple: les plus grandes dendrimères ou des biomolécules. L'évaluation du dépôt de silice avec le coefficient de perméabilité, qui peut être extrait à partir des informations collectées par SECM, serait d'un intérêt le plus élevé. Certains efforts ont été faits dans cette direction (**voir section 7.1**) mais des études plus approfondies sont nécessaires.

L'électrogénération de silice a été effectuée sur le côté de la phase aqueuse de l'interface liquide - liquide et sa morphologie est régie par la diffusion hémisphérique de CTA⁺. Des propriétés intéressantes peuvent être obtenues si l'intérieur de pores, où le transfert est seulement limité par la diffusion linéaire, peut être modifié de la même manière. La géométrie confinée à l'intérieur des pores miniaturisés peut affecter différemment la morphologie des dépôts de silice et par conséquent leurs propriétés de tamisage. La sélectivité de l'interface liquide - liquide modifiée avec des dépôts de silice peut être également améliorée par fonctionnalisation chimique. Le procédé Sol - Gel permet l'introduction permanente des groupes organiques au cadre de la silice sur le trajet de co-condensation entre les organosilanes avec des alcoxy-silanes. Des résultats préliminaires concernant les dépôts de silice fonctionnalisés sur l'interface liquide – liquide sont présentés dans la **section 7.2** de la partie des résultats préliminaires.

La première méthode qui a été utilisée pour modifier l'interface liquide – liquide avec le matériau de silice a été basée sur un transfert électrochimique des molécules du tensioactif – CTA^+ (initialement présent dans la phase organique) vers la phase aqueuse contenant un précurseur de silice hydrolysé. La variation locale du pH à l'interface liquide – liquide peut être le deuxième moyen de déclenchement d'un dépôt de silice (les réactions d'hydrolyse et de condensation sont sensibles au pH). Le cation triméthylbenzhydrylammonium (PH^+), photosensible et actif à l'interface, a été synthétisé et ensuite utilisé pour modifier le pH du côté aqueux de l'interface liquide – liquide. Les conclusions de cette partie de la thèse sont comme suit:

7. Le transfert électrochimique de $PH_{org \rightarrow aq}^+$ par irradiation UV a résulté en la formation d'un carbocation réactif (qui réagit avec de l'eau en formant du benzhydre) et du proton;
8. Le pH global de la phase aqueuse a été également affecté par la réduction de l'eau qui a lieu à l'électrode auxiliaire de la phase aqueuse;
9. Les mesures locales du pH (effectuées au-dessus de l'interface liquide - liquide en utilisant des microélectrodes de Pt modifiées par l'oxyde d'iridium) ont montré que le pH diminue une fois que les cations PH^+ sont photodécomposés et transférés dans la phase aqueuse;
10. La baisse locale du pH a été montrée pour catalyser l'hydrolyse de silice suivie par condensations (dans cette configuration le précurseur de silice - TEOS - a été dissous dans la phase organique tandis que le CTA^+ était présent dans la phase aqueuse) et a abouti à la formation de matériau de silice à l'interface liquide – liquide;
11. La miniaturisation a stabilisé mécaniquement l'interface liquide - liquide en présence de CTA^+ (dissous dans la phase aqueuse) qui ont déstabilisé l'interface liquide - liquide macroscopiques;
12. La formation de mésostructure était pauvre et les structures vermiculaires étaient présents même lorsque la silice a été déposée en absence de CTA^+ dans la phase aqueuse.

Une étude plus approfondie est nécessaire pour améliorer des propriétés de mésostructure du matériau synthétisé.

Le facteur qui influence la structuration de la silice est la concentration de CTA^+ . Une étude électrochimique réalisée à l'interface liquide – liquide macroscopique en présence de

$[\text{CTA}^+]_{\text{aq}}$ en concentration élevée était impossible. Il fallait donc utiliser les systèmes miniaturisés (l'interface liquide – liquide miniaturisée était mécaniquement stable jusqu'à $[\text{CTA}^+]_{\text{aq}} = 2,02 \text{ mM}$, des concentrations plus élevées n'ont pas été étudiées). Le dépôt de silice à l'interface peut être déclenché aussi par l'augmentation du pH local. Les espèces actives interfacialement (initialement présents dans la phase organique) qui sont fonctionnalisées avec le centre de base, par exemple un atome d'azote avec une paire d'électrons isolée, peuvent être employés pour contrôler des réactions d'hydrolyse et de condensation par voie électrochimique (pour plus de détails, voir **section 7.3**, partie résultats préliminaires).

7. Further directions

Certain scientific questions and improvements concerning this work still remain challenging. (i) Further effort could be directed towards evaluation of silica deposits permeability and scanning electrochemical microscopy (SECM) is of highest interest in this regard. (ii) The selectivity of the liquid – liquid interface modified with the silica deposits can be further improved by chemical functionalization, for instance by introduction of organosilane species to the sol. In this way, the parameters such as the charge, hydrophobicity or some specific ligand – host interaction could be tuned depending on the functional group used. (iii) Mesoporous and well-ordered silica materials can be also obtained by evaporation induced self-assembly technique. Resulting material deposited at the membrane supporting nano- or microITIES could be employed as molecular sieve. (iv) Triggering the condensation of silica by local pH change induced by the ion transfer reaction from the organic phase could be used to control the silica deposit formation. The design of the interfacially active ions functionalized with chemical moiety affecting the concertation of protons in the aqueous media is a requirement. (v) Interfacial silica gel electrogeneration can form a scaffold for molecules or particles undergoing interfacial adsorption. This phenomenon might be employed for development of new silica templating methods or for encapsulation of species being adsorbed at the interface. Some preliminary results concerning few of the above mentioned ideas are given in the following subsections.

7.1. Silica deposits – SECM characterization

SECM allows the study of electrochemical behavior of the system at the local scale. In SECM configuration the electrochemical interaction between the tip and studied interface was investigated. Two working modes can be distinguished in SECM: (i) generation/collection mode – where one side of the electrochemical cell, say tip, is electrochemically detecting the probe which is generated at the second side, say support and (ii) the feedback mode which can be negative (drop in current once the tip is approaching the surface – insulator) or positive (increase in current in close vicinity of the surface – conductor). In the negative feedback mode the probe

from the bulk of the liquid media gives the steady state current which above the insulating surface is decreased due to hindered diffusion profile of the tip. The positive feedback is when the species being the reason of charge transfer and resulting current at the tip in the bulk are regenerated at the conductive support (tip approach result in current increase in this case).

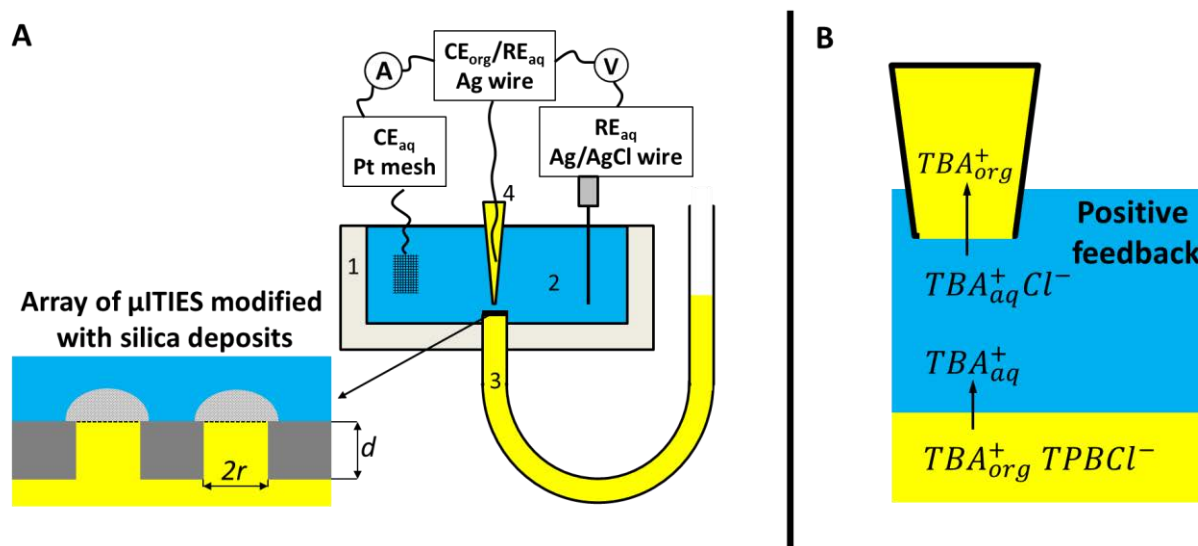


Figure 6.1. A – The set-up design to study local properties of silica deposits. Designations stand for: 1 – is the PTFE cell; 2 – is the aqueous phase being the solution of TBA^+Cl^- ; 3 – is the DCE solution of TBA^+TPBCl^- and 4 – is the SECM tip filled with the DCE solution of 10 mM $BTPPA^+TPBCl^-$. The array of microITIES was modified with silica deposits. B – Schematic representation of the positive feedback recorded at the ITIES.

SECM can be employed to probe the properties of porous membranes,^{247,269} and hence it could be employed to study the microITIES modified with silica deposits. The set-up which could be used for such experiment is shown on **Figure 6.1 A**. In this configuration the steady state current at the tip (**for the tip preparation refer to Appendix I**) arise from the TBA^+ transfer from the aqueous to the organic phase – the interface is polarized with an external power source. The second liquid – liquid interface, which is supported with the array of microITIES modified with silica deposits, is nonpolarizable. It is constituted between the aqueous solution of TBA^+Cl^- and organic solution of TBA^+TPBCl^- in DCE (**see Figure 6.1 B**). Series of preliminary experiments are shown on **Figure 6.2**. Each graph is the normalized current (overall current divided by limiting current) presented in function of normalized distance (tip – support distance divided by tip radius). The drop in current in the vicinity of the silicon substrate as well as above the pure DCE was observed as expected (**see Figure 6.2 A and B** respectively). Once TBA^+ was

present in the organic phase being the lower density phase of non-polarized liquid – liquid

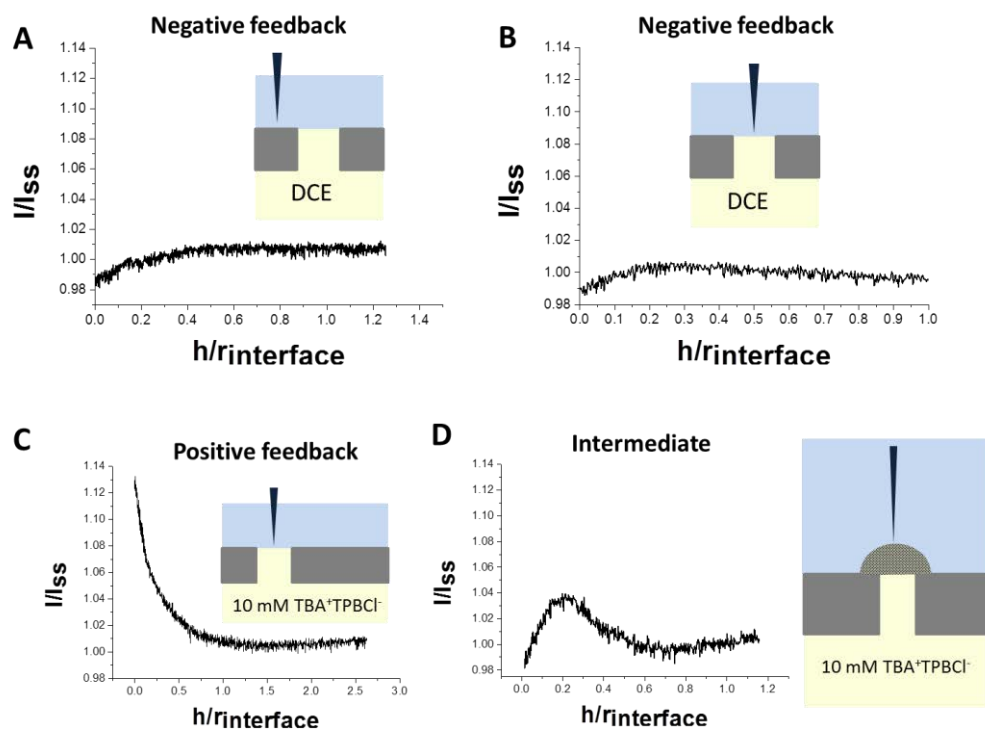


Figure 6.2. SECM approach curves recorded A – above the silicon wafer; B – above the pure DCE; C – above the 10 mM TBA⁺TPBCl⁻ solution in DCE and D – above the silica deposit modified μ ITIES supporting 10 mM TBA⁺TPBCl⁻ in DCE.

interface the positive feedback was recorded (see **Figure 6.2 C**). Intermediate response was observed in the presence of silica deposits as shown on **Figure 6.2 D**. Information such as the permeability coefficient or the kinetics of ion transfer across the silica deposits still have to be extracted from SECM results.

7.2. Silica deposits functionalization

Different functionalities can be introduced to the silica framework on the basis of co-condensation between alkoxy silanes and organosilanes species. The electrodeposition of such silica functionalized materials can be easily performed at the liquid – liquid interface. A preliminary investigation has been done and the results are found to be promising. The co-condensation was performed with two organosilanes: (3-mercaptopropyl)trimethoxysilane

(MPTMS) and (3-azidopropyl)trimethoxysilane (AzPTMS). Cyclic voltammetry (see **Figure 6.3**) was used as a method for silica deposits generation. The cationic surfactant being initially dissolved in the organic phase was transferred on forward polarization (from more positive to more negative potential) to the aqueous phase where it has catalyzed and self-assembly with condensing silica precursor species.

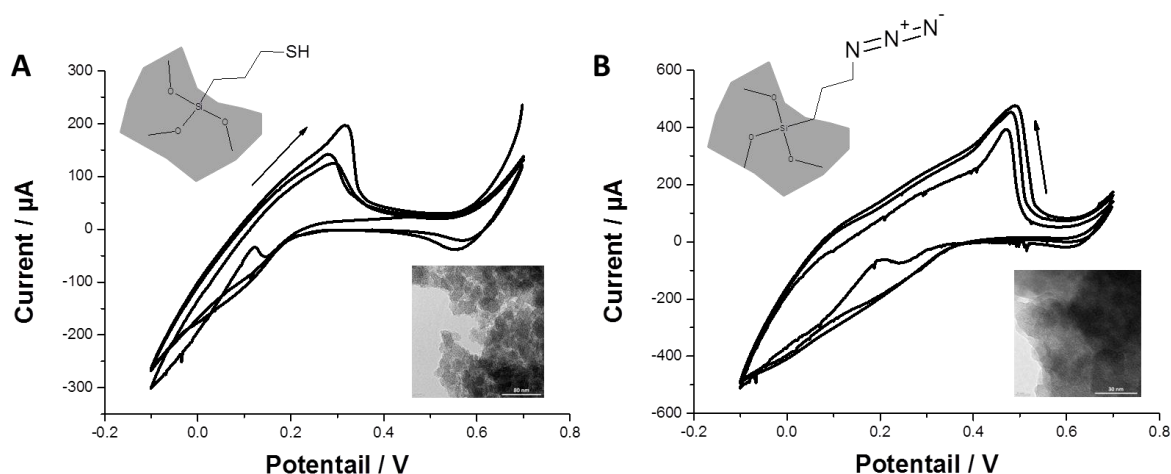


Figure 6.3. The CVs recorded during silica deposit formation at macroscopic ITIES in the presence of A – 5% of MPTMS and B – 15% AzPTMS in the initial sol solution. The experimental conditions: $[\text{CTA}^+]_{\text{org}} = 14 \text{ mM}$; $[x\% \text{ organosilane} + 100 - x\% \text{ TEOS}]_{\text{aq}} = 300 \text{ mM}$; scan rate was 1 mV/s. Insert are the TEM images for electrogenerated silica material.

Interfacial silica deposition was performed for different concentration of organosilanes in the initial sol solution (from 5% up to 25%). Resulting silica deposits were collected from the liquid – liquid interface and spectroscopic characterization (data not shown) was performed. Thiol bond evolution was followed with Raman spectroscopy whereas the presence of azide group was confirmed with the infra-red spectroscopy.

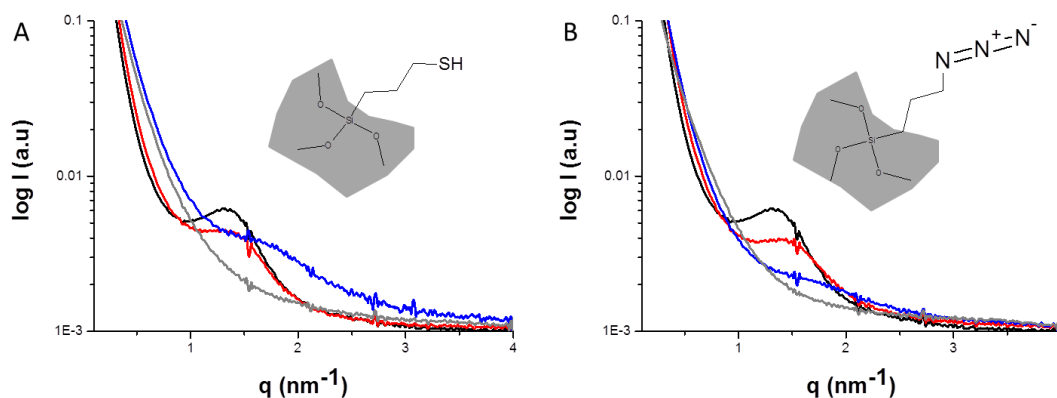


Figure 6.4. Variation of SAXS patterns for A – thiol and B – AzPTMS functionalized silica deposit. The deposits were prepared under following initial conditions: $[CTA^+]_{org} = 14$ mM; $x\%$ organosilane + $100 - x\%$ TEOS] $_{aq} = 300$ mM; scan rate was 1 mV/s. Black line correspond to pure TEOS, red to 5%, blue to 15% and gray to 25% of organosilanes in the initial sol solution.

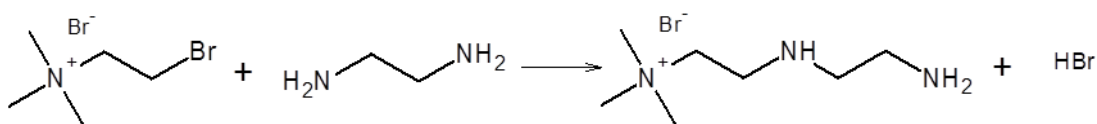
The morphological characterization was conducted with SAXS. The results are shown on **Figure 6.4**. Similar tendency was observed for both functionalities: (i) the broadness of the peak from SAXS pattern was increasing with the increasing concentration of the organosilanes in the initial sol solution (indicating increase in the average pore center-to-center distance) and (ii) the peak intensity tend to drop for the samples containing higher amount of organic groups suggesting deterioration of mesoporous properties.

As a continuation, other functionalities can be introduced to the silica framework (co-condensation or post grafting can be employed). In the second step, the miniaturized ITIES could be modified with the functionalized silica deposits, which can be finally, evaluate with a range of interfacially active analytes.

7.3. Interfacially active base

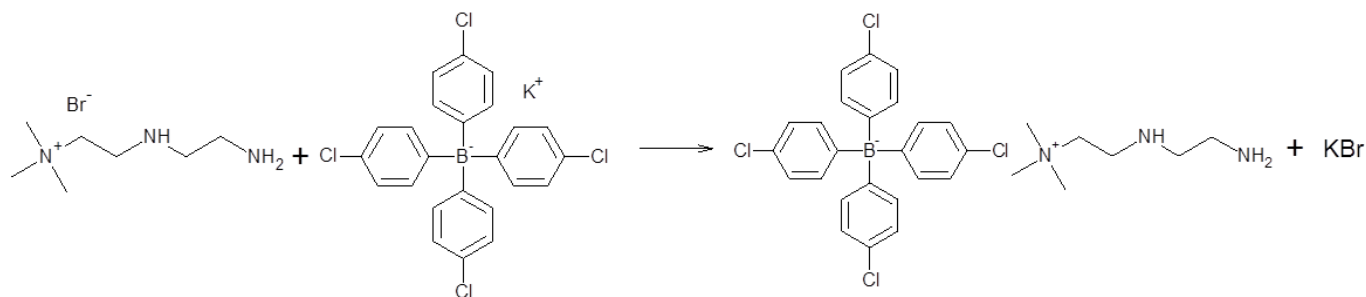
The local pH increase of the aqueous phase near the liquid – liquid interface could be performed with the ion transfer reaction, once the ion initially present in the organic phase would be functionalized with a base. Such compound could be a quaternary ammonium cation, which is

substituted, for instance, with an alkyl chain terminated with a nitrogen atom with a lone electron pair (i.e. (n-aminoalkyl)trimethylammonium cation). Surprisingly such compounds are nearly inaccessible and very expensive despite the fact that their synthesis seems to be easy. The amination reaction of an alkyl halide containing quaternary ammonium cation with ethylenediamine is one of the ways to obtain the product of interest:



Scheme 6.1. Amination reaction of (2-bromoethyl)trimethylammonium cation with ethylenediamine.

The reaction is not selective and may lead to the formation of di-, tri- and quaternary substituted amines hence ethylenediamine has to be used in high excess. Next step is the precipitation of the product from the reaction mixture with TPBCl⁻ anions in order to form a molecule soluble in DCE:



Scheme 6.2. Amination reaction product precipitation with TPBCl.

Obtained molecule was characterized with the ¹H NMR spectroscopy (see **Figure 6.5**). The singlet at around 3.1 ppm can be attributed to the methyl groups protons attached to the quaternary nitrogen atom. The triplet between 3.2 and 3.3 ppm arises from 2 protons of –CH₂– attached to the quaternary ammonium nitrogen atom. Next the two –CH₂– group of the secondary ammonium group give signal at around 3.0 ppm and finally the last –CH₂– attached to primary ammonium group can be seen at around 2.9 ppm. The series of bands from 3.4 to 3.7 ppm may arise from contamination.

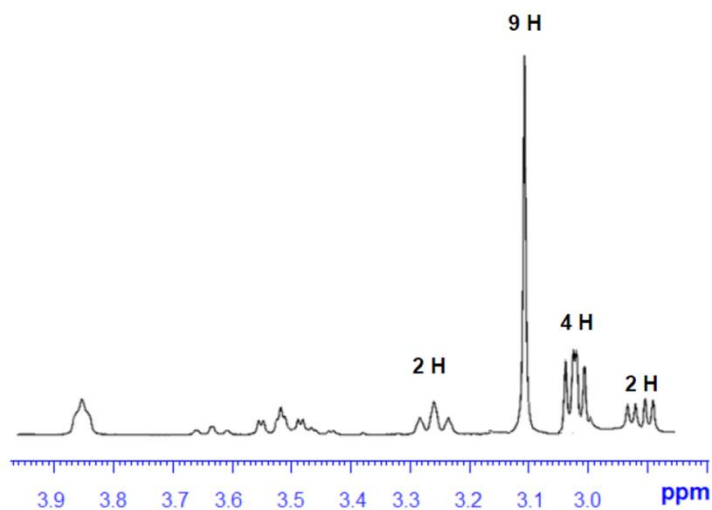


Figure 6.5. ^1H NMR spectra for the product of amination reaction.

In future the electroanalytical evaluation of the synthesized molecule can be performed at the electrified liquid – liquid interface. The change in pH has to be evidenced experimentally. The system employing interfacially active base can be used to trigger interfacial silica deposition (which can be further characterized in order to evaluate its structure).

8. References

- (1) Samec, Z. Electrochemistry at the Interface between Two Immiscible Electrolyte Solutions (IUPAC Technical Report). *Pure Appl. Chem.* **2004**, *76*, 2147–2180.
- (2) Samec, Z.; Langmaier, J.; Kakiuchi, T. Charge-Transfer Processes at the Interface between Hydrophobic Ionic Liquid and Water. *Pure Appl. Chem.* **2009**, *81*, 1473–1488.
- (3) Dryfe, R. A. W. The Electrified Liquid-Liquid Interface. *Adv. Chem. Phys.* **2009**, *141*, 153–215.
- (4) Fermi, D.; Lee, H. J.; Girault, H. H.; Reymond, F.; Fermin, D. Electrochemistry at Liquid/liquid Interfaces: Methodology and Potential Applications. *Electochim. Acta* **2000**, *45*, 2647–2662.
- (5) Girault, H. H. Electrochemistry at the Interface between Two Immiscible Electrolyte Solutions. *Electochim. Acta* **1986**, *43*, 383–385.
- (6) Peljo, P.; Girault, H. H. Electrochemistry at the Liquid/liquid Interface. *Encycl. Anal. Chem.* **2012**, 1–28.
- (7) Samec, Z. Dynamic Electrochemistry at the Interface between Two Immiscible Electrolytes. *Electochim. Acta* **2012**, *84*, 21–28.
- (8) Senda, M.; Kakiuchi, T.; Osakai, T. Electrochemistry at the Interface between Two Immiscible Electrolyte Solutions. *Electochim. Acta* **1991**, *36*, 253–262.
- (9) Girault, H. H. Charge Transfer across Liquid-Liquid Interfaces. *Mod. Asp. Electrochem.* **1993**, *25*, 1–62.
- (10) Verwey, E. J.; Niessen, K. F. XL. The Electrical Double Layer at the Interface of Two Liquids. *Philos. Mag.* **1939**, *28*, 435–446.
- (11) Gavach, C.; Seta, P.; D'Epenoux, B. J. The Double Layer and Ion Adsorption at the Interface between Two Non Miscible Solutions: Part I: Interfacial Tension Measurements for the Water-Nitrobenzene Tetraalkylammonium Bromide Systems. *J. Electroanal. Chem. Interfacial Electrochem.* **1977**, *83*, 225–235.
- (12) Gros, M.; Gromb, S.; Gavach, C. The Double Layer and Ion Adsorption at the Interface between Two Non-Miscible Solution; Part II: Electrocapillary Behaviour of Some

- Water-Nitrobenzene Systems. *J. Electroanal. Chem. Interfacial Electrochem.* **1978**, *89*, 29–36.
- (13) Girault, H.H.; Schiffrin, D. J. Thermodynamic Surface Excess of Water and Ionic Solvation at the Interface between Immiscible Liquids. *J. Electroanal. Chem. Interfacial Electrochem.* **1983**, *150*, 43–49.
- (14) Girault, H. H. J.; Schiffrin, D. J. Thermodynamics of a Polarised Interface between Two Immiscible Electrolyte Solutions. *J. Electroanal. Chem. Interfacial Electrochem.* **1984**, *170*, 127–141.
- (15) Rowlinson, J. S.; Widom, B. *Molecular Theory of Capillarity*; 2002; p. 327.
- (16) Benjamin, I. Theoretical Study of the Water/1,2-Dichloroethane Interface: Structure, Dynamics, and Conformational Equilibria at the Liquid–liquid Interface. *J. Chem. Phys.* **1992**, *97*, 1432–1445.
- (17) Benjamin, I. Chemical Reactions and Solvation at Liquid Interfaces: A Microscopic Perspective. *Chem. Rev.* **1996**, *96*, 1449–1476.
- (18) Schlossman M.L. Liquid-Liquid Interfaces: Studied by X-Ray and Neutron Scattering. *Curr. Opin. Colloid Interface Sci.* **2002**, *7*, 235–243.
- (19) Wang, H.; Borguet, E.; Eisenthal, K. B. Generalized Interface Polarity Scale Based on Second Harmonic Spectroscopy. *J. Phys. Chem. B* **1998**, *5647*, 4927–4932.
- (20) Higgins, D. A.; Corn, R. M. Second Harmonic Generation Studies of Adsorption at a Liquid - Liquid Electrochemical Interface. *J. Phys. Chem.* **1993**, *97*, 489–493.
- (21) Sabela, A.; Mareček, V.; Samec, Z.; Fuocot, R.; Fuoco, R.; Marecek, V. Standard Gibbs Energies of Transfer of Univalent Ions From Water To 1,2-Dichloromethane. *Electrochim. Acta* **1992**, *37*, 231–235.
- (22) Koryta, J. Electrochemical Polarization Phenomena at the Interface of Two Immiscible Electrolyte Solutions. *Electochim. Acta* **1979**, *24*, 293–300.
- (23) Shao, Y.; Osborne, M. D.; Girault, H. H. Assisted Ion Transfer at Micro-ITIES Supported at the Tip of Micropipettes. *J. Electroanal. Chem. interfacial Electrochem.* **1991**, *318*, 101–109.
- (24) Lagger, G.; Tomaszewski, L.; Osborne, M. D.; Seddon, B. J.; Girault, H. H. Electrochemical Extraction of Heavy Metal Ions Assisted by Cyclic Thioether Ligands. *J. Electroanal. Chem.* **1998**, *451*, 29–37.
- (25) Lee, H. J.; Lagger, G.; Pereira, C. M.; Silva, A. F.; Girault, H. H. Amperometric Tape Ion Sensors for cadmium(II) Ion Analysis. *Talanta* **2009**, *78*, 66–70.

- (26) Katano, H.; Tatsumi, H.; Hibi, T. Electrochemical Study of the Assisted Transfer of Silver Ion by 1,5-Cyclooctadiene at the 1,6-Dichlorohexane | Water Interface. *Anal. Sci.* **2005**, *21*, 901–905.
- (27) Zhan, D.; Xiao, Y.; Yuan, Y.; He, Y.; Wu, B.; Shao, Y. Electrochemical Recognition of Alkali Metal Ions at the Micro-Water 1,2-Dichloroethane Interface Using a calix[4]arene Derivative. *J. Electroanal. Chem.* **2003**, *553*, 43–48.
- (28) Kaykal, F.; Bingol, H.; Sariguney, A. B.; Coskun, A.; Akgemci, E. G. Synthesis and Electrochemical Properties of a Novel calix[4]arene Derivative for Facilitated Transfer of Alkali Metal Ions across water/1,2-Dichloroethane Micro-Interface. *Supramol. Chem.* **2011**, *23*, 570–578.
- (29) Durmaz, M.; Zor, E.; Kocabas, E.; Bingol, H.; Akgemci, E. G. Voltammetric Characterization of Selective Potassium Ion Transfer across Micro-water/1,2-Dichloroethane Interface Facilitated by a Novel calix[4]arene Derivative. *Electrochim. Acta* **2011**, *56*, 5316–5321.
- (30) Bingol, H.; Kaykal, F.; Akgemci, E. G.; Sirit, A. Facilitated Transfer of Alkali and Alkaline-Earth Metal Ions by a Calix[4]arene Derivative Across Water/1,2-Dichloroethane Microinterface: Amperometric Detection of Ca(2+). *Electroanalysis* **2010**, *22*, 2825–2833.
- (31) O' Dwyer, P.; Cunnane, V. J. Selective Transfer of Ag⁺ at the water|1,2-Dichloroethane Interface Facilitated by Complex Formation with a Calixarene Derivative. *J. Electroanal. Chem.* **2005**, *581*, 16–21.
- (32) Kivlehan, F.; Mace, W. J.; Moynihan, H. A.; Arrigan, D. W. M. Study of Electrochemical Phosphate Sensing Systems: Spectrometric, Potentiometric and Voltammetric Evaluation. *Electrochim. Acta* **2009**, *54*, 1919–1924.
- (33) Reymond, F.; Steyaertb, G.; Pagliarab, A.; Carruptb, P.; Testab, B. 141 . Transfer Mechanism of Ionic Drugs : Piroxicam as an Agent Facilitating Proton Transfer. *Helv. Chim. Acta* **1996**, *79*, 1651–1669.
- (34) Cai, C.; Mirkin, M. V. Electron Transfer Kinetics at Polarized Nanoscopic Liquid/liquid Interfaces. *J. Am. Chem. Soc.* **2006**, *128*, 171–179.
- (35) Barker, A. L.; Gonsalves, M.; Macpherson, J. V.; Slevin, C. J.; Unwin, P. R. Scanning Electrochemical Microscopy: Beyond the Solid/liquid Interface. *Anal. Chim. Acta* **1999**, *385*, 223–240.
- (36) Geblewicz, G.; Schiffrin, D. J. Electron Transfer between Immiscible Solutions. The Hexacyanoferrate-Lutetium Biphthalocyanine System. *J. Electroanal. Chem.* **1988**, *244*, 27–37.

- (37) Samec, Z.; Mareček, V.; Jan, W. Charge Transfer between Two Immiscible Electrolyte Solutions. Part IV. Electron Transfer between hexacyanoferrate(III) in Water and Ferrocene in Nitrobenzene Investigated by Cyclic Voltammetry with Four-Electrode System. *J. Electroanal. Chem.* **1979**, *103*, 11–18.
- (38) Cheng, Y.; Schiffrin, D. J. A.C. Impedance Study of Rate Constants for Two-Phase Electron-Transfer Reactions. *J. Chem. Soc. Faraday Trans.* **1993**, *89*, 199–205.
- (39) Samec, Z.; Mareček, V.; Weber, J. Detection of an Electron Transfer across the Interface between Two Immiscible Electrolyte Solutions by Cyclic Voltammetry with Four-Electrode System. *J. Electroanal. Chem.* **1978**, *96*, 1977–1979.
- (40) Rodgers, A. N. J.; Booth, S. G.; Dryfe, R. A. W. Particle Deposition and Catalysis at the Interface between Two Immiscible Electrolyte Solutions (ITIES): A Mini-Review. *Electrochem. commun.* **2014**, *47*, 17–20.
- (41) Eugster, N.; Fermi, D. J.; Girault, H. H. Photoinduced Electron Transfer at Liquid | Liquid Interfaces: Dynamics of the Heterogeneous Photoreduction of Quinones by Self-Assembled Porphyrin Ion Pairs. *J. Am. Chem. Soc.* **2003**, *125*, 4862–4869.
- (42) Fermin, D. J.; Jensen, H.; Moser, J. E.; Girault, H. H. Organisation and Reactivity of Nanoparticles at Molecular Interfaces. Part II. ‡ Dye Sensitisation of TiO₂ Nanoparticles Assembled at the Water/1,2-Dichloroethane Interface. *PhysChemPhys* **2003**, *4*, 85–89.
- (43) Zhang, L.; Kitazumi, Y.; Kakiuchi, T. Potential-Dependent Adsorption and Transfer of Poly(diallyldialkylammonium) Ions at the Nitrobenzene|water Interface. *Langmuir* **2011**, *27*, 13037–13042.
- (44) Kitazumi, Y.; Kakiuchi, T. Potential-Dependent Adsorption of Decylsulfate and Decylammonium prior to the Onset of Electrochemical Instability at the 1,2-Dichloroethane|water Interface. *Langmuir* **2009**, *25*, 8062–8068.
- (45) Samec, Z.; Trojánek, A.; Krtíl, P. Dynamics of Phospholipid Monolayers on Polarised Liquid-Liquid Interfaces. *Faraday Discuss.* **2005**, *129*, 301–313.
- (46) Uyanik, I.; Cengelöglu, Y. Voltammetric and Visual Evidence of Adsorption Reactions at the Liquid-liquid Interfaces Supported on a Metallic Electrode. *Electrochim. Acta* **2012**, *62*, 290–295.
- (47) Patri, A. K.; Majoros, I. J.; Baker, J. R. Dendritic Polymer Macromolecular Carriers for Drug Delivery. *Curr. Opin. Chem. Biol.* **2002**, *6*, 466–471.
- (48) Perez, G. P.; Crooks, R. M. Selectively Permeable Dendrimers as Molecular Gates. *Electrochem. Soc. Interface* **2001**, *10*, 34–38.

- (49) Hedden, R. C.; Bauer, B. J.; Smith, A. P.; Grohn, F.; Amis, E. Templating of Inorganic Nanoparticles by PAMAM/PEG Dendrimer – Star Polymers. *Polymer (Guildf)*. **2002**, *43*, 5473–5481.
- (50) Berduque, A.; Scanlon, M. D.; Collins, C. J.; Arrigan, D. W. M. Electrochemistry of Non-Redox-Active Poly(propylenimine) and Poly(amidoamine) Dendrimers at Liquid-Liquid Interfaces. *Langmuir* **2007**, *23*, 7356–7364.
- (51) Calderon, M.; Monzón, L. M. A.; Martinelli, M.; Juarez, A. V.; Strumia, M. C.; Yudi, L. M. Electrochemical Study of a Dendritic Family at the water/1,2-Dichloroethane Interface. *Langmuir* **2008**, *24*, 6343–6350.
- (52) Cheung, D. L.; Carbone, P. How Stable Are Amphiphilic Dendrimers at the Liquid-liquid Interface? *Soft Matter* **2013**, *9*, 6841–6850.
- (53) Herzog, G.; Flynn, S.; Johnson, C.; Arrigan, D. W. M. Electroanalytical Behavior of Poly-L-Lysine Dendrigrfts at the Interface between Two Immiscible Electrolyte Solutions. *Anal. Chem.* **2012**, *84*, 5693–5699.
- (54) Berduque, A.; Scanlon, M. D.; Collins, C. J.; Arrigan, D. W. M. Electrochemistry of Non-Redox-Active Poly(propylenimine) and Poly(amidoamine) Dendrimers at Liquid-Liquid Interfaces.pdf. *Langmuir* **2007**, *23*, 7356–7364.
- (55) Scanlon, M. D.; Strutwolf, J.; Arrigan, D. W. M. Voltammetric Behaviour of Biological Macromolecules at Arrays of Aqueous|organogel Micro-Interfaces. *Phys. Chem. Chem. Phys.* **2010**, *12*, 10040–10047.
- (56) Herzog, G.; Kam, V.; Arrigan, D. W. M. Electrochemical Behaviour of Haemoglobin at the Liquid/liquid Interface. *Electrochim. Acta* **2008**, *53*, 7204–7209.
- (57) Kitazumi, Y.; Kakiuchi, T. Electrochemical Instability in Liquid-Liquid Two-Phase Systems. *Bull. Chem. Soc. Jpn.* **2011**, *84*, 1312–1320.
- (58) Cousens, N. E. A.; Kucernak, A. R. Electrochemistry of the Ionic Liquid|oil Interface: A New Water-Free Interface between Two Immiscible Electrolyte Solutions. *Electrochem. Commun.* **2013**, *31*, 63–66.
- (59) Kakiuchi, T.; Tsujioka, N. Electrochemical Polarizability of the Interface between an Aqueous Electrolyte Solution and a Room-Temperature Molten Salt. *J. Electroanal. Chem.* **2007**, *599*, 209–212.
- (60) Toth, P. S.; Dryfe, R. A. . Novel Organic Solvents for Electrochemistry at the Liquid/liquid Interface. *Analyst* **2015**, *140*, 1947–1954.
- (61) Valent, O.; Koryta, J.; Panoch, M. Voltammetric Study of Ion Transfer across the Water/o-Nitrophenyloctyl Ether Interface. *J. Electroanal. Chem.* **1987**, *226*, 21–25.

- (62) Samec, Z.; Trojánek, A.; Samcová, E. A Four-Electrode Microcell for Electrochemical Measurements at the Interface between Two Immiscible Electrolyte Solutions. *J. Electroanal. Chem.* **1995**, *386*, 225–228.
- (63) Katano, H.; Tatsumi, H.; Senda, M. Ion-Transfer Voltammetry at 1,6-Dichlorohexane|water and 1,4-Dichlorobutane|water Interfaces. *Talanta* **2004**, *63*, 185–193.
- (64) Ulmeanu, S. M.; Jensen, H.; Samec, Z.; Bouchard, G.; Carrupt, P.-A.; Girault, H. H. Cyclic Voltammetry of Highly Hydrophilic Ions at a Supported Liquid Membrane. *J. Electroanal. Chem.* **2002**, *530*, 10–15.
- (65) Cousens, N. E. A.; Kucernak, A. R. Increasing the Potential Window of the Interface between Two Immiscible Electrolyte Solutions to More than 1.2V. *Electrochem. commun.* **2011**, *13*, 1539–1541.
- (66) Y. Shao, A. A. S.; Girault, H. H. Determination of the Half-Wave Potential of the Species Limiting the Potential Window. *J. Chem. Soc. Faraday Trans.* **1991**, *87*, 2593–2597.
- (67) Markin, V. S.; Volkov, A. G. Electrocapillary Phenomena at Polarizable and Reversible Interfaces between Two Immiscible Liquids: The Generalized Electrocapillary Equation in Hansen's Representation. **1990**, *35*, 715–724.
- (68) Markin, V. S.; Volkov, A. G. Potentials at the Interface between Two Immiscible Electrolyte Solutions. *Adv. Colloid Interface Sci* **1990**, *31*, 111–152.
- (69) Ding, Z.; Quinn, B. M.; Bard, A. J. Kinetics of Heterogeneous Electron Transfer at Liquid/Liquid Interfaces As Studied by SECM. *J. Phys. Chem. B* **2001**, *105*, 6367–6374.
- (70) Kakiuchi, T. Potential-Dependent Adsorption and Partitioning of Ionic Components at a Liquid|liquid Interface. *J. Electroanal. Chem.* **2001**, *496*, 137–142.
- (71) Kakiuchi, T. Electrochemical Instability of the Liquid|liquid Interface in the Presence of Ionic Surfactant Adsorption. *J. Electroanal. Chem.* **2002**, *536*, 63–69.
- (72) Kitazumi, Y.; Kakiuchi, T. A Model of the Electrochemical Instability at the Liquid|liquid Interface Based on the Potential-Dependent Adsorption and Gouy's Double Layer Theory. *J. Electroanal. Chem.* **2010**, *648*, 8–14.
- (73) Kakiuchi, T.; Chiba, M.; Sezaki, N.; Nakagawa, M. Cyclic Voltammetry of the Transfer of Anionic Surfactant across the Liquid-liquid Interface Manifests Electrochemical Instability. *Electrochem. Commun.* **2002**, *4*, 701–704.
- (74) Kakiuchi, T.; Nishi, N.; Kasahara, T.; Chiba, M. Regular Irregularity in the Transfer of Anionic Surfactant across the Liquid/liquid Interface. *Chemphyschem* **2003**, *4*, 179–185.

- (75) Kasahara, T.; Nishi, N.; Yamamoto, M.; Kakiuchi, T. Electrochemical Instability in the Transfer of Cationic Surfactant across the 1,2-Dichloroethane/water Interface. *Langmuir* **2004**, *20*, 875–881.
- (76) Kakiuchi, T. Electrochemical Instability in Facilitated Transfer of Alkaline-Earth Metal Ions across the Nitrobenzene|water Interface. *J. Electroanal. Chem.* **2004**, *569*, 287–291.
- (77) Scanlon, M. D.; Arrigan, D. W. M. Enhanced Electroanalytical Sensitivity via Interface Miniaturisation: Ion Transfer Voltammetry at an Array of Nanometre Liquid-Liquid Interfaces. *Electroanalysis* **2011**, *23*, 1023–1028.
- (78) Collins, C. J.; Arrigan, D. W. M. Ion-Transfer Voltammetric Determination of the Beta-Blocker Propranolol in a Physiological Matrix at Silicon Membrane-Based Liquid|liquid Microinterface Arrays. *Anal. Chem.* **2009**, *81*, 2344–2349.
- (79) Taylor, G.; Girault, H. H. Ion Transfer Reaction across a Liquid - Liquid Interface Supported on a Micropipette Tip. *J. Electroanal. Chem.* **1986**, *208*, 179–183.
- (80) Stockmann, T. J.; Zhang, J.; Wren, J. C.; Ding, Z. Hydrophobic Alkylphosphonium Ionic Liquid for Electrochemistry at Ultramicroelectrodes and Micro Liquid|liquid Interfaces. *Electochim. Acta* **2012**, *62*, 8–18.
- (81) Amemiya, S.; Wang, Y.; Mirkin, M. V. *Electrochemistry*; Wadhawan, J. D.; Compton, R. G., Eds.; Electrochemistry; Royal Society of Chemistry: Cambridge, 2013; Vol. 12.
- (82) Scanlon, M. D.; Strutwolf, J.; Blake, A.; Iacopino, D.; Quinn, A. J.; Arrigan, D. W. M. Ion-Transfer Electrochemistry at Arrays of Nanointerfaces between Immiscible Electrolyte Solutions Confined within Silicon Nitride Nanopore Membranes. *Anal. Chem.* **2010**, *82*, 6115–6123.
- (83) Zazpe, R.; Hibert, C.; O'Brien, J.; Lanyon, Y. H.; Arrigan, D. W. M. Ion-Transfer Voltammetry at Silicon Membrane-Based Arrays of Micro-Liquid-Liquid Interfaces. *Lab Chip* **2007**, *7*, 1732–1737.
- (84) Davies, T. J.; Compton, R. G. The Cyclic and Linear Sweep Voltammetry of Regular and Random Arrays of Microdisc Electrodes: Theory. *Anal. Lett.* **2005**, *585*, 63–82.
- (85) Silicon - properties and uses, RSC Periodic Table <http://www.rsc.org/periodic-table/element/14/silicon> (accessed May 12, 2015).
- (86) Information about Si - scifinder.cas.org.
- (87) Ralph K. Iler. *The Chemistry of Silica: Solubility, Polymerization, Colloid and Surface Properties and Biochemistry of Silica*; 1979.

-
- (88) Lev, O.; Sampath, S. Sol-Gel Electrochemistry: Silica and Silicates. In *Electroanal. Chem., A Series of Advances: Volume 23*; 2010.
- (89) Rouquerol, J.; Avnir, D.; Fairbridge, C. W.; Everett, D. H.; Haynes, J. H.; Pernicone, N.; Ramsay, J. D. F.; Sing, K. S. W.; Unger, K. K. Recommendations for the Characterization of Porous Solids. **1994**, *66*, 1739–1758.
- (90) Walcarius, A. Template-Directed Porous Electrodes in Electroanalysis. *Anal. Bioanal. Chem.* **2010**, *396*, 261–272.
- (91) Velev, O. D.; Lenhoff, A. M. Colloidal Crystals as Templates for Porous Materials. *Curr. Opin. Colloid Interface Sci.* **2000**, *5*, 56–63.
- (92) Grosso, D.; Cagnol, F.; Soler-Illia, G. J. de A. A.; Crepaldi, E. L.; Amenitsch, H.; Brunet-Bruneau, a.; Bourgeois, a.; Sanchez, C. Fundamentals of Mesostructuring Through Evaporation-Induced Self-Assembly. *Adv. Funct. Mater.* **2004**, *14*, 309–322.
- (93) Lu, Y.; Gangull, R.; Drewien, C. A.; Anderson, M. T.; Brinker, C. J.; Gong, W.; Guo, Y.; Soyez, H.; Dunn, B.; Huang, M. H.; et al. Continuous Formation of Supported Cubic and Hexagonal Mesoporous Films by Sol – Gel Dip-Coating. *Nature* **1997**, *389*, 651–655.
- (94) Etienne, M.; Cortot, J.; Walcarius, A. Preconcentration Electroanalysis at Surfactant-Templated Thiol-Functionalized Silica Thin Films. *Electroanalysis* **2007**, *19*, 129–138.
- (95) Kong, D.; Yang, H.; Wei, S.; Li, D.; Wang, J. Gel-Casting without de-Airing Process Using Silica Sol as a Binder. *Ceram. Int.* **2007**, *33*, 133–139.
- (96) Olding, T.; Sayer, M.; Barrow, D. Ceramic Sol-gel Composite Coatings for Electrical Insulation. *Thin Solid Films* **2001**, *398-399*, 581–586.
- (97) Walcarius, A.; Sibottier, E.; Etienne, M.; Ghanbaja, J. Electrochemically Assisted Self-Assembly of Mesoporous Silica Thin Films. *Nat. Mater.* **2007**, *6*, 602–608.
- (98) Goux, A.; Etienne, M.; Aubert, E.; Lecomte, C.; Ghanbaja, J.; Walcarius, A. Oriented Mesoporous Silica Films Obtained by Electro-Assisted Self-Assembly (EASA). *Chem. Mater.* **2009**, *21*, 731–741.
- (99) Etienne, M.; Goux, A.; Sibottier, E.; Walcarius, A. Oriented Mesoporous Organosilica Films on Electrode: A New Class of Nanomaterials for Sensing. *J. Nanosci. Nanotechnol.* **2009**, *9*, 2398–2406.
- (100) Guillemin, Y.; Etienne, M.; Aubert, E.; Walcarius, A. Electrogeneration of Highly Methylated Mesoporous Silica Thin Films with Vertically-Aligned Mesochannels and Electrochemical Monitoring of Mass Transport Issues. *J. Mater. Chem.* **2010**, *20*, 6799.

- (101) Herzog, G.; Sibottier, E.; Etienne, M.; Walcarius, A. Electrochemically Assisted Self-Assembly of Ordered and Functionalized Mesoporous Silica Films: Impact of the Electrode Geometry and Size on Film Formation and Properties. *Faraday Discuss.* **2013**, *164*, 259–273.
- (102) Vilà, N.; Ghanbaja, J.; Aubert, E.; Walcarius, A. Electrochemically Assisted Generation of Highly Ordered Azide-Functionalized Mesoporous Silica for Oriented Hybrid Films. *Angew. Chemie* **2014**, *126*, 2989–2994.
- (103) Guainazzi, M.; Silvestri, G.; Serravalle, G. Electrochemical Metallization at the Liquid-Liquid Interfaces of Non-Miscible Electrolytic Solutions. *J.C.S. Chem. Comm.* **1975**, 200–201.
- (104) Su, B.; Abid, J.-P.; Fermín, D. J.; Girault, H. H.; Hoffmannová, H.; Krtíl, P.; Samec, Z. Reversible Voltage-Induced Assembly of Au Nanoparticles at Liquid/liquid Interfaces. *J. Am. Chem. Soc.* **2004**, *126*, 915–919.
- (105) Younan, N.; Hojeij, M.; Ribeaucourt, L.; Girault, H. H. Electrochemical Properties of Gold Nanoparticles Assembly at Polarised Liquid|liquid Interfaces. *Electrochem. Commun.* **2010**, *12*, 912–915.
- (106) Schaming, D.; Hojeij, M.; Younan, N.; Nagatani, H.; Lee, H. J.; Girault, H. H. Photocurrents at Polarized Liquid|liquid Interfaces Enhanced by a Gold Nanoparticle Film. *Phys. Chem. Chem. Phys.* **2011**, *13*, 17704–17711.
- (107) Cheng, Y.; Schiffrin, D. J. Electrodeposition of Metallic Gold Clusters at the water/1,2-Dichloroethane Interface. *J. Chem. Soc. Faraday Trans.* **1996**, *92*, 3865.
- (108) Gründer, Y.; Ho, H. L. .; Mosselmans, J. F. .; Schroeder, S. L. M.; Dryfe, R. A. W. Inhibited and Enhanced Nucleation of Gold Nanoparticles at the water|1,2-Dichloroethane Interface. *Phys. Chem. Chem. Phys.* **2011**, *13*, 15681–15689.
- (109) Gründer, Y.; Mosselmans, J. F. W.; Schroeder, S. L. M.; Dryfe, R. a W. In Situ Spectroelectrochemistry at Free-Standing Liquid-Liquid Interfaces: UV-Vis Spectroscopy, Microfocus X-Ray Absorption Spectroscopy, and Fluorescence Imaging. *J. Phys. Chem. C* **2013**, *117*, 5765–5773.
- (110) Uehara, A.; Hashimoto, T.; Dryfe, R. A. W. Au Electrodeposition at the Liquid-Liquid Interface: Mechanistic Aspects. *Electochim. Acta* **2014**, *118*, 26–32.
- (111) Kaminska, I.; Jonsson-Niedziolka, M.; Kaminska, A.; Pisarek, M.; Hołyst, R.; Opallo, M.; Niedziolka-Jonsson, J. Electrodeposition of Well-Adhered Multifarious Au Particles at a Solid|Toluene|Aqueous Electrolyte Three-Phase Junction. *J. Phys. Chem. C* **2012**, *116*, 22476–22485.

- (112) Edel, J. B.; Kornyshev, A. A.; Urbakh, M.; Campus, S. K.; Sw, L.; Kingdom, U.; Aviv, T. Self-Assembly of Nanoparticle Arrays for Use as Mirrors, Sensors, and Antennas. *ACS Nano* **2013**, *7*, 9526–9532.
- (113) Fang, P.-P.; Chen, S.; Deng, H.; Scanlon, M. D.; Gumy, F.; Lee, H. J.; Momotenko, D.; Amstutz, V.; Cortés-Salazar, F.; Pereira, C. M.; et al. Conductive Gold Nanoparticle Mirrors at Liquid/Liquid Interfaces. *ACS Nano* **2013**, *7*, 9241–9248.
- (114) Zeiri, L.; Younes, O.; Efrima, S.; Deutsch, M. Interfacial Electrodeposition of Silver. *J. Phys. Chem. B* **1997**, *101*, 9299–9308.
- (115) Zeiri, L.; Efrima, S.; Deutsch, M. AC-Driven Interfacial Electrodeposition of Silver. *Langmuir* **1997**, *13*, 4722–4728.
- (116) Zeiri, L.; Efrima, S. Interfacial Electrodeposition of Silver: The Role of Wetting. *Langmuir* **1998**, *12*, 5180–5187.
- (117) Guo, J.; Takahira, T.; Othman, R.; Unwin, P. R. Formation of Mesoscopic Silver Particles at Micro- and Nano- Liquid/liquid Interfaces. *Electrochem. commun.* **2003**, *5*, 1005–1010.
- (118) Li, F.; Edwards, M.; Guo, J.; Unwin, P. R. Silver Particle Nucleation and Growth at Liquid/Liquid Interfaces: A Scanning Electrochemical Microscopy Approach. *J. Phys. Chem. C* **2009**, *113*, 3553–3565.
- (119) Scholz, F.; Hasse, U. Controlling the Morphology of Silver Deposition at Liquid|liquid Interfaces: From Nano-Wires to Super Smooth Films. *Electrochem. commun.* **2005**, *7*, 541–546.
- (120) Hasse, U.; Palm, G. J.; Hinrichs, W.; Schäfer, J.; Scholz, F. The Growth of Single Crystal Silver Wires at the Nitrobenzene|water Interface. *Phys. Chem. Chem. Phys.* **2011**, *13*, 12254–12260.
- (121) Mirceski, V.; Gulaboski, R. Simple Electrochemical Method for Deposition and Voltammetric Inspection of Silver Particles at the Liquid - Liquid Interface of a Thin-Film Electrode. *J. Phys. Chem. B* **2006**, *110*, 2812–2820.
- (122) Trojánek, A.; Langmaier, J.; Samec, Z. Random Nucleation and Growth of Pt Nanoparticles at the Polarised Interface between Two Immiscible Electrolyte Solutions. *J. Electroanal. Chem.* **2007**, *599*, 160–166.
- (123) Platt, M.; Dryfe, R. A. W. Electrodeposition at the Liquid/liquid Interface: The Chronoamperometric Response as a Function of Applied Potential Difference. *J. Electroanal. Chem.* **2007**, *599*, 323–332.

- (124) Johans, C.; Lahtinen, R.; Kontturi, K.; Schiffrin, D. J. Nucleation at Liquid|liquid Interfaces: Electrodeposition without Electrodes. *J. Electroanal. Chem.* **2000**, *488*, 99–109.
- (125) Johans, C.; Liljeroth, P.; Kontturi, K. Electrodeposition at Polarisable Liquid|liquid Interfaces: The Role of Interfacial Tension on Nucleation Kinetics. *Phys. Chem. Chem. Phys.* **2002**, *4*, 1067–1071.
- (126) Platt, M.; Dryfe, A. W.; Roberts, E. P. L. Controlled Deposition of Nanoparticles at the Liquid – Liquid Interface. *Chem. Commun.* **2002**, 2324–2325.
- (127) Platt, M.; Dryfe, R. A. W.; Roberts, E. P. L. Electrodeposition of Palladium Nanoparticles at the Liquid–liquid Interface Using Porous Alumina Templates. *Electrochim. Acta* **2003**, *48*, 3037–3046.
- (128) Lahtinen, R.; Johans, C.; Hakkarainen, S.; Coleman, D.; Kontturi, K. Two-Phase Electrocatalysis by Aqueous Colloids. *Electrochem. commun.* **2002**, *4*, 479–482.
- (129) Nieminen, J. J.; Hatay, I.; Ge, P.; Méndez, M. a; Murtomäki, L.; Girault, H. H. Hydrogen Evolution Catalyzed by Electrodeposited Nanoparticles at the Liquid/liquid Interface. *Chem. Commun.* **2011**, *47*, 5548–5550.
- (130) Trojánek, A.; Langmaier, J.; Samec, Z. Electrocatalysis of the Oxygen Reduction at a Polarised Interface between Two Immiscible Electrolyte Solutions by Electrochemically Generated Pt Particles. *Electrochem. commun.* **2006**, *8*, 475–481.
- (131) Nelson, D. L.; Cox, M. M. *Principles of Biochemistry*; 2004.
- (132) Richter, R. P.; Derat, R.; Brisson, A. R. Formation of Supported Lipid Bilayers Formation of Solid-Supported Lipid Bilayers: An Integrated View. *Langmuir* **2006**, *22*, 3497–3505.
- (133) Castellana, E. T.; Cremer, P. S. Solid Supported Lipid Bilayers: From Biophysical Studies to Sensor Design. *Surf. Sci. Rep.* **2006**, *61*, 429–444.
- (134) McConnell, H. M. Structures and Transitions in Lipid Monolayers at the Air-Water Interface. *Annu. Rev. Phys. Chem.* **1991**, *42*, 171–195.
- (135) Santos, H. A.; García-Morales, V.; Pereira, C. M. Electrochemical Properties of Phospholipid Monolayers at Liquid-Liquid Interfaces. *Chemphyschem* **2010**, *11*, 28–41.
- (136) Jänchenová, H.; Štulík, K.; Mareček, V. Adsorption and Ion-Pairing Interactions of Phospholipids in the System of Two Immiscible Electrolyte Solutions. Part II: The Formation and Behaviour of a Lecithin Layer at the water/1,2-Dichloroethane

- Interface in the Presence of Multivalent Anions in the. *J. Electroanal. Chem.* **2007**, *604*, 109–114.
- (137) Jänchenová, H.; Lhotský, A.; Štulík, K.; Mareček, V. Adsorption and Ion-Pairing Interactions of Phospholipids in the System of Two Immiscible Electrolyte Solutions Part I. The Behaviour of Lecithin at the water/1,2-Dichloroethane Interface, Compared with that of Trimethyloctadecylammonium Cation. *J. Electroanal. Chem.* **2007**, *601*, 101–106.
- (138) Jänchenová, H.; Štulík, K.; Mareček, V. Adsorption and Ion-Pairing Interactions of Phospholipids in the System of Two Immiscible Electrolyte Solutions. *J. Electroanal. Chem.* **2008**, *612*, 186–190.
- (139) Kontturi, A.-K.; Kontturi, K.; Murtoms, L.; Quinn, B.; Cunnane, V. J. Study of Ion Transfer across Phospholipid Monolayers Adsorbed at Micropipette ITIES. *J. Electroanal. Chem.* **1997**, *424*, 69–74.
- (140) Murtoma, L. Surface Pressure Control of Phospholipid Monolayers at the Water/1,2-Dichloroethane Interface. *Langmuir* **1998**, *14*, 556–559.
- (141) Grandell, D.; Murtomaki, L.; Kontturi, K.; Sundholm, G. Phospholipid Monolayers Studied by a Combination of Cyclic Voltammetry and Langmuir Techniques at the Water 1,2-Dichloroethane Interface. *J. Electroanal. Chem.* **1999**, *463*, 242–247.
- (142) Malkia, A.; Liljeroth, P.; Kontturi, A.-K.; Kontturi, K. Electrochemistry at Lipid Monolayer-Modified Liquid-Liquid Interfaces as an Improvement to Drug Partitioning Studies. *J. Phys. Chem. B* **2001**, *105*, 10884–10892.
- (143) Malkia, A.; Liljeroth, P.; Kontturi, K. Membrane Activity of Ionisable Drugs – a Task for Liquid–liquid Electrochemistry? *Electrochem. Commun.* **2003**, *5*, 473–479.
- (144) Santos, H. A.; García-Morales, V.; Murtomäki, L.; Manzanares, J. A.; Kontturi, K. Preparation of Nanostructures Composed of Dextran Sulfate/ruthenium Nanoparticles and Their Interaction with Phospholipid Monolayers at a Liquid–liquid Interface. *J. Electroanal. Chem.* **2007**, *599*, 194–202.
- (145) Santos, H. A.; García-Morales, V.; Roozeman, R.-J.; Manzanares, J. A.; Kontturi, K. Interfacial Interaction between Dextran Sulfate and Lipid Monolayers: An Electrochemical Study. *Langmuir* **2005**, *21*, 5475–5484.
- (146) Santos, H. A.; Carlsson, S.; Murtomäki, L.; Kontturi, K. Effect of Gramicidin on Phospholipid-Modified Monolayers and on Ion Transfer at a Liquid-Liquid Interface. *Chemphyschem* **2007**, *8*, 913–920.

- (147) Murtomaki, L.; Manzanares, J. A.; Mafe, S.; Kontturi, K. *Liquid Interfaces in Chemical, Biological and Pharmaceutical Applications. Chapter 22: Phospholipids at Liquid-Liquid Interfaces and Their Effect on Charge Transfer*; 2001.
- (148) Pichot, R.; Watson, R. L.; Norton, I. T. Phospholipids at the Interface: Current Trends and Challenges. *Int. J. Mol. Sci.* **2013**, *14*, 11767–11794.
- (149) Cunnane, V. J.; Evans, U. Formation of Oligomers of Methyl- and Phenyl-Pyrrole at an Electrified Liquid/Liquid Interface. *Chem. Commun.* **1998**, 2163–2164.
- (150) Johans, C.; Clohessy, J.; Fantini, S.; Kyosti Kontturi; Cunnane, V. J. Electrosynthesis of Polyphenylpyrrole Coated Silver Particles at a Liquid – Liquid Interface. *Electrochem. Commun.* **2002**, *4*, 227–230.
- (151) Maeda, K.; Janchenova, H.; Lhotsky, A.; Stibor, I.; Budka, J.; Vladimir Marecek. Formation of a Polymer Layer from Monomers Adsorbed at a Liquid Liquid Interface. *J. Electroanal. Chem.* **2001**, *516*, 103–109.
- (152) Gorgy, K.; Fusalba, F.; Evans, U.; Kontturi, K.; Cunnane, V. J. Electropolymerization of 2,2': 5',2'' Terthiophene at an Electrified Liquid-Liquid Interface. *Synth. Met.* **2002**, *125*, 365–373.
- (153) Evans-Kennedy, U.; Clohessy, J.; Cunnane, V. J. Spectroelectrochemical Study F 2,2':5',2''-Terthiophene Polymerization at a Liquid / Liquid Interface Controlled by Potential-Determining Ions. *Macromolecules* **2004**, *37*, 3630–3634.
- (154) Vignali, M.; Edwards, R. a. H.; Serantoni, M.; Cunnane, V. J. Electropolymerized Polythiophene Layer Extracted from the Interface between Two Immiscible Electrolyte Solutions: Current–time Analysis. *J. Electroanal. Chem.* **2006**, *591*, 59–68.
- (155) Vignali, M.; Edwards, R.; Cunnane, V. J. Characterization of Doping and Electropolymerization of Free Standing Films of Polyterthiophene. *J. Electroanal. Chem.* **2006**, *592*, 37–45.
- (156) Knake, R.; Fahmi, A. W.; Tofail, S. A. M.; Clohessy, J.; Mihov, M.; Cunnane, V. J. Electrochemical Nucleation of Gold Nanoparticles in a Polymer Film at a Liquid-Liquid Interface. *Langmuir* **2005**, *21*, 1001–1008.
- (157) Lepková, K.; Clohessy, J.; Cunnane, V. J. The pH-Controlled Synthesis of a Gold Nanoparticle/polymer Matrix via Electrodeposition at a Liquid–liquid Interface. *J. Phys. Condens. Matter* **2007**, *19*, 375106.
- (158) Lepková, K.; Clohessy, J.; Cunnane, V. J. Electrodeposition of Metal-Based Nanocomposites at a Liquid–liquid Interface Controlled via the Interfacial Galvani Potential Difference. *Electochim. Acta* **2008**, *53*, 6273–6277.

- (159) Biswas, S.; Drzal, L. T. A Novel Approach to Create a Highly Ordered Monolayer Film of Graphene Nanosheets at the Liquid–Liquid Interface. *Nano Lett.* **2009**, *9*, 167–172.
- (160) Toth, P. S.; Ramasse, Q. M.; Velický, M.; Dryfe, R. A. W. Functionalization of Graphene at the Organic/water Interface. *Chem. Sci.* **2015**, *6*, 1316–1323.
- (161) Asuri, P.; Karajanagi, S. S.; Dordick, J. S.; Kane, R. S. Directed Assembly of Carbon Nanotubes at Liquid - Liquid Interfaces: Nanoscale Conveyors for Interfacial Biocatalysis. *J. Am. Chem. Soc.* **2006**, *128*, 1046–1047.
- (162) Tan, S.; Hojeij, M.; Su, B.; Meriguet, G.; Eugster, N.; Girault, H. H. 3D-ITIES Supported on Porous Reticulated Vitreous Carbon. *J. Electroanal. Chem.* **2007**, *604*, 65–71.
- (163) Toth, P. S.; Rodgers, A. N. J.; Rabiou, A. K.; Dryfe, R. A. W. Electrochemical Activity and Metal Deposition Using Few-Layer Graphene and Carbon Nanotubes Assembled at the Liquid–liquid Interface. *Electrochem. commun.* **2015**, *50*, 6–10.
- (164) Ge, P.; Scanlon, M. D.; Peljo, P.; Bian, X.; Vubrel, H.; O'Neill, A.; Coleman, J. N.; Cantoni, M.; Hu, X.; Kontturi, K.; et al. Hydrogen Evolution across Nano-Schottky Junctions at Carbon Supported MoS₂ Catalysts in Biphasic Liquid Systems. *Chem. Commun.* **2012**, *48*, 6484.
- (165) Bian, X.; Scanlon, M. D.; Wang, S.; Liao, L.; Tang, Y.; Liu, B.; Girault, H. H. Floating Conductive Catalytic Nano-Rafts at Soft Interfaces for Hydrogen Evolution. *Chem. Sci.* **2013**, *4*, 3432.
- (166) Trewyn, B. G.; Giri, S.; Slowing, I. I.; Lin, V. S.-Y. Mesoporous Silica Nanoparticle Based Controlled Release, Drug Delivery, and Biosensor Systems. *Chem. Commun. (Camb)*. **2007**, 3236–3245.
- (167) Angelomé, P. C.; Fuertes, M. C.; Soler-Illia, G. J. A. A. Multifunctional, Multilayer, Multiscale: Integrative Synthesis of Complex Macroporous and Mesoporous Thin Films with Spatial Separation of Porosity and Function. *Adv. Mater.* **2006**, *18*, 2397–2402.
- (168) Gaffney, D.; Cooney, J.; Magner, E. Modification of Mesoporous Silicates for Immobilization of Enzymes. *Top. Catal.* **2012**, *55*, 1101–1106.
- (169) Magner, E. Immobilisation of Enzymes on Mesoporous Silicate Materials. *Chem. Soc. Rev.* **2013**, *42*, 6213 – 6222.
- (170) Hudson, S.; Cooney, J.; Magner, E. Proteins in Mesoporous Silicates. *Angew. Chem. Int. Ed. Engl.* **2008**, *47*, 8582 – 8594.

- (171) Qi, G.; Wang, Y.; Estevez, L.; Duan, X.; Anako, N.; Park, A.-H. A.; Li, W.; Jones, C. W.; Giannelis, E. P. High Efficiency Nanocomposite Sorbents for CO₂ Capture Based on Amine-Functionalized Mesoporous Capsules. *Energy Environ. Sci.* **2011**, *4*, 444–452.
- (172) Yuliarto, B.; Zhou, H.; Yamada, T.; Honma, I.; Katsumura, Y.; Ichihara, M. Effect of Tin Addition on Mesoporous Silica Thin Film and Its Application for Surface Photovoltage NO₂ Gas Sensor. **2004**, *76*, 6719–6726.
- (173) Edler, K. J.; Yang, B. Formation of Mesostructured Thin Films at the Air-Liquid Interface. *Chem. Soc. Rev.* **2013**, *42*, 3765–3776.
- (174) Etienne, M.; Walcarius, A. Evaporation Induced Self-Assembly of Templated Silica and Organosilica Thin Films on Various Electrode Surfaces. *Electrochem. Commun.* **2005**, *7*, 1449–1456.
- (175) Niedziolka, J.; Opallo, M. Stabilising Electrode|redox Liquid|aqueous Solution System with Hydrophobic Silicate Film. *Electrochem. Commun.* **2004**, *6*, 475–479.
- (176) Niedziolka, J.; Opallo, M. Electrochemically Assisted Sol-gel Process at a Three Phase Junction. *Electrochem. Commun.* **2008**, *10*, 1445–1447.
- (177) Schachat, S.; Huo, Q.; Voigt-Martin, I. G.; Stucky, G. D.; Schuth, F. Oil-Water Interface Templating of Mesoporous Macroscale Structures. *Science (80-)*. **1996**, *273*, 768 – 771.
- (178) Huo, Q.; Zhao, D.; Feng, J.; Weston, K.; Buratto, S. K.; Stucky, G. D.; Scacht, S.; Shuth, F. Room Temperature Growth of Mesoporous Silica Fibres: A New High-Surface-Area Optical Waveguide. *Adv. Mater.* **1997**, *9*, 974–978.
- (179) F. Kleitz, F. Marlow, G.D. Stucky, F. S. Mesoporous Silica Fibers Synthesis, Internal Structure, and Growth Kinetics. *Chem. Mater.* **2001**, *13*, 3587 – 3595.
- (180) Faget, L.; Berman, A.; Regev, O. Synthesis of Unsupported Mesoporous Silica Interphasic Films at the Oil . Water Boundary. *Thin Solid Films* **2001**, *386*, 6–13.
- (181) He, J. X.; Cui, M. Y.; Zheng, Y. Y.; Tang, W. H.; Chen, B. Y.; Tsukamoto, K.; Li, C. R. Self-Assembly of Modified Silica Nanospheres at the Liquid/liquid Interface. *Mater. Lett.* **2010**, *64*, 463–465.
- (182) Ravera, F.; Santini, E.; Loglio, G.; Ferrari, M.; Liggieri, L. Effect of Nanoparticles on the Interfacial Properties of Liquid/liquid and Liquid/air Surface Layers. *J. Phys. Chem. B* **2006**, *110*, 19543–19551.
- (183) Whitby, C. P.; Fornasiero, D.; Ralston, J.; Liggieri, L.; Ravera, F. Properties of Fatty Amine-Silica Nanoparticle Interfacial Layers at the Hexane-Water Interface. *J. Phys. Chem. C* **2012**, *116*, 3050–3058.

- (184) Kulkarni, M. M.; Bandyopadhyaya, R.; Sharma, A. Janus Silica Film with Hydrophobic and Hydrophilic Surfaces Grown at an Oil–water Interface. *J. Mater. Chem.* **2008**, *18*, 1021–1028.
- (185) Biswas, K.; Rao, C. N. R. Nanocrystalline Janus Films of Inorganic Materials Prepared at the Liquid-Liquid Interface. *J. Colloid Interface Sci.* **2009**, *333*, 404–410.
- (186) Dryfe, R. A. W.; Holmes, S. M. Zeolitic Rectification of Electrochemical Ion Transfer. *J. Electroanal. Chem.* **2000**, *483*, 144–149.
- (187) Lillie, G. C.; Dryfe, R. A. W.; Holmes, S. M. Zeolite-Membrane Modulation of Simple and Facilitated Ion Transfer. *Analyst* **2001**, *126*, 1857–1860.
- (188) Senthilkumar, S.; Dryfe, R. A. W.; Saraswathi, R. Size-Selective Voltammetry: Modification of the Interface between Two Immiscible Electrolyte Solutions by Zeolite Y. *Langmuir* **2007**, *23*, 3455–3461.
- (189) Stephenson, M. J.; Holmes, S. M.; Dryfe, R. a W. Electrochemically Controlled Ion Exchange: Proton Exchange with Sodium Zeolite Y. *Angew. Chem. Int. Ed. Engl.* **2005**, *44*, 3075–3078.
- (190) Chen, Y.; Bian, S.; Gao, K.; Cao, Y.; Wu, H.; Liu, C.; Jiang, X.; Sun, X. Studies on the Meso-Sized Selectivity of a Novel Organic/inorganic Hybrid Mesoporous Silica Membrane. *J. Memb. Sci.* **2014**, *457*, 9–18.
- (191) Yamaguchi, A.; Kaneda, H.; Fu, W.; Teramae, N. Structural Control of Surfactant-Templated Mesoporous Silica Formed Inside Columnar Alumina Pores. *Adv. Mater.* **2008**, *20*, 1034–1037.
- (192) Jiang, X.; Gao, K.; Hu, D.; Wang, H.; Bian, S.; Chen, Y. Ion-Transfer Voltammetric Determination of Folic Acid at Meso-Liquid–liquid Interface Arrays. *Analyst* **2015**, *140*, 2823–2833.
- (193) Mareček, V.; Jänchenová, H. Electrochemically Controlled Formation of a Silicate Membrane at a Liquid|liquid Interface. *J. Electroanal. Chem.* **2003**, *558*, 119–123.
- (194) Jänchenová, H.; Štulík, K.; Mareček, V. Preparation of a Silicate Membrane at a Liquid|liquid Interface and Its Doping with a Platinum Ion. *J. Electroanal. Chem.* **2006**, *591*, 41–45.
- (195) Jensen, K. H.; Hanson, J. E. Synthesis and Photochemistry of Tertiary Amine Photobase Generators. *Chem. Mater.* **2002**, *14*, 918–923.
- (196) Stockmann, T. J.; Montgomery, A.-M.; Ding, Z. Determination of Alkali Metal Ion Transfers at Liquid|liquid Interfaces Stabilized by a Micropipette. *J. Electroanal. Chem.* **2012**, *684*, 6–12.

- (197) Arrigan, D. W. M.; Herzog, G.; Scanlon, M. D.; Strutwolf, J. Bioanalytical Applications of Electrochemistry at Liquid-Liquid Microinterfaces. *Electroanal. Chem., A Ser. Adv.* **2013**, *25*, 105–178.
- (198) Katakya, R.; Lopes, P. Chiral Detection at a Liquid-Liquid Interface. *Chem. Commun.* **2009**, 1490–1492.
- (199) Lopes, P.; Katakya, R. Chiral Interactions of the Drug Propranolol and A 1-Acid-Glycoprotein at a Micro Liquid – Liquid Interface. *Anal. Chem.* **2012**, *84*, 2299–2304.
- (200) Chemin, N.; Klotz, M.; Rouessac, V.; Ayrál, a.; Barthel, E. Mechanical Properties of Mesoporous Silica Thin Films: Effect of the Surfactant Removal Processes. *Thin Solid Films* **2006**, *495*, 210–213.
- (201) Guli, M.; Zhang, L.; Yao, J.; Li, X. Effect of Template-Removing Methods and Modification to Mesoporous Blank Silica and Compositated Silica. *Powder Technol.* **2012**, *219*, 271–275.
- (202) Parida, S. K.; Dash, S.; Patel, S.; Mishra, B. K. Adsorption of Organic Molecules on Silica Surface. *Adv. Colloid Interface Sci.* **2006**, *121*, 77–110.
- (203) Lin-Vien, D.; Colthup, N. B.; Fateley, W. G.; Grasselli, J. G. *The Handbook of Infrared and Raman Characteristic Frequencies of Organic Molecules*; 1991.
- (204) Sing, K. S. Z. *Reporting Physisorption Data for Gas/solid Systems with Special Reference to the Determination of Surface Area and Porosity*; 1982; Vol. 54.
- (205) Zhou, Y.; Schattka, J. H.; Antonietti, M. Room-Temperature Ionic Liquids as Template to Monolithic Mesoporous Silica with Wormlike Pores via a Sol–Gel Nanocasting Technique. *Nano Lett.* **2004**, *4*, 477–481.
- (206) Sepulveda, L.; Cortes, J. Ionization Degrees and Critical Micelle Concentrations of Hexadecyltrimethylammonium and Tetradecyltrimethylammonium Micelles with Different Counterions. *J. Phys. Chem.* **1985**, *89*, 5322–5324.
- (207) Liu, S.; Cool, P.; Collart, O.; Van Der Voort, P.; Vansant, E. F.; Lebedev, O. I.; Van Tendeloo, G.; Jiang, M. The Influence of the Alcohol Concentration on the Structural Ordering of Mesoporous Silica: Cosurfactant versus Cosolvent. *J. Phys. Chem. B* **2003**, *107*, 10405–10411.
- (208) Pabisch, S.; Feichtenschlager, B.; Kickelbick, G.; Peterlik, H. Effect of Interparticle Interactions on Size Determination of Zirconia and Silica Based Systems - A Comparison of SAXS, DLS, BET, XRD and TEM. *Chem. Phys. Lett.* **2012**, *521*, 91–97.
- (209) Berduque, A.; Lanyon, Y. H.; Beni, V.; Herzog, G.; Watson, Y. E.; Rodgers, K.; Stam, F.; Alderman, J.; Arrigan, D. W. M. Voltammetric Characterisation of Silicon-Based

- Microelectrode Arrays and Their Application to Mercury-Free Stripping Voltammetry of Copper Ions. *Talanta* **2007**, *71*, 1022–1030.
- (210) Morf, W. E.; Rooij, N. F. De. Performance of Amperometric Sensors Based on Multiple Microelectrode Arrays. *Sens. Actuators, B* **2000**, *44*, 538–541.
- (211) Kim, H.; Lim, K. Sizes and Structures of Micelles of Cationic Octadecyl Trimethyl Ammonium Chloride and Anionic Ammonium Dodecyl Sulfate Surfactants in Aqueous Solutions. *Bull. Korean Chem. Soc.* **2004**, *25*, 382–388.
- (212) Dean, J. A. *Lange's Handbook of Chemistry*; 1999.
- (213) Dale, S. E. C.; Unwin, P. R. Polarised Liquid/liquid Micro-Interfaces Move during Charge Transfer. *Electrochem. Commun.* **2008**, *10*, 723–726.
- (214) Silver, B. R.; Fülöp, V.; Unwin, P. R. Protein Crystallization at Oil/water Interfaces. *New J. Chem.* **2011**, *35*, 602–606.
- (215) Gupta, R.; Chaudhury, N. K. Entrapment of Biomolecules in Sol-Gel Matrix for Applications in Biosensors: Problems and Future Prospects. *Biosens. Bioelectron.* **2007**, *22*, 2387–2399.
- (216) Ho, M.; Pemberton, J. E. Alkyl Chain Conformation of Octadecylsilane Stationary Phases by Raman Spectroscopy. 1. Temperature Dependence. *Anal. Chem.* **1998**, *70*, 4915–4920.
- (217) Booth, S. G.; Cowcher, D. P.; Goodacre, R.; Dryfe, R. A. W. Electrochemical Modulation of SERS at the Liquid/liquid Interface. *Chem. Commun. (Camb.)* **2014**, *50*, 4482–4484.
- (218) Veres, M.; Füle, M.; Tóth, S.; Koós, M.; Pócsik, I. Surface Enhanced Raman Scattering (SERS) Investigation of Amorphous Carbon. *Diam. Relat. Mater.* **2004**, *13*, 1412–1415.
- (219) Silvester, D. S.; Arrigan, D. W. M. Array of Water|room Temperature Ionic Liquid Micro-Interfaces. *Electrochem. Commun.* **2011**, *13*, 477–479.
- (220) Fermin, D. J. Linear and Non-Linear Spectroscopy at the Electrified Liquid-Liquid Interface. In *Diffraction and Spectroscopic Methods in Electrochemistry*; Alkire, R. C.; Kolb, D. M.; Lipkowski, J.; Ross, P. N., Eds.; Wiley- VCH: Weinheim, 2006; pp. 127–162.
- (221) Ding, Z.; Wellington, R. G.; Brevet, P.-F.; Girault, H. H. Differential Cyclic Voltabsorptometry and Chronoabsorptometry Studies of Ion Transfer Reactions at the water|1,2-Dichloroethane Interface. *J. Electroanal. Chem.* **1997**, *420*, 35–41.
- (222) Izquierdo, D.; Martinez, A.; Heras, A.; Lopez-Palacios, J.; Ruiz, V.; Dryfe, R. A. W.; Colina, A. Spatial Scanning Spectroelectrochemistry. Study of the Electrodeposition of Pd Nanoparticles at the Liquid/liquid Interface. *Anal. Chem.* **2012**, *84*, 5723–5730.

- (223) Grunder, Y.; Mosselmans, J. F. W.; Schroeder, S. L. M.; Dryfe, R. A. . W. In Situ Spectroelectrochemistry at Free-Standing Liquid–Liquid Interfaces: UV–vis Spectroscopy, Microfocus X-Ray Absorption Spectroscopy, and Fluorescence Imaging. *J. Phys. Chem. C* **2013**, *117*, 5765–5773.
- (224) Kakiuchi, T.; Ono, K.; Takasu, Y.; Bourson, J.; Valeur, B. Voltage-Controlled Fluorometry of the Transfer of Nonfluorescent Ions across the 1,2-Dichloroethane/Water Interface Using Fluorescent Ionophores. *Anal. Chem.* **1998**, *70*, 4152–4156.
- (225) Kakiuchi, T.; Takasu, Y. Ion Selectivity of Voltage-Scan Fluorometry at the 1,2-Dichloroethane/water Interface. *J. Electroanal. Chem.* **1994**, *365*, 293–297.
- (226) Nagatani, H.; Iglesias, R. A.; Fermin, D. J.; Brevet, P.-F.; Girault, H. H. Adsorption Behavior of Charged Zinc Porphyrins at the Water/1,2-Dichloroethane Interface Studied by Potential Modulated Fluorescence Spectroscopy. *J. Phys. Chem. B* **2000**, *104*, 6869–6876.
- (227) Amatore, C.; Bonhomme, F.; Bruneel, J.-L.; Servant, L.; Thouin, L. Mapping Dynamic Concentration Profiles with Micrometric Resolution near an Active Microscopic Surface by Confocal Resonance Raman Microscopy. Application to Diffusion near Ultramicroelectrodes: First Direct Evidence for a Conproportionation Reaction. *J. Electroanal. Chem.* **2000**, *484*, 1–17.
- (228) Szunerits, S.; Garrigue, P.; Bruneel, J.-L.; Servant, L.; Sojic, N. Fabrication of a Sub-Micrometer Electrode Array: Electrochemical Characterization and Mapping of an Electroactive Species by Confocal Raman Microspectroscopy. *Electroanal.* **2003**, *15*, 548–555.
- (229) Edwards, H. G. M.; Hughes, M. A.; Smith, D. N. Raman Microscopic Studies of the Liquid-Liquid Interface between an Organic Layer and an Aqueous Solution Containing Metal Ions. *Vib. Spectrosc.* **1996**, *10*, 281–289.
- (230) Yamamoto, S.; Watarai, H. Surface-Enhanced Raman Spectroscopy of Dodecanethiol-Bound Silver Nanoparticles at the Liquid/liquid Interface. *Langmuir* **2006**, *22*, 6562–6569.
- (231) Das, B.; Maitra, U.; Biswas, K.; Varghese, N.; Rao, C. N. R. Surface-Enhanced Raman Scattering of Molecules Adsorbed on Nanocrystalline Au and Ag Films Formed at the Organic–aqueous Interface. *Chem. Phys. Lett.* **2009**, *477*, 160–163.
- (232) Guo, S.; Dong, S.; Wang, E. Rectangular Silver Nanorods: Controlled Preparation, Liquid–Liquid Interface Assembly, and Application in Surface-Enhanced Raman Scattering. *Cryst. Growth Des.* **2009**, *9*, 372–377.

- (233) De Serio, M.; Mohapatra, H.; Zenobi, R.; Deckert, V. Investigation of the Liquid–liquid Interface with High Spatial Resolution Using near-Field Raman Spectroscopy. *Chem. Phys. Lett.* **2006**, *417*, 452–456.
- (234) Ibañez, D.; Plana, D.; Heras, a.; Fermín, D. J.; Colina, a. Monitoring Charge Transfer at Polarizable Liquid/liquid Interfaces Employing Time-Resolved Raman Spectroelectrochemistry. *Electrochem. commun.* **2015**, *54*, 14–17.
- (235) Kato, M.; Abe, I.; Taniguchi, Y. Raman Study of the Trans–gauche Conformational Equilibrium of 1,2-Dichloroethane in Water: Experimental Evidence for the Hydrophobic Effect. *J. Chem. Phys.* **1999**, *110*, 11982–11986.
- (236) Durig, J. R.; Little, T. S.; Gounev, T. K.; Gardner Jr, J. K.; Sullivan, J. F. Infrared and Raman Spectra, Conformational Stability, Vibrational Assignment, and Ab Initio Calculations of Chloromethyl Isocyanate. *J. Mol. Struct.* **1996**, *375*, 83–94.
- (237) Laforge, F. O.; Carpino, J.; Rotenberg, S. A.; Mirkin, M. V. Electrochemical Attosyringe. *Proc. Natl. Acad. Sci. U.S.A.* **2007**, *104*, 11895–11900.
- (238) Wangchareansak, T.; Keniry, M. A.; Liu, G.; Craig, V. S. J. Coadsorption of Low-Molecular Weight Aromatic and Aliphatic Alcohols and Acids with the Cationic Surfactant, CTAB, on Silica Surfaces. *Langmuir* **2014**, *30*, 6704–6712.
- (239) Guillemin, Y.; Ghanbaja, J.; Aubert, E.; Etienne, M.; Walcarius, A. Electro-Assisted Self-Assembly of Cetyltrimethylammonium- Templated Silica Films in Aqueous Media : Critical Effect of Counteranions on the Morphology and Mesostructure Type. *Chem. Mater.* **2014**, *26*, 1848–1858.
- (240) Badiei, A.-R.; Cantournet, S.; Morin, M.; Bonneviot, L. Anion Effect on Surface Density of Silanolate Groups in As-Synthesized Mesoporous Silicas. *Langmuir* **1998**, *14*, 7087–7090.
- (241) Adeniran, B.; Mokaya, R. On the Shelf Life and Aging Stability of Mesoporous Silica: Insights on Thermodynamically Stable MCM-41 Structure from Assessment of 12-Year-Old Samples. *Chem. Mater.* **2012**, *24*, 4450–4458.
- (242) Wonorahardjo, S.; Ball, G. E.; Hook, J.; Moran, G. H. NMR Relaxation Monitoring of Gelation in Tetramethoxysilane Sol-Gels. *J. Non-Cryst. Solids* **2000**, *271*, 137–146.
- (243) Marlow, F.; Mcgehee, M. D.; Zhao, D.; Chmelka, B. F.; Stucky, G. D. Doped Mesoporous Silica Fibers : A New Laser Material **. *ADV MATER* **1999**, *11*, 632–636.
- (244) Young, M. D.; Borjemscaia, N. C.; Wladkowski, B. D. Quantitative Determination of the Rotameric Energy Differences of 1,2-Dihaloethanes Using Raman Spectroscopy. An Experimental Project for the Physical Chemistry Laboratory. *J. Chem. Educ.* **2005**, *82*, 912.

- (245) Olaya, A. J.; Méndez, M. A.; Cortes-Salazar, F.; Girault, H. H. Voltammetric Determination of Extreme Standard Gibbs Ion Transfer Energy. *J. Electroanal. Chem.* **2010**, *644*, 60–66.
- (246) Shao, Y.; Stewart, A. A.; Girault, H. H. Determination of the Half-Wave Potential of the Species Limiting the Potential Window. Measurement of Gibbs TRansfer Energies at the water/1,2-Dichloroethane Interface. *J. Chem. Soc. Faraday Trans.* **1991**, *87*, 2593–2597.
- (247) Ishimatsu, R.; Kim, J.; Jing, P.; Striemer, C. C.; Fang, D. Z.; Fauchet, P. M.; McGrath, J. L.; Amemiya, S. Ion-Selective Permeability of an Ultrathin Nanoporous Silicon Membrane as Probed by Scanning Electrochemical Microscopy Using Micropipet-Supported ITIES Tips. *Anal. Chem.* **2010**, *82*, 7127–7134.
- (248) Persello, J. Adsorption on Silica Surfaces. In *Adsorption on Silica Surfaces, Surf. Sci. Ser. Vol. 90*; Papirer, E., Ed.; Marcel Dekker: New York, 2000; pp. 317–318.
- (249) Sakae, H.; Nagatani, H.; Morita, K.; Imura, H. Spectroelectrochemical Characterization of Dendrimer-Porphyrin Associates at Polarized Liquid|liquid Interfaces. *Langmuir* **2014**, *30*, 937–945.
- (250) Nagatani, H.; Sakamoto, T.; Torikai, T.; Sagara, T. Encapsulation of Anilino-naphthalenesulfonates in Carboxylate-Terminated PAMAM Dendrimer at the Polarized water|1,2-Dichloroethane Interface. *Langmuir* **2010**, *26*, 17686–17694.
- (251) Nagatani, H.; Ueno, T.; Sagara, T. Spectroelectrochemical Analysis of Ion-Transfer and Adsorption of the PAMAM Dendrimer at a Polarized Liquid|liquid Interface. *Electrochim. Acta* **2008**, *53*, 6428–6433.
- (252) Hinoue, T.; Ikeda, E.; Watariguchi, S.; Kibune, Y. Thermal Modulation Voltammetry with Laser Heating at an Aqueous|nitrobenzene Solution Microinterface: Determination of the Standard Entropy Changes of Transfer for Tetraalkylammonium Ions. *Anal. Chem.* **2007**, *79*, 291–298.
- (253) Devarakonda, B.; Hill, R. A.; de Villiers, M. M. The Effect of PAMAM Dendrimer Generation Size and Surface Functional Group on the Aqueous Solubility of Nifedipine. *Int. J. Pharm.* **2004**, *284*, 133–140.
- (254) Collinson, M. M.; Moore, N.; Deepa, P. N.; Kanungo, M. Electrodeposition of Porous Silicate Films from Ludox Colloidal Silica. *Langmuir* **2003**, *19*, 7669–7672.
- (255) Shacham, R.; Avnir, D.; Mandler, D. Electrodeposition of Methylated Sol-Gel Films on Conducting Surfaces. *Adv. Mater.* **1999**, *11*, 384–388.
- (256) Shacham, R.; Avnir, D.; Mandler, D. Electrodeposition of Dye-Doped Titania Thin Films. *J. Sol-Gel Sci. Technol.* **2004**, *31*, 329–334.

- (257) Liu, L.; Mandler, D. Electro-Assist Deposition of Binary Sol-gel Films with Graded Structure. *Electrochim. Acta* **2013**, *102*, 212–218.
- (258) Raveh, M.; Liu, L.; Mandler, D. Electrochemical Co-Deposition of Conductive Polymer-Silica Hybrid Thin Films. *Phys. Chem. Chem. Phys.* **2013**, *15*, 10876–10884.
- (259) Suyama, K.; Shirai, M. Photobase Generators: Recent Progress and Application Trend in Polymer Systems. *Prog. Polym. Sci.* **2009**, *34*, 194–209.
- (260) Tsunooka, M.; Suyama, K.; Okumura, H.; Shirai, M. Development of Photoacid and Photobase Generators as the Key Materials for Design of Novel Photopolymers. *J. Photopolym. Sci. Technol.* **2006**, *19*, 65–71.
- (261) Wipf, D. O.; Ge, F.; Spaine, T. W.; Baur, J. E. Microscopic Measurement of pH with Iridium Oxide Microelectrodes. *Anal. Chem.* **2000**, *72*, 4921–4927.
- (262) Wang, M.; Yao, S.; Madou, M. A Long-Term Stable Iridium Oxide pH Electrode. *Sensors Actuators, B Chem.* **2002**, *81*, 313–315.
- (263) Zhao, P.; Cai, W. J. pH Polymeric Membrane Microelectrodes Based on Neutral Carriers and Their Application in Aquatic Environments. *Anal. Chim. Acta* **1999**, *395*, 285–291.
- (264) Nomura, S.; Nakao, M.; Nakanishi, T.; Takamatsu, S.; Tomita, K. Real-Time Imaging of Microscopic pH Distribution with a Two-Dimensional pH-Imaging Apparatus. *Anal. Chem.* **1997**, *69*, 977–981.
- (265) Honda, T.; Murase, K.; Hirato, T.; Awakura, Y. pH Measurement in the Vicinity of a Cathode Evolving Hydrogen Gas Using an Antimony Microelectrode. *J. Appl. Electrochem.* **1998**, *28*, 617–622.
- (266) Etienne, M.; Lhenry, S.; Cornut, R.; Lefrou, C. Optimization of the Shearforce Signal for Scanning Electrochemical Microscopy and Application for Kinetic Analysis. *Electrochim. Acta* **2013**, *88*, 877–884.
- (267) McClelland, R. a.; Kanagasabapathy, V. M.; Banait, N. S.; Steenken, S. Flash-Photolysis Generation and Reactivities of Triarylmethyl and Diarylmethyl Cations in Aqueous Solutions. *J. Am. Chem. Soc.* **1989**, *111*, 3966–3972.
- (268) Léonard, A.; Su, B.-L. A Novel and Template-Free Method for the Spontaneous Formation of Aluminosilicate Macro-Channels with Mesoporous Walls. *Chem. Commun.* **2004**, 1674–1675.
- (269) Cornut, R.; Lefrou, C. Studying Permeable Films with Scanning Electrochemical Microscopy (SECM): Quantitative Determination of Permeability Parameter. *J. Electroanal. Chem.* **2008**, *623*, 197–203.

(270) Company Sutter Instrument. Operation Manual P-2000 Micropipette Puller, 52.

Appendix I. Nanopipette preparation and silanization

All pipettes were pulled with P-2000 micropipette puller fabricated by Sutter Instrument Company (**Figure 1**). The protocol allows the preparation of the nanopipettes with the diameters ranging from 150 to 600 nm. Inner walls silanization prevents the ingress of the aqueous phase inside the nanopipette.

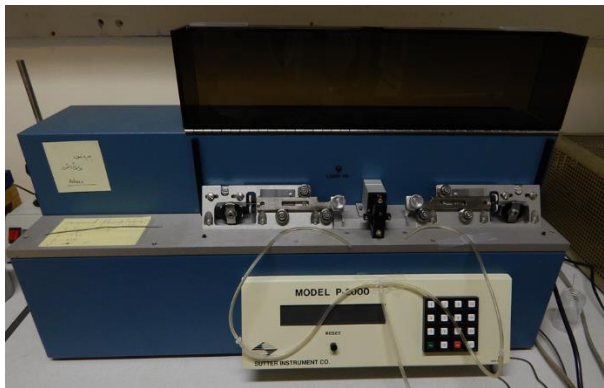


Figure 1. Pipette puller P-2000 from Sutter Instruments Company

1. The quartz capillaries with outer diameter (O.D.) = 1.2 mm and inner diameter (I.D.) = 0.9 mm were pulled with the following parameters:
 - **Heat: 810 – 870** (the energy supplied to the glass allows the control of the nanopore diameter. For higher energy longer tip and smaller pore was obtained. In order to obtain visible changes – factor change should be at least 10);
 - **Filament: 3** (this parameter regulate the scanning pattern of the laser spot and control the heat distribution within the scanning length);
 - **Velocity: 45** (this parameter specifies the velocity at which the glass carriage must be moving before hard pull);
 - **Delay: 150** (the parameter which controls the hard pull)
 - **Pull: 90** (the force applied when pulling).¹⁷

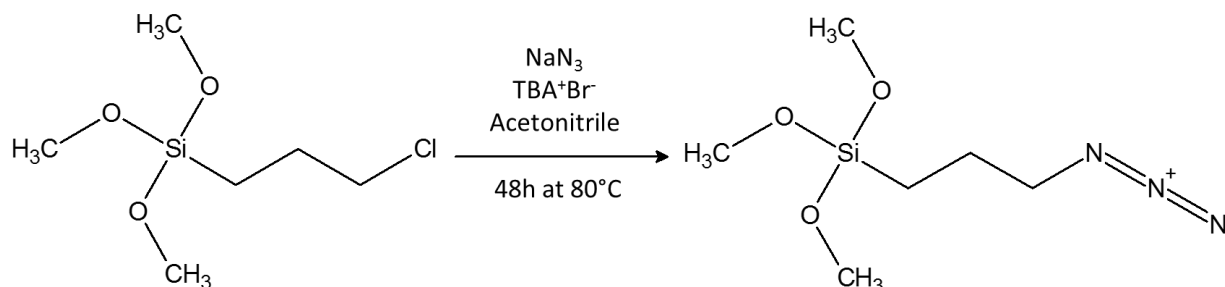
2. Each pulled capillary was observed with an optical microscope in order to verify effectiveness of applied pulling parameters.
3. Nanopipettes were then filled with the chlorotrimethylsilane so that the small volume of the solution ($\sim 1\mu\text{L}$) was placed inside the capillary in the close vicinity of the bigger entrance. Vertical position of the nanopipette, with the tip oriented upwards, was maintained all the time.
4. The nanopipette with the solution inside was left for 20 min (in vertical position!) under the fume hood.
5. After this time the residual solution was removed from inside the capillary and it was stored overnight in the oven at 130°C .
6. The nanopipette characterization was performed with the ion-transfer voltammetry. Prior to electrochemical measurement, nanopipettes were filled with the 10 mM solution of $\text{BTPPA}^+\text{TPBCl}^-$ in DCE. Frequently, during pipette filling air space separated the very end of the filled tip from the rest of organic solution filling the capillary. In order to remove this empty space from inside the tip, glass fiber (pulled out from Pasteur pipette above the Bunsen burner) could be used with diameter smaller than the inner diameter of the tip filled with the air bubble. The limiting current recorded at micro- and nanopipette can be calculated with the equation (1).

$$I_{ss} = 3.35\pi C F D n r \quad (\text{I.1})$$

where I_{ss} is the limiting current, C is the concentration of analyte in mol/cm^3 , D is the diffusion coefficient in cm^2/s , F is the Faraday constant ($96485 \text{ A}\cdot\text{s}/\text{mol}$) and n is the net charge of the analyte.

Appendix II. Protocol of preparation of 3-azidopropyltrimethoxysilane

The protocol was developed in LCPME laboratory.¹⁸ Overall reaction can be written as:



The protocol of preparation can be divided into few stages:

- 100 ml of acetonitrile was placed in round bottom two-neck flask. Top neck was covered with stopper. Side neck was covered with turn-over Flang stopper. N_2 passed through the solvent for 30 min. In order to do so, two needles were situated inside the turn-over Flang stopper, first – N_2 inlet immersed inside the solution and the second – outlet of the gas.
- After 30 minutes, 2.16 grams of sodium azide (NaN_3), 1.29 gram of tetrabutylammonium bromide (TBA^+Br^-) and 4 grams of 3-chloropropyltrimethoxysilane were added to vigorously stirred solvent inside the round bottom flask.
- Reaction mixture was stirred at 80°C (under reflux) for 48h in the set-up depicted on **Figure 2.15**.
- After this time, solvent was reduced with rotary evaporator **Figure 2.16**. Resulting crude oil was diluted in cyclohexane and filtered under gravity with paper filter.
- Cyclohexane was removed under reduced pressure with rotary evaporator. Azido functionalized silica precursor was collected and analyzed with Infra-Red (**Figure II.2**).

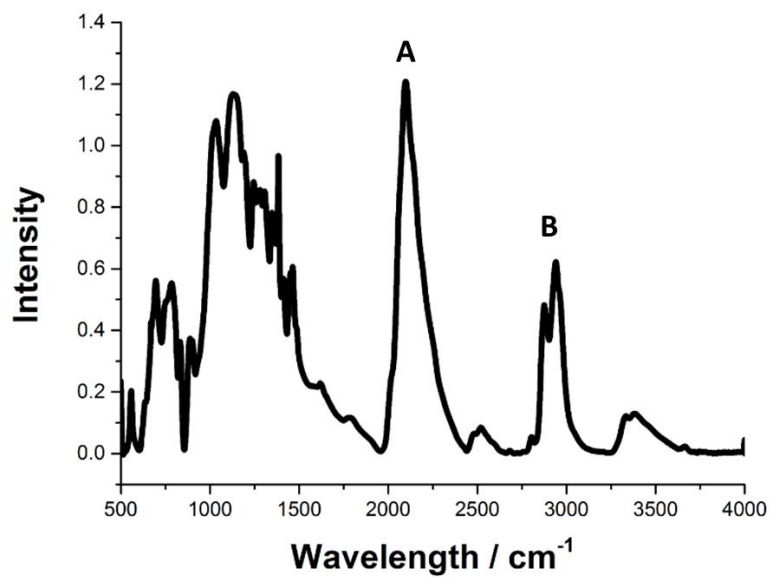


Figure II.2. FT-IR spectra recorded for AzPTMOS (few drops were put on glass support, dried in oven at 130°C for 4 hours and then scraped out, grated with KBr and pressed to form pellet). A – is the peak corresponding to N₃ vibrational mode; B – is the CH₂ and CH₃ vibrational modes.